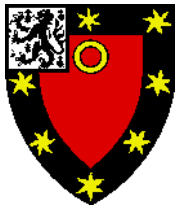
Calibration of the LEP collision energy during the 1995 Z^0 resonance scan and measurement of the inclusive leptonic decays of the Z^0 with the DELPHI detector

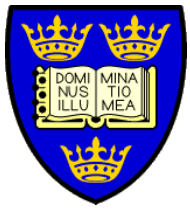
Kin Yip

St. John's College

Department of Particle and Nuclear Physics

University of Oxford





A thesis submitted for the degree of Doctor of Philosophy

at the University of Oxford

Michaelmas Term 1996

Calibration of the LEP collision energy during the 1995 Z^0 resonance scan and measurement of the inclusive leptonic decays of the Z^0 with the DELPHI detector

Kin Yip
St. John's College

Department of Particle and Nuclear Physics
University of Oxford

Abstract

During the 1995 LEP energy scan, both the energy measurements by resonant depolarization and by NMR probes in the LEP tunnel have confirmed that the LEP beam energy rises typically by about several MeV per beam during a fill. This was finally tracked down to be due to the currents flowing on the beampipe arising from the leakage currents from the trains running around Geneva. The full extent of these energy rises was not taken into account in the previous analysis of the 1993 scan.

In this thesis, various energy models, which attempt to describe the beam energy rise in a fill, are described and compared. The calculation of the LEP collision energies for all four LEP experiments and the systematic studies due to the uncertainty in the energy models are elaborated. The total errors due to the uncertainties of the absolute LEP energy scale on the mass and width of Z^0 boson in the 1995 scan are estimated to be about 1.5 and 1.7 MeV.

This thesis also contains an analysis of the process $e^+e^- \to l^+l^-$ of the Z^0 decays using the data collected by the DELPHI detector in 1993 and 1994 at energies within ± 2 GeV from the peak of Z^0 resonance. Charged leptons from the Z^0 decays were selected without discriminating between different lepton types, thus making it an inclusive or flavour-independent analysis.

The results of the measurements of cross-sections and forward-backward asymmetries are compared with those from the lepton-identified analyses and they are found to be generally consistent with each other. The values of cross-sections and asymmetries from the inclusive leptonic analysis together with the DELPHI hadronic cross-sections are used to extract various Z^0 resonance parameters. The leptonic partial width, Γ_l, is well constrained by this analysis and it is found to be : $\Gamma_l = 84.16 \pm 0.23$ MeV. All the fitted results obtained are consistent with the Standard Model predictions.

Submitted for the degree of Doctor of Philosophy at the University of Oxford
Michaelmas Term 1996

To My Parents

ACKNOWLEDGEMENTS

This thesis would not be possible without the explicit and implicit help from many people in Oxford and Switzerland.

I have had great supervision and guidance from my supervisors at Oxford. I am very grateful to Guy Wilkinson for taking care of me from the beginning to the end, and for his patience and wisdom in tackling all kinds of my physics and personal problems. I would also like to thank Pete Renton for introducing me to be a member of the LEP Energy working group and especially for carrying me through with his patient supervision in the energy analysis. My research life would have been very different without the enormous number of letters and signatures from Gerald Myatt and I sincerely thank him for being so considerate with me in physics and also finance.

I would also like to thank Tiziano Camporesi for providing me with the funding and chance to stay at CERN to work for the LEP Energy working group in the autumn of 1995. It was also extremely kind of Rhodes Trustees to provide additional financial support (which was like another annual stipend) for me to stay about six more months in Switzerland.

Thanks also go to Simon for giving me a view of another side of the British, which is the one side I feel easier to adapt to. No one could have surpassed Paula as my best skiing coach and I very much regret having insulted British cuisine in her presence. I sympathize with Ainsley for having to put up with me for three years in the same offices.

My first year multi-national neighbours in St. John Street were so wonderful that I have wished every year in Oxford was like the first one. In particular, Lisa with her counselling talent and widely open mind has helped me overcome a lot of my personal difficult times during the last three years. Volker is a very tolerant neighbour and I am very moved that he still keeps playing squash with me even after I chipped his molar.

The Christmas with O.B. and her family in her chalet at Villars was another unforgettable memory in the last three years, particularly for her overwhelmingly warm hospitality and the fascinating scenery of the gorgeous Alps.

I also owe 'my secretary' Beverly for her immeasurable time used for proof-reading my English writings including many of my application letters.

There are probably a great deal of other names which I have not mentioned. In this 'subtle way', I thank all of 'them'.

Contents

Contents v

List of Figures x

List of Tables xii

Introduction 1

Chapter 1. Standard Model 3
- 1.1 Local gauge invariance . . . 3
- 1.2 Standard Electroweak theory . . . 5
- 1.3 The Process $e^+e^- \to f^+f^-$ . . . 7
- 1.4 Cross-sections and Forward-Backward Asymmetries . . . 9
- 1.5 t-channel Bhabha scattering . . . 10
- 1.6 A few words about QCD . . . 11
- 1.7 Radiative corrections . . . 11
  - 1.7.1 Photonic Corrections . . . 13
  - 1.7.2 Non-photonic Corrections . . . 13
  - 1.7.3 QCD Corrections . . . 14
- 1.8 Improved Born Approximation . . . 14
- 1.9 Extraction of electroweak parameters . . . 16

Chapter 2. The Accelerator and the Detector 17
- 2.1 LEP, the accelerator . . . 17
- 2.2 DELPHI, the detector . . . 20
  - 2.2.1 Tracking Detectors . . . 22
  - 2.2.2 Calorimeter . . . 27
  - 2.2.3 Luminosity Monitors and Luminosity Measurements . . . 29

Chapter 3. The Inclusive Leptonic Analysis **33**
3.1 Data Processing in DELPHI . . . 33
3.1.1 Online: Data Acquisition System and Trigger . . . 33
3.1.2 Offline: From Raw Data to DST . . . 34
3.1.3 Event reconstruction . . . 34
3.1.4 Detector Simulation . . . 35
3.1.5 Event Tagging . . . 35
3.1.6 Reprocessing . . . 35
3.1.7 Microdst . . . 36
3.2 About the analysis . . . 36
3.3 Selection cuts . . . 37
3.3.1 Run-selection . . . 37
3.3.2 Preliminary cuts . . . 38
3.3.3 $P_{fastest} \geq 3$ GeV . . . 38
3.3.4 Topology cuts . . . 38
3.3.5 Missing Transverse Momentum ≥ 0.4 GeV . . . 40
3.3.6 Tight VD cuts . . . 41
3.4 Data Sample . . . 44

Chapter 4. Background and Efficiencies **46**
4.1 Cosmic Background . . . 46
4.1.1 1993 Cosmic Background Estimation . . . 46
4.1.2 1994 Cosmic Background Estimation . . . 48
4.1.3 Total Cosmic background . . . 48
4.2 Two-photon Background . . . 49
4.3 Hadronic Background . . . 51
4.4 Trigger Efficiency . . . 51
4.5 Detector Efficiencies . . . 51
4.5.1 θ and ϕ cracks in TPC . . . 52
4.5.2 Live Space Efficiency, ε^{live} . . . 56
4.5.3 Selection cut efficiencies, C^{cuts} . . . 58
4.5.4 Consistency check in Monte Carlo . . . 58
4.5.5 Final electron and muon selection efficiencies . . . 59
4.6 Tau efficiency . . . 60
4.6.1 Raw selection efficiency . . . 60
4.6.2 Correction from the real data . . . 60
4.6.3 Final Tau selection efficiency . . . 62

Chapter 5. Cross-Section and Forward-Backward Asymmetry **63**
5.1 Cross-Section . . . 63
5.2 Uncertainties on the cross-section measurement . . . 68
5.2.1 Statistical Errors . . . 68
5.2.2 Systematic Errors . . . 69
5.3 Forward-Backward Asymmetry . . . 72
5.4 Uncertainties on the forward-backward asymmetry . . . 76
5.4.1 Statistical Errors . . . 76
5.4.2 Systematic Errors . . . 77

Chapter 6. LEP Collision Energy **81**
6.1 History and Importance of Energy Measurements at LEP . . . 81
6.2 Principle of Resonant Depolarization . . . 83
6.2.1 Calibration accuracy . . . 85
6.2.2 From beam energy to centre-of-mass energy . . . 86
6.3 Parameters Affecting the Beam Energy . . . 86
6.3.1 Basic formulation . . . 87
6.3.2 Magnetic dipole and quadrupole fields . . . 89
6.3.3 Dipole field effects . . . 90
6.3.4 Quadrupole field effects . . . 93
6.3.5 e^+ beam energy . . . 97
6.4 IP-dependent Corrections . . . 97
6.4.1 Collision energy correction from the RF system . . . 97

Chapter 7. 1995 LEP Energy Scan **102**
7.1 Operating Conditions During 1995 LEP Scan . . . 102
7.1.1 Scan performance and strategy . . . 102
7.1.2 Bunch train operation . . . 103
7.1.3 Calibration strategy and statistics . . . 103
7.1.4 Monitoring of the beam energy in a fill . . . 103
7.1.5 Superconducting RF cavities . . . 104
7.1.6 Other aspects . . . 105
7.2 Monitoring system . . . 106
7.3 Preparation of data for analysis . . . 110

Chapter 8. New effects and corrections in 1995 **112**
8.1 Investigation of the magnetic dipole field at LEP . . . 112
8.1.1 Stability of the dipole field in a fill . . . 112
8.1.2 Train Effect . . . 115
8.1.3 Confirmation from long calibration experiments . . . 123
8.1.4 Conclusion on the LEP dipole field . . . 123
8.2 Vertical Dispersion Correction . . . 124
8.3 Bending Modulation . . . 127
8.4 Corrector . . . 130
8.5 RF complication in 1995 . . . 130

Chapter 9. Analysis and systematic studies of the LEP Energy in 1995 **132**
9.1 Pseudo device for measuring the dipole energy, NMR48 132
9.2 Temperature Coefficient 133
9.3 Determination of NMR48 Temperature coefficients 133
9.3.1 Facts and Difficulties 133
9.3.2 Calculations 134
9.3.3 Subtleties 137
9.3.4 Further Comments 139
9.3.5 Evaluating C_T^{48} at different energies 140
9.3.6 C_T^{48} compared with C_T^{ring} 141
9.4 NMR48 behaviour during a fill and day 142
9.5 Modelling beam energy rise during a fill 142
9.5.1 Direct NMR48 model 142
9.5.2 Average NMR48 model 144
9.5.3 Fitted depolarization and NMR48 models 145
9.5.4 Comparison among different models 147
9.6 Energy Model and the LEP Energies 148
9.7 Revision of 1993 Energies 150
9.8 Systematic studies in 1995 155
9.9 Energy Files and Error Covariance Matrix 162
9.10 Energy spread 163
9.11 Conclusion 166

Chapter 10. Discussion of Results **168**
10.1 Comparison between the results from the inclusive and identified leptonic analyses 168
10.2 Standard Model Fit 170
10.2.1 5-parameter fit 170
10.2.2 Derived parameters 172
10.3 Conclusion 175

Appendix A. t-channel correction in A_{FB} **176**

Appendix B. Momentum compaction factor **178**

References **180**

List of Figures

1.1 $e^+e^- \to l^+l^-$ process at Born level. 7
1.2 $e^+e^- \to e^+e^-$ process via t-channel 10
1.3 Theoretical behaviour of t-channel contribution 12
1.4 Radiative Corrections 13
1.5 QED correction on lineshape 14

2.1 LEP and the four experiments. 18
2.2 Schematic layout of DELPHI 21
2.3 Perspective view of Microvertex detector 23
2.4 Time projection chamber (TPC) 24
2.5 An azimuthal sector of the MUB 26
2.6 HPC cathode pad 28
2.7 A $\tau^+\tau^-$ event seen in the HCAL 29
2.8 Layout of the STIC region 32

3.1 Cross-section per fill 39
3.2 Distributions of missing transverse momenta 41
3.3 Impact Parameters in $R\phi$ and z 42
3.4 Impact parameters distribution $I^1_{R\phi}$ vs $I^2_{R\phi}$ 44
3.5 Momentum distribution for the fastest charged track 45

4.1 Impact parameter distribution of tracks (2D) 47
4.2 Two photon process. 49
4.3 modulo(ϕ, 60°) distribution 53
4.4 TPC cracks in θ 54
4.5 modulo(ϕ, 60°) distribution in θ crack 55

5.1 A_{FB} vs the centre-of-mass energy 76

6.1 Depolarization Resonance condition 85
6.2 Measured change of beam energy as a function of the RF frequency . 88
6.3 Temperature coefficient measurement (fill 1734 in 1993) 90
6.4 Sectional view of LEP dipole magnet 92
6.5 Tidal deformation of the Earth crust 94
6.6 Tide Experiments 95

6.7 Transverse beam position and LEP energy 96
6.8 RF sawtooth at LEP 98
6.9 Consistency checks in the RF model 101

7.1 Average temperature of the dipole magnets 105
7.2 Calculated Q_s - Measured Q_s 109

8.1 NMR readings during a typical fill 113
8.2 Anti-correlation between NMROCT4 and NMROCT8 114
8.3 Field Measurement of NMROCT8 during a typical fill 115
8.4 Correlation between fluxloop and NMR measurements 116
8.5 Correlation of earth cable currents within LEP 118
8.6 Train Effect 120
8.7 Typical online display of Vernier scans 126
8.8 Responses of 4 NMR's during bending modulations in 1995 128
8.9 Field increase after bending modulation 129

9.1 The changes of successive NMR readings 135
9.2 The temperature coefficients of NMR48 136
9.3 The temperature coefficients of NMR48 137
9.4 The temperature coefficients of the reference NMRREF 138
9.5 The temperature coefficients of the NMR's at IP 4 and 8 ($|\Delta$NMR$| <$ 2 MeV) 139
9.6 The temperature coefficients of the NMR's at IP 4 and 8 ($|\Delta$NMR$| <$ 4 MeV) 140
9.7 NMR48 behaviour in 1995. 143
9.8 BOF - EOF calibrations in 1995 and comparison with the energy model 146
9.9 Comparison between the energy model and the calibration measurements 150
9.10 Exhibition of the modelled beam energy variations during two fills . . 151
9.11 Comparison of NMR48 rises at P$-$2 and P+2 160

10.1 Comparison of Γ_l measurement with the Standard Model prediction . 174

List of Tables

1.1 Fermions and Bosons 4

2.1 Number of Z^0's collected by DELPHI in LEP1 20

3.1 Run-selection 37

4.1 Cosmic Backgrounds 49
4.2 Hadronic and two-photon Backgrounds 50
4.3 Trigger efficiencies in 1993 and 1994 51
4.4 Efficiency $\varepsilon_{\theta\phi}$ 56
4.5 Live Space efficiencies 57
4.6 Correction due to various realistic cuts, C^{cuts} 58
4.7 Final selection efficiencies 59
4.8 Tau selection efficiencies in 1993 and 1994 60
4.9 Tau correction factors in 1993 and 1994 61
4.10 Migration correction factors in 1993 and 1994 62
4.11 Final tau selection efficiencies in 1993 and 1994 62

5.1 Energy, luminosity and lepton candidates selected 64
5.2 R^{geom} 65
5.3 The values of the ratio $\frac{\sigma(s+t)}{\sigma(s)}$ 65
5.4 Correction factors for the leptonic cross-sections 67
5.5 Beam spread correction factors 68
5.6 Cross-sections and statistical errors 68
5.7 Theoretical uncertainties of TOPAZ0 and ALIBABA 71
5.8 Systematic errors on cross-section 72
5.9 Raw forward-backward asymmetry, A_{FB}^{raw} 73
5.10 Fractions of 1-1 events, F^{1-1} 74
5.11 A^{t-chan} 74
5.12 Correction factors for forward-backward asymmetry 75
5.13 Forward-Backward Asymmetries and statistical errors 75
5.14 Systematic errors on A_{FB} 79

6.1 Values of M_Z and Γ_Z 83

9.1 Temperature Coefficients of the NMR48 138
9.2 Temperature Coefficients of the NMRREF 138
9.3 Temperature Coefficients of NMR48 at different energies 141
9.4 Effects of the dipole field rise terms on the centre-of-mass energies . . 147
9.5 Preliminary LEP energies in 1995 150
9.6 Errors in the previous analysis of the LEP energy in 1993 152
9.7 Systematic errors on the centre-of-mass energies 157
9.8 Shifts in E_{CM} without certain corrections 161
9.9 Energy common error matrix 163
9.10 Centre-of-mass energy spread in 1995 165

10.1 Comparison of the inclusive and lepton-identified analyses 170
10.2 The results of the 5-parameter fit 171
10.3 The covariance matrix for the set of 5 parameters 172
10.4 Derived parameters from 5-parameter fit 172

Introduction

From the summer in 1989 to the autumn in 1995, LEP has been run at energies near the peak of Z^0 resonance. During this period, the precision on the resonance parameters of Z^0 decays, such as the mass of Z^0 (M_Z), has been improved by orders of magnitudes. This has been accomplished as a result of the precise measurements of cross-sections and asymmetries by the four LEP experiments and the accurate determination of the LEP collision energy by the LEP Energy working group.

As a member of the DELPHI collaboration as well as a member of the LEP Energy working group, the author has participated in both these endeavours. This thesis includes the analysis of energy calibration at LEP (mainly for the 1995 energy scan) and the measurement of the cross-sections and forward-backward asymmetries in the inclusive leptonic channel $e^+e^- \to l^+l^-$ of Z^0 decays recorded at the DELPHI experiment, using the 1993 and 1994 data.

The structure of this thesis is described as follows.

Chapter 1 provides an outline of the Standard Model focusing on the theoretical predictions of $e^+e^- \to l^+l^-$ near the peak of Z^0 resonance. Chapter 2 includes a brief description of the LEP collider and the DELPHI detector from which the data used in the following analyses were taken.

Chapters 3 to 5 cover the part of the inclusive leptonic analysis. In Chapter 3, the selection of events for the inclusive leptonic analysis from the data of the DELPHI experiment is described. Chapter 4 elaborates on how various backgrounds and efficiencies related to this analysis are calculated. The last chapter in this part, Chapter 5, presents the method of calculation and the results of the cross-sections and forward-backward asymmetries of the process $e^+e^- \to l^+l^-$ at different energies in 1993 and 1994.

Chapters 6 to 9 form the part devoted to the LEP collision energy calibration. Chapter 6 outlines the history of energy calibration at LEP, the general principles of energy calibration and the parameters which were known to affect the LEP energy before the 1995 scan. In Chapter 7, the operating conditions in the 1995 scan and the efforts made to log the data for the LEP energy analysis are described. Chapter 8 discusses the new effects encountered during the 1995 scan. Based on the previous three chapters, Chapter 9 describes how the energy model is constructed and used to interpolate the LEP energy between calibration measurements. Various systematic uncertainties and the preliminary energy error matrix for the 1993 and 1995 scans are also given in this chapter.

Finally, Chapter 10 compares the results of the inclusive leptonic analysis with those of the DELPHI lepton-identified analyses, and fits the results obtained in earlier chapters of this thesis against the Standard Model predictions to extract various Z^0 resonance parameters.

Chapter 1

Standard Model

The present package of theories dealing with all interactions among elementary particles is known as the Standard Model. In this Standard Model of elementary particle physics, matter is made up of 3 generations of quarks and leptons, both of which are called fermions (spin-$\frac{1}{2}$), as shown in Table 1.1. In addition, there are also various types of vector bosons, without which no interaction between particles is possible, also shown in Table 1.1.

In the scope of elementary particle physics [1], there are only three known and well-established interactions among those particles, i.e., strong, electromagnetic and weak, which are decreasing in strength in that order. The so-called Standard Model is a kind of quantum field theory, namely, the *gauge theory*, which essentially unifies the above three interactions,

1.1 Local gauge invariance

The present belief is that all particle interactions may be described by so-called local gauge symmetries.

In the framework of Lagrangian field theory, a Lagrangian is the starting point for describing the interaction of a system that we are interested in. Local gauge symmetry then means requiring the Lagrangian to be invariant under certain local gauge transformation; that is, a transformation which is a function of position in space-time x, in contrast to a global gauge transformation, which is the same everywhere in space-time.

[1] This just means that the gravitational interaction is neglected here.

Quarks

			I	I_3	Y	$Q = I_3 + Y/2$
$\begin{pmatrix} u \\ d' \end{pmatrix}_L$	$\begin{pmatrix} c \\ s' \end{pmatrix}_L$	$\begin{pmatrix} t \\ b' \end{pmatrix}_L$	$1/2$	$+1/2$ $-1/2$	$+1/3$	$+2/3$ $-1/3$
u_R	c_R	t_R	0	0	$+4/3$	$+2/3$
d'_R	s'_R	b'_R	0	0	$-2/3$	$-1/3$

Leptons

$\begin{pmatrix} \nu_e \\ e \end{pmatrix}_L$	$\begin{pmatrix} \nu_\mu \\ \mu \end{pmatrix}_L$	$\begin{pmatrix} \nu_\tau \\ \tau \end{pmatrix}_L$	$1/2$	$+1/2$ $-1/2$	-1	0 -1
e_R	μ_R	τ_R	0	0	-2	-1

Vector Bosons

$\begin{pmatrix} W^+ \\ Z^0 \\ W^- \end{pmatrix}$	1	$+1$ 0 -1	0	$+1$ 0 -1
γ	0	0	0	0
gluon	0	0	0	0

Scalar Boson

H^0	$1/2$	$-1/2$	1	0

Table 1.1: Three generations of quarks and leptons — fermions, vector and scalar bosons, and their respective quantum numbers. These form the basic constituents in the Standard Model of elementary particle physics. Note that, though γ and gluon have the same quantum numbers in this chart, γ only couples to electric charges while gluon only couples to colour charges.

In the case of QED (**Q**uantum **E**lectro-**D**ynamics), requiring the Lagrangian (constructed out of the field ψ) to be invariant under a local gauge (or phase) transformation such that

$$\psi' \rightarrow e^{i\alpha(x)}\psi \ ,$$

forces us to introduce a new gauge field, A_μ, which couples to charged particles in exactly the same way as the photon field. In fact, this family of phase transformation $\mathrm{U}(\alpha(x)) \equiv e^{i\alpha(x)}$, forms a unitary Abelian group known as the U(1) group, i.e., the the generators of U(1) commute with each other. This Abelian symmetry also means that the underlying field, i.e., photon, is not self-interacting.

However, in general, a gauge group can also be non-Abelian. The first application of local gauge invariance to a non-Abelian symmetry was due to Yang and Mills [1], who formulated a SU(2) gauge symmetry in an isospin space to account for the symmetry between the proton and the neutron in strong interactions.

Theories must be renormalizable, i.e., observables can be calculated to any order in the perturbation process in terms of a finite number of parameters, to be meaningful and useful. It has been shown [2] that for a theory to be renormalizable, it must be a Yang-Mills theory, that is, a theory with a local gauge invariance.

The full gauge group in the Standard Model is $\mathrm{SU(3)_c} \times \mathrm{SU(2)_L} \times \mathrm{U(1)_Y}$. It may be seen as a combination of unified electroweak theory in $\mathrm{SU(2)_L} \times \mathrm{U(1)}$ and QCD (**Q**uantum **C**hromo-**D**ynamics) in the form of $\mathrm{SU(3)_c}$ gauge group, formed from transformations of the 3 colours.

1.2 Standard Electroweak theory

The unified electroweak theory was first developed by Glashow, Salam and Weinberg [3] using Yang-Mills theory.

The basic interaction consists of an isotriplet of vector fields W_μ^i coupled with strength g to the weak isospin current J_μ^i, together with a single vector field B_μ coupled to the weak hypercharge current j_μ^Y with strength conventionally taken to the $g'/2$:

$$-ig(J^i)^\mu W_\mu^i - i\frac{g'}{2}(j^Y)^\mu B_\mu \ . \tag{1.1}$$

W_μ^i (i = 1, 2, 3) arise from local gauge invariance under $\mathrm{SU(2)}_L$ transformation on the weak isospin I. The subscript L on SU(2) is to remind us that the weak isospin

current couples only left-handed fermions. B_μ comes from local gauge invariance under $U(1)_Y$ transformation in the weak hypercharge Y. The weak hypercharge Y is related to the electric charge Q and the third component of weak isospin I_3 by

$$Q = I_3 + Y/2 \ . \tag{1.2}$$

These gauge fields are so far all massless. Introduction of mass terms in a Lagrangian would violate the SU(2) and U(1) gauge symmetry as well as render the theory unrenormalizable. In real life, however, we know that weak interactions are mediated by massive bosons of masses of the order of 100 GeV [4]. The heart of this electroweak theory lies in the spontaneous symmetry breaking under the Higgs mechanism to generate masses to the gauge bosons and at the same time the theory still remains renormalizable. The price we pay is that there should exist at least one Higgs boson (H^0), which has yet to be observed, and the mass of Higgs boson M_H is not predicted by the theory either. Finally, the resultant physical gauge fields are :

$$W_\mu^\pm = \frac{1}{\sqrt{2}}(W_\mu^1 \mp i W_\mu^2) \tag{1.3}$$

$$Z_\mu = \cos\theta_W W_\mu^3 - \sin\theta_W B_\mu \tag{1.4}$$

$$A_\mu = \sin\theta_W W_\mu^3 + \cos\theta_W B_\mu \tag{1.5}$$

where the first two equations represent the three massive bosons $W^\pm$ and Z^0 while the last equation is identified with the massless photon (γ) and θ_W is known as the Weinberg or weak mixing angle.

For the consistency of the electroweak theory with ordinary QED (with coupling constant $\alpha = e^2/4\pi$), the coupling constants, the weak mixing angle, the mass of $W^\pm$ (M_W) and the mass of Z^0 (M_Z) are related by the following equations :

$$\boxed{g \sin\theta_W = g' \cos\theta_W = e} \tag{1.6}$$

$$\boxed{\sin^2\theta_W = 1 - \frac{{M_W}^2}{{M_Z}^2}} \tag{1.7}$$

Applying the electroweak theory in lowest order to the muon lifetime with the result of Fermi model (with an effective coupling constant G_F), we have :

$$\boxed{\frac{G_F}{\sqrt{2}} = \frac{g^2}{8{M_W}^2}} \tag{1.8}$$

Note that in this lowest order, since α (fine structure constant) and G_F are known with practically negligible experimental errors, $\mathrm{M_W}$ and $\sin^2\theta_W$ are fixed once $\mathrm{M_Z}$ has been specified.

The relations (1.6 – 1.8) are in general modified by the inclusion of radiative corrections depending on the details of a chosen scheme. Here, the popular "on-shell" scheme [5] is adopted, in which the equation 1.7 is valid to all orders of perturbation theory. In this scheme, the physical content is represented by the set :

$$\boxed{\alpha,\ \mathrm{M_W},\ \mathrm{M_Z},\ \mathrm{M_H}, \{m_f\}} \tag{1.9}$$

(where $\{m_f\}$ is the set of fermion masses) as input (fundamental) parameters, together with the physical fields

$$W_\mu^\pm,\ Z_\mu,\ A_\mu\ . \tag{1.10}$$

As a result, equation 1.8 is modified to be

$$\frac{G_F}{\sqrt{2}} = \frac{g^2}{8{\mathrm{M_W}}^2} \times \frac{1}{1-\Delta r} \qquad \text{or} \qquad {\mathrm{M_W}}^2 = \frac{\pi\alpha}{\sqrt{2}G_F \sin^2\theta_W} \times \frac{1}{1-\Delta r} \tag{1.11}$$

The radiative correction Δr contains the photon vacuum polarization and weak corrections which depend on all parameters of the model, in particular, the mass of the Higgs boson, $\mathrm{M_H}$ and the mass of the top quark, $\mathrm{m_t}$.

1.3 The Process $e^+e^- \to f^+f^-$

In the lowest order (also known as the Born or tree level), the process $e^+e^- \to f^+f^-$ through the exchange of photon and $\mathrm{Z^0}$ in s-channel can be described by the Feynman diagrams in Fig. 1.1. If the final states are also e^+e^-, the t-channel exchange diagram would also contribute (see section 1.5).

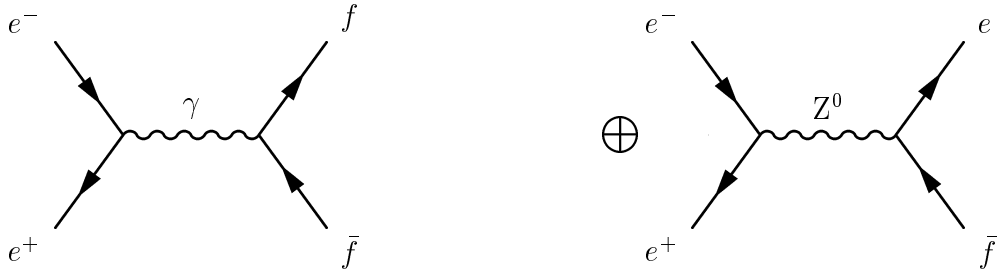
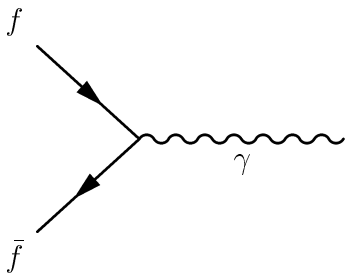
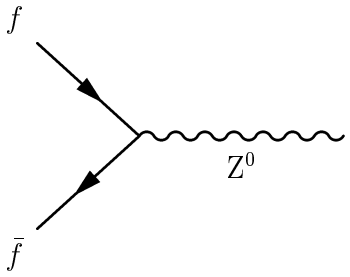


Figure 1.1: $e^+e^- \to l^+l^-$ process at Born level.

The Feynman rules for the above vertices are as follows :



$$\boxed{-ieQ_f\gamma^\mu}$$



$$\boxed{-i\frac{g}{\cos\theta_W}\ \gamma^\mu\ \frac{1}{2}(v_f - a_f\gamma^5)}$$

where v_f and a_f are respectively the vector and axial vector coupling constants between fermions and are given by

$$v_f = \mathrm{I}_3^f - 2Q_f \sin^2\theta_W \ ; \tag{1.12}$$

$$a_f = \mathrm{I}_3^f \ . \tag{1.13}$$

where I_3^f and Q_f denote the third isospin component and the electric charge of a given fermion species.

The propagators in Fig. 1.1 are :

$$\begin{cases} \gamma \text{ (Massless)} & : \quad \dfrac{-ig_{\mu\nu}}{q^2} & (1.14) \\ \mathrm{Z}^0 \text{ (Massive)} & : \quad \dfrac{-i(g_{\mu\nu} - q_\mu q_\nu)/\mathrm{M_Z}}{q^2 - {\mathrm{M_Z}}^2 + i\mathrm{M_Z}\Gamma_\mathrm{Z}} & (1.15) \end{cases}$$

where we have included the finite resonance width Γ_Z in the lowest order Breit-Wigner approximation, which is important when $\sqrt{s} \sim \mathrm{M_Z}$.

Neglecting the mass of fermions, the matrix element of the process $e^+e^- \to f^+f^-$ in Fig.1.1 is therefore given by : $\mathcal{M} = \mathcal{M}_\gamma + \mathcal{M}_{\mathrm{Z}^0}$ such that

$$\mathcal{M}_\gamma = ie^2Q_f(\ \bar{f}\gamma^\mu f\ )\frac{1}{q^2}(\ \bar{e}\gamma_\mu e\ ) \tag{1.16}$$

$$\mathcal{M}_{\mathrm{Z}^0} = \frac{ig^2}{4\cos^2\theta_W}\left[\bar{f}\ \gamma^\mu(v_f - a_f\gamma_5)\ f\right]\frac{1}{q^2 - {\mathrm{M_Z}}^2 + i\mathrm{M_Z}\Gamma_\mathrm{Z}}\left[\ \bar{e}\gamma_\mu(v_e - a_e\gamma_5)e\ \right] \tag{1.17}$$

e and $\bar{e}$ represents the initial states of e^-e^+ pairs, and f and $\bar{f}$ are the final states of $f\bar{f}$.

Deriving from the above matrix element, the differential cross section for the process $Z^0 \to f^+f^-$ is :

$$\frac{d\sigma}{d\Omega} = \frac{\alpha^2}{4s} N_C^f \cdot \Big[G_1(s) \cdot (\ 1 \ + \ \cos^2\theta \ ) \ + \ G_3(s) \cdot 2\cos\theta \Big] \tag{1.18}$$

where

$$\begin{aligned} G_1(s) &= Q_f^2 - 2v_e v_f Q_f \mathrm{Re}(\chi_0(s)) \ + \ (\ v_e^2 \ + \ a_e^2 \ )(\ v_f^2 \ + \ a_f^2 \ )|\chi_0(s)|^2 \\ G_3(s) &= -2a_e a_f Q_f \mathrm{Re}(\chi_0(s)) \ + \ 4v_e a_e v_f a_f |\chi_0(s)|^2 \end{aligned}$$

and

$$\chi_0(s) = \frac{1}{4\sin^2\theta_W \cos^2\theta_W} \frac{s}{s - \mathrm{M_Z}^2 + i\mathrm{M_Z}\Gamma_\mathrm{Z}}$$

with

$$\Gamma_\mathrm{Z} = \sum_f \left[\ N_C^f \, \frac{\alpha}{12} \, \mathrm{M_Z} \, \frac{(\ v_f^2 \ + \ a_f^2 \ )}{\sin^2\theta_W \cos^2\theta_W} \right] \tag{1.19}$$

in which $\sqrt{s}$ is the centre-of-mass energy, θ is the polar angle between e^- and f, v's and a's are the vector and axial vector coupling constants and N_C^f is the colour factor (which is 1 for leptons and 3 for quarks in the lowest order). The terms without χ dependence are due to the photon (γ) exchange, the ones involving $|\chi_0(s)|^2$ are due to the Z^0 exchange, whereas the ones with $\mathrm{Re}(\chi_0(s))$ are due to the $Z^0 - \gamma$ interference.

1.4 Cross-sections and Forward-Backward Asymmetries

From the differential cross-section in equation 1.18, the total cross-section σ_T is given :

$$\sigma_T = \oint \frac{d\sigma}{d\Omega} d\Omega \ = \frac{4\pi\alpha^2}{3s} N_C^f G_1(s) \tag{1.20}$$

and the forward-backward asymmetry A_{FB} :

$$A_{FB} = \frac{\sigma_F - \sigma_B}{\sigma_F + \sigma_B} = \frac{3}{4} \frac{G_3(s)}{G_1(s)} \tag{1.21}$$

with

$$\sigma_F = 2\pi \int_0^1 \frac{d\sigma}{d\Omega} d\cos\theta \ , \qquad \sigma_B = 2\pi \int_{-1}^0 \frac{d\sigma}{d\Omega} d\cos\theta \ .$$

Around the peak of Z^0, the terms due to photon exchange and $Z^0 - \gamma$ interference become much smaller than the term due to Z^0 exchange. The total cross-section and the forward-backward asymmetry can therefore be simplified to be :

$$\sigma_T = \frac{\alpha^2(\ v_e^2\ +\ a_e^2\ )(\ v_f^2\ +\ a_f^2\ )}{12\sin^4\theta_W\cos^4\theta_W} N_C^f \frac{s}{(s\ -\ \mathrm{M_Z})^2\ +\ \mathrm{M_Z}^2\Gamma_\mathrm{Z}^2} \tag{1.22}$$

and

$$A_{FB} = \frac{3}{4} A_f A_e \tag{1.23}$$

where

$$A_f = \frac{2v_f a_f}{v_f^2\ +\ a_f^2} \qquad \text{and} \qquad A_e = \frac{2v_e a_e}{v_e^2\ +\ a_e^2}\ .$$

In fact, we can also express the above total cross-section near the Z^0 peak in terms of partial widths $\Gamma_\mathrm{Z}^\mathrm{f}$ (for fermions) and $\Gamma_\mathrm{Z}^\mathrm{e}$ (for electrons) as :

$$\sigma_T = \sigma_0 \left[\frac{s{\Gamma_\mathrm{Z}}^2}{(s\ -\ {\mathrm{M_Z}}^2)^2\ +\ {\mathrm{M_Z}}^2{\Gamma_\mathrm{Z}}^2} \right] \tag{1.24}$$

where

$$\Gamma_\mathrm{Z}^\mathrm{f} = N_C^f \frac{\alpha}{12} \mathrm{M_Z} \frac{(\ v_f^2\ +\ a_f^2\ )}{\sin^2\theta_W\cos^2\theta_W} \ =\ N_C^f \frac{G_F {\mathrm{M_Z}}^3}{6\sqrt{2}\pi} (\ v_f^2\ +\ a_f^2\ ) \tag{1.25}$$

and σ_0 is the peak cross-section, given by

$$\sigma_0 = \frac{12\pi\Gamma_\mathrm{Z}^\mathrm{e}\Gamma_\mathrm{Z}^\mathrm{f}}{{\mathrm{M_Z}}^2{\Gamma_\mathrm{Z}}^2}\ . \tag{1.26}$$

1.5 t-channel Bhabha scattering

So far, we have assumed that the process $e^+e^- \to f^+f^-$ occurs via s-channels, i.e., the pair of diagrams in Fig. 1.1. However, when the final state fermions are e^+e^-, there is another possible pair of diagrams one has to take into consideration, as in Fig.1.2. These are called t-channel diagrams.

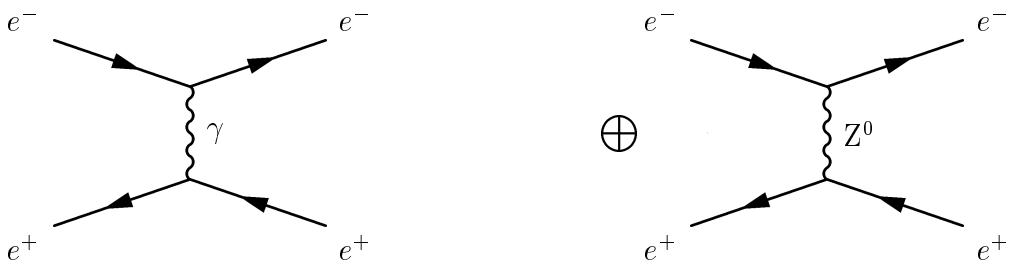


Figure 1.2: $e^+e^- \to e^+e^-$ process (Bhabha scattering) via t-channel.

The fraction of the overall cross-section σ and the corresponding forward-backward asymmetry A_{FB} for the process $e^+e^- \to e^+e^-$ due to t-channel effects varies with the centre-of-mass energies $\sqrt{s}$. The theoretical behaviour of the t-channel contribution in cross-section and asymmetry is shown in Fig. 1.3.

If the principle of lepton universality is assumed in the analysis of the process of $e^+e^- \to l^+l^-$ (where l stands for any lepton), this part of the contribution (including interference between s- and t-channels) should be subtracted. This will be further discussed in the later analysis.

1.6 A few words about QCD

Quantum Chromodynamics, QCD in short, is the local gauge invariant theory describing the strong interaction. In QCD, the strong interaction is interpreted as the interaction between "coloured" quarks, in which colour charge is just another kind of quantum number. There are three colours and correspondingly three anti-colours. The interaction between coloured quarks is mediated by colour field quanta (also known as gauge particles) called gluons. The requirement of gauge invariance of the group $\mathrm{SU(3)_c}$ leads to the existence of eight kinds of gluons.

The structure of non-Abelian $\mathrm{SU(3)_c}$ gives rise to a fundamentally different behaviour of QCD compared to QED. The strong coupling constant, α_s in the lowest order can be expressed as :

$$\alpha_s(Q^2) = \frac{12\pi}{(33 - 2\,n_f)\ln(Q^2/\Lambda^2)} \tag{1.27}$$

where Q^2 is the absolute value of the four-momentum transfer squared, Λ is the scale parameter and n_f is the number of active quark flavours. From this equation, one can see that the strong interaction becomes weaker at higher Q^2 (or smaller length scale), and vice versa. This leads to the so-called *asymptotic freedom* at infinite momentum (or zero length scale) and *confinement* at zero momentum (or infinite length scale). This behaviour in particular distinguishes QCD from QED.

1.7 Radiative corrections

A full discussion of radiative corrections may be consulted in [5] and a brief description is given below. Radiative corrections to the process $e^+e^- \to f^+f^-$ distort the

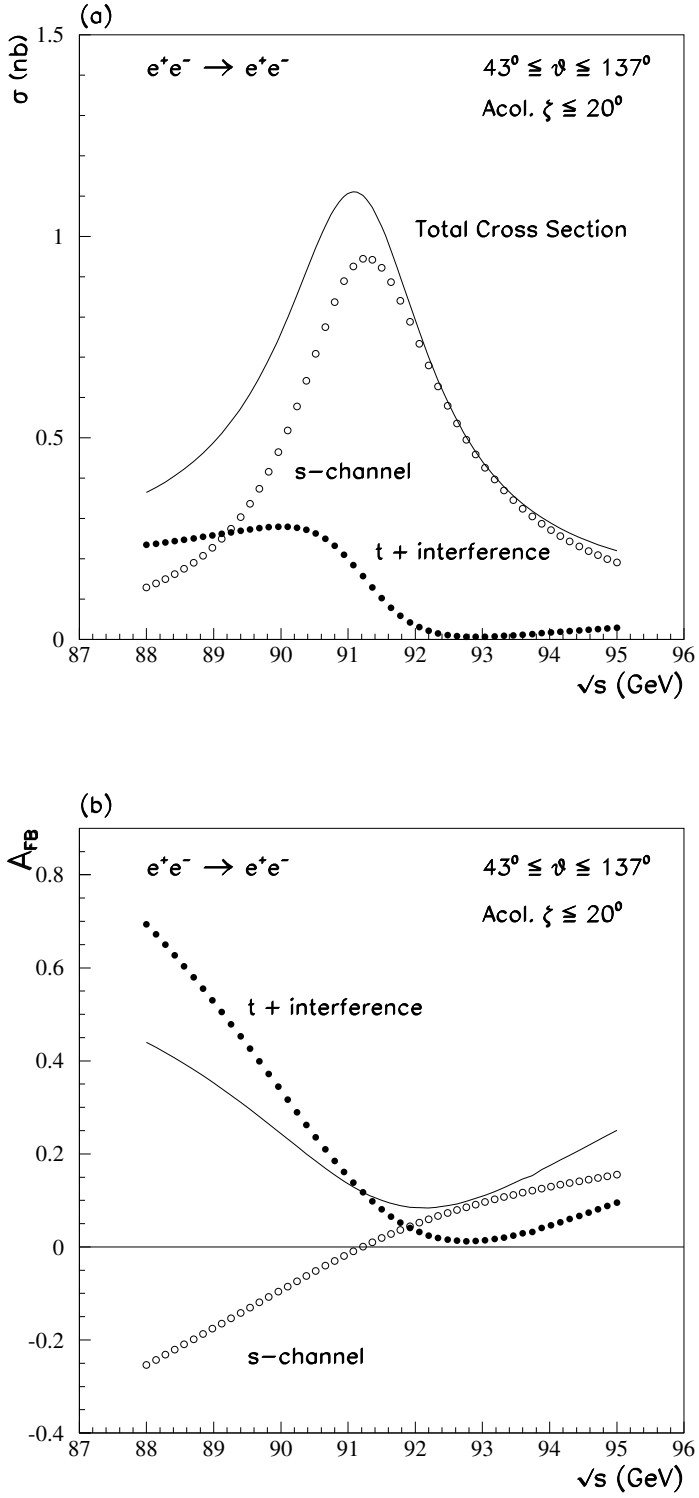


Figure 1.3: Theoretical behaviour of t-channel contribution in the cross-section and asymmetry for Bhabha scattering $e^+e^- \to e^+e^-$. In both figures (a) and (b), the solid lines represent the theoretical prediction for the full (s + t) channel. Here the experimental cuts on the polar angle ϑ and the acollinearity ζ are also included in the theoretical calculation.

corresponding cross-section and asymmetry near the Z^0 peak — Z^0 lineshape. The corrections can be classified into 3 categories, as shown in Fig. 1.4.

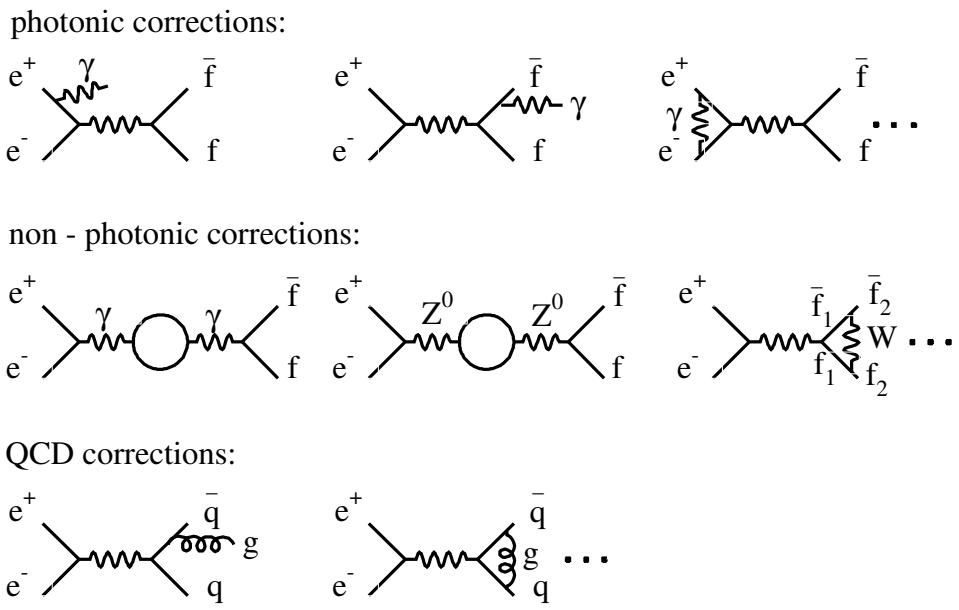


Figure 1.4: 3 categories of radiative corrections to the process $e^+e^- \to f^+f^-$.

1.7.1 Photonic Corrections

These are the corrections due to purely QED processes. They involve photons as initial or final state bremsstrahlungs, or in loop diagrams. This effect is large at Z^0 energies and it substantially alters the Breit-Wigner lineshape of cross-section. This results in about 30% reduction of the Born level peak cross-section, shifting the peak to a higher value of $\sqrt{s}$ and giving a significant production of Z^0 well above the peak, as shown in Fig. 1.5.

In terms of decay width Γ_Z, the photon corrections give a multiplicative factor $(1 + \delta_{\rm QED})$, where

$$\delta_{\rm QED} = \frac{3\alpha}{4\pi} Q_f^2 \tag{1.28}$$

which is $\lesssim 0.17\%$ [6].

1.7.2 Non-photonic Corrections

These are due to the residual weak corrections. They include propagator corrections (loop corrections to the boson propagators), vertex corrections (loop corrections

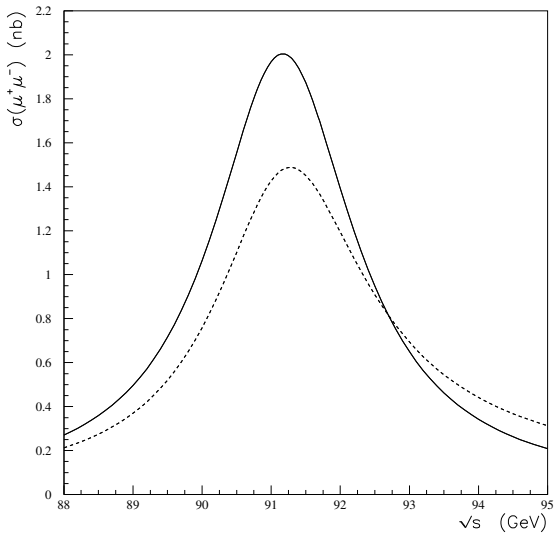


Figure 1.5: Muon pair cross section as a function of centre-of-mass energy $\sqrt{s}$. The solid curve is the Born approximation cross section and the dashed curve is the $\mathcal{O}(\alpha)$ QED corrected curve.

to vertices) and box corrections (multiple boson interchange between the initial e^+e^- pair and the outgoing fermion pair).

Though these corrections are small, they are crucial in the precision tests of the standard electroweak theory as they depend upon the unknown and poorly known parameters of the Standard Model, namely, the masses of the top quark and the Higgs boson.

1.7.3 QCD Corrections

These corrections are due to gluon radiation from $q\bar{q}$ final states. The effect on the partial width Γ_Z^{had} of hadrons can be parameterized as a multiplicative correction of $(1 + \delta_{QCD})$, where δ_{QCD} is an expansion of the strong coupling parameter [7] :

$$\delta_{QCD} = \frac{\alpha_s}{\pi} + \mathcal{O}({\alpha_s}^2) \tag{1.29}$$

with α_s at $Q^2 = {M_Z}^2$ as defined in section 1.6 (~ 0.12).

1.8 Improved Born Approximation

The Improved Born Approximation [5] is a way of accounting for the above corrections in the calculation of cross-sections and asymmetries, achieving a good approximation to the full calculation and yet retaining the simple Born level structure. The

corrections are mostly absorbed by redefining a few crucial parameters involved in the cross-sections and asymmetries as follows :

$$\sin^2\theta_W \;\mapsto\; \sin^2\theta_W^{eff} \;= 1 \;-\; \frac{{\rm M_W}^2}{\rho_{eff}{\rm M_Z}^2} \tag{1.30}$$

$$v_f \;\mapsto\; \bar{v}_f(s) \;= \sqrt{\rho_{eff}}\,(\mathrm{I}_3^f \;-\; 2Q_f \sin^2\theta_W^{eff}) \tag{1.31}$$

$$a_f \;\mapsto\; \bar{a}_f(s) \;= \sqrt{\rho_{eff}}\,\mathrm{I}_f^3 \tag{1.32}$$

$$\Gamma_{\rm Z} \;\mapsto\; \Gamma_{\rm Z}(s) \;= \frac{s}{\rm M_Z}\cdot\Gamma_{\rm Z}(s={\rm M_Z}^2) \tag{1.33}$$

The ρ_{eff} parameter, which specifies the relative strength of the neutral and charged current weak interactions, is introduced in the above redefinition. Comparing equation 1.30 with equation 1.7, one can see that $\rho_{eff} = 1$ at Born level.

This parameterization leads to the partial width and cross-section near the Z^0 peak redefined as :

$$\Gamma_{\rm Z}^{\rm f}(s) = N_C^f \frac{G_F {\rm M_Z}^3}{6\sqrt{2}\pi}(\,\bar{v}_f^2 \;+\; \bar{a}_f^2\,)(1 \;+\; \delta_{\rm QED})(1 \;+\; \delta_{\rm QCD}) \tag{1.34}$$

$$\sigma_T(s) = \frac{\sigma_0}{(1 \;+\; \delta_{\rm QED})}\left[\frac{s{\Gamma_{\rm Z}}^2}{(s \;-\; {\rm M_Z}^2)^2 \;+\; {\rm M_Z}^2{\Gamma_{\rm Z}}^2}\right] \tag{1.35}$$

where the factors $\delta_{\rm QCD}$ and $\delta_{\rm QED}$ are those given in sections 1.7.1 and 1.7.3, and σ_0 is as defined in equation 1.26 but with the partial widths replaced by the form in equation 1.34. Note that the term $1 \;+\; \delta_{\rm QCD}$ only exists when the final states $f\bar{f}$ are quarks.

Note that the decay width scales with ρ_{eff} parameter in terms of $\bar{v}_f$ and $\bar{a}_f$ and ρ_{eff} involves the electroweak corrections depending on the masses of the top quark and the Higgs boson as :

$$\rho_{eff} = 1 + \frac{3G_F\,{\rm m_t}^2}{8\pi^2\sqrt{2}} - \frac{11G_F{\rm M_Z}^2\sin^2\theta_W^{eff}}{12\pi^2\sqrt{2}}\left[\ln\left(\frac{\rm M_H}{\rm M_W}\right) - \frac{5}{12}\right] + \cdots \tag{1.36}$$

The forward-backward asymmetry after the redefinition can be formulated as :

$$A_{FB}(s) = \frac{3}{4}\bar{A}_f\bar{A}_e + \Delta_f^{\rm res} \tag{1.37}$$

where

$$\bar{A}_f = \frac{2\bar{v}_f\bar{a}_f}{\bar{v}_f^2 \;+\; \bar{a}_f^2} \qquad \text{and} \qquad \bar{A}_e = \frac{2\bar{v}_e\bar{a}_e}{\bar{v}_e^2 \;+\; \bar{a}_e^2}\ .$$

The term $\Delta_f^{\rm res}$ represents the flavour-dependent residual contribution from photon exchange and weak corrections in the propagator and box diagram.

Further formulation details can be found in [5].

1.9 Extraction of electroweak parameters

From the previous discussion, we see that the cross-section and forward-backward asymmetry are sensitive to a whole set of parameters such as M_Z, Γ_Z, $\bar{v}_l$, $\bar{a}_l$ etc. From equation 1.34, it is clear that Γ_Z is very sensitive to radiative corrections through its dependence on $\bar{v}_l$ and $\bar{a}_l$ (which depends on ρ_{eff} and $\sin^2\theta_W^{eff}$) as well as directly due to the QED correction ($\delta_{\rm QED}$). In fact, since the measurement of the cross-section is sensitive to $\bar{v}_l^2 + \bar{a}_l^2$ and the measurement of forward-backward asymmetry is sensitive to $\bar{v}_l^2/\bar{a}_l^2$, a combined fit to both cross-section and asymmetry can give values of both $\bar{v}_l^2$ and $\bar{a}_l^2$. Besides, due to presence of the QCD corrections, these measurements at $\sqrt{s} \approx M_Z$ are also sensitive to the running coupling constant α_s at $Q^2 = {M_Z}^2$ to some extent.

A comparison of the experimentally determined cross-sections and asymmetries can be made with the corresponding theoretical prediction of the Standard Model by using **ZFITTER** [8]. One can use ZFITTER to calculate theoretical cross-section (and asymmetry) as a function of various lineshape parameters. Because of that, it is therefore possible to extract different electroweak parameters such as Γ_l from the best fitted lineshape. In fact, the inclusive leptonic analysis shown in the later chapters is most sensitive to the value of Γ_l (proportional to $\bar{v}_l^2 + \bar{a}_l^2$) in one way of parameterization. Because the extraction of Γ_l is basically obtained from the leptonic information; whereas the extraction of the other electroweak parameters are mostly due to the cross-sections of hadronics which have far more statistics and thus provide more stringent constraint in the fit. This work will be elaborated in section 10.2.

Chapter 2

The Accelerator and the Detector

2.1 LEP, the accelerator

LEP stands for the Large Electron Positron Collider, currently the largest accelerator in the world, located at CERN, Switzerland. It is an e^+e^- synchrotron storage ring with a circumference of 26.7 km, at a depth of between 50 and 170 m below the surface, striding over the Franco-Swiss border near Geneva, Fig. 2.1. The LEP tunnel is not a perfect circle. It consists of 8 straight sections, four of which house the four experiments : L3, ALEPH, OPAL and DELPHI.

LEP was designed with a cost-optimized energy of about 90 GeV per beam. From Aug. 1989 to about Oct. 1995 (LEP1), LEP has been running at energies near the Z^0 mass, with a centre-of-mass (CM) energy about 90 GeV. In late 1995, the CM energy at LEP was increased to about 135 GeV. In 1996, LEP energy was raised up to the threshold for the production of W^+W^-, about 161 GeV (LEP2).

In general, the rate of an elementary particle physics process is given by

$$\frac{dN}{dt} = \mathcal{L}\sigma \tag{2.1}$$

where $\mathcal{L}$ is the luminosity (a measure of the useful flux of beam particles) and σ is the cross-section of the process. In an ideal LEP machine, the luminosity can be described by the following equation :

$$\mathcal{L} = \frac{\mathrm{fbN_1N_2}}{4\pi\sigma_x\sigma_y} \tag{2.2}$$

where f is the LEP revolution frequency, N_1 and N_2 are the number of particles in a bunch, b is the number of bunches per beam and σ_x and σ_y represent the RMS

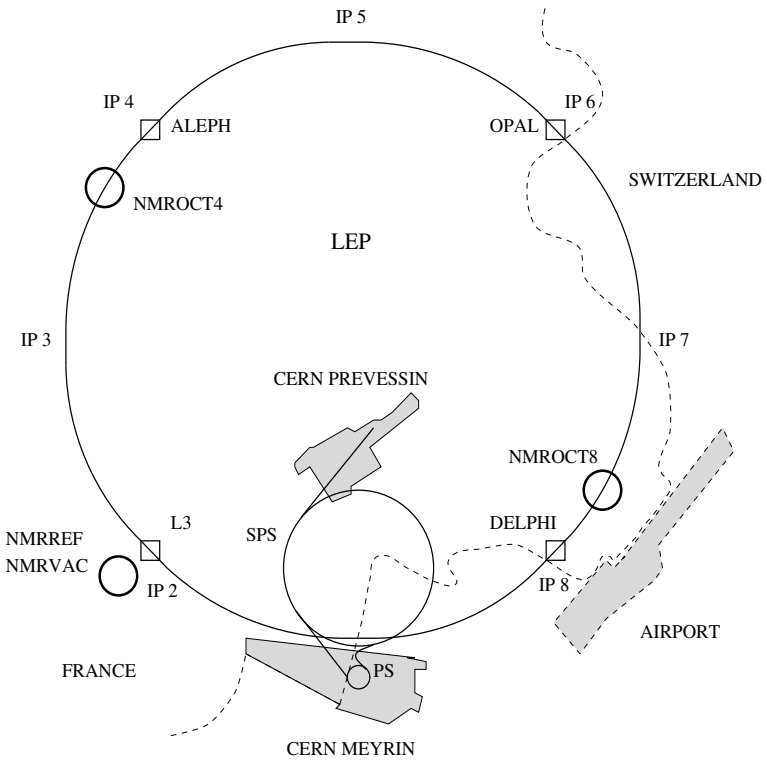


Figure 2.1: LEP and the four experiments at four interaction points, IP 2, 4. 6, and 8.

beam dimensions perpendicular to the beam direction. Nevertheless, the actual luminosity is determined from the rate of small angle Bhabha scattering which is a well understood process. The design luminosity at LEP1 is about $1.6 \times 10^{31} \mathrm{cm}^{-2}\mathrm{s}^{-1}$.

To accelerate the electron and positron beams, a chain of five accelerators are involved :

- Positrons are produced by bombarding an intense electron beam of 200 MeV from a linac (linear accelerator) onto a tungsten target.
- A second linac accelerates both electrons and positrons to 600 MeV and are then accumulated in the EPA (Electron Positron Accumulator).
- Injecting into the PS (Proton Synchrotron), e^-e^+ beams are accelerated to 3.5 GeV.
- SPS further accelerates the beams to 20 GeV.
- Finally, inside the LEP storage ring, electron and positron beams are boosted to about 45 GeV and beyond.

The particle beams are bent to circulate inside LEP mainly by about 3300 dipole magnets and are focussed and defocussed by about 1500 quadrupole and sextupole magnets. There are also horizontal and vertical dipole correctors individually powered so as to allow 'steering' of the beam through the centre of the LEP aperture. In order to increase the luminosity and particle production rate, a set of superconducting quadrupoles with very strong field gradients are used at each experimental collision point in LEP to 'squeeze' the beam to the sizes of $\sigma_x = 250\mu$m and $\sigma_y = 10\mu$m.

The vacuum chamber of LEP has been pumped down to very low pressure around 10^{-11} torr in order to minimize particle losses due to collisions with residual gas molecules. However, as an e^-e^+ machine, LEP suffers from energy loss due to synchrotron radiation which is proportional to E^4/ρ where E is the beam energy and ρ is the radius of curvature. The energy loss due to synchrotron radiation at LEP1 is about 125 MeV per turn of revolution. This energy is replenished by acceleration in the RF (Radio-frequency) cavities placed diametrically opposite to each other across LEP, close to OPAL and L3. At LEP1, the RF system consists of 128 five-cell copper cavities powered by sixteen 1 MW klystrons. At LEP2, a total of 60 superconducting RF cavities maintaining gradients about 6 MV/m (design value) with circulating beam have been added so that the beam energy can be increased beyond the threshold of W^+W^- .

From mid-1992 to the end of 1994, LEP was operated in 'Pretzel' mode colliding eight equally spaced bunches of particles. During this period, the beam intensity has been improved to well above the original design luminosity. In order to further raise the luminosity, primarily for LEP2, LEP since 1995 has been operated with 4 equidistant trains of short bunches in each beam ('bunch train'). Each train consists of up to 4 bunches (wagons) and is about 220 m long corresponding to about 750 ns. The usual mode of operation was with 3 bunches in each train.

Vertical electrostatic closed orbit bumps (separators) installed at either side of each IP are used in the 'bunch train' scheme to separate the beams at the parasitic collision points, i.e. to allow beam collision to happen only at the interaction points (IP's) in the experiments and nowhere else. These separators keep the two beams between 5 mm and 33 mm apart from each other. Unfortunately, a rather significant vertical dispersion is produced at the interaction points. The vertical dispersion of

the two beams is roughly equal but of opposite signs. This affects the CM energy spread and shifts the average CM energy at each IP. A scheme of maximizing the luminosity called "Vernier scan" is being used to reduce the energy shift. This will be further discussed in section 8.2.

Throughout the period of LEP1, each experiment has collected about 4 millions of Z^0 events. The number of hadronic Z^0 events collected in a typical LEP experiment from 1989 to 1995 can be found in Table 2.1. In 1993 and 1995, LEP runs were devoted to three point beam energy scans, with one point at the peak of the Z^0 resonance and two points roughly 880 MeV below and above the peak, which has the primary goal to improve the precision measurements of the Z^0 boson mass M_Z and its width Γ_Z. Particularly, the measurement of Γ_Z relies on off-peak fills. The precision of 2 parts in 10^5 has been achieved in the measurement of the mass of Z^0. In 1994, LEP was running solely at the Z^0 peak and produced a record of luminosity of 65 pb^{-1}. At the end of 1995, LEP with an energy about 135 GeV has attained a total luminosity about 5 pb^{-1}. Direct production of W^+W^- has also been successfully started in 1996.

Year	1989	1990	1991	1992	1993	1994	1995	Total
Off-peak	4K	30K	52K	—	243K	—	236K	617K
Total	13K	125K	275K	751K	755K	1484K	750K	4153K

Table 2.1: Numbers of hadronic Z decays recorded by DELPHI in each year of operation in LEP1, in a running period normally lasting from May to November. The number recorded at energies off the peak of the Z resonance, during scans of the Z line shape, are noted separately.

2.2 DELPHI, the detector

DELPHI (DEtector with Lepton, Photon and Hadron Identification) is designed to provide high granularity over a 4π solid angle, allowing powerful particle identification and precise vertex determination. The DELPHI ensemble, shown in Fig. 2.2, is cylindrical in shape, having a length of 10 m and a radius of 5 m, with the beam pipe of LEP running along its axis.

In the standard DELPHI coordinate system, the z axis is along the electron beam direction (electrons circulate anti-clockwise around the LEP ring), the x axis points towards the centre of LEP, and the y axis points upwards. The polar angle

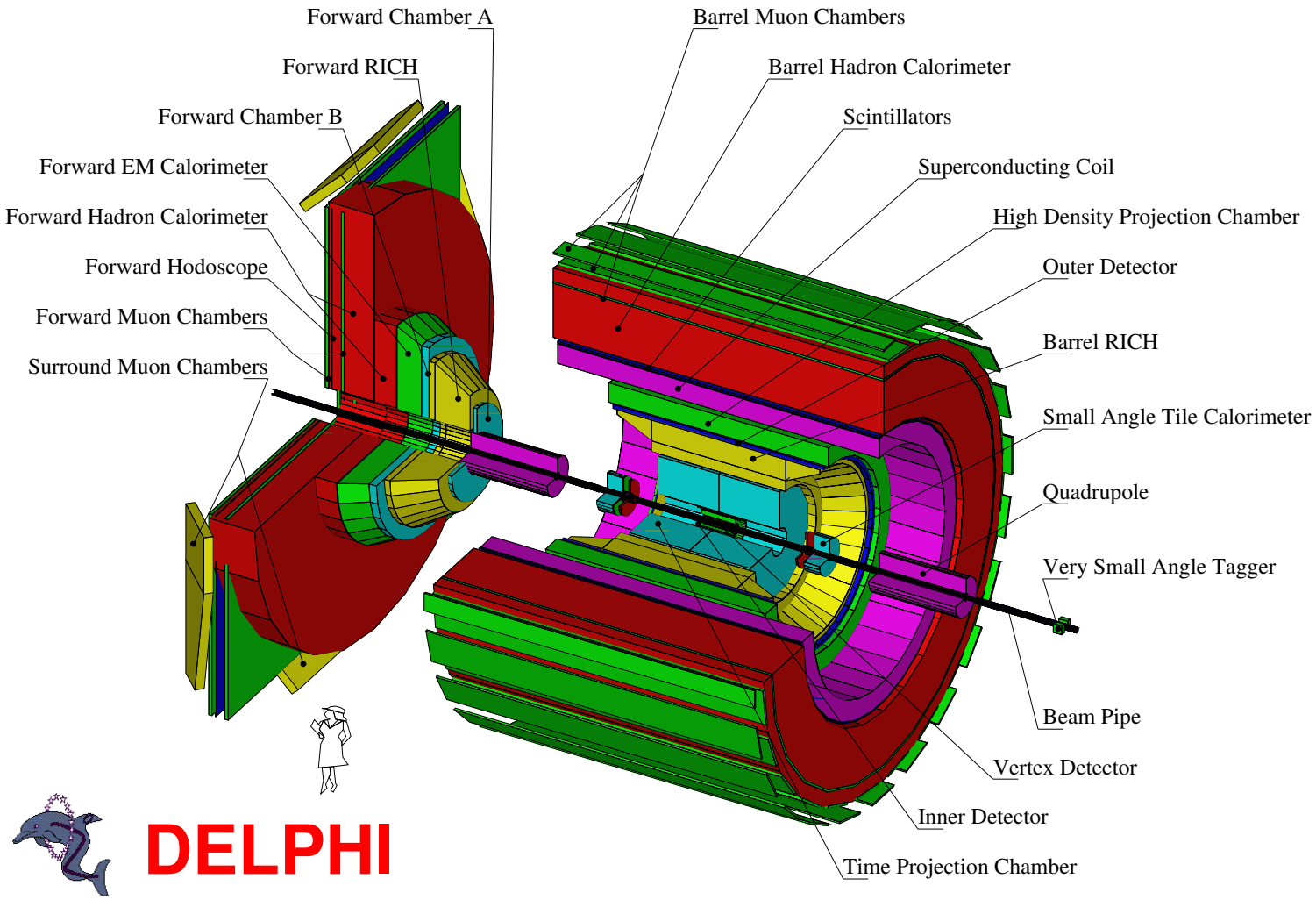


Figure 2.2: Schematic layout of DELPHI (note that Forward Chamber A is actually fixed to the Time Projection Chamber but for clarity it is shown here attached to the endcap.)

to the z axis is called θ and the azimuthal angle around the z axis is called ϕ ; the radial coordinate is $R = \sqrt{x^2 + y^2}$.

The detector consists of a central 'barrel' region of θ typically from 40° to 140° and two endcaps covering the "forward" regions. The endcaps can be moved to allow access to the sub-detectors. When the endcaps are closed, mobile shielding around the beam pipe follows this movement, thus allowing access even during beam collision anywhere outside the detector, which is self-shielding.

The superconducting solenoid provides a highly uniform magnetic field of 1.23 Tesla parallel to the z axis throughout the central tracking volume, i.e. the volume containing the barrel tracking detectors – namely the **V**ertex **D**etector (**VD**), the **I**nner **D**etector (**ID**), the **T**ime **P**rojection **C**hamber (**TPC**) and the **O**uter **D**etector (**OD**) – and also the forward tracking chambers (Forward Chambers A and B).

The following sections comprise a brief overview of DELPHI, concentrating on those sub-detectors on which the analysis in this thesis relies. More details can be found in [9] and [10].

The sub-detectors will be presented under three categories : tracking detectors, calorimeters and luminosity monitors.

2.2.1 Tracking Detectors

The tracking system is segmented into a relatively large number of independent tracking devices. Major tracking sub-detectors are described first, followed by a brief survey of the results obtained from the combined tracking system.

Vertex Detector (VD)

The VD, illustrated in Fig. 2.3, consists of three coaxial cylindrical layers of AC coupled silicon strip detectors at average radii of 6.3, 9.0 and 10.9 cm. Each layer covers the full azimuthal angle in 24 sectors with overlaps between adjacent sectors. There are 4 detectors along the beam direction in each sector. For polar angles of $44° \leq \theta \leq 136°$, a particle track originated from the interaction point would cross all three layers of the VD. The readout pitch (strip width) is 50 μm in the $R\phi$ plane perpendicular to the beam direction; whereas in z the pitch varies between 50–150 μm. The $R\phi$ coordinate hit precision is better than 10 μm and that of z is comparable to $R\phi$.

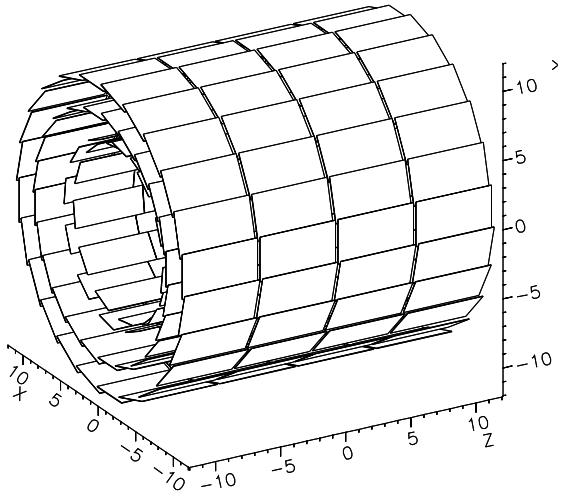


Figure 2.3: Perspective view of the three layers of Microvertex detector, each shell consisting of 24 modules which are made up of 4 silicon detectors with strips parallel to the beam direction. The unit on the axes is in cm.

Since the start of 1994, the first and third layers have been equipped with double-sided silicon detectors, having strips orthogonal to each other on opposite sides of the detector wafer, giving measurements also in the z direction.

Inner Detector (ID)

Before 1995, ID consisted of two parts : the JET chamber and the Trigger Layer (TL).

The inner JET chamber is actually a drift chamber, subdivided into 24 azimuthal sectors of 15° in ϕ, each providing up to 24 $R\phi$ points per track between radii of 12 and 23 cm. For polar angles in the range $23° \leq \theta \leq 157°$, a track crosses a volume of the detector sensed by a minimum of 10 wires.

Surrounding the jet-chamber, the TL consists of 5 cylindrical MWPC layers with sense wires spaced by about 8 mm (192 wires per layer) and with circular cathode strips giving R_z information. The $R\phi$ measurements are mainly used in triggering, but also provide the possibility of resolving the left/right drift ambiguities inherent in the jet-chamber. The polar angle coverage is $30° \leq \theta \leq 150°$.

Since the beginning of 1995, a new longer ID has been operational. The entire polar angle acceptance has been increased to $15° \leq \theta \leq 165°$. The TL is replaced by 5 cylindrical layers of straw tube detectors (192 tubes per layer).

Time Projection Chamber (TPC)

The TPC is the principal tracking device of DELPHI, the information it provides forms the basis of pattern recognition performed in event processing. The size of the TPC is limited by the inclusion of the RICHes (Ring Imaging Čerenkov Counters which aimed at providing superior charged particle identification) and other tracking chambers were added such as OD and Forward Chambers A & B to improve the momentum resolution.

The TPC is divided into two halves of drift chambers, each of length 150 cm and radius of 120 cm, by a HT (about 20 kV) plate which produces a uniform electric field of 187 V cm^{-1} pointing parallel to the z-axis and hence also the magnetic field. The chambers are filled with a gas mixture of 80% Ar and 20% CH_4 at atmospheric pressure. Both end-plates of the TPC are divided into 6 azimuthal (60°) sectors of MWPC's, the first boundary being at $\phi = 30°$, Fig. 2.4. Each sector has 16 circular rows of totally 1680 pads (cathode readout) with constant spacing and 192 sense (anode) wires aligned perpendicular to the radial line running through the centre of each sector. It should be noted that the volume immediately around the six sector boundaries and the central plane at $z = 0$ are dead regions which are not sensitive to particle ionization.

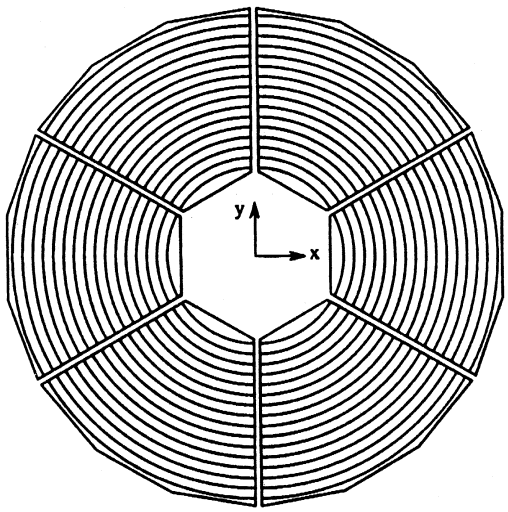


Figure 2.4: Time projection chamber (TPC): one readout plane formed by six sectors, each with 16 circular rows of pads and 192 sense wires.

A charged particle crossing the TPC produces ionization of around 70 electrons per cm of gas (avalanches) near the anode wires which induce pulses on the cathode

plane. The transverse motion of electrons is damped by the presence of magnetic field and the electrons perform helical oscillations about the line of drift. The arrival time of the drifted electrons gives the z position while the ϕ position is determined from the centre of gravity of the induced charges on the cathode plane and the measurement of R mainly comes from the sense wire hits.

The TPC thus provides up to 16 space points per particle trajectory at radii of 40 to 110 cm between polar angles of $39^\circ \leq \theta \leq 141^\circ$. At least three pad rows are crossed down to polar angles of $20^\circ \leq \theta \leq 160^\circ$. The precision on the track elements is about 150 μm in $R\phi$ and about 600 μm in z. Moreover, the presence of the sense wires also means that up to 192 dE/dx ionization measurements can be performed on each track, which provides particle identification up to about 2 GeV/c.

Outer Detector (OD)

The OD consists of 5 layers of drift tubes, operated in the limited streamer mode, located between radii of 197 and 206 cm. Successive layers are staggered and adjacent modules of the 24 azimuthal sectors overlap, giving full azimuthal coverage. Three layers are equipped to read the z coordinate by timing the signals at the ends of the anode wires. The active length of the detector corresponds to polar angles of $42^\circ \leq \theta \leq 138^\circ$.

The single point precision of OD is of $\sigma(R\phi) = 110$ μm, independent of the drift distance, with a single cell efficiency above 99.5%. The precision in the z coordinate is $\sigma(z) = 3.5$ cm. The presence of the OD improves the momentum resolution of fast tracks and provides fast trigger information.

Barrel Muon Chamber (MUB)

There are 3 concentric regions of MUB (Fig. 2.5) : inner, outer and peripheral modules of a total of 1372 drift chambers. Inner modules are installed within the iron of the Hadron Calorimeter and contain 14 chambers stacked in three layers : 5, 4 and 5 respectively. Outer and Peripheral modules are mounted on the outside of DELPHI and contain 7 chambers stacked in two layers : 4 and 3 respectively. Such an arrangement comprises one MUB sector.

The MUB covers an angular range in ϕ of 0° to 360° and 52° to 132° in θ, though there is a dead space in the polar angle θ between chambers at $z = 0$ ($\theta = 90^\circ$)

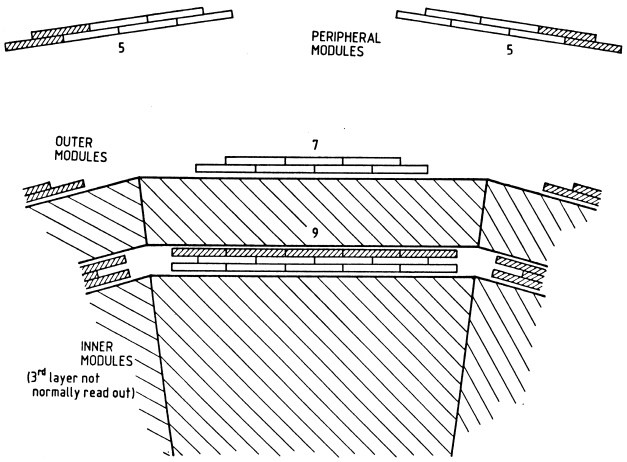


Figure 2.5: An azimuthal sector of the MUB, showing the 3 modules and the calorimeter iron.

which is about 3° wide. This hole also divides the MUB into two 'hemibarrels'. The hemibarrel along negative-z is called the A side while that along positive-z is called the C side. Each hemibarrel is divided in ϕ into 24 sectors such that each sector subtends 15° in ϕ. Peripherals are displaced by 7.5° in ϕ relative to the Outers of the same sector in order to cover the gaps in the Outers for cables and pipes. In addition there are two anomalous sectors around the magnet legs, each containing Outer and Peripheral modules only. A typical chamber is 20.8 cm wide, 2.6 cm high and 365 cm along the z-axis of DELPHI. Individual chambers have typical resolutions of $\sigma_{R\phi} \sim 1$ mm and $\sigma_z \sim 10$ mm , where $R\phi$ is measured by the drift coordinate and z by a delay line.

Global Alignment

At LEP1, the global alignment of the tracking chambers is performed mainly using $Z^0 \rightarrow \mu^+\mu^-$ (dimuon) events in order to exploit the constraint on the momentum derived from the beam energy. To align the barrel detectors, the OD is chosen as reference since the wire positions are known to a precision of 30 μm from optical and mechanical surveys and the detector has a good time stability and a long lever arm with respect to the interaction point. The position of the VD with respect to the OD is determined assuming the two muons form a single track. Then, the ID and TPC are aligned using the reference tracks formed by the VD and OD, imposing a fixed momentum but relaxing the collinearity constraint.

After correction for distortions in the individual barrel detectors, muon tracks reconstructed in the TPC are extrapolated to the sub-detectors in the forward region.

On aligning the full tracking system, tracks from the dimuon sample are again extrapolated through the detector to align the barrel electromagnetic calorimeter (HPC) and the Ring Imaging Čerenkov Counters.

2.2.2 Calorimeter

The calorimetry system of DELPHI measures the energy of charged and neutral particles by reconstructing the showers of secondary particles produced as a result of interaction between the calorimeters and the particles. The precise form of such showers may be used to identify the type of particle that caused them. In the barrel region, electromagnetic calorimetry is provided by the High Density Projection Chamber (HPC) while the hadronic calorimetry is provided by the Hadron CALorimeter (HCAL).

High Density Projection Chamber, HPC

The DELPHI barrel electromagnetic calorimeter, HPC, consists of 144 modules arranged in 6 rings inside the magnetic field. Each ring consists of 24 modules coaxially arranged around the beam axis with an inner (outer) radius of 208 (260) cm and a total length of 496 cm along the beam axis. The full detector covers the angular region between 43° and 137° in θ. Each HPC module is a 'small TPC' with layers of high density material in the gas volume. These layers are made from lead wires which serve not only as converter material, but also help provide the drift field as well. The total converter thickness is 18 $X_0/\sin\theta$ [1].

The charge deposited by electromagnetic showers is sampled in the 8 mm wide gas gaps between the lead walls, which are filled with Ar/CH_4 (in the ratio 80/20). The charge is then drifted by an electric field towards one end of the module, where it is collected by proportional counters (gain $\sim 10^4$) and sampled with a frequency of 15 MHz. The sampling frequency determines a granularity of about 4 mm in the drift coordinate (z). In each module, the cathode of the proportional counters is segmented into 128 pads arranged in 9 rows. These pads provide a granularity about 1° in ϕ as a function of the depth and nine-fold radial sampling (Fig. 2.6).

[1] X_0 is one unit of radiation length, i.e., the thickness of material that reduces the mean energy of an electron by a factor of e (natural number), as indicated by the energy loss equation : $dE/E = -dx/X_0$, $E = E_0 e^{-x/X_0}$.

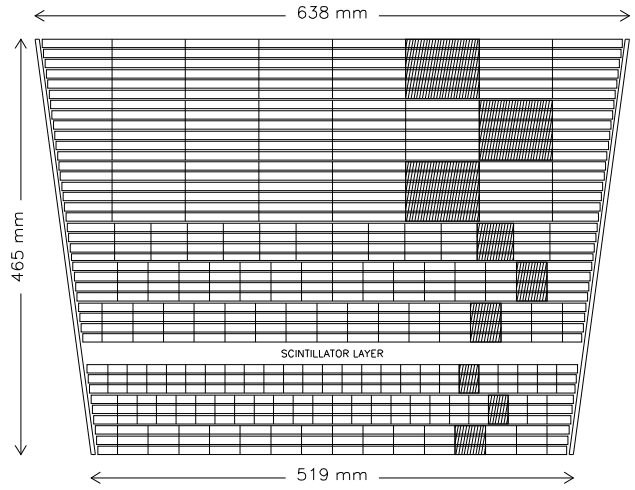


Figure 2.6: The cathode pad segmentation in the HPC readout proportional counters.

The relative precision on the measured energy in HPC has been found to be $\sigma(E)/E = 0.043 \oplus 0.32/\sqrt{E}$ (E in GeV) and the angular precisions for high energy photons are ± 1.7 mrad in ϕ and ± 1.0 mrad in θ.

Hadron Calorimeter, HCAL

The HCAL is installed in the return yoke of the DELPHI solenoid. It is made of 2 endcaps, each consisting of 12 sectors, and a barrel section which consists of 24 modules. The whole Hadron Calorimeter covers almost the full solid angle : $11^\circ < \theta < 169^\circ$. More than 19000 limited streamer tubes (8 cm in width, and varying in length between 40 to 410 cm) are installed in the 18 mm wide slots between the 40 mm thick iron plates.

The limited streamer tubes are mounted on copper clad readout boards which hold up to 64 pads, each pad covering a fixed angular region of $\Delta\phi = 3.75^\circ$ and $\Delta\theta = 2.96^\circ$. In the barrel part, five pads in the radial direction, called a 'tower', are read out together by the same electronic channel. The tower information is reconstructed in the form of clusters. In the barrel region, the energy precision in the hadron calorimeter has been found to be $\sigma(E)/E = 0.21 \oplus 1.12/\sqrt{E}$ (E in GeV). The fixed term in this expression is due to the material between the hadron calorimeter and the electromagnetic calorimeter.

Before 1994, only the pads were read out. To increase the granularity of the detector, a new system has been developed which reads out the cathodes of individ-

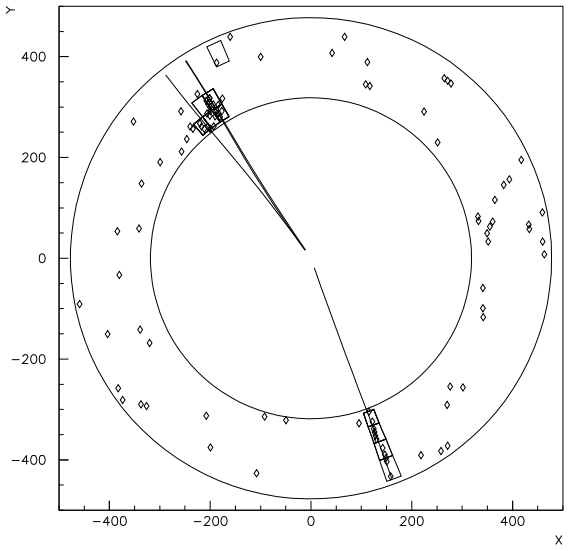


Figure 2.7: A $\tau^+\tau^-$ event seen in the HCAL with cathode readout. One τ decays into three pions, the other one into a μ. The unit on the axes is in cm.

ual streamer tubes [2]. This new system is independent of the present pad readout and improves the granularity in ϕ by a factor of 3 and in R by a factor of 5. The combination of the two readout systems has been demonstrated to provide, among other aspects, better π/μ separation and more precise hadron energy measurement. The number of hits in the readout has also been observed to be quasi-linearly correlated with the energy deposit up to 40 GeV. A typical event seen in the HCAL is presented in Fig. 2.7.

2.2.3 Luminosity Monitors and Luminosity Measurements

Before 1994, the absolute measurement of the luminosity was based on the SAT (Small Angle Tagger), but the relative luminosity at the off-peak points was taken from the VSAT (Very Small Angle Tagger) data. Since the 1994 run, the STIC (Small Angle TIle Calorimeter) replaced the SAT.

The luminosity is obtained from the ratio of the number of events measured in small angle Bhabha scattering ($e^+e^- \to e^+e^-$) [3] and the theoretical prediction for the cross-section of this process within the acceptance of the luminosity monitor(s). Bhabha scattering is chosen because of its clear experimental signature, high statistics and its cross-section having been calculated theoretically with high precision.

[2] However, the new cathode readout system is not used in this thesis.

[3] It proceeds almost entirely through the exchange of a photon in the t-channel at small polar angles.

SAT and its measurement

The SAT consists of alternating layers of lead sheets and plastic scintillating fibres concentric with the LEP beam, covering the polar angle range from 43 to 135 mrad. The fiducial volume is accurately defined by a precisely machined tungsten mask in front of one of the calorimeters. The transition region where energy deposition drops from 85% to 0% is less than 100 μm, which also defines the accuracy of the acceptance radius. A second mask (the "ϕ" mask) covers the junction in the vertical plane of the two halves of the masked calorimeter.

For the 1993 running, the SAT was equipped with a tracker consisting of 2 planes of silicon strips in front of the calorimeter opposite the masked calorimeter. The use of the tracker data gave a better definition of the fiducial region in the unmasked calorimeter which allowed a considerable reduction in the systematic error. The SAT Bhabha trigger required a coincidence of coplanar energy deposits of greater than 12 GeV and was measured to have an efficiency of close to 100%.

The theoretical visible cross-section was evaluated using the Monte Carlo event generator BHLUMI V4.02 [11] and the detector response was simulated using the GEANT package [12]. The theoretical uncertainty on the visible Bhabha cross-section was taken to be $\pm 0.17\%$. The experimental uncertainty of the SAT luminosity measurement arises mainly from the geometrical definition of the masks, the acceptance cuts and the sensitivity to the LEP interaction point and the beam tilts. In 1993, it was found to be 0.29%.

VSAT and its measurement

The VSAT in each arm is composed of two rectangular tungsten-silicon calorimeter stacks, 24 X_0 deep, 7.7 m away from the interaction point, beyond the superconducting quadrupole. They cover the angular regions between 5 and 7 mrad in θ and 45° in ϕ around the horizontal axis. Being at the very low angle region, the acceptance cross-section is about 400 nb, 10 times the Z_0 rate on the peak. This high statistics makes the relative luminosity measurements from the VSAT very accurate and useful, though its absolute luminosity measurement is much less accurate than SAT due to its position being behind the quadrupole.

In 1993, the VSAT data taken off the Z^0 peak were used to determine the relative point-to-point luminosity while the data taken at the Z^0 peak were used to normalize

the VSAT luminosity to the SAT absolute luminosity. For 1994 data, the VSAT luminosity was used only to check the run to run stability of the STIC measurement.

STIC and its measurement

From 1994 onwards, the SAT was replaced by a new calorimeter, the STIC. It is a sampling lead-scintillator calorimeter formed by two cylindrical detectors placed on either side of the DELPHI interaction region at a distance of 2.2 m, and covers a wider angular region between 29 and 185 mrad in θ with respect to the beam line. The total length of the detector is 27 X_0. Each STIC arm is divided into 10 rings and 16 sectors, giving an $R\phi$ segmentation of 3 cm $\times$ 22.5°.

The blue light produced in the scintillator is read by wavelength shifting fibres placed perpendicularly to the scintillator planes. This light collection scheme and its quasi-projective geometry (i.e. no cracks pointing to the interaction region) provide a very uniform energy response and an excellent energy resolution, $\sigma(E)/E \simeq 2.7\%$ (E in GeV) at 45.6 GeV.

The major improvements with respect to the SAT can be summarized as follows :

1. The excellent energy resolution allows for an easy separation of Bhabha scattering events from the background due to off momentum particles from beam-gas interactions.

2. The accuracy in the definition of the internal geometry of the detector, the absence of discontinuities and the good spatial resolution allow for a very precise definition of the geometrical acceptance.

The luminosity was measured with the same "mask technique" used by the SAT. A high precision tungsten ring projective to the interaction region, called the "nose", with a total thickness of 17 X_0, covers the inner 35 mm of the acceptance of one of the calorimeters, Fig.2.8. A cut on the shower energy detected in the masked calorimeter ($E_{Masked} > 65\%\ E_{Beam}$) translates into a very sharp cut on the inner radius, with a precision of 20 μm.

The same programs as for the SAT were used to calculate the Bhabha cross-section theoretically. The theoretical precision was estimated to be 0.16%. The overall experimental systematic error has been evaluated to be 0.09%, which is better than the design goal of the STIC luminometer.

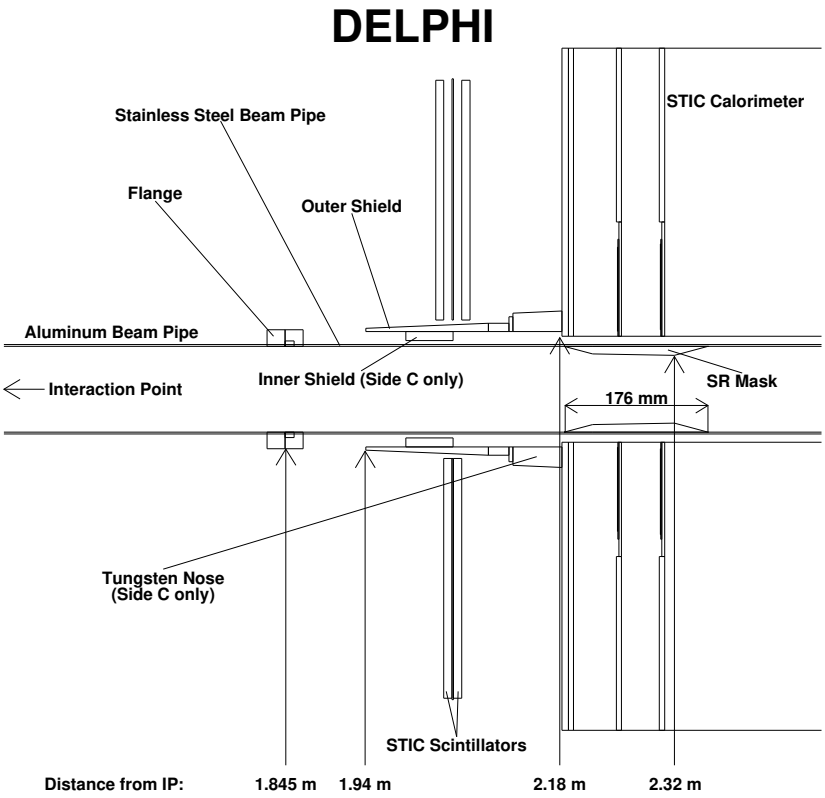


Figure 2.8: Layout of the STIC region.

Chapter 3

The Inclusive Leptonic Analysis

3.1 Data Processing in DELPHI

There are two main stages of data processing. The online system controls the running of sub-detectors and the accumulation of data immediately after the physics collisions at DELPHI, and finally produces the 'Raw Data'. The offline system processes the Raw Data into a form which is suitable for physics analysis. The important ingredients of data processing at DELPHI are outlined as follows.

3.1.1 Online: Data Acquisition System and Trigger

The Data Acquisition System (DAS) aims to read out data from the individual sub-detectors at each beam cross over (BCO), store this data in memory while a trigger decision as to whether to keep the event is made.

The trigger system has two hardware levels, T1 and T2, which provide a decision after 3 μs and 39 μs respectively, and also two asynchronous software triggers, T3 and T4, with a typical processing time of 300 ms. Almost all sub-detectors contribute to the DELPHI trigger, though those with longer drift times such as the TPC cannot participate at the first level.

The purpose of the trigger system is to efficiently detect those physical final states originating from e^+e^- interactions while rejecting background and empty events. There are usually more than one trigger subset for each type of physical events and any of these trigger subsets can give a positive trigger decision. This kind of redundancy in the trigger system enables the efficiency of the individual components to be determined and provides backups in case of hardware failure.

After a positive T4 decision is made, the data collected is written into tapes of Raw Data.

More details about the DELPHI DAS and trigger system can be found in [13] and [14].

3.1.2 Offline: From Raw Data to DST

The DELPHI data pass through 3 main offline stages before they can be used for physics analysis :

1. Raw Data : These are the online data with events passing through various trigger components and written to tapes in the DELPHI control room.

2. Tanagra Data : A central analysis program known as DELANA (see section 3.1.3) processes the Raw Data by performing a detailed reconstruction to produce a high level and flexible data structure called TANAGRA (**T**rack **ANA**lysis **GRA**phics package) [15].

3. The large volume and inconvenience of the TANAGRA data means that a further reduction to DST (Data Summary Tapes) [16] is necessary for physics analysis. It is the program called PXDST which converts the TANAGRA data into the DST structure.

3.1.3 Event reconstruction

The DELANA (**DEL**PHI **ANA**lysis) processing can be divided into the following stages :

1. For each detector, a sub-detector code is activated to reconstruct the space points or hits (TDs).

2. For the tracking detectors, TDs are clustered into track elements (TEs).

3. A track fit is performed to join together TEs into tracks : TKs.

4. Tracks are then extrapolated to calorimeters, muon chambers and RICHes and are associated with the hits and energy deposits in those detectors. This in turn produces particle identification information.

5. Finally, neutral tracks are made from those energy deposits left unassociated to the reconstructed charged tracks.

3.1.4 Detector Simulation

The DELPHI Monte Carlo data are generated by a program called DELSIM [17] (**DEL**PHI **SIM**ulation). With the help of different routines for each type of physics interactions, it generates the so-called **truth particles**, models their interaction with all DELPHI sub-detectors subject to different detector responses and the material encountered, and also allows for secondary processes. The output from DELSIM is raw data in the same format as the real data. The simulated raw data are then subjected to the same processing chain as the real data, as described in 3.1.2 and 3.1.3. In addition, the simulated history of the event, containing information about all truth particles, is propagated to the DST, known as the **truth information (truth tracks)**.

3.1.5 Event Tagging

After the DELANA processing, a tagging algorithm is applied to categorize the event. The event is labelled as a leptonic Z^0 candidate, a hadronic Z^0 candidate, a Bhabha detected in the SAT or STIC, a cosmic/beam gas or as unknown. Various sets of DST are produced with the above-mentioned tags. The leptonic analysis in this thesis is derived from the leptonic DST. It includes all events which have less than 7 charged tracks, or at least two back-to-back (to within 25°) electromagnetic clusters with energies greater than 5 GeV or one electromagnetic cluster with energy greater than 15 GeV. These tags are loose in order to avoid losing any genuine lepton candidates.

The program PHYANA [18] is used here to unpack the DST information into convenient arrays, which are then further manipulated by the author.

3.1.6 Reprocessing

Often, improvements are made in DELANA and bugs in the code are fixed. Various sub-detector experts may also update and correct the alignment and calibration of their sub-detectors by studying simple topology events such as $e^+e^- \to \mu^+\mu^-$, for example. This would improve the quality of the track fitting process. Therefore, data are reprocessed 'periodically' with the above ingredients included. For any LEP run, there are various DST versions derived from the same Raw Data. For the 1991 data, for instance, there have been so far six versions from 91A to 91F.

In this thesis, the 1993 and 1994 DELPHI data are used in the inclusive leptonic analysis. For the 1993 analysis, the DELPHI 93B processing is used; whereas for the 1994 analysis, the 94B processing is used.

3.1.7 Microdst

In order to minimize analysis processing time, the leptonic DST data was further 'stripped' down to make a **'microdst'** which contains only that information of use in the cross-section and asymmetry analysis. This has greatly reduced the size of data and hence the time of processing. Only events with charged multiplicities N_c such that $1 \leq N_c \leq 8$ are written onto the microdst. This includes all the events that could pass the leptonic selection cuts.

3.2 About the analysis

The inclusive leptonic analysis studies the leptonic decays of Z^0 ($e^+e^- \rightarrow l^+l^-$) without attempting to distinguish one lepton family from another, i.e, flavour-independent. Without having the problem of inter-favour contamination, tight cuts used to separate three flavours are relaxed and this gives a slightly higher selection efficiency of leptonic events. The event selection criteria for this analysis is rather independent of that of the other lepton-identified analyses and this analysis therefore offers a good consistency check.

Lepton universality is implicitly assumed throughout this analysis. Nevertheless, this analysis can never truly be flavour-independent, since the t-channel electrons must be removed. This means that individual selection efficiencies for different flavours have to be calculated, which results in systematics uncertainties. Moreover, the slightly different behaviour of different leptons in the detectors also makes it difficult for a detailed evaluation of the detector efficiencies and backgrounds without actually distinguishing between them. As a result, the inclusive leptonic analysis is not more accurate than the individual lepton-identified analyses.

Though the principles used in the 1993 and 1994 analyses are the same, there are small differences, for instance, in the cosmic cuts. Other differences will be mentioned where necessary. Because of time constraints, it was not possible to reanalyze the 1993 data using the methods of 1994, but the 1993 results are nevertheless valid.

3.3 Selection cuts

This analysis does not need to distinguish between electrons, muons and taus. However, it has to avoid the contamination of background sources such as hadronics, cosmics and two-photons. Several cuts have been used to attain a high purity as well as a good efficiency.

3.3.1 Run-selection

In the cross-section measurement, the observed number of events are corrected for the selection efficiency. An overall mean value for this efficiency is applied to the whole data set; therefore it is desirable to only consider those periods of data taking where the selection is properly represented by such a mean value.

A run-selection is applied to eliminate any anomaly due to any inefficiencies in one or a few detectors, whilst still retaining the bulk of the statistics. The details of run-selection are shown in Table 3.1. Since this analysis does not involve identification of any particular type of leptons, run-selection is applied to the main tracking detector (TPC) but not to muon chambers and calorimeters. This implies a slightly higher selection efficiency than those of the lepton-identified analyses.

Year	TPC Flag	SAT Flag	status in the luminosity file
1993	6 – 7	7	Lumi Flag ≤ 1
1994	6 – 7	NA	Lumi Flag ≤ 1

Table 3.1: Run-selection requirements for this analysis. Detector flag of 6 means (95 – 99)% of the detector being nominal, while that of 7 means 99% of the detector being nominal. Luminosity flags of 0 and 1 correspond to acceptable performance of the luminosity monitors as assigned by the DELPHI luminosity group.

Here, luminosity run-selection flag is only applied for the cross-section analysis, but not for the asymmetry analysis.

In addition, certain data tapes considered bad in the hadronic lineshape analysis were removed from the analysis, due to strong indication of luminosity problems or highly anomalous hadronic cross-sections [1]. Furthermore, the leptonic cross-section was determined separately for every tape retained after the selection, to check whether the sample was then consistent. Some periods of especially low efficiency

[1] Hadronic cross-section is about 7 times as large as that of visible leptons.

were found in 1993. These were traced to the TPC timing problems and the related tapes were also discarded. Fig. 3.1 shows the cross-section per fill after the run-selection against fill number in 1994.

3.3.2 Preliminary cuts

A few preliminary cuts are used to select those events with reasonably good tracks for further examination.

All tracks have to satisfy the following basic cuts before further considerations are made :

- Impact Parameter in $R\phi$ plane $\leq$ 3.0 cm and Impact Parameter along the z-axis $\leq$ 4.5 cm ;
- Momentum $\geq$ 0.2 GeV .

Events with 2 – 6 'good' tracks passing the above cuts, in which at least 2 of them are in the barrel region, ie., θ between 43° and 137°, are selected at this stage. This should have already suppressed most of the hadronic background. However, further cuts are needed to obtain a pure sample of lepton candidates.

3.3.3 $P_{fastest} \geq$ 3 GeV

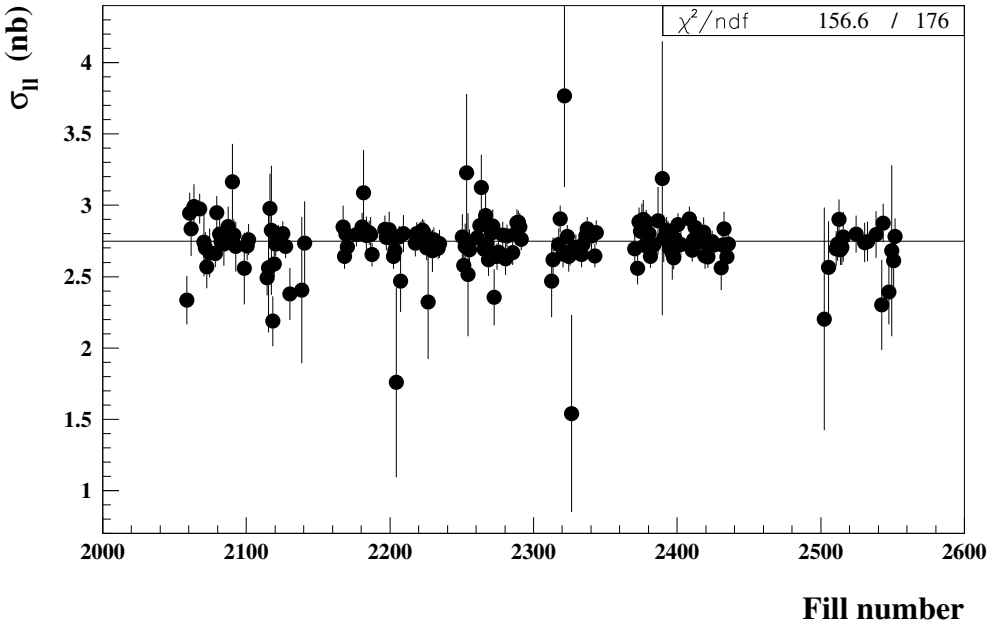
To reduce the contamination of beam gas and two-photon background events, it is required that the fastest 'good' track has momentum bigger than 3 GeV (P_{min}). To minimize any selection efficiency biases at different energies, this cut is changed for 1993 analysis to P'_{min} such that :

$$P'_{min} = P_{min} \times \frac{E_{CM}}{M_Z} .$$

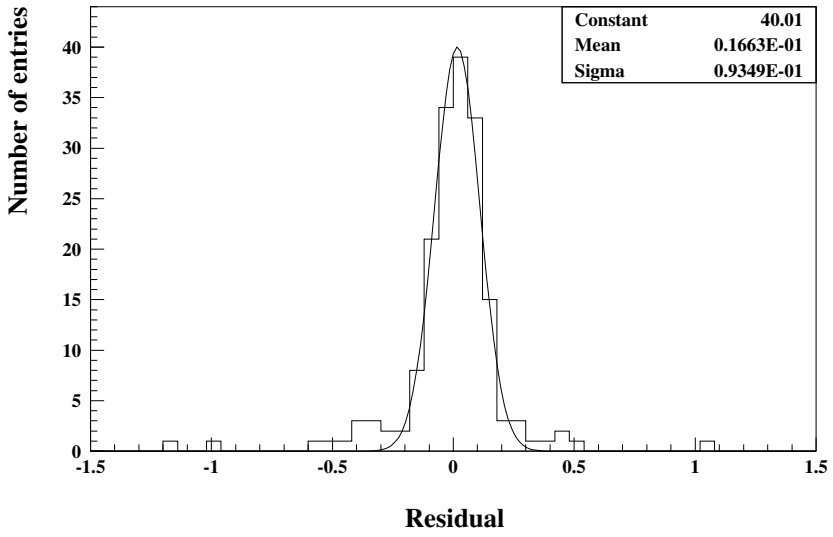
3.3.4 Topology cuts

It is also demanded that the events have two groups of well isolated tracks, which are nearly back-to-back and well collimated.

1. Multiplicity of 1–N (N = 1, ..., 5) :
   Divided by a plane perpendicular to the thrust axis, tracks lie in two opposite hemispheres. One of the hemisphere is required to contain only 1 charged track, and the other between 1 to 5 tracks. This is hereafter referred to as the 'jet'.



(a) Raw leptonic cross-section vs fill number



(b) Residual : $(\sigma_{\text{fill}} - < \sigma >)/\delta_{\text{fill}}$

Figure 3.1: Cross-section per fill in 1994. Figure (a) shows the raw cross-section against the fill number. Figure (b) is a plot of the residual $(\sigma_{\text{fill}} - < \sigma >)/\delta_{\text{fill}}$, where σ_{fill} is the raw cross-section for a certain fill, $< \sigma >$ is the average cross-section and δ_{fill} is the error of the cross-section on the raw cross-section. It is approximately a Gaussian distribution with a width ≈ 1.

2. Acollinearity $\leq 20^\circ$:

   It is required that the angle between the resultant momentum of the jet and the backward projection of the isolated track (ie. the acollinearity) be less than 20°.

3. Jet Opening angle $\leq 30^\circ$:

   The angle between any track in the jet and the resultant momentum of the jet (ie. the jet opening angle) is demanded to be less than 30°. This corresponds to an isolation angle of 150° between the isolated track and any track in the jet.

These topology cuts are applied to reject hadronics but retain most genuine tau events. However, these cuts reject $\tau^+\tau^-$ events having a 3 vs. 3 prong decay topology, but the corresponding loss of events is negligible compared to the increase in the backgrounds (mostly hadronics) if this condition is not imposed.

3.3.5 Missing Transverse Momentum $\geq$ 0.4 GeV

Events from the two-photon channel are often back-to-back in the $R-\phi$ plane, due to their typically low invariant mass at small scattering angles. A cut demanding some missing transverse momentum is therefore useful to suppress the two-photon backgrounds. However, e^+e^- and $\mu^+\mu-$ final state events also have back-to-back topologies. Hence, it is required that there is an imbalance in the transverse momentum of greater than 0.4 GeV, but this is only applied in the case when both the two fastest tracks in the event of 1-1 topology have momenta less than 10 GeV.

An examination of Monte Carlo shows that the number of e^+e^- and $\mu^+\mu^-$ events with both tracks this soft ($<$ 10 GeV) is negligible and thus this cut is safe in this case. In the case of $\tau^+\tau^-$ final states, the total transverse momentum is large and not 'compensated' due to the emission of neutrinos. Fig. 3.2 shows the distributions of of missing transverse momenta for events having both of the fastest tracks less than 10 GeV in the data and tau Monte Carlo. It may be seen that the excess at low missing momenta in the data is due to the two-photon background. It was found that the loss due to this cut in the $\tau^+\tau^-$ Monte Carlo was lower than 0.2%.

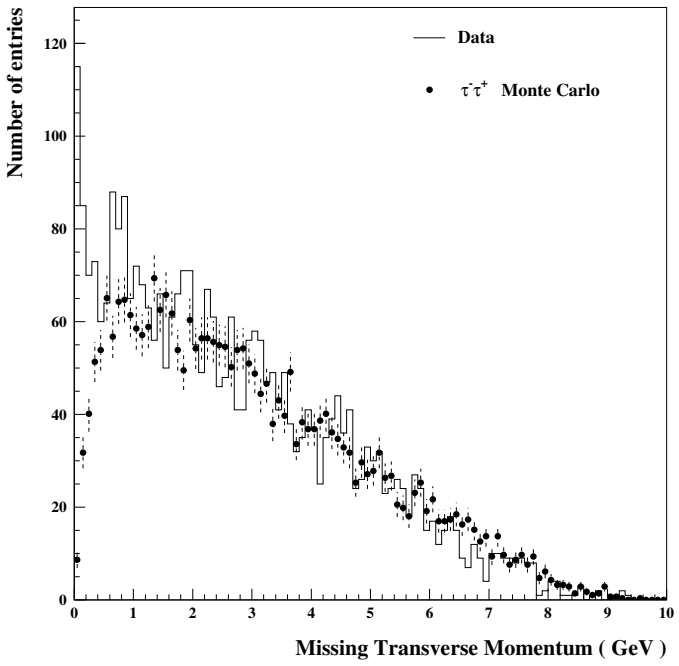


Figure 3.2: Distributions of missing transverse momenta for events having both of the fastest tracks less than 10 GeV in the data and $\tau^+\tau^-$ Monte Carlo. All standard leptonic cuts except the missing transverse momentum cut have been applied. The Monte Carlo distribution has been normalized to that of data.

3.3.6 Tight VD cuts

For events of 1 vs. 1 topology, we impose tight VD cuts to further suppress the background due to cosmic ray muons. The parameter involved is the impact parameter in the $R-\phi$ plane, $I_{R\phi}$. The analyses in 1993 and 1994 have adopted slightly different schemes.

1993

- For events with **both** tracks having associated VD hits and in runs with a well determined beamspot (status flag less than 2 in the beamspot database), it was demanded that both tracks satisfy the condition that $|I_{R\phi}| < 0.15$ cm.
- Otherwise, $|I_{R\phi}|$ was relaxed to be < 1.5 cm.

This is based on the fact that, in the distribution of impact parameters of tracks with VD hits, cosmic muon tracks occupy a flat continuum (outside the interaction

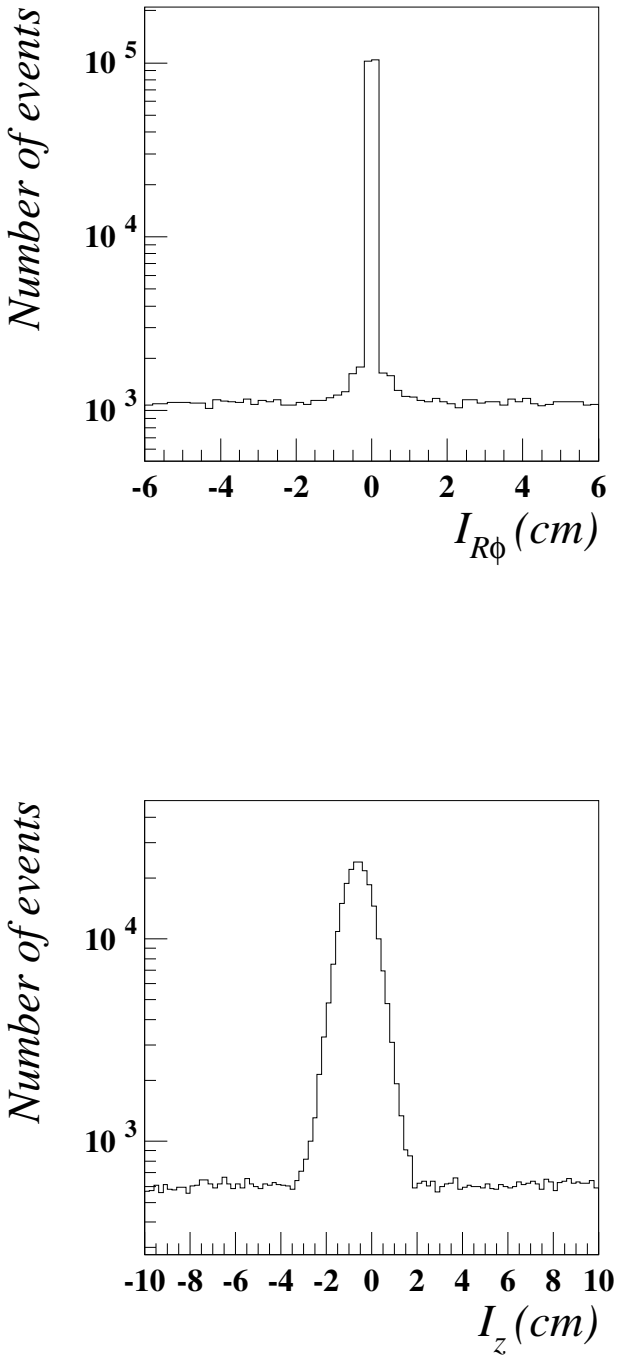


Figure 3.3: Impact Parameters in $R\phi$ and z of tracks with VD hits in the analysis sample.

region) whereas the genuine lepton candidates lie right in the interaction region (the central Gaussian), as shown in Fig. 3.3.

Owing to the limitation of the resolution in the impact parameter along the z direction, no further cut on z impact parameter is made.

1994

For the 1994 data, following the identified leptonic analyses, the tight VD cut for events which have both tracks with associated VD hits with a well determined beamspot has been modified. The tight VD cut for those events without VD hits or a well determined beamspot is the same as in 1993.

Instead of requiring both tracks to have very small $I_{R\phi}$, the event was kept as a good lepton pair candidate if $|I_{R\phi}|$ of either track is smaller than 0.15 cm, i.e.,

$$|I^1_{R\phi}| \ < \ 0.15 \text{ cm} \quad \text{or} \quad |I^2_{R\phi}| \ < \ 0.15 \text{ cm}$$

where $|I^{1/2}_{R\phi}|$ are the impact parameters of the two tracks (1/2) in the $R-\phi$ plane.

The reason is as explained below.

There exists a characteristic correlation between the impact parameters of both tracks in cosmic events which motivated this strategy. Consider a cosmic event in the $R\phi$ plane. In general this misses the beamspot; and two tracks would be reconstructed with impact parameters (almost) equal in magnitude but opposite in sign [2]. For a genuine lepton candidate, no such correlation exists. Both tracks should have an impact parameter of zero, independently smeared by the resolution of the VD.

Figure 3.4 shows $I_{R\phi}$ of the first leading track vs $I_{R\phi}$ of the second leading track. Because of the above explained relations, cosmics describe a diagonal band across the plot ($I^1_{R\phi} = -I^2_{R\phi}$), while genuine lepton event have a dense population centred on the origin. In Fig. 3.3 where the impact parameter of all tracks with VD hits is shown on a common axis, one may eliminate the majority of cosmics by discarding any event with a track $I_{R\phi}$ exceeding a certain cut value. From the two-dimensional plot, however, it is clear that by only vetoing events where both tracks have large impact parameters, more lepton pairs are retained for the same cosmic rejection. Those events with a single badly measured track survive the selection.

[2] The sign of the impact parameter is positive if the scalar product between the unit vector along the thrust axis and the momentum vector of the charged track is positive, and vice versa.

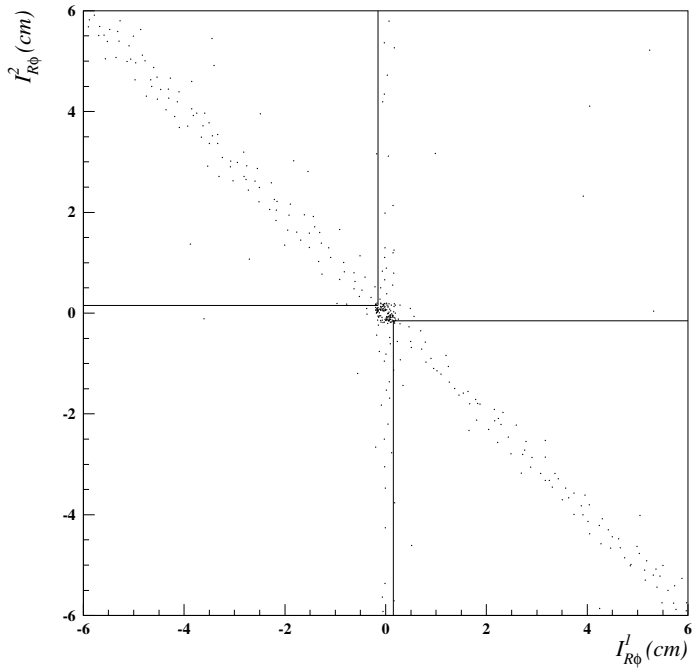


Figure 3.4: Impact parameters distribution $I^1_{R\phi}$ vs $I^2_{R\phi}$.

All these cuts are so positioned as to avoid the loss of genuine lepton candidate events to the level $\sim 0.5\%$. The fraction of background surviving the selection is directly proportional to the cosmic flux per unit area and the size of the acceptance region.

This tight VD cut depends heavily on the tracks making hits in the VD. The fractions of events with both tracks registered hits in the VD and in runs with a well determined beamspot in 1993 and 1994 were respectively 94% and 96%, i.e., very high.

3.4 Data Sample

Using the selection criteria described in the previous section, the number of events selected for the cross-section analysis in 1993 were 65622 at an integrated luminosity of 35.4 pb^{-1}, and 124066 at an integrated luminosity of 45.1 pb^{-1} in 1994. The total integrated luminosity for each of the years was calculated from luminosity files provided by the DELPHI luminosity group from the luminosity measurements by the SAT and VSAT in 1993 and the STIC in 1994.

For the forward-backward asymmetry analysis, only events of 1-1 topology with oppositely-charged tracks are used. This is to avoid uncertainties associated with the track superposition and confusion in the charge determination in τ decays to more than one charged particle. Consequently, 51198 and 99137 events were selected for the asymmetry analysis in 1993 and 1994 respectively.

Fig. 3.5 shows the momentum distribution of the fastest tracks of the selected lepton candidates for this analysis. This clearly shows the electron and muon peak superimposed on the much wider tau distribution.

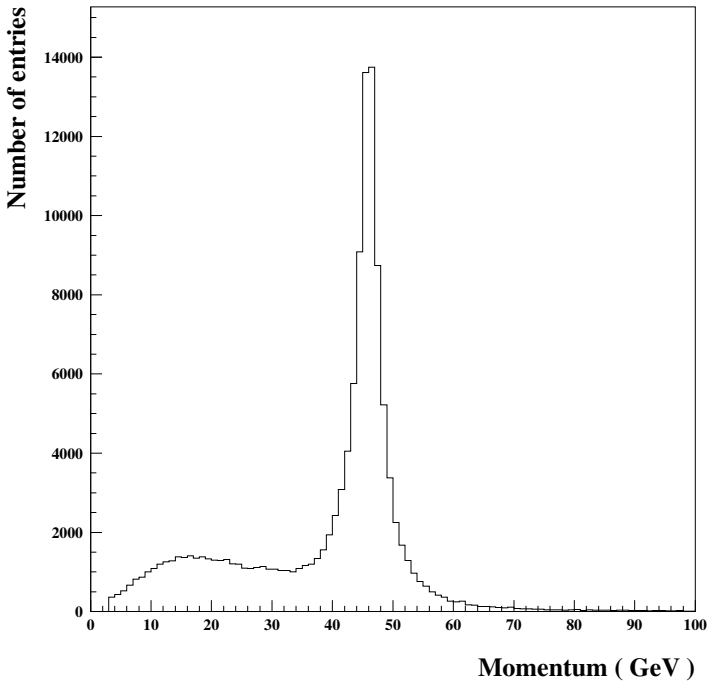


Figure 3.5: Momentum distribution for the fastest charged tracks of the selected lepton candidates for this analysis. The peak around 45 GeV is due to the high momentum electrons and muons, whereas the low momentum region is occupied mainly by the particles from tau decays. The momentum resolution at DELPHI at 45 GeV is about 3%.

Chapter 4

Background and Efficiencies

Though various cuts have been applied in the selection of the data sample, there are still some residual backgrounds faking genuine lepton events. The main backgrounds are due to cosmic rays, two-photon processes and hadronic events. The estimations of these backgrounds are given below, followed by a detailed discussion on the trigger efficiencies and selection efficiencies for all three leptonic channels.

4.1 Cosmic Background

Cosmic rays produce a considerable flux of muons through the whole DELPHI detector. These cosmic ray tracks are of high momenta and therefore are only little deflected by the magnetic field in the detector. The tracks are rather straight and oriented largely 'top-to-bottom' in the detector. The cosmic tracks look the same as muon pairs if they pass close to the interaction region.

The distribution of impact parameters of cosmics within DELPHI is uniform as can be seen from the Fig 4.1. By knowing the density of this distribution, we can estimate the cosmic background within the restricted region defined by the vertex cut.

As described in the section 3.3.6, we have applied slightly different vertex cuts to veto cosmic background in 1993 and 1994 data. The details of background estimation are presented separately.

4.1.1 1993 Cosmic Background Estimation

Since cosmic radiation distribution is uniform on the horizontal plane at DELPHI, the density of cosmic muon distribution is the same everywhere. (See Fig. 3.3 and

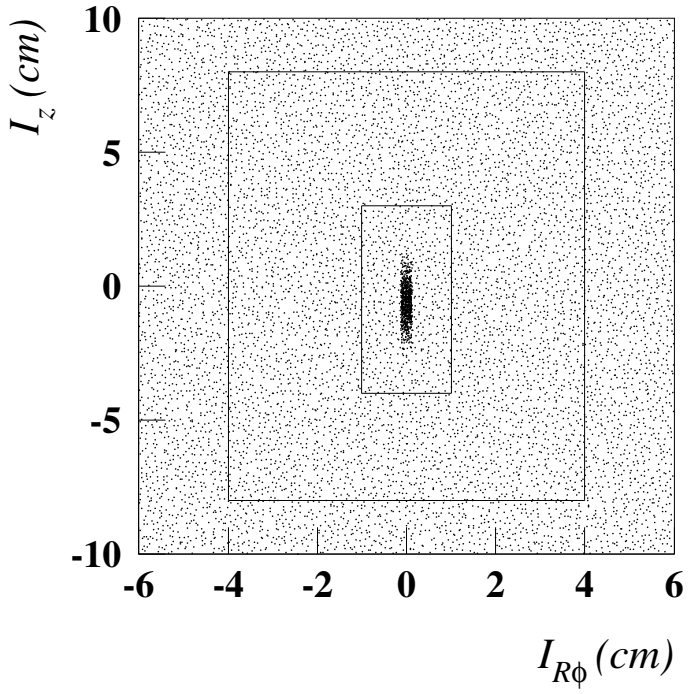


Figure 4.1: Distribution of longitudinal (I_z) and transverse ($I_{R\phi}$) track impact parameters. The genuine lepton candidates populate the centre of the figure while the cosmic muons are uniformly distributed everywhere. The cosmic muon density is equal to the number of entries in the area between the two bounded boxes in the figure divided by that area. In this way, the genuine muons in the interaction region are excluded.

Fig. 4.1). The genuine muons from the Z^0 decays are confined to the interaction region. Thus, one can easily evaluate the density of cosmic muon distribution outside the interaction region. An area away from the interaction region was chosen to calculate the cosmic density. As different cuts have been used to select 1-1 topology events and events of multiplicities ≥ 3, the cosmic densities for each of these categories were determined differently, as ρ^{1-1} and $\rho^{\geq 3}$.

The total cosmic background for events of 1-1 topology, N^{1-1}_{cosmic}, can be determined by the following equation :

$$N^{1-1}_{cosmic} = \left(f^{1-1}_{VD} \cdot A^{1-1}_{VD} \; + \; f^{1-1}_{no\ VD} \cdot A^{1-1}_{no\ VD} \right) \cdot \rho^{1-1} \; . \tag{4.1}$$

where f^{1-1}_{VD} is the fraction of events with VD hits and good beamspots, $f^{1-1}_{no\ VD} = 1 - f^{1-1}_{VD}$, A^{1-1}_{VD} ($A^{1-1}_{no\ VD}$) is the vertex acceptance area on the $I_{R\phi} - I_z$ plane with

(without) VD hits and good beamspots.

Not all cosmic muons appear as 2 tracks of 1-1 topology events because cosmic muons of high momenta may produce additional tracks through electromagnetic interactions when they traverse DELPHI. The total cosmic background for events with ≥ 3 tracks, $N_{cosmic}^{\geq 3}$, is given by :

$$N_{cosmic}^{\geq 3} = A^{\geq 3} \cdot \rho^{\geq 3}. \tag{4.2}$$

where $A^{\geq 3}$ is the vertex acceptance area (on the $I_{R\phi} - I_z$ plane) for events with 3 or more tracks.

4.1.2 1994 Cosmic Background Estimation

The tight VD cut applied for the 1994 data was only different to that of 1993 for those events with VD hits and good beamspots. (Refer to section 3.3.6.) So, it is this category which needs a slightly different treatment, i.e.,

$$N_{cosmic}^{1-1} = \left(f_{VD}^{1-1} \cdot L_{VD}^{1-1} \ + \ f_{no\ VD}^{1-1} \cdot L_{no\ VD}^{1-1} \right) \cdot \rho^{1-1}. \tag{4.3}$$

where L_{VD}^{1-1} (L_{noVD}^{1-1}) is the vertex acceptance length of the 45° diagonal on the $I_{R\phi}^1 - I_{R\phi}^2$ plane with (without) VD hits and good beamspots.

4.1.3 Total Cosmic background

The total number of cosmic background, N_{cosmic}^{total}, is therefore :

$$N_{cosmic}^{total} = N_{cosmic}^{1-1} \ + \ N_{cosmic}^{\geq 3}. \tag{4.4}$$

Table 4.1 gives the total cosmic backgrounds in 1993 and 1994 as fractions of events in the sample for the cross-section σ and forward-background asymmetry A_{FB} analyses. The cosmic background is significantly higher for the cross-section analysis because events with topologies other than 1-1 are also selected in the cross-section analysis and the VD cut for these events is much looser.

In 1993, the analysis is divided into 4 different energy points. The total cosmic backgrounds should be divided into these 4 energy points proportional to their respective integrated running time. Since the integrated luminosity (to a very good approximation) is proportional to the integrated running time, the cosmic

Year		Cosmic Background
1993	for σ analysis	$(0.96 \pm 0.02)\%$
	for A_{FB} analysis	$(0.58 \pm 0.01)\%$
1994	for σ analysis	$(0.42 \pm 0.01)\%$
	for A_{FB} analysis	$(0.17 \pm 0.01)\%$

Table 4.1: Cosmic backgrounds in 1993 and 1994 as fractions in the sample of the cross-section σ and forward-background asymmetry A_{FB} analyses. The numbers here for 1993 correspond to the total number of cosmic backgrounds for all energy points. Errors shown are statistical.

backgrounds found above are distributed proportionally to the integrated luminosity collected at the energy point in question :

$$N^i_{cosmic} = N^{total}_{cosmic} \times \frac{\mathcal{L}_i}{\mathcal{L}_{total}} \tag{4.5}$$

where $\mathcal{L}_{total}$ is the total integrated luminosity of all energy points, N^i_{cosmic} and $\mathcal{L}_i$ are the number of cosmics and the integrated luminosity respectively at energy point i.

4.2 Two-photon Background

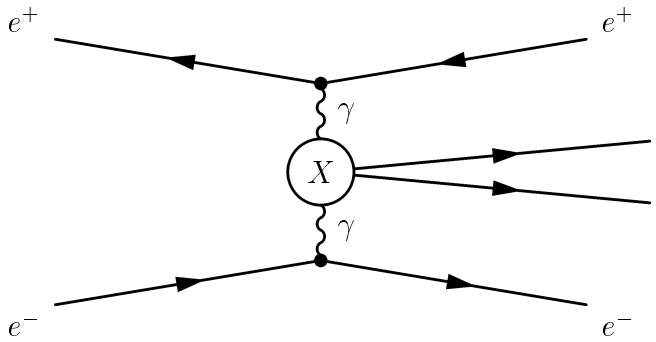


Figure 4.2: Two photon process.

When two virtual photons from the electron and positron beams interact to provide a fermionic intermediate state, it is said to be a two-photon process (Fig. 4.2) :

$$e^-e^+ \rightarrow e^-e^+\mathrm{X}, \tag{4.6}$$

where X represents a leptonic ($l\bar{l}$) or hadronic ($q\overline{q}$) final state.

The characteristic of the two-photon events is the presence of the initial e^+e^- pair in the final state, which usually carries a large fraction of the initial momentum and

suffers only minimal deflection. Thus, the e^+e^- pairs are rarely seen in the detector as they pass down the beampipe and simulations show that there is a negligible contribution in the barrel region, defined previously in the event selection. However, the fermions produced from the fermionic intermediate states may have significant amount of transverse momenta and therefore give rise to a small number of charged tracks in the barrel region. Since these events do not come from the Z^0 decays, they must be categorized as a background.

The calculation of the two-photon background was performed using different Monte Carlos for different two-photon final states. The same selection process as used for selecting leptonic candidates in the data was applied on these Monte Carlo samples and the background $N_{\gamma\gamma}^{bkg}$ was calculated from the intrinsic cross-section of the two-photon process at the generation level (equation 4.7) :

$$\mathrm{N}_{\gamma\gamma}^{\mathrm{bkg}} = \sigma_{\gamma\gamma}^{\mathrm{gen}} \times \frac{\mathrm{N}_{\gamma\gamma}^{\mathrm{sel}}}{\mathrm{N}_{\gamma\gamma}^{\mathrm{gen}}} \times \mathcal{L} \tag{4.7}$$

where $\sigma_{\gamma\gamma}^{gen}$ is the visible cross-section of the two-photon process in the generator, $N_{\gamma\gamma}^{sel}$ is the number of events selected from the two-photon Monte Carlo after all the cuts, $N_{\gamma\gamma}^{gen}$ is the number of two-photon events generated and $\mathcal{L}$ is the integrated luminosity at that energy.

For 1993, two-photon background in the cross-section analysis was estimated to be 6.1 ± 0.3 pb , and 5.2 ± 0.2 pb for 1994. (See Table 4.2.) The errors come from the Monte Carlo statistics. Different generators have been used in both years and this uncertainty will be taken into account in the systematic estimation later.

Year		Two-photon selected σ	Hadronic
1993	for σ analysis	6.1 ± 0.3 pb	$(0.117 \pm 0.012)\%$
	for A_{FB} analysis	4.9 ± 0.2 pb	0
1994	for σ analysis	5.2 ± 0.2 pb	$(0.121 \pm 0.010)\%$
	for A_{FB} analysis	4.2 ± 0.2 pb	0

Table 4.2: Hadronic backgrounds as fractions in the sample of lepton candidates and two-photon backgrounds as selected equivalent cross-sections for the cross-section σ and forward-background asymmetry A_{FB} analyses in 1993 and 1994. The errors are statistical.

4.3 Hadronic Background

Though a cut requiring low multiplicity is applied to combat the hadronic events, the tail of the multiplicity distribution of the hadronic data extends below 6 charged tracks. Therefore, hadronic events still exist as a background in our final selected sample of lepton candidates. Again, Monte Carlo samples are used to estimate the extent of hadronic contamination. The estimation of the hadronic backgrounds was evaluated in the same way as that for the two-photon background and the backgrounds were also distributed according to the integrated luminosity and the hadronic cross-section (obtained from the DELPHI hadronic lineshape team [19]) at each energy point.

Table 4.2 shows the hadronic backgrounds in 1993 and 1994 as fractions in the sample of the cross-section σ and forward-background asymmetry A_{FB} analyses.

4.4 Trigger Efficiency

The lepton trigger efficiency was calculated as the average of the electron, muon and tau trigger efficiencies, which were calculated by each team on the respective lepton-identified analyses. The individual trigger efficiencies were calculated by comparing independent trigger subsets, each consisting of several different detectors [20]. The trigger efficiencies of different years are shown in Table 4.3.

Year	Trigger efficiencies (%)			Average trigger efficiency (%)
	e^+e^-	$\mu^+\mu^-$	$\tau^+\tau^-$	
1993	99.95 ± 0.05	99.88 ± 0.01	99.98 ± 0.01	99.94 ± 0.02
1994	100.00 ± 0.1	99.73 ± 0.05	100.00 ± 0.1	99.91 ± 0.05

Table 4.3: Individual trigger efficiencies and the average lepton trigger efficiencies in 1993 and 1994. The trigger efficiencies for 1994 in channels of electrons and taus are only preliminary estimates.

4.5 Detector Efficiencies

Although the analysis described here treats the lepton families equally in application of event selection cuts, that approach cannot be simply carried over into the

business of efficiency calculation. Different characteristics of the three lepton families mean that different approaches to the efficiency calculations must be used. It is straightforward to produce high purity samples of electrons and muons without using those detectors involved in the event selections, and these may thus be used as independent data for efficiency calculations. The detection efficiencies for electrons and muons can thus be calculated without heavy reliance on Monte Carlo. However, this is not the case for taus as there is no way of identifying taus without relying on the tracking detectors which have been used in the event selection. Therefore, the detector efficiencies for e^-e^+ and $\mu^-\mu^+$ were determined from the data, whereas that for $\tau^-\tau^+$ was mainly from the Monte Carlo.

4.5.1 θ and ϕ cracks in TPC

There are certain small regions in the DELPHI barrel where the track reconstruction is less efficient than in other regions, mainly due to the design of the TPC. There is a gap between 2 halves of TPC at $\theta = 90°$, i.e. on the plane defined by $z = 0$. Moreover, there are also small gaps in-between 6 sectors of the TPC in the $R\phi$ plane. When tracks go through or close to these gaps, they may not be reconstructed and thus the reconstruction efficiency in these regions is expected to be lower than normal.

To separate the e^+e^- and $\mu^+\mu^-$ events from the taus with reasonable purity in the following efficiency analysis, one additional cut was set : the fastest and the second fastest tracks in an event were required to have momenta greater than 40 GeV and 20 GeV respectively.

The TPC sector boundaries are centred at ϕ values where modulo(ϕ, 60°) = 30°. Therefore, a folded ϕ distribution is used to illustrate the loss in this ϕ crack, as shown in Fig. 4.3. This plot shows events from the normal selection with the additional requirements that the two fastest tracks in the event should have momenta greater than 40 GeV and 20 GeV respectively, so as to provide a high purity sample of $\mu^+\mu^-$ and e^+e^-. The histogram here is filled with the fastest track in each event.

The ϕ distribution of leptonic tracks from the Z^0 decays should be flat for a perfect detector. From the folded ϕ distributions, the loss is quantified by fitting a horizontal line to the data lying outside the central region of the histogram and using the result of that fit to estimate the number of lost events in the central bins.

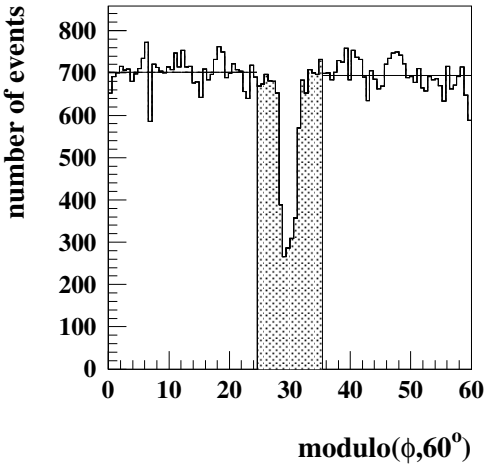


Figure 4.3: modulo(ϕ, 60°) distribution. The shaded area is the crack region. The two lines are the fitted lines outside the crack region.

The overall fraction of tracks lost, $1 - \varepsilon_\phi$, and the efficiency for detecting an event inside the ϕ crack, $\varepsilon^{\phi-in}$ were evaluated as follows :

$$1 - \varepsilon_\phi = \frac{N_\phi^{pred} - N_\phi^{obs}}{N_\phi^{pred} - N_\phi^{obs} + N^{total}} \qquad \text{and} \qquad \varepsilon^{\phi-in} = \frac{N_\phi^{obs}}{N_\phi^{pred}}, \tag{4.8}$$

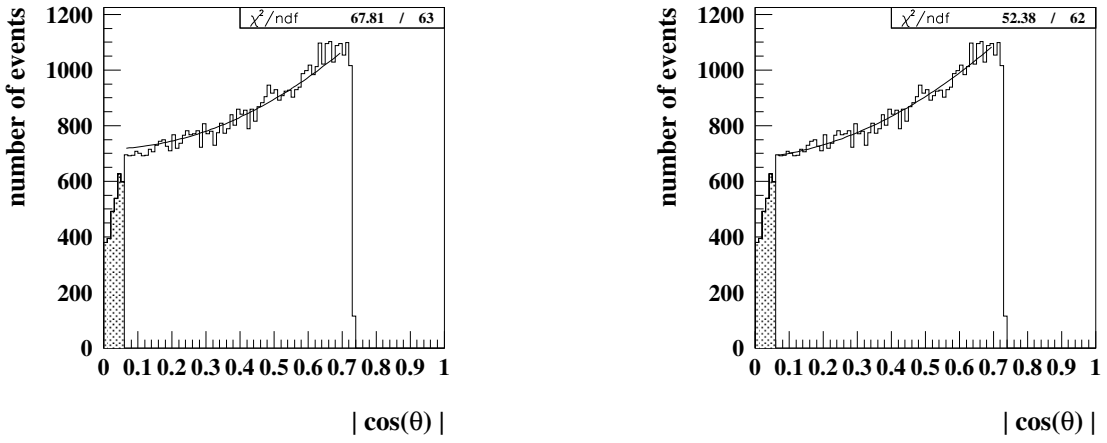
where N_ϕ^{pred} is the predicted number of events if there is no inefficiency due to ϕ crack, N_ϕ^{obs} is the observed number of events in the ϕ crack and N^{total} is total number of events observed over the whole azimuthal angle ϕ.

Losses due to the TPC centre plane can be seen in Fig. 4.4. The inefficiency in θ crack can be evaluated in a similar way as in the case of ϕ crack. As $|\cos\theta|$ is used, it is valid to obtain N_θ^{pred} (the predicted number of events if there was no θ crack) in the crack region by extrapolation of a $\kappa(1 + \cos^2\theta)$ function. Assuming the distribution follows this functional form allows the number of events in a range, $\cos\theta \in (0, x_1)$, N_θ^{pred}, to be obtained by integration,

$$N_\theta^{pred} = \frac{\kappa}{\Delta x} \int_0^{x_1} (1 + x^2) dx, \tag{4.9}$$

where $x = \cos\theta$, Δx is the bin width used and κ is the normalization constant obtained by fitting in a 'good' region of θ.

In reality, one can see that $\cos\theta$ distribution shown in Fig. 4.4 is not strictly ($1 + \cos^2\theta$). Because it contains t-channel electrons which tend to be in the forward region and any contamination of tau decays would also distort the ($1 + \cos^2\theta$)



(a) (b)

Figure 4.4: TPC cracks in θ. (a) The curve represents the fit of the form ($1 + \cos^2\theta$) to the distribution. (b) The curve represents the fit of the form ($1 + A\cos\theta + \cos^2\theta$) to the distribution.

distribution. Different distributions such as ($1 + A\cos\theta + \cos^2\theta$, A is a constant) have been used to fit the $\cos\theta$ distribution and the variation in result thus gives rise to a systematic error. This uncertainty in the determination of inefficiency around θ crack will be taken into account in the systematic calculation.

The overall fraction of tracks lost, $1-\varepsilon_\theta$, and the efficiency for detecting an event inside the θ crack, $\varepsilon^{\theta-in}$, were calculated from N_θ^{pred} and N_θ^{obs} (the observed number of the events in the θ crack) in the same fashion as described in equation 4.8.

Overall Efficiency, $\varepsilon_{\theta\phi}$

One may assume that the θ and ϕ cracks are independent, i.e. a track passing through a ϕ crack would have no inefficiency in terms of θ and vice versa. Thus, the overall reconstruction efficiency due to detector imperfection can be combined in the following way :

$$\varepsilon_{\theta\phi} = P^{\theta-out} \times \varepsilon^{\theta-out}(\phi) + P^{\theta-in} \times \varepsilon^{\theta-in} \tag{4.10}$$

where $P^{\theta-out/\theta-in}$ is the fraction of the theta crack in the TPC, $\varepsilon^{\theta-in}$ is the efficiency of detecting an event which has track(s) inside the θ crack (as explained before) and $\varepsilon^{\theta-out}$ is the ϕ efficiency for events outside the θ crack.

$\varepsilon^{\theta-out}$ may be found indirectly by the following relation :

$$\varepsilon_{\phi} = P^{\theta-out} \times \varepsilon^{\theta-out}(\phi) + P^{\theta-in} \times \varepsilon^{\theta-in}(\phi), \tag{4.11}$$

where $\varepsilon^{\theta-in}(\phi)$ is equal to one due to the independence of ϕ and θ crack assumption.

This is a good approximation but is not exactly true. When one plots the modulo(ϕ, 60°) distribution of those tracks passing through the θ crack, a small inefficiency in the usual crack position still exists, Fig 4.5. This shows that there exists some small correlation between θ and ϕ cracks.

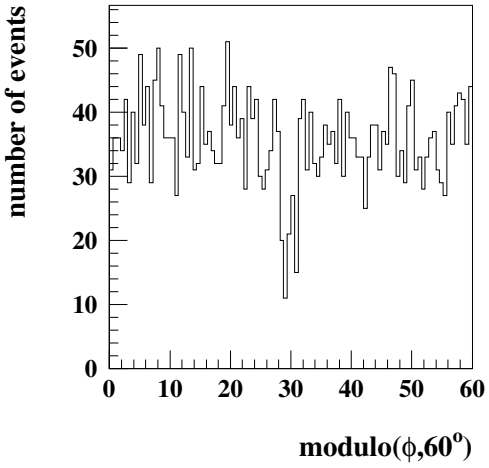


Figure 4.5: modulo(ϕ, 60°) distribution for tracks which are in θ crack. This shows that ϕ crack and θ are not anti-correlated.

In 1994, a slightly different method of combining the efficiencies is used. This is based on the fact that one can actually select tracks which pass through a certain region to calculate the efficiency in that particular region. There are 4 cases to be considered :

- Inside θ crack but outside ϕ crack $\{\theta - in, \phi - out\}$;
- Outside θ crack but inside ϕ crack $\{\theta - out, \phi - in\}$;
- Inside θ crack but inside ϕ crack $\{\theta - in, \phi - in\}$;
- Outside θ crack and outside ϕ crack $\{\theta - out, \phi - out\}$.

The overall detection efficiency can therefore be formulated as :

$$\begin{aligned} \varepsilon_{\theta\phi} &= P_{\theta-in,\phi-out} \cdot \varepsilon_{\theta-in,\phi-out} + P_{\theta-out,\phi-in} \cdot \varepsilon_{\theta-out,\phi-in} \\ &+ P_{\theta-in,\phi-in} \cdot \varepsilon_{\theta-in,\phi-in} + P_{\theta-out,\phi-out} \cdot \varepsilon_{\theta-out,\phi-out} \ , \end{aligned} \tag{4.12}$$

and

$$P_{\theta-in,\phi-out} + P_{\theta-out,\phi-in} + P_{\theta-in,\phi-in} + P_{\theta-out,\phi-out} = 1 \qquad (4.13)$$

where $P_{\theta-in,\phi-out}$ is probability of a track passing through the θ crack but not the ϕ crack, $\varepsilon_{\theta-in,\phi-out}$ is the detector efficiency for a track passing through the θ crack but not the ϕ crack and the other terms have the similar meaning in terms of "$-in$" and "$-out$".

The efficiencies $\varepsilon_{\theta-in,\phi-out}$ and $\varepsilon_{\theta-out,\phi-in}$ were found in similar ways as for $\varepsilon^{\phi-in}$ and $\varepsilon^{\theta-in}$ as shown before, but only with the regions of consideration being restricted accordingly. $\varepsilon_{\theta-out,\phi-out}$ is 1 by definition, and $\varepsilon_{\theta-in,\phi-in} = \varepsilon_{\theta-in,\phi-out} \cdot \varepsilon_{\theta-out,\phi-in}$.

Though different methods have been used, it has been checked that the absolute difference in the efficiencies calculated by the two different methods is only about 0.1%.

The overall efficiencies $\varepsilon_{\theta\phi}$ in 1993 and 1994 taking into account the θ and ϕ cracks in the TPC, using equations 4.10 and 4.12 respectively, are given in Table 4.4.

Year	Efficiency $\varepsilon_{\theta\phi}$
1993	$(94.86 \pm 0.12)\%$
1994	$(95.19 \pm 0.07)\%$

Table 4.4: Efficiency $\varepsilon_{\theta\phi}$ in the tracking detectors (mainly TPC) after taking into account the θ and ϕ cracks, where the errors are statistical only. For 1993, $\varepsilon_{\theta\phi}$ was calculated using equation 4.10; whereas equation 4.12 was used to calculate $\varepsilon_{\theta\phi}$ for 1994.

4.5.2 Live Space Efficiency, ε^{live}

It is possible that there is some residual tracking inefficiency even in regions which have full coverage by DELPHI sub-detectors. This inefficiency is obtained from the data by selecting events which include a high momentum electron or muon candidate, and then looking for another track of reasonably good quality back to back with the first one. The events selected here were as follows :

- Outside any θ and ϕ cracks ,
- The impact parameter in $R\phi$ and z coordinates within 1.5 cm and 3.0 cm of the beamspot respectively .

Very tight cuts were applied to select muons and electrons. The purpose here was to select a high purity sample of electrons and muons at the cost of lower statistics.

For electrons :

- An energy deposit of ≥ 30 GeV in the HPC ,
- No associated hits in muon chambers ,
- A momentum ≥ 25 GeV .

For muons :

- An energy deposit of ≤ 1 GeV in the HPC ,
- ≥ 1 associated hit in muon chambers ,
- A momentum ≥ 25 GeV .

Had a track been identified as an electron or a muon, we looked for another track (in the opposite hemisphere) with acollinearity to the first of less than 10° and with momentum greater than 5 GeV. A missing track indicates a tracking loss. However, the efficiencies determined by this way is not a true estimate of the live space efficiencies, as there is an inherent kinematic loss of tracks due to the momentum and acollinearity cuts. This kinematic loss was accounted for by carrying out the same procedure on the Monte Carlo where live space efficiency is negligible. The final live space efficiencies, ε^{live}, are shown in Table 4.5.

Year		Live Space Efficiencies
1993	e^+e^-	$(100.00 - 0.15)\%$
	$\mu^+\mu^-$	$(99.25 \pm 0.11)\%$
1994	e^+e^-	$(99.78 \pm 0.07)\%$
	$\mu^+\mu^-$	$(99.63 \pm 0.06)\%$

Table 4.5: Live Space efficiencies after comparing data with Monte Carlos, where the errors are statistical only.

4.5.3 Selection cut efficiencies, C^{cuts}

There are some cuts applied in the selection process for lepton candidates which would cost us the loss of small numbers of genuine lepton events. This also has to be considered as an additional correction factor (C^{cuts}) in the calculation of the final selection efficiencies. This loss was estimated from the Monte Carlos for the cuts mentioned in section 3.3.2 except the momentum cut on the leading tracks and also the acollinearity cut. The latter two would be corrected for at a later stage by ZFITTER. The results are given in Table 4.6.

Year		C^{cuts}
1993	e^+e^-	$(99.74 \pm 0.02)\%$
	$\mu^+\mu^-$	$(99.41 \pm 0.02)\%$
1994	e^+e^-	$(99.29 \pm 0.02)\%$
	$\mu^+\mu^-$	$(99.25 \pm 0.02)\%$

Table 4.6: Correction due to various realistic cuts, C^{cuts} for electrons and muons in 1993 and 1994, where the errors are due to Monte Carlo statistics.

4.5.4 Consistency check in Monte Carlo

The above-mentioned exercise of calculating the detector efficiencies has also been done in the Monte Carlo sample of electrons and muons. The results were compared with the respective fractions of Monte Carlo events selected in the same sample if we applied the standard selection cuts as we did for the data. This is to check whether the way the detector efficiencies were calculated from the data was consistent with the cuts we have applied in the selection process.

But, there are a couple of points worth noting here :

- No live space inefficiency was considered as this kind of inefficiency is essentially absent in the Monte Carlo.

- Even at the 'truth information level' of the Monte Carlo sample of electrons, there is a significant intrinsic inefficiency in the θ and ϕ cracks. This is because only events with at least one track were selected in our microdst sample and events with both tracks not reconstructed would be lost. In the regions of TPC cracks, the reconstruction of tracks only relies on the ID and OD but

OD has very low efficiency in reconstructing electron tracks because of the confusing nature of electron hits. Correction has been made in comparing the efficiencies in the Monte Carlo sample of electrons.

For the 1993 comparison, it was found that there is a good agreement (within the error encountered in the calculation) in the electron efficiency, but a discrepancy of $(0.60 \pm 0.06)\%$ (where the error here is statistical) in the muon efficiency. We take half of that (i.e., $(100 - 0.30)\%$) as a correction ($C^{corr}(\mu^+\mu^-)$) towards the final muon selection and another half as a systematic error.

For the 1994 comparison, the story is the same for electron; nevertheless a smaller discrepancy (as compared with that in 1993) of $(0.28 \pm 0.05)\%$ (where the error here is statistical) was found in the muon efficiency. Again, we take half of that (i.e., $(100 - 0.14)\%$) as a correction ($C^{corr}(\mu^+\mu^-)$) towards the final muon selection and the remaining half as a systematic error.

4.5.5 Final electron and muon selection efficiencies

The final electron and muon selection efficiencies are therefore :

$$\varepsilon^{sel} = \varepsilon_{\theta\phi} \times \varepsilon^{live}(e/\mu) \times C^{cuts}(e/\mu) \times C^{corr}(e/\mu) \tag{4.14}$$

Table 4.7 shows the final selection efficiencies for electrons and muons. The errors are statistical.

Year		Selection Efficiencies
1993	e^+e^-	$(94.61 \pm 0.19)\%$
	$\mu^+\mu^-$	$(93.31 \pm 0.16)\%$
1994	e^+e^-	$(94.30 \pm 0.10)\%$
	$\mu^+\mu^-$	$(93.99 \pm 0.09)\%$

Table 4.7: Final selection efficiencies of electrons and muons (in the barrel region) after all corrections. The errors shown here are only statistical.

4.6 Tau efficiency

4.6.1 Raw selection efficiency

The tracking efficiency for tau is very difficult to calculate from the data. Because the tau decays into a variety of final states, a high purity sample cannot be easily isolated by simple kinematics and particle identification, as is the case for muons and electrons. Therefore, the tau selection efficiency was determined by using Monte Carlo, with corrections applied to account for residual data–Monte Carlo discrepancy.

The same selection process applied to the real data has been used here for the Monte Carlo sample. The raw tau selection efficiency $\varepsilon^{raw}_{\tau^+\tau^-}$ is given by the ratio of the number of events selected to the number of events in the original Monte Carlo sample. The result is shown in Table 4.8.

Year	Tau selection efficiency $\varepsilon^{raw}_{\tau^+\tau^-}$ (%)
1993	$53.62 \pm 0.17\%$
1994	$53.72 \pm 0.12\%$

Table 4.8: Tau selection efficiencies in 1993 and 1994 evaluated from the sample of Monte Carlo, where the errors come from the Monte Carlo statistics.

4.6.2 Correction from the real data

Corrections have been applied to account for data and Monte Carlo disagreement.

Discrepancy in the crack inefficiencies

The track reconstruction inefficiencies around the crack regions are not perfectly modelled in the Monte Carlo compared with the real data. The same method used in 4.5.1 has been applied to calculate reconstruction efficiencies in tau Monte Carlos and in the real data. Here only events of 1-3 topology were selected for this calculation so as to obtain the purest possible sample of taus. The correction factor $C^{crack}_{\tau^+\tau^-}$ is the ratio of the track reconstruction efficiency determined from the data to that from the Monte Carlo. This is indicated in Table 4.9. The error above in 1993 is solely statistical. One would expect that the error for 1994 should be smaller

Year	Tau correction factor $C^{crack}_{\tau^+\tau^-}$ (%)
1993	99.97 ± 0.46
1994	100.43 ± 0.46

Table 4.9: Tau correction factors in 1993 and 1994 due to the discrepancy in the modelling of crack inefficiencies in Monte Carlo. The error shown in 1993 is solely statistical while the error of 1994 is set to be equal to that of 1993.

because of more statistics. However, due to the similar problem as mentioned in 4.5.5 in the determination of inefficiency around θ crack, it is decided conservatively that the uncertainty in this correction in 1994 would not be better than the value in 1993, and that error in 1993 was used for 1994 as well.

Topology migration – Radiative correction

In an event, when radiated photons convert to e^+e^- or e^+e^- and $\mu^+\mu^-$ are created as radiation effects in primary processes, the resultant charged multiplicity and hence the topology in an event will be changed. This kind of topology migration due to photon conversions or radiation effects can change, for instance, 1-3 or 1-1 topology events into 3-3 topology events, which are rejected in this analysis. When additional material is not properly modelled in the Monte Carlo, there will be a difference in this aspect and it should also be considered as another correction factor for the final tau efficiency.

Events with 2 to 6 tracks in the electron and muon Monte Carlo sample were selected and the events were also required to have at least a pair of electrons and muons satisfying the criteria listed in section 4.5.2. Events with 2 charged tracks only after this selection are events with 1-1 topology of electrons and muons which have no photon conversion nor radiation from the primary processes; whereas events with more than 2 charged tracks (of 1–N topologies, N = 1, ..., 5) are due to photon conversions or radiations from the primary processes. The same procedure was applied to both real data and Monte Carlo samples and the fractions of events with photon conversions or radiation effects in real data and Monte Carlo for both electrons and muons were found. The ratios of these fractions in real data and Monte Carlo were calculated and the average of these two ratios for electrons and muons is the 'migration correction ratio', $R^{mig}_{\tau^+\tau^-}$.

Moreover, the fraction of rejected events in Monte Carlo due to photon conversions or radiation effects (which disturb the topologies of events and therefore render those events failing the topology cuts) were also found, $f^{mig}_{rejected}$. The correction factor, $C^{mig}_{\tau^+\tau^-}$ to be applied to the Monte Carlo to take into account the topology migration due to photon conversions or radiation effects is :

$$C^{mig}_{\tau^+\tau^-} = \frac{1 - R^{mig}_{\tau^+\tau^-} \times f^{mig}_{rejected}}{1 - f^{mig}_{rejected}} \tag{4.15}$$

The 'migration correction factors', $C^{mig}_{\tau^+\tau^-}$, for 1993 and 1994 are listed in Table 4.10.

Year	Migration correction factor $C^{mig}_{\tau^+\tau^-}$ (%)
1993	99.87 ± 0.04
1994	99.94 ± 0.02

Table 4.10: Migration correction factors to tau efficiencies in 1993 and 1994 due to photon conversions or radiation effects from the primary processes causing topology migrations.

4.6.3 Final Tau selection efficiency

Finally, the tau selection efficiency can be obtained as :

$$\varepsilon^{final}_{\tau^+\tau^-} = \varepsilon^{raw}_{\tau^+\tau^-} \cdot C^{crack}_{\tau^+\tau^-} \cdot C^{mig}_{\tau^+\tau^-} \tag{4.16}$$

For 1993 and 1994, the values of the final tau selection efficiencies $\varepsilon^{final}_{\tau^+\tau^-}$ are shown in Table 4.11.

Year	Final Tau selection efficiency $C^{final}_{\tau^+\tau^-}$ (%)
1993	53.53 ± 0.30
1994	53.92 ± 0.27

Table 4.11: Final tau selection efficiencies in 1993 and 1994 after corrections. The errors shown here are not only statistical but also include the possible systematic effects.

Chapter 5

Cross-Section and Forward-Backward Asymmetry

Evaluation of cross-sections and forward-backward asymmetries and their errors in 1993 and 1994 are given in this chapter. The comparison between this inclusive leptonic analysis and the lepton-identified analyses and the discussion of all these results in the framework of Standard Model will be made in Chapter 10.

5.1 Cross-Section

Taking into account of various backgrounds and efficiencies, the experimental cross-section (σ) for the inclusive leptonic analysis is calculated as follows :

$$\sigma = \left(\frac{N_l - N_{bkg}}{\varepsilon_{ave}^{trig} \cdot \varepsilon_{ave}^{sel}} \; - \; N_e^{t-chan} \; - \; N_{\gamma\gamma} \right) \cdot \frac{C^{cuts}}{3 \cdot \mathcal{L}} \cdot (1 \; + \; f_s) \tag{5.1}$$

The meaning of each of the above terms is given below :

1. N_l represents the number of lepton candidates selected as shown in Table 5.1.

2. N_{bkg} is the total number of cosmic and hadronic backgrounds as estimated in sections 4.1 and 4.3.

3. ε_{ave}^{trig} represents the average trigger efficiency. The average trigger efficiencies in 1993 and 1994 are shown in 4.3.

Year	Energy (GeV)	Luminosity (nb^{-1})	Lepton candidates selected (N_l)
1993	91.293 (PS)	9475.3	15157
	89.430 (P-2)	10416.6	10404
	91.184 (P)	5566.7	28381
	93.013 (P+2)	9939.0	11680
1994	91.198 (P)	45102.8	124066

Table 5.1: Energy, luminosity and lepton candidates selected for the cross-section analysis. 'PS', 'P-2', 'P' and 'P+2' stand for the periods of pre-scan, peak-2, peak and peak+2 during the entire year of LEP run in 1993.

4. ε_{ave}^{sel} represents the average selection efficiencies over the full solid angle (4π) coverage of the detector, i.e.,

$$\varepsilon_{ave}^{sel} = (\varepsilon_e^{4\pi} + \varepsilon_\mu^{4\pi} + \varepsilon_\tau^{4\pi})/3,$$

where $\varepsilon_{e/\mu/\tau}^{4\pi}$ are the selection efficiencies for $e/\mu/\tau$ respectively. The tau selection efficiency $\varepsilon_\tau^{4\pi}$ can be found in Table 4.11. Table 4.7 shows the selection efficiencies for e and μ within the barrel region, $\varepsilon_{e/\mu}^{4\pi}$. To convert to the efficiencies over 4π, they have to be multiplied by a geometrical factor R^{geom},

$$\varepsilon_{e/\mu}^{4\pi} = R^{geom} \cdot \varepsilon_{e/\mu}^{\text{barrel}} \tag{5.2}$$

and R^{geom} is defined by

$$R^{geom} = \frac{\sigma(\text{barrel, 3 GeV, } 20^\circ)}{\sigma(4\pi, \text{ 3 GeV, } 20^\circ)} \tag{5.3}$$

where the numerator and the denominator represent the s-channel cross-sections for $e^+e^- \to e^+e^-/\mu^+\mu^-$ with cuts on the polar angle acceptance in the barrel region (i.e. $43^\circ \leq \theta \leq 137^\circ$), minimum lepton momentum and maximum acollinearity. This ratio was evaluated using TOPAZ0 [21] (which calculates the required cross-sections with the above cuts) and the values are shown in Table 5.2.

5. N_e^{t-chan} represents the theoretically estimated number of events from t-channel Bhabha scattering. Assuming lepton universality, the number of electrons N_e in the lepton sample in an ideal detector (a detector with no inefficiency) is

$$N_e = R_{st} N_{\mu/\tau}. \tag{5.4}$$

Year	Energy	R^{geom}
1993	PS	0.6449
	P-2	0.6443
	P	0.6450
	P+2	0.6420
1994	P	0.6450

Table 5.2: The ratios used to extrapolate the barrel electron and muon efficiencies to 4π, R^{geom}.

where $R_{st} = \sigma(s+t)/\sigma(s)$ (ie., the ratio of the total cross-section of Bhabha scattering to that in s-channel only), and $N_{\mu/\tau}$ is the number of μ/τ.

The decays of Z^0's into $\mu^+\mu^-$ and $\tau^+\tau^-$ pairs are via the s-channel annihilation, whereas for the e^+e^-, there exists the t-channel Bhabha scattering in addition to the s-channel process. The assumption of lepton universality in this analysis means that only the s-channel process should be included and thus the t-channel Bhabha scattering should be subtracted.

The behaviour of the electron t-channel cross-section is well understood and two programs called ALIBABA [22] and TOPAZ0 [21] were used to estimate the extent of its contribution in our final sample. The average of the two calculations is applied to evaluate the contribution of t-channel Bhabha and the discrepancy between these two is treated as a systematic error to the analysis. Table 5.3 shows the values of R_{st}.

Year	Energy	$R_{st} = \sigma(\mathrm{s+t})/\sigma(\mathrm{s})$			
		ALIBABA	TOPAZ0	Average	|Difference|
1993	PS	1.1497	1.1482	1.1489	0.0015
	P-2	1.8695	1.8678	1.8687	0.0017
	P	1.1727	1.1711	1.1719	0.0016
	P+2	1.0157	1.0130	1.0143	0.0027
1994	P	1.1712	1.1723	1.1718	0.0011

Table 5.3: The values of the ratio $\frac{\sigma(s+t)}{\sigma(s)}$ using ALIBABA and TOPAZ0 for various energy points in 1993 and 1994. The calculations involved both leptons in the barrel region satisfying the cuts on the minimum lepton momenta (≥ 3 GeV) and maximum acollinearities ($\leq 20^\circ$).

In order to find the number of electrons in the lepton sample, one also has to know the fraction of electron e_f present in the sample which can be written as

$$e_f = \frac{N_e^{det}}{N_e^{det} + N_\mu^{det} + N_\tau^{det}}$$

$$= \frac{R_{st}\varepsilon_e^{4\pi}}{R_{st}\varepsilon_e^{4\pi} + \varepsilon_\mu^{4\pi} + \varepsilon_\tau^{4\pi}}$$
$$= \frac{R_{st}\varepsilon_e^{barrel}R_{geom}}{R_{st}\varepsilon_e^{barrel}R_{geom} + \varepsilon_\mu^{barrel}R_{geom} + \varepsilon_\tau^{4\pi}} \quad (5.5)$$
$$(5.6)$$

where $N_{e/\mu/\tau}^{det}$ represents the number of $e/\mu/\tau$ seen in DELPHI and hence depends on the respective selection efficiency.

The number of electrons in the lepton sample which we have selected is then

$$N_e = N^{obs} \times e_f \quad (5.7)$$

where $N^{obs} = (\ N_l\ - N_{bkg}\ ) / (\ \varepsilon^{trig}\ \cdot\ \varepsilon_{ave}^{sel}\ )$., representing the total number of leptonic sample corrected for the hadronic and cosmic backgrounds and the trigger and selection efficiencies, and thus the number of 't-channel and s-t channel (interference)' electrons becomes :

$$N_e^{t-chan} = N^{obs} \times e_f \times \left(1 - \frac{\sigma(s)}{\sigma(s+t)}\right)$$
$$= N^{obs} \times e_f \times \left(1 - \frac{1}{R_{st}}\right) \quad (5.8)$$

6. $N_{\gamma\gamma}$ is the background due to two-photon process which has been described in section 4.2. Again, assuming lepton universality, this background is equally divided into each leptonic channel, i.e.,

$$N_{\gamma\gamma} = \frac{N_{\gamma\gamma}^{bkg}}{3} \cdot \left(\frac{1}{\varepsilon_e^{4\pi}} + \frac{1}{\varepsilon_\mu^{4\pi}} + \frac{1}{\varepsilon_\tau^{4\pi}}\right) \quad (5.9)$$

7. $\mathcal{L}$ represents the integrated luminosity.

8. C^{cuts} represents the correction factors due to cuts we have made inherently in the analysis.

   - Before using ZFITTER to correct for momentum and acollinearity cuts, it should be noted that ZFITTER only constrains the anti-lepton in calculation. However, the analysis procedure constrains both the lepton and anti-lepton to be in barrel region. TOPAZ0 was used to corrected for this possible bias and this correction factor R^{barrel} is :

$$R^{barrel} = \frac{\sigma(1 \text{ track in barrel})}{\sigma(2 \text{ tracks in barrel})} \quad (5.10)$$

where $\sigma(1/2$ track(s) in barrel) denotes the theoretical cross-section given by TOPAZ0 for leptons with 1/2 track(s) in the barrel region of $43^\circ \leq \theta \leq 137^\circ$.

- The loss of leptonic events due to the momentum cut ($\geq$ 3 GeV) on the fastest track and the accollinearity cut ($\leq 20^\circ$) can be corrected for by the program ZFITTER [8]. This correction factor $R^{3/20}$ can be calculated as :

$$R^{3/20} = \frac{\sigma^{\mathrm{ZFIT}}(\text{no cuts})}{\sigma^{\mathrm{ZFIT}}(\text{cuts})} \tag{5.11}$$

where σ^{ZFIT}(nocuts/cuts) represents the theoretical cross-section calculated by ZFITTER for leptons with / without cuts.

The correction factors $R^{3/20}$ and R^{barrel} given in Table 5.4.

Year	Energy	R^{barrel}	$R^{3/20}$
1993	PS	1.0019	1.0177
	P-2	1.0022	1.0338
	P	1.0018	1.0178
	P+2	1.0060	1.0259
1994	P	1.0018	1.0178

Table 5.4: Correction factors for the leptonic cross-sections. $R^{3/20}$ corrects for the momentum and acollinearity cut while R^{barrel} corrects for the fact that ZFITTER only constrains 1 track in the barrel region.

Therefore, the overall correction due to the above cuts C^{cuts} is :

$$C^{cuts} = R^{3/20} \times R^{barrel} \ . \tag{5.12}$$

9. $(1 + f_s)$ is the small correction applied to the measured cross-sections to account for the finite Gaussian spread in LEP beam energy, a spread which arises from the emission of synchrotron radiation. Convoluting this effect with the rapidly changing shape of the Z^0 resonance [1] , the effective cross-sections at each energy point is shifted slightly with respect to the cross-section which

[1] The convolution may be expressed as :

$$\sigma(\text{measured}) = \int [\sigma(E) G(E - E_0)]\, dE \ ,$$

where E is the beam energy, $G(E)$ is the gaussian distribution with a mean E_0.

would be measured if the beam energy was monochromatic. Correction factors were calculated through knowledge of the spread in beam energy [23] and [24] and through the resonance shape taken from ZFITTER. The values are listed in Table 5.5.

Year	Energy	$1 + f_s$
	PS	1.0012
1993	P-2	0.9994
	P	1.0012
	P+2	0.9995
1994	P	1.0012

Table 5.5: Beam spread correction factors $1 + f_s$

10. The factor 3 in equation 5.1 means that the cross-section is corresponding to that for one generation assuming lepton universality.

The resultant cross-sections at different centre-of-mass energies in 1993 and 1994 are tabulated in Table 5.6.

Year	Energy	Cross-Section (nb)	Statistical Error (nb)
	PS	1.4946	0.0129
1993	P-2	0.4872	0.0064
	P	1.4847	0.0094
	P+2	0.6776	0.0064
1994	P	1.5014	0.0046

Table 5.6: Inclusive leptonic cross-section results with all the above-mentioned corrections and the statistical errors in 1993 and 1994.

5.2 Uncertainties on the cross-section measurement

5.2.1 Statistical Errors

The statistical error of the cross-section σ depends on the raw number of selected events, i.e.,

$$\delta\sigma \propto \sqrt{N_l} \tag{5.13}$$

where N_l represents the number of lepton candidates selected as given at the beginning of this chapter. Based on equation 5.1, the total statistical error on the cross-section is :

$$\delta\sigma = \left(\frac{\sqrt{N_l}}{\varepsilon_{ave}^{trig} \cdot \varepsilon_{ave}^{sel}} \right) \cdot \frac{C^{cuts}}{3 \cdot \mathcal{L}} \cdot (1 \ + \ f_s) \tag{5.14}$$

The statistical errors in 1993 and 1994 are listed in Table 5.6.

5.2.2 Systematic Errors

Background subtraction :

- Estimation of the two-photon background depends on the Monte Carlo generators. Different generators have been used for 1993 and 1994 (for practical reasons), and there are some differences between the intrinsic cross-sections in the generators quoted by the authors. A conservative uncertainty of 0.5 pb (comparable to the difference between the total cross-sections of the two-photon background) was assigned and this translates to a systematic error of up to 0.061% (due to off-peak) in 1993 and 0.019% (on-peak) in 1994.
- Hadronic backgrounds were found to be very low because of the power of the multiplicity cut. The percentages of hadronic events passing the leptonic cuts in both years were very much the same. The statistical errors in the calculation translate to a systematic error of 0.013% in 1993 and 0.010% in 1994.
- The cosmic backgrounds were estimated directly from the data. The uncertainty comes from the statistical error in the estimation of cosmic density. This translates to errors of 0.018% in 1993 and 0.010% in 1994.

Trigger efficiency : The trigger efficiency of leptons was taken to be the average of the efficiencies of three individual channels. Note that only the trigger efficiencies for individual lepton channels in 1993 and muon channel in 1994 are deemed to be final; whereas those of electrons and taus in 1994 are only preliminary estimates (at the time of writing this thesis). The overall systematic errors due to the trigger efficiencies are 0.017% and 0.05% in 1993 and 1994 respectively.

Selection efficiency : The selection efficiencies were used to help us obtain the cross-section in full solid angle of a perfect detector. In calculating the errors, we have considered the systematic effect in the calculation of selection efficiencies as well as the statistical errors. The uncertainty in the θ crack calculation due to the fitting of $|\cos\theta|$ distribution is about 0.1% in the final efficiencies of electrons and muons. Moreover, the uncertainties of muon selection efficiencies of 0.30% and 0.14% (see section 4.5.4) in 1993 and 1994 respectively were used to propagate into the final systematic errors. Taking into account of all these, they translate to an error of 0.28% in 1993 and 0.16% in 1994.

t-channel subtraction : The t-channel subtraction is determined by averaging the values calculated using ALIBABA and TOPAZ0. Two categories of systematic errors were considered.

- The difference between the programs TOPAZ0 and ALIBABA in the theoretical calculation in t-channel subtraction is treated as a source of systematic errors. The differences shown in Table 5.3 translate to systematic errors of up to 0.10% in 1993 (due to off-peak points), 0.02% in 1994 (on-peak).

- The theoretical uncertainties in TOPAZ0 and ALIBABA due to incomplete treatment of the higher order perturbative effects in the calculation of cross-sections for Bhabha scattering also lead to systematic errors. The fractional error on the ratio R_{st} ($\sigma(s+t)/\sigma(s)$) can be expressed as

$$\frac{\delta R_{st}}{R_{st}} = \left[\left(\frac{\delta\sigma(s+t)}{\sigma(s+t)} \right)^2 + \left(\frac{\delta\sigma(s)}{\sigma(s)} \right)^2 - 2\rho \left(\frac{\delta\sigma(s+t)}{\sigma(s+t)} \right) \left(\frac{\delta\sigma(s)}{\sigma(s)} \right) \right]^{1/2} \tag{5.15}$$

  where ρ is the correlation.

  Table 5.7 shows the errors assigned by the authors of TOPAZ0 and ALIBABA [26].

  There is no information about the correlation between the errors from TOPAZ0 authors. Including or omitting higher order terms in the perturbation should lead to positive correlation between $\sigma(s+t)$ and $\sigma(s)$. Then, the maximum uncertainty in the ratio R_{st} corresponds to $\rho = 0$.

Source	TOPAZ0		ALIBABA
	peak	off-peak	peak
$\delta\sigma(s)/\sigma(s)$	0.2%	0.3%	0.5%
$\delta\sigma(s+t)/\sigma(s+t)$	0.3%	0.5%	0.4%

Table 5.7: Theoretical uncertainties of TOPAZ0 and ALIBABA due to incomplete treatment of the higher order perturbative terms in the calculation of Bhabha scattering. There are no error assignments for off-peak points from the authors of ALIBABA.

Applying equation 5.15 with $\rho = 0$, and then propagating to the final cross-sections, the uncertainties were found to be a maximum of 0.29% at P-2, but only 0.13% at peak.

The correlation between the errors in ALIBABA was assigned to be $\rho = 0.2$. Similarly, applying equation 5.15 and propagating into the cross-section formula, the uncertainty was found to be 0.23%.

It has to be noted that the items of errors in the theoretical calculation are correlated to some degree as they all originate from the source — the incomplete treatment of higher order terms in perturbative calculation. Adopting a conservative approach, 0.29% is assigned to be the systematic error for 1993 from this source, and 0.23% for 1994 which is on the peak energy only.

Polar angle θ : The polar angle θ was the result of a full detector fit to each track. An uncertainty in the determination of θ would give rise to an error in the extrapolation of the cross-section from the barrel region to the full solid angle. At the polar cut in this analysis, ie. 43°, the accuracy of θ is $\lesssim 0.3$ mrad [25].

The error, due to the uncertainty in θ, was estimated by extending or shrinking the angular range by 0.3 mrad and checking how many more or fewer events were accepted. The changes were found to be 0.041% and 0.034% in 1993 and 1994 respectively, which are therefore the corresponding systematic errors due to the polar angle uncertainty.

M_H and m_t: Various corrections were made using theoretical calculations such as ALIBABA, TOPAZ0 and ZFITTER. The calculations involved depend on the values of m_t and M_H. In the calculation, masses of m_t and M_H were taken to be 175 GeV and 300 GeV. The uncertainty due to m_t is now very small and comparatively the uncertainty due to M_H is larger. M_H was set to extreme

values such as 1000 GeV and all the correction factors involved due to the above 3 programs were re-calculated. The maximum deviation due to this cause was found to be at P-2, where the t-channel contribution is the largest (due to the lower energy). (See Fig. 1.3.) This corresponds to 0.033% in 1993. In 1994, the correction at peak point is less sensitive to the radiative correction due to M_H and m_t and the systematic error was evaluated to be only 0.007%.

Summing up all the above items in an uncorrelated manner, the total systematic errors for the cross-sections due to the above effects are 0.41% and 0.29% in 1993 and 1994 respectively. Table 5.8 gives the summary for all the cross-section systematic errors.

Source	1993	1994
Background subtraction	0.06%	0.02%
Trigger efficiency	0.02%	0.05%
Selection efficiency	0.28%	0.16%
t-channel subtraction	0.29%	0.23%
Polar angle	0.04%	0.03%
M_H and m_t	0.03%	0.01%
Total	0.41%	0.29%

Table 5.8: Absolute values of systematic errors on cross-sections in 1993 and 1994.

5.3 Forward-Backward Asymmetry

The selection process for the forward-backward asymmetry (A_{FB}) analysis is almost the same as for the cross-section analysis, except for the following :

- As luminosity knowledge is not needed in this analysis, the requirement for the luminosity flag in the run-selection was dropped ;
- Only events of 1-1 topology were selected ;
- The events inside the θ crack were discarded ;
- Events of like-sign were excluded .

A counting method — counts the number of events having the negative tracks (leptons) in the forward or backward region — is used to calculate the forward-backward asymmetry. The overall formula is the following :

$$A_{FB} = \left(A_{FB}^{raw} \times A_{scale} - A_{t-chan} + A^{1\ \mathrm{trk}} \right) \times C^{4\pi} \tag{5.16}$$

Each of the above terms will be explained below :

1. The raw forward-backward A_{FB}^{raw} is defined by :

$$A_{FB}^{raw} = \frac{N_F \ - \ N_B}{N_F \ + \ N_B} \tag{5.17}$$

where N_F and N_B are the number of negatively charged particles selected in the forward and backward regions respectively.

Replacing N_F and N_B by the number of positively charged particles in the forward and backward regions respectively, we expect to get an asymmetry with the same magnitude but opposite sign. However, due to imperfect reconstruction (and detector), there are some tiny differences. We take the average magnitude of the asymmetries determined by these two methods as A_{FB}^{raw}. The values are shown in Table 5.9.

Year	Energy	Lepton		Anti-Lepton		A_{FB}^{raw}
		N_F^-	N_B^-	N_F^+	N_B^+	average
1993	PS	6041	5570	5566	6045	0.0409
	P-2	4538	3678	3676	4540	0.1049
	P	11894	10659	10668	11885	0.0544
	P+2	4813	4005	4011	4807	0.0910
1994	P	52101	47036	47032	52105	0.0511

Table 5.9: Raw forward-backward asymmetries, A_{FB}^{raw}, which are the averages of two methods considering respectively negative tracks and positive tracks.

2. A_{scale} is the correction factor due to cosmic and two-photon backgrounds. From Monte Carlo, no hadronic events pass the leptonic cuts. Both the cosmic and two-photon backgrounds have no asymmetries and so these events dilute the signed asymmetry [2]. This is corrected by the factor A_{scale}:

$$A_{scale} = \frac{N_{total}}{N_{total} \ - \ N_{cosmic} \ - \ N_{\gamma\gamma}} \tag{5.18}$$

[2] Because the numerator in equation 5.17 would be the same with or without the backgrounds; whereas the denominator would be larger with the backgrounds and thus give a smaller A_{FB}^{raw}.

where N_{cosmic} and $N_{\gamma\gamma}$ are the cosmic and two-photon backgrounds respectively, and N_{total} is the total number of events selected for the asymmetry analysis (i.e., the sum of N_F and N_B in equation 5.17).

3. Again, the t-channel events in Bhabha scattering have to be subtracted and it is done in the following way :

$$A_{t-chan} = e_f(asym) \times (A_{FB}(s+t) \; - \; A_{FB}(s)) \tag{5.19}$$

where $e_f(asym)$ denotes the fraction of electron present in the sample for the asymmetry analysis, $A_{FB}(s+t)$ and $A_{FB}(s)$ are the forward-backward asymmetries (theoretically) calculated by ALIBABA and TOPAZ0 for (s+t)- and s-channels respectively [3]. A simple proof of the above expression is given in Appendix A. Here, $e_f(asym)$ is calculated as :

$$e_f(asym) = \frac{R_{st}\varepsilon_e^{4\pi}F_e^{1-1}}{R_{st}\varepsilon_e^{4\pi}F_e^{1-1} \; + \; \varepsilon_\mu^{4\pi}F_\mu^{1-1} + \varepsilon_\tau^{4\pi}F_\tau^{1-1}} \tag{5.20}$$

where $F_{e/\mu/\tau}^{1-1}$ represents the fraction of events of 1-1 topology in the sample for $e/\mu/\tau$. Table 5.10 lists F^{1-1} for different channels in 1993 and 1994 and Table 5.11 shows the calculation results of A^{t-chan}.

	F^{1-1}	
	1993	1994
e^+e^-	$88.50 \pm 0.27\%$	$87.23 \pm 0.11\%$
$\mu^+\mu^-$	$96.54 \pm 0.05\%$	$96.63 \pm 0.04\%$
$\tau^+\tau^-$	$58.11 \pm 0.22\%$	$56.23 \pm 0.23\%$

Table 5.10: Fractions of 1-1 events, F^{1-1}, for electrons, muons and taus in 1993 and 1994. The errors shown are statistical.

Year	Energy	A^{t-chan}
1993	PS	0.1099 ± 0.0010
	P-2	0.4599 ± 0.0008
	P	0.1251 ± 0.0006
	P+2	0.0138 ± 0.0010
1994	P	0.1237 ± 0.0017

Table 5.11: Corrections due to t-channel and s–t interference in the forward-backward asymmetry calculation, A^{t-chan}. The errors shown are the absolute differences between the results calculated by TOPAZ0 and ALIBABA.

4. Similar to the case for the cross-section analysis, TOPAZ0 was used to correct for the fact that ZFITTER only constrains the anti-lepton in calculation.

$$A^{1 \text{ track}} = A_{FB}^{1 \text{ track}} \; - \; A_{FB}^{2 \text{ tracks}} \tag{5.21}$$

where $A^{1/2 \text{ track(s)}}$ denotes the theoretical forward-backward asymmetries given by TOPAZ0 for leptons with 1/2 track(s) in the barrel region of $43^\circ \leq \theta \leq 137^\circ$. The values of this correction are shown in Table 5.12.

[3] The θ crack has been excluded in the calculation.

5. Finally, $C^{4\pi}$ was used to extrapolate the s-channel asymmetries (from the value valid for the barrel region) to full solid angle. It was evaluated from ZFITTER with the following definition :

$$C^{4\pi} = \frac{A_{FB}^{4\pi}(ZFIT)}{A_{FB}^{barrel}(ZFIT)} \tag{5.22}$$

where $A_{FB}^{4\pi}(ZFIT)$ stands for the asymmetry calculated over the full solid angle using ZFITTER and $A_{FB}^{barrel}(ZFIT)$ over the barrel region only (excluding the θ crack region). The values of this extrapolation factor are tabulated in Table 5.12.

Year	Energy	$A^{1\text{ track}}$	$C^{4\pi}$
	PS	-0.0004	1.1623
1993	P-2	-0.0010	1.1596
	P	-0.0004	1.1091
	P+2	-0.0004	1.1558
1994	P	-0.0004	1.2887

Table 5.12: Correction factors for forward-backward asymmetry. $A^{1\text{ track}}$ corrects for the fact that ZFITTER only constrains the anti-lepton in calculation, while $C^{4\pi}$ extrapolates the asymmetry to full solid angle.

It should be noticed that the forward-backward asymmetry calculated here is not corrected for the momentum and acollinearity cuts. In fitting these results within ZFITTER, these cuts are accounted for.

Table 5.13 gives the values of final forward-backward asymmetries after all the above corrections at different energy points in 1993 and 1994.

Year	Energy	Forward-Backward Asymmetry (A_{FB})	Statistical Error
	PS	-0.0050	0.0108
1993	P-2	-0.1606	0.0127
	P	0.0027	0.0074
	P+2	0.1002	0.0123
1994	P	0.0002	0.0041

Table 5.13: Inclusive leptonic forward-backward asymmetries with all the above-mentioned corrections and the statistical errors in 1993 and 1994.

Fig. 5.1 shows the results of the analysis of forward-backward asymmetries A_{FB} and the theoretical prediction, according to the Standard Model, is given for comparison. The agreement is reasonable.

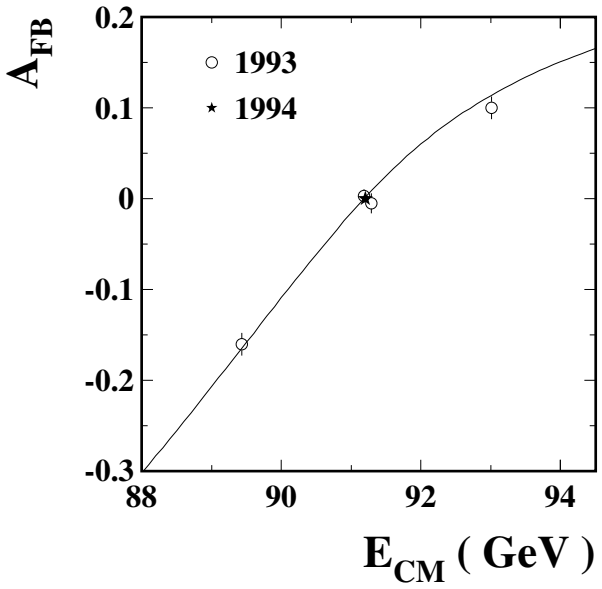


Figure 5.1: Measurements of forward-backward asymmetries A_{FB} in 1993 and 1994 against the centre-of-mass energy. The curve is the Standard Model prediction for A_{FB} using ZFITTER with the following set of Z^0 resonance parameters : $M_Z = 91.186$ GeV, $m_t = 175$ GeV, $M_H = 300$ GeV, and the cuts on the minimum lepton momenta (≥ 3 GeV) and maximum acollinearities ($\leq 20°$) for both leptons.

5.4 Uncertainties on the forward-backward asymmetry

5.4.1 Statistical Errors

Replacing N_F and N_B in equation 5.17 with n and N such that $n = N_F$ and $N = N_F + N_B$, one obtains

$$A_{FB}^{raw} = \frac{2n - N}{N} \tag{5.23}$$

which implies

$$\delta(A_{FB}^{raw}) = \frac{2}{N} \times \delta(n) \tag{5.24}$$

The error on n is equal to the standard deviation of the binomial distribution, i.e., $\delta(n) = \sqrt{n\ \left(1\ -\ \frac{n}{N}\right)}$, and therefore we have

$$\delta(A_{FB}^{raw}) = \frac{2}{N} \times \sqrt{n\ \left(1\ -\ \frac{n}{N}\right)}\ , \tag{5.25}$$

Using equation 5.16, the overall statistical error on the forward-backward asymmetry is given by

$$\delta(A_{FB}) = \frac{2}{N} \times \sqrt{n\ \left(1\ -\ \frac{n}{N}\right)} \times A_{scale} \times C^{4\pi}\ . \tag{5.26}$$

These statistical errors of forward-backward asymmetries are given in Table 5.13.

5.4.2 Systematic Errors

Various systematic effects, which may alter the calculated values of forward-backward asymmetries, have been considered and described as follows :

Background subtraction : The low backgrounds from cosmic rays, two-photon events and hadronics have the effect of diluting the asymmetries. Owing to the small size of the background, the error on the asymmetries has been estimated to be < 0.0001 in 1993 and negligible in 1994.

Selection efficiency : Though not as influential as in the measurement of cross-sections, selection efficiencies still have influences in the determination of $e_f(asym)$, the fraction of electrons in the analysis sample. The statistical and systematical uncertainties on the selection efficiencies (the same as for the cross-section analysis) have been carried through $e_f(asym)$ in the overall calculation of A_{FB} and they translate to total errors on A_{FB} of 0.0004 and 0.0001 in 1993 and 1994 respectively.

$\mathbf{F^{1-1}}$: The fraction of events of 1-1 topologies in the entire sample selected, F^{1-1}, was also involved in the determination of $e_f(asym)$. Similar to the treatment of uncertainties of selection efficiency, the uncertainties shown in Table 5.10 translate to errors of 0.0005 and 0.0001 in 1993 and 1994 respectively.

t-channel subtraction : Two types of possible errors involved in the t-channel subtraction in 5.19 are considered :

- As in the cross-section analysis, the difference between TOPAZ0 and ALIBABA involved in the t-channel subtraction in A_{FB} is treated as a source of systematic errors. The differences shown in Table 5.11 can give rise to a systematic error of 0.0003 in 1993 and 0.0005 in 1994 respectively.
- The theoretical uncertainties in TOPAZ0 and ALIBABA can also lead to systematic errors in A_{FB}. Using a similar procedure to that for the cross-section, the largest systematic error is for P-2 and is of 0.0008.

A systematic error of 0.0009 is assigned for both 1993 and 1994.

M_H and m_t : Similar to the case in the cross-section analysis, the above masses were changed, and all the correction factors were re-calculated. A systematic error of 0.0007 was found in 1993 and 0.0002 in 1994.

Like-sign events : Approximately 0.7% of events in the selected samples in both years had two lepton candidates of the same assigned charge because of confusions in the track fit. Attempts have been made to establish reliably which track was the negative lepton for such events. However, the result was not satisfactory. It would give rise to a larger systematic error than the reduced statistical error obtained with the inclusion of those like-sign events. It was therefore decided to discard the like-sign events from the analysis.

To estimate the uncertainty due to the appearance of like-sign events, the differences in the values of A_{FB} before and after reclaiming [4] some of those like-sign events were evaluated.

It was found that the systematic errors on the asymmetries from this source in both 1993 and 1994 were < 0.0001.

Both signs wrong : It is possible that both tracks in an event were assigned the wrong charges. Since the fraction of like-sign events was found to be about

[4] The reclaim method here is based on the positioning of the energy cluster of the track in the HPC. The distinguishing quantity is $\Delta\phi = \phi_2 - \phi_1 - 180°$ (adding 360° if the resulting $\Delta\phi$ is less than $-180°$), differs with the charges of the tracks, where ϕ_1 refer to the ϕ angle of the electromagnetic shower in the HPC associated with the fastest track and ϕ_2 with the second fastest track.

0.7%, the chance that both tracks were assigned of wrong signs is approximately $(0.7\%)^2$, in which the correlation (of wrong charge assignment) between the two tracks is assumed to be negligible. The systematic error due to this is about $(0.7\%)^2/\mathrm{N_{total}}$ where $\mathrm{N_{total}}$ is the total number of events in the sample. This quantity was found to be negligible at the level of precision of this analysis.

Polar angle θ : Similar to the treatment in the cross-section analysis, the polar angle acceptance was changed and the change in asymmetry at each energy point was found to be 0.0003 in 1993 and negligible in 1994.

+ve and −ve track asymmetries : The asymmetries determined by using positive tracks A_B^+ and by negative tracks A_{FB}^- were slightly different. This is due to the differences in the measurements of the polar angle θ in the forward and and backward hemispheres of the TPC. An average was used in the final calculation and the difference should induce a systematic error proportional to

$$\left| \frac{A_{FB}^+ - A_{FB}^-}{\sqrt{2}} \right| \quad .$$

The systematic error due to this source was calculated to be 0.0008 and 0.0001 in 1993 and 1994 respectively.

As a result, the overall systematic errors are 0.0016 in 1993 and 0.0009 in 1994. Table 5.14 summarize and lists all the systematic errors in 1993 and 1994 for the asymmetry analysis.

Source	1993	1994
Background subtraction	0.0001	negligible
Selection efficiency	0.0004	0.0001
F^{1-1}	0.0005	0.0001
t-channel subtraction	0.0009	0.0009
Like-sign events	0.0001	0.0001
Polar angle	0.0003	negligible
$\mathrm{M_H}$ and $\mathrm{m_t}$	0.0007	0.0002
+ve/−ve track asymmetries	0.0008	0.0001
Total	0.0016	0.0009

Table 5.14: Absolute values of systematic errors on A_{FB} in 1993 and 1994.

The comparison between the results on the cross-sections and asymmetries from the inclusive leptonic analysis and the lepton-identified analyses will be given in Chapter 10. The parameters one may extract from these measurements in the framework of Standard Model will be also made there.

Chapter 6

LEP Collision Energy

This chapter introduces various aspects in the measurements of the collision energy at LEP. The principle of absolute energy calibration by Resonant Depolarization is given and followed by some "well-known" parameters which can affect the LEP collision energy.

6.1 History and Importance of Energy Measurements at LEP

Particle collisions at different collision energies (or called centre-of-mass energies) around the Z^0 resonance peak, known as an *'energy scan'*, allow a direct measurement of the resonance line shape, especially the Z^0 mass, M_Z, which is one of the fundamental ingredients of the Standard Model, and its resonance width, Γ_Z, which provides a very sensitive test of the theoretical model. The latter is due to higher order radiative corrections in the cross-section lineshape as described in 1.7, which give information not directly seen at LEP energies such as the masses of the top quark and the Higgs boson.

It should be noted here that the peak energy point of the energy scan is chosen such that the cross-section measurements do not have any sensitivity to the uncertainties of the absolute energy scale. In terms of a (cross-section) lineshape, this is the point where the derivative of the cross-section to the centre-of-mass energy is equal to zero. This also means that the measurements of M_Z and Γ_Z are insensitive to the peak energy of an energy scan.

The four LEP experiments measure and determine errors on the cross sections and forward-backward asymmetries while the LEP Energy working group [1] contributes by evaluating the collision energy and its error. These results are then combined by the LEP Electroweak working group taking into account the common systematic errors between all the four LEP experiments. Uncertainty on the LEP collision energy (as well as the theoretical error on the luminosity measurement) is the main component of the common systematic errors .

LEP had its first energy scans in 1989 and 1990. From the data taken up to the end of 1990 by the four LEP experiments, the statistical error on the value of M_Z was 5 MeV compared to the uncertainties in the LEP energy scale of 20 MeV [27]. Since then, it was clear that a better absolute energy calibration at LEP was necessary in order to improve the precision of the values of M_Z and Γ_Z. In 1991, an energy scan of seven different energies within $\pm$ 3 GeV was performed and the energy calibration by resonant depolarization was commissioned [2], which is the most accurate method for calibrating the beam energy of e^+e^- storage rings. The 1991 energy scan resulted in a precision on the measurement of M_Z of 7 MeV, where the error was still dominated by the knowledge of the absolute energy scale (about 6 MeV) [27].

In 1992, LEP started to operate in 'Pretzel' mode and this resulted in much higher statistics of Z^0 decays. Meanwhile, more knowledge on the determination of the absolute energy scale was also gained. The precision on the values of M_Z and Γ_Z was significantly improved by the 1993 energy scan with three different energies within $\pm$2 GeV (see Table 5.1). The scan strategy of three energy points was chosen to be optimal for the least error on Γ_Z. Table 6.1 shows the results of these measurements of M_Z and Γ_Z at LEP including data up to the 1993 energy scan [28].

Table 6.1 shows the significant improvement in the accuracy of the measurements of M_Z and Γ_Z in the 1993 scan, as compared with that in the previous energy scan in 1991. The absolute energy scale was determined to very high precision (about 2 in 10^5). For the first time, the errors in the measurements of M_Z and Γ_Z were dominated by the experimental errors, which were mainly statistical, rather than

[1] The author has been a member of this group since the beginning of 1995.

[2] In 1991, the energy calibrations by resonant depolarization were done only at the energy point P-2.

	M_Z (MeV)	Γ_Z (MeV)
Mean	91188.3	2497.4
Δ_{TOTAL}	2.2	3.1
Δ_{ENERGY}	1.4	1.5
Δ_{EXP}	1.8	2.7

Table 6.1: Measurements of M_Z and Γ_Z at LEP including data up to the 1993 energy scan. Δ_{TOTAL} denotes the total errors, Δ_{ENERGY} the errors due to LEP energy uncertainties and Δ_{EXP} the errors from LEP experiments.

the uncertainties on the absolute energy scale. Since the measurement was statistics limited, there were good grounds for accumulating additional off-peak luminosity. After discussion within the LEP community, it was decided in 1995 to have a final energy scan around Z^0 resonance at the end of the LEP1 period. This aimed to reduce the experimental statistical errors on the measurements of M_Z and Γ_Z to the level of systematic errors. In addition, improvements in the determination of the parameters controlling these systematic errors were foreseen.

The details of the energy scan in 1995 will be presented in the following parts of this thesis. One point which should be mentioned here is that the accuracy and the absolute LEP energy scale itself previously determined for the 1993 scan (Table 6.1) were found to be overestimated after new knowledge was gained in the 1995 scan.

6.2 Principle of Resonant Depolarization

This section briefly describes how the average beam energy can be measured instantaneously by the method of resonant depolarization.

In an ideal e^+e^- storage ring the beams naturally polarize along the direction of the bending field due to the emission of synchrotron radiation [29]. With purely vertical magnetic fields, the vertical component of the electron spin vectors is conserved. The ensemble average of all spin vectors is defined as the polarization vector, $\vec{P}$. Due to the Sokolov-Ternov effect, vertical polarization can build up to a maximum of 92.4%. Any non-vertical magnetic fields reduce the equilibrium degree of polarization below its maximum and perturb the spin precession.

In fact, the spin vector of each electron precesses on average $a_e\gamma$ times during one turn of revolution around the ring, where a_e is the electron magnetic moment anomaly and γ is the average Lorentz factor of this electron. The *spin tune* is defined

as $a_e\gamma$ and the time-averaged spin tune, ν, of each electron is proportional to the average beam energy, E :

$$\nu_0 = a_e\gamma = \frac{a_e E}{m_e c^2} = \frac{E[\mathrm{MeV}]}{440.6486(1)[\mathrm{MeV}]} \ , \tag{6.1}$$

where m_e is the mass of the electron and c is the speed of light.

The spin precession frequency of the polarization vector is precisely measured by inducing a resonant depolarization of the beam with an oscillating radial field from an RF-magnet[3]. If the perturbation from the RF-magnet is in phase with the spin precession, the spin rotations about the radial direction add up coherently from turn to turn. The RF-magnet field oscillating at a frequency f_{dep} is in resonance with the spin precession if

$$f_{dep} = (k \pm [\nu]) \cdot f_{rev} \ , \tag{6.2}$$

where f_{rev} is the revolution frequency of the particles ($f_{rev} = 11.25$ kHz at LEP) and k is an integer. $[\nu]$ denotes the non-integer part of the spin tune. Its integer part is determined from the setting of the bending field. The frequencies f_{dep} used at LEP correspond to the cases $k = 0$ or $k = 1$. The resonance condition is depicted in Fig. 6.1. The frequency f_{dep} is varied until a depolarization is observed. The spin tune can then be calculated with equation 6.2 from the measured f_{dep} and the average beam energy E is obtained from equation 6.1. This method is often referred to as **energy calibration by resonant depolarization** and has been used extensively for accurate beam energy calibrations (such as in [30] and [31]).

Experimentally, the frequency of the RF-magnet field is slowly varied with time over a given range. The difference, $\delta\nu_{scan}$, in frequency between the start and the end of the "sweep" determines the resolution of the spin tune measurement and is chosen to be small enough to match the requirements of precise energy calibration. For standard energy calibrations $\delta\nu_{scan}$ was set to 0.002, which corresponds to 0.9 MeV in the beam energy.

Two additional measurements are required to uniquely determine the beam energy because a single energy calibration cannot resolve all ambiguities. A measured

[3]The operating frequency of this magnet is about 5 kHz, approximately half of the revolution frequency of e^+e^- beams. This is very fast compared with that of a normal iron magnet (typically 20 Hz) and that is where the term 'RF-magnet' comes from.

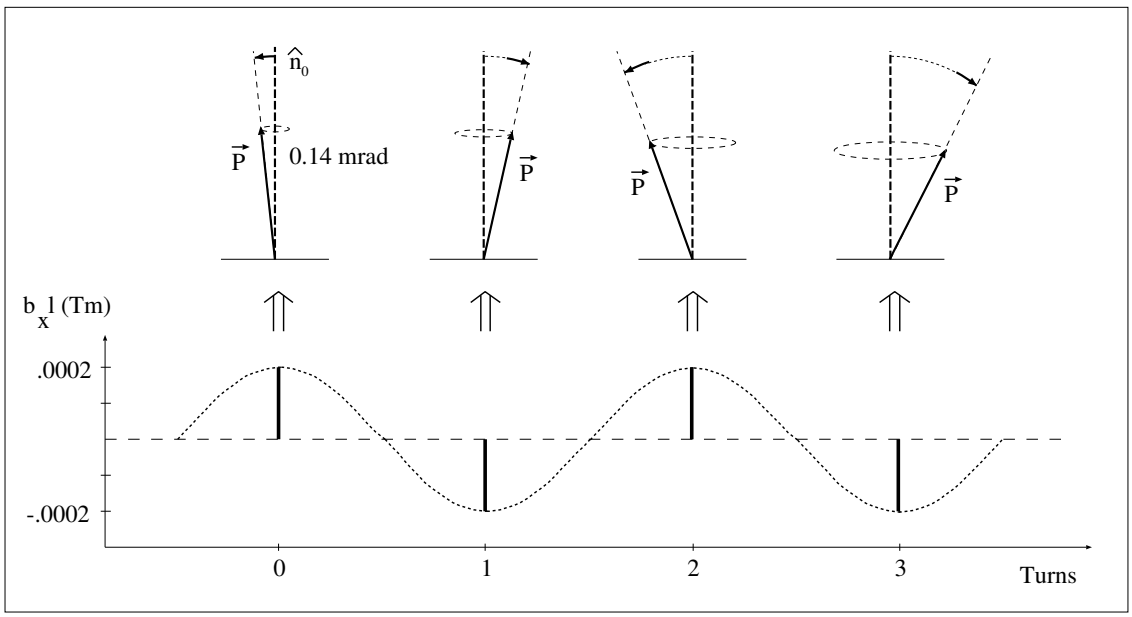


Figure 6.1: Resonance condition between the nominal spin precession with $[\nu] = 0.5$ and the radial perturbation from the RF-magnet.

non-integer part of the spin tune $[\nu]$ is compatible with a mirrored spin tune of $1 - [\nu]$. To solve this mirror ambiguity, the beam energy is varied and the corresponding change of f_{dep} is measured. The beam energy is varied by changing the RF frequency, to avoid modifying the magnetic set up. Depolarization can also occur on synchrotron satellites which appear at spin tunes of $\nu_{sides} = \nu \pm Q_s$, where Q_s is the synchrotron tune, defined as the number of synchrotron (i.e. longitudinal) oscillations per turn of the revolution of the particle. The main resonance ν can be separated from the satellites ν_{side} because it is not shifted by a change of Q_s.

6.2.1 Calibration accuracy

The complete study of systematic errors on an individual energy calibration at LEP by using the method of resonance depolarization has been described in [32]. The total systematic error on energy calibration by resonant depolarization is estimated to be about 0.2 MeV on the Z^0 peak, which was obtained using theoretical studies. The theoretical estimates could be verified experimentally with only limited precision. A systematic error of 0.5 MeV was used to account for the uncertainty in the measurement of energy.

6.2.2 From beam energy to centre-of-mass energy

In general, the beam energy of LEP is subject to fluctuations due to the LEP machine settings and to different "environmental conditions". Their impact on the energy can be minimized or corrected by a tight control of the running conditions (temperature and excitation of the magnets, RF frequency etc.), a good understanding and prediction of the effects (like tidal deformations) and a continuous monitoring of critical parameters such as temperature and magnet currents. During the period of energy scan, every effort has been made to maintain the maximum stability of the LEP machine as well as the detectors in the four experiments.

In spite of all efforts, beam energies may still vary from fill to fill and also within a fill; whereas the energy calibration by resonant depolarization can only provide the average beam energy at the particular moment when the measurement takes place. For practical reasons, the technique of resonant depolarization cannot possibly be applied to calibrate the beam energy continuously during the scan. In fact, there is a considerable fraction of fills during scans which have not been calibrated at all. It is important to understand the effects which can make the beam energy evolve from fill to fill or during a fill and be different from that at the time of calibration. The knowledge of these effects would help us establish an 'energy model' to interpolate the beam energy at the time between calibrations.

The instantaneous beam energy varies as the e^+e^- beams travel around the LEP tunnel. This is because of the energy loss in the synchrotron radiation and the accelerating RF system at LEP. An IP-dependent RF correction on top of the average beam energy interpolated is therefore needed. The RF correction will be described in more details in section 6.4.1.

Moreover, the centre-of-mass energy is not just the sum of the beam energies of e^+ and e^- because of the existence of dispersion effects at the IP's. This dispersion effect is particularly important in the 'bunch train' mode used in LEP since 1995 and will be explained in section 8.2.

6.3 Parameters Affecting the Beam Energy

This section introduces the basic mathematical formulation of the beam energy in terms of certain parameters, such as the magnetic field inside the accelerator, and

describes the effects which can possibly affect beam energy. Only those effects which have been known before the 1995 scan will be elaborated here and those new effects discovered in 1995 will be described later in the following chapters.

6.3.1 Basic formulation

The relativistic energy-momentum equation, $E^2 = (pc)^2 + (mc^2)^2$, underlines the relation between the beam energy E and the momentum p, where m is the mass of the particle and c is the speed of light. This in turns leads to the equality of relative energy and momentum changes :

$$\frac{\Delta E}{E} = \frac{\Delta p}{p} \tag{6.3}$$

For a plane storage ring operating with $\gamma \gg 1$, the energy of the beam is basically determined by the following two relations [33] :

1. Equating the Lorentz force and centripetal force follows the proportionality of the particle momentum $p(s)$ with the magnetic field $B(s)$ and the local radius of curvature $\rho(s)$:

$$p(s) = qB(s)\rho(s). \tag{6.4}$$

where q is the charge of the particle. The integral of the beam deflection along the path of the particle s, given by the ratio of $qB(s)ds$ upon $p(s)$, has to be equal to 2π to obtain a closed orbit :

$$\oint \frac{ds}{\rho} = \oint \frac{qB(s)}{p(s)}\, ds = 2\pi \tag{6.5}$$

A closed orbit is the self-consistent solution of the equation of motion with periodic constraints and represents the equilibrium path in a storage ring.

2. The particle is kept synchronous to the RF (radio-frequency) phase of the accelerating structure during stable beam operation. For ultra-relativistic particles, the length of the closed orbit, L, has to be a multiple of the RF wavelength

$$L = \beta h_f \lambda_{RF} \cong h_f \lambda_{RF} \tag{6.6}$$

where β is the ratio of the speeds of the particle and light, h_f is harmonic number which represents the number of RF cycles per particle revolution. h_f is 31324 at LEP.

In other words, the orbit length L is constant as long as the RF wavelength does not change.

A very simple equation comes from equation 6.4, i.e.,

$$\frac{\Delta p}{p} = \frac{\Delta \rho}{\rho} + \frac{\Delta B}{B}. \tag{6.7}$$

The orbit separation is characterised by the *momentum compaction factor* α_c which is defined as,

$$\alpha_c = \frac{\Delta \rho}{\rho} \Big/ \frac{\Delta p}{p} = \frac{\Delta L}{L} \Big/ \frac{\Delta p}{p} \tag{6.8}$$

A more detailed description of the meaning of the momentum compaction factor α_c can be found in Appendix B.

From equations 6.3 and 6.6, and the fact that $c = \lambda_{RF} \times f_{RF}$, we end up with the relation

$$\frac{\Delta E}{E} = \frac{1}{\alpha_c}\frac{\Delta L}{L} = -\frac{1}{\alpha_c}\frac{\Delta f_{RF}}{f_{RF}}. \tag{6.9}$$

The momentum compaction factor α_c has been measured. The RF frequency was changed and the corresponding energy change (measured by resonant depolarization) was used to extract α_c. One set of measurements is shown in Fig. 6.2. The measured value of α_c is $(1.860 \pm 0.020) \times 10^{-4}$ which is in excellent agreement with the theoretical expectation of $\alpha_c = 1.859 \times 10^{-4}$ obtained from simulation of LEP.

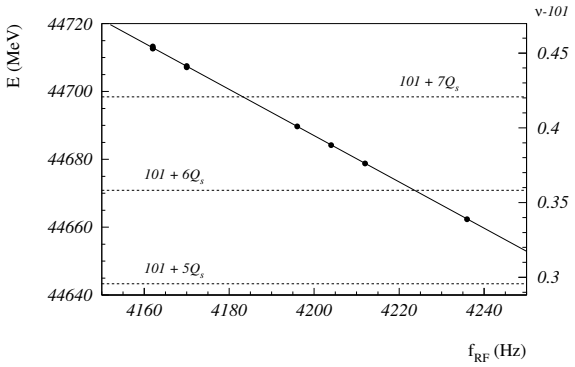


Figure 6.2: Measured change of beam energy E as a function of the RF frequency f_{RF}. Only the last four digits of f_{RF} are indicated. The nominal RF frequency f_{RF} used at LEP is 352 254 170 Hz). The errors on the energy measurements are smaller than the symbols used in this figure.

As we will see later, the circumference (or equivalently the radius) of the LEP tunnel can be changed. When the length of the beam orbit is fixed by the constant RF frequency (which is the case during normal physics running), the change in

circumference C_c would force the particles to move off-centre in the focusing magnets where they receive an extra deflection. This leads to a change in the beam energy ΔE :

$$\frac{\Delta E}{E} = -\frac{1}{\alpha_c}\frac{\Delta C_c}{C_c} \tag{6.10}$$

To summarize, *when the RF frequency is fixed, either a change in the magnetic field or the circumference of tunnel gives rise to a corresponding change in the beam energy.* The following sections in this chapter will be devoted to explain what factors can affect either the magnetic field or the circumference of the LEP tunnel.

6.3.2 Magnetic dipole and quadrupole fields

At LEP, the electron and positron beams are bent and focused in a piecewise circular trajectory by strings of magnets. The magnets can be divided into 2 main categories :

1. *Bending or Dipole magnets* : Dipole magnets produce a constant dipole field which does not depend on the transverse position, i.e., $B(x) = B_0$, where x represents the transverse displacement. The dipole field determines more than 99.9% of the beam energy.

2. *Focusing magnets* : These magnets produce higher order fields which are proportional to the transverse displacement to different orders. Most importantly, quadrupole magnets produce fields which are linear with the transverse displacement, i.e., $B(x) = kx$, where k denotes the quadrupole strength. [4]

If the beam traverses the magnets on the nominal orbit, the beam energy would be completely determined by the dipole field of magnets (no stray fields and machine distortions assumed). The average beam energy is then directly proportional to the integral dipole field. However, when a particle goes off-centre through a quadrupole magnet, it sees the quadrupole field. That is, the quadrupole field relates beam energy with beam transverse position.

The beam energy is governed by both the dipole and quadrupole fields. Effects which affect the beam energy by changing dipole field and quadrupole field are treated differently and are discussed separately below.

[4] The alternating polarity of the quadrupoles provides the alternating-gradient **(A. G.)** focusing or **'strong'** focusing in modern accelerators such as LEP.

6.3.3 Dipole field effects

Magnet Temperature

The bending field of the LEP dipole magnets has a significant dependence on the magnet core temperature because of the steel-concrete structure of the magnets [34]. The variation of the steel permeability due to a stress variation induced by a difference in the thermal expansion coefficient of steel and concrete gives rise to a large temperature coefficient (magnetostriction effect [35]). The temperature coefficient, C_T^{ring}, is defined as :

$$C_T^{ring} = \frac{1}{E}\,\frac{\Delta E}{\Delta T} \tag{6.11}$$

where T is the average temperature of 34 out of more than 3300 dipole magnet cores. The 34 sensors are evenly distributed in all octants.

The temperature coefficient C_T^{ring} of the LEP dipoles (inside the tunnel) has been measured on several occasions with energy measurements by resonant depolarization performed in a period of large temperature fluctuation. Fig. 6.3 shows one measurement of C_T^{ring} during the fill 1734 in 1993.

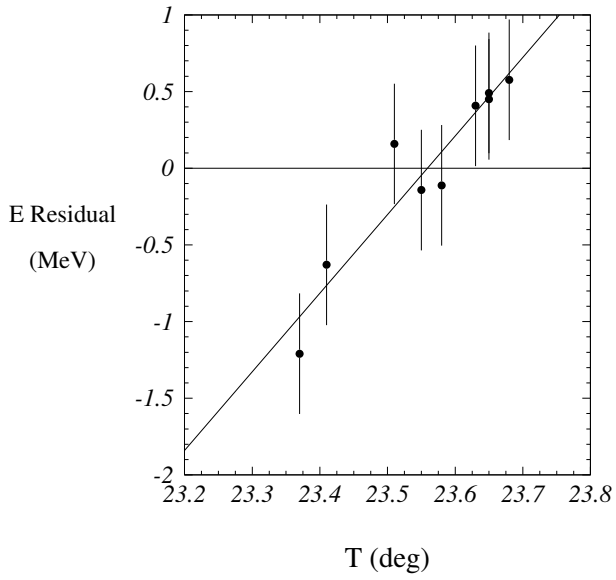


Figure 6.3: The residual energy variation (after correction for RF frequency changes and tides) is shown as a function of the average magnet temperature (fill 1734 in 1993).

The magnetic characteristics of some dipole cores were tested in a laboratory at CERN and the temperature dependence of the the magnetic field was clearly shown to be genuine, rather than an accidental instrumental effect. The temperature coefficient measured in the laboratory was comparable to the temperature coefficients observed in the LEP tunnel.

QFQD compensation coil

LEP runs with significantly different phase advances for the horizontal and vertical planes and there is a net current around the ring arising from the fact that the current required in the focusing quadrupoles (QF) is larger than that in the defocusing quadrupoles (QD). To cancel the magnetic fields created by this current asymmetry, a compensating current loop, i.e., the so-called "QFQD compensation coil", has been installed in the LEP ring. Owing to a mistake, this loop was reversed or turned off for periods of data taking during the 1993 energy scan. Fortunately, the current in the loop, I_{Qfd}, was logged during the whole scan. The loop is positioned about 1 m from the beam path and at the same height, so that the magnetic field due to this current has a vertical component at the beam position. Because of the presence of many shielding objects, such as dipole and quadrupole magnets, it is not possible to calculate accurately the effect on the energy of the beams. The magnitude of this effect was measured directly in a dedicated experiment by comparing the LEP energy, measured by resonant depolarization, before and after inverting the current in the loop. For a typical 70 A change of the current I_{Qfd}, it was found to have a change of $\Delta E = -3.0 \pm 1.4$ MeV on average, which is in good agreement with the theoretical estimate. A correction based on the logged value of the current I_{Qfd} and the above conversion factor was included in the 1993 beam energy calculation. Fortunately, this mistake did not happen again in the 1995 scan.

Instrumentation for measuring the dipole field

Nuclear **M**agnetic **R**esonance (NMR) probes and induction coils are used to measure the LEP dipole field. The detailed information and working principle of NMR can be found in [36]. Only a brief description is provided below.

The principle used by the LEP NMR is based on a fast passage through the nuclear magnetic resonance of a proton sample (water). A transverse field B_1 is superimposed on an homogeneous external field B_0 (which we want to measure) and B_1 would produce a detectable rotating vertical magnetization. By measuring the energy absorption signal at resonance, one obtains B_0.

The NMR gauss-meters at LEP can be used to measure magnetic fields ranging from 450 G to 20.5 kG. It is designed for an absolute precision of 5×10^{-6} with a

reproducibility of better than 2 mG integrated over the cross section of the probe-head.

The induction coils including the fluxloop and the flipcoil measure the change of magnetic flux.

- The fluxloop measurement covers a large fraction of the accelerator's dipole field; whereas the NMR measurement is much more localized. Under controlled conditions, fluxloops determine the average dipole field throughout a complete octant with a precision of 10^{-4} [37]. There is one fluxloop measurement for each of the 8 octants of LEP.

- A flipcoil is mounted in the reference magnet, and was used to track the magnetic field with a precision of 10^{-4} [37].

NMR probes are only useful at measuring a very homogeneous field ; whereas induction loops may work in virtually all field environment, independent of the field quality. Nevertheless, NMR probes deliver the most precise measurements of the magnetic dipole field, while induction loop measurements are used as a cross-check.

Fig. 6.4 shows the C-shaped iron yoke of a typical LEP dipole magnet installed with NMR and fluxloop in the tunnel.

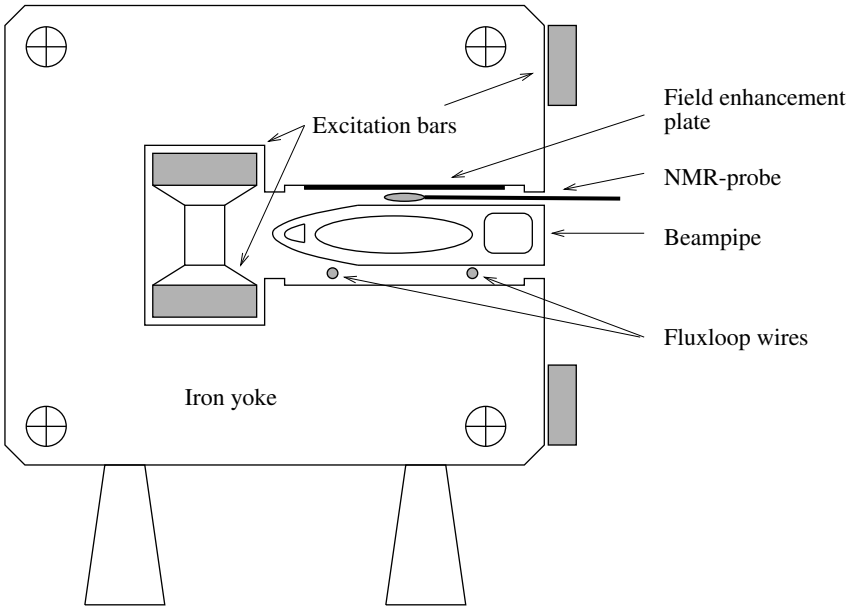


Figure 6.4: A cross-sectional view of a typical LEP dipole magnet installed with NMR and fluxloop. The four excitation bars carry the current to generate the magnetic field.

Each dipole magnet at LEP is composed of a stack of low-carbon steel laminations, 1.5 mm thick and separated by 4 mm gaps. The gaps (or so-called cores) of the tunnel dipoles are filled with cement mortar for maximum mechanical stability. However, the core in the reference magnet (which is installed in a surface building at IP2, i.e., outside the LEP tunnel) does not have mortar inside and a rather sophisticated mechanical stabilization system has been installed instead. This reference magnet is connected in series with the LEP main dipole magnets and is intended to exhibit the same hysteresis effects as the LEP dipoles. It has a very small temperature coefficient [38]. The reference magnet is also used for the fluxloop calibration.

At the time of the 1993 scan, only one NMR placed inside the reference magnet was installed. This NMR is denoted as NMRREF hereafter. More NMR's have been installed in 1995 which will be discussed in section 7.1.4.

6.3.4 Quadrupole field effects

Terrestrial Tides

The gravitational attraction from the moon and the sun is not uniform over the surface of the Earth because of the $1/r^2$ dependence of the gravitational forces, where r is the distance between two interacting bodies. As a result, the gravitational and centrifugal forces are not everywhere in equilibrium, which results in a small elastic deformation of the Earth's body producing two daily tide bulges. (See Fig. 6.5.) The lunar and the weaker solar tides interfere to produce tide bulges that can move the crust up and down by up to $\sim$ 25 cm in the Geneva area. This corresponding to a local fraction change of the earth radius of $4 \cdot 10^{-8}$. The strain modifies the circumference of LEP C_c by 1 mm [39].

From equation 6.10, and the fact that the momentum compaction factor α_c ($= 1.86 \cdot 10^{-4}$) is very small (which is due to the strong quadrupole focusing of LEP), tiny changes of the circumference are enhanced by 4 orders of magnitude and result in measurable changes of energy as large as about 10 MeV.

In a good approximation, the horizontal strain (i.e. the change of circumference) is proportional to the change in gravity Δg, a quantity that can be predicted by computer codes with reasonable accuracy [40]. In terms of energy change, the tide

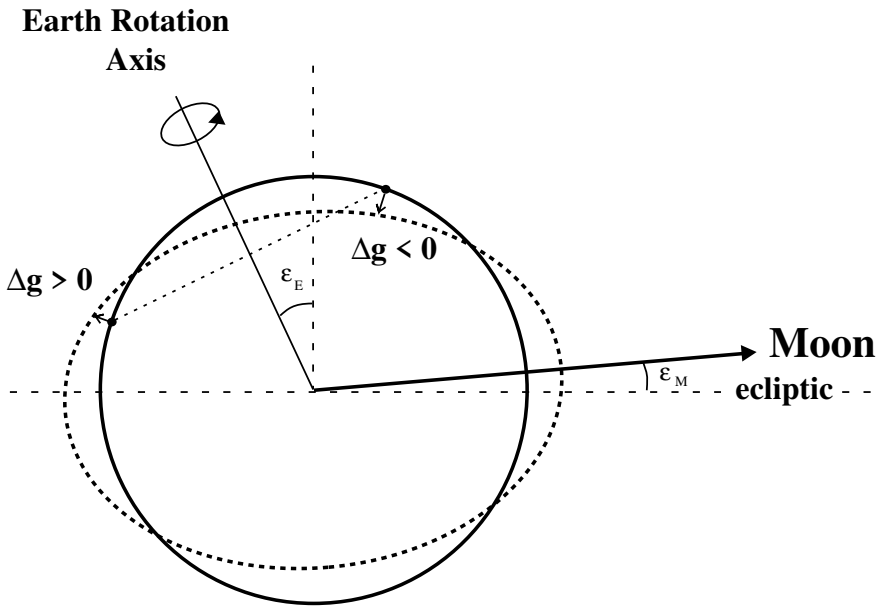


Figure 6.5: Tidal deformation of the Earth crust due to the presence of the moon. One tide bulge is formed in the direction of the moon and another one just opposite of it. The changes in gravity associated to the tidal deformations Δg are indicated for an observer at a latitude of about 45°. Here, the inclination of the Earth rotational axis ϵ_E is 23°26′ and that of the lunar orbital plane ϵ_M is 5°8′.

coefficient κ_{tide} relates Δg to ΔE :

$$\frac{\Delta E}{E} = \kappa_{tide} \Delta g \tag{6.12}$$

A high tide Δg exceeds 140 μgal in Geneva (1 gal = 1 cm s^{-2}). Since 1993, the CTE tide model [40] has been adopted as the standard. The results of 3 long and stable experiments are shown in Fig. 6.6. The measured energy changes follow the CTE tide predictions fairly well. Using all measurements, the value of κ_{tide} is extracted from the CTE model [39] as :

$$\kappa_{tide} = (-8.6 \pm 0.8) \cdot 10^{-7} / \mu gal \tag{6.13}$$

This measurement of κ_{tide} is very well supported by another measurement of Earth elasticity which gives essentially the same κ_{tide} within the error quoted above.

Actually, it is the equation 6.12 together with the CTE tide model which is used in our energy model to correct for the effect of terrestrial tides on the LEP beam energy.

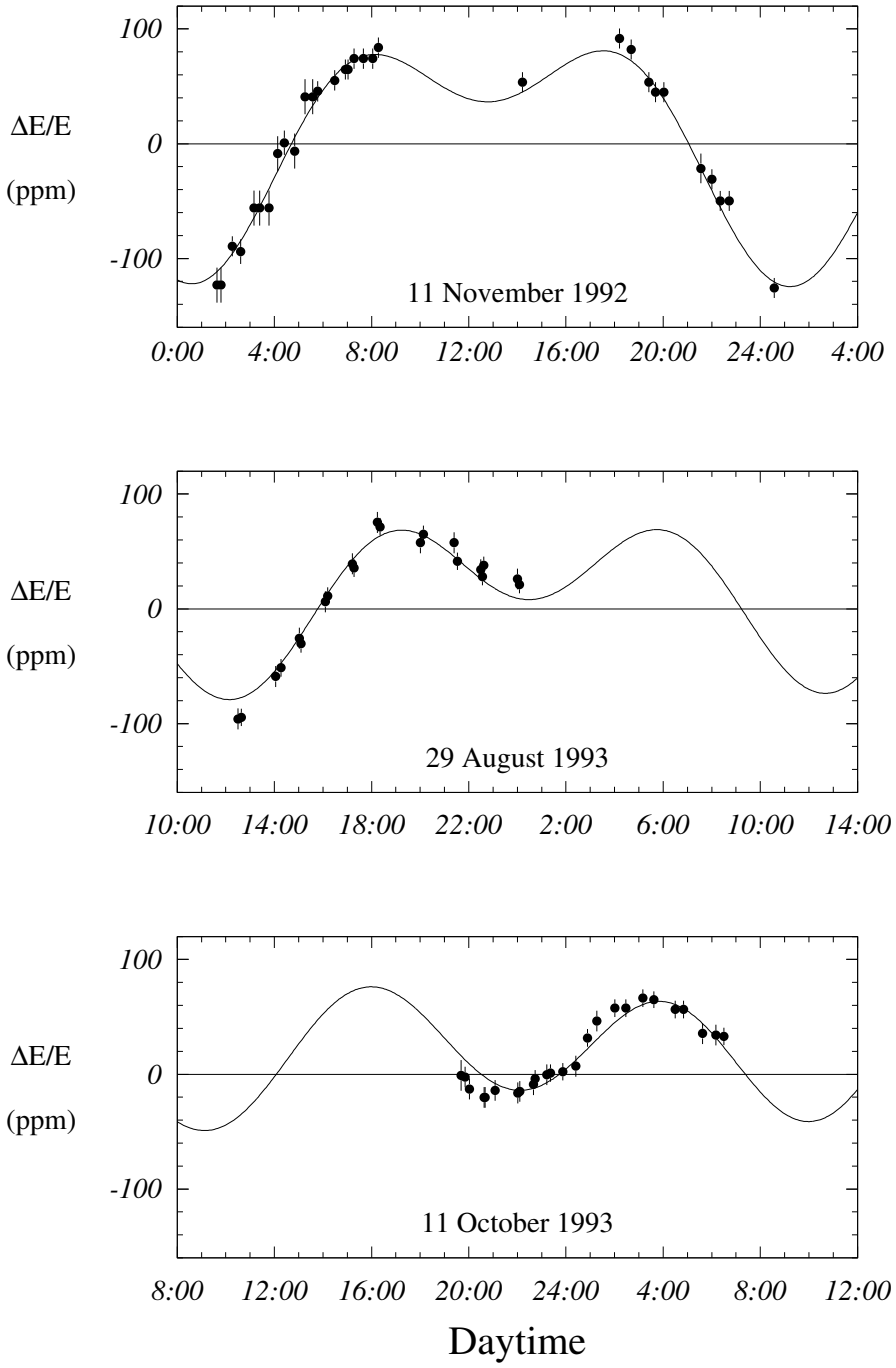


Figure 6.6: Evolution of the relative beam energy variation due to tides as a function of time in November 1992, August and October 1993. The solid line is the predicted evolution from the CTE tide model. The average value of κ_{tide} has been used in all pictures. The October 1993 experiment corresponds to a situation close to half moon, while the November 1992 experiment was performed during full moon.

Beam orbit correction

As said before, quadrupole fields relate beam energy with beam position as a particle going off-centre would experience quadrupole field proportional to the offset position. In fact, the energy of LEP changes by about 1 MeV for a 13 μm transverse movement of the beam relative to the centre of the quadrupole magnets.

The horizontal beam orbit position during the energy scan 1993 is shown in Fig. 6.7, after correction for the effects of tides and dipole field. There is a rise of the beam energy of about 12 MeV during the last part of the 1993 scan, which can also be seen in the LEP energy calibration measurements over the whole year, also shown in Fig. 6.7. This is attributed to slow geological and hydrological changes (possibly the rainfall and the variations in the water level of the nearby Lake Leman [41]) in the rock surrounding the LEP tunnel, which causes changes in the circumference of the ring of a few parts in 10^8. Although it is difficult to make an accurate model by taking into account the variations of rainfall and water level of Lake Leman, the radial beam movement has been tracked down and was then used to correct for the LEP beam energy. By including this effect in the energy model via the beam orbit information, the scatter of the calibration data with respect to the model prediction is reduced by a factor of two.

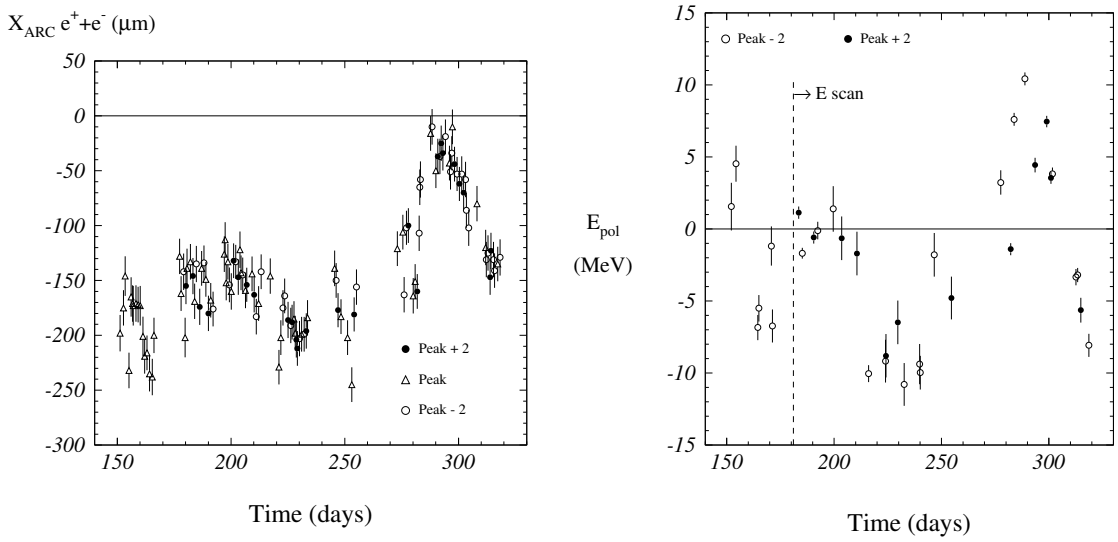


Figure 6.7: Left: mean X position of the beam versus time in 1993. Right: average beam energy measured by resonant depolarization versus time in 1993. The energy has been corrected for changes in the integrated dipole field and for tidal effects. A constant offset has been subtracted from the data at each energy point in order to allow both sets to be plotted on the same figure.

Instrumentation for measuring the beam orbit

The relative transverse position of the beam with respect to the quadrupoles can be monitored by the Narrow Band **B***eam* **O***rbit* **M***onitor* (**BOM**) system located in the LEP arcs [42], which consists of a series of capacitive pickups that measure the positions of electrons and positrons with a relative precision of a few μm. The fill-to-fill reproducibility of the BOM system has been studied through the variations of the beam orbit position in the vertical plane (which are less sensitive to geological movements) and found to be at the level of 15 μm [42].

6.3.5 e^+ beam energy

The energy of e^+ beam can be different from that of e^- beam due to imperfections of the LEP lattice. It should be noted that the polarimeter is normally configured to measure the polarization of only the e^- beam, when the two beams are separated during calibration, and therefore energy calibration by resonant depolarization is usually performed just for electrons. A few special calibrations were performed in 1993 and 1994 to measure the e^- and e^+ beam energies as close to simultaneously as possible. The difference between the e^- and e^+ beam energies was determined to be 0.3 ± 0.3 MeV. A correction of +0.3 MeV to the energy of e^+ beam with respect to the e^- beam was included in the 1993 energy model and its uncertainty (0.3 MeV) was assigned as a systematic error.

6.4 IP-dependent Corrections

For the 1993 scan, there is only one IP-dependent correction, namely the RF correction, which is to be described below. For the 1995 scan, a new additional IP-dependent correction is also needed to be considered, which is discussed in section 8.2.

6.4.1 Collision energy correction from the RF system

The energy of the beam is not constant as it goes around the LEP ring. The circulating electrons and positrons lose about 125 MeV per turn in synchrotron radiation on their curved path through the dipoles in the LEP arcs. This energy loss is compensated by acceleration in the RF cavities placed on either side of the

L3 and OPAL interaction points, which are diametrically opposite each other across LEP.

The deviation of the beam energy from the mean energy as a function of the position around the ring in a typical fill is shown in Fig. 6.8.

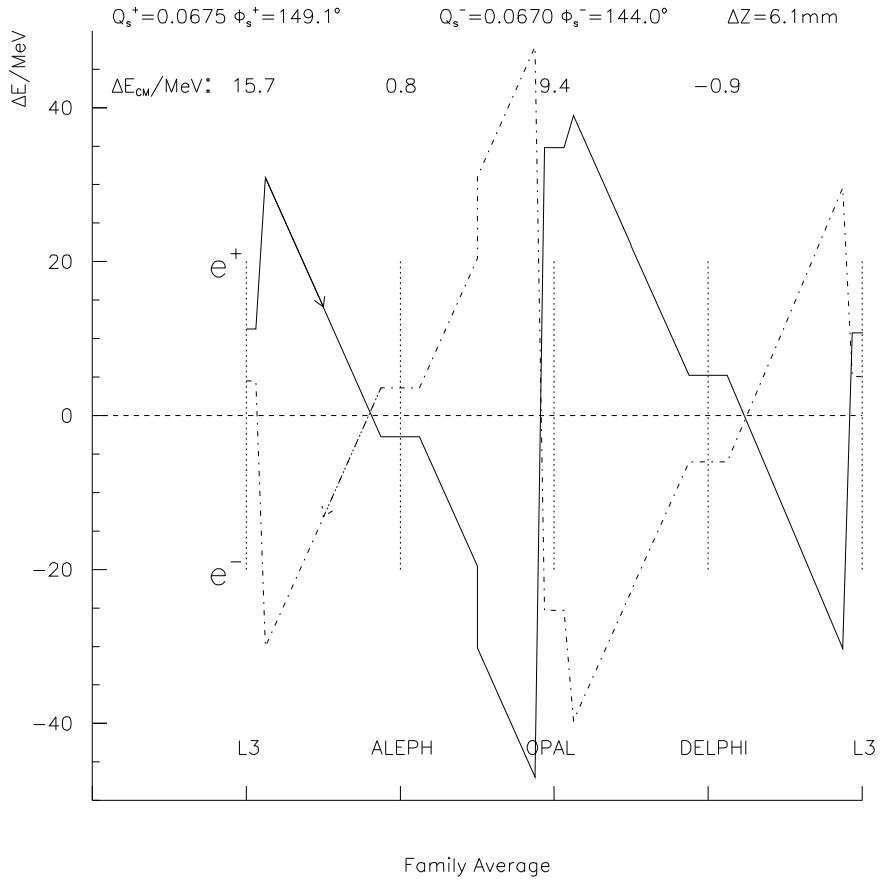


Figure 6.8: Deviations from the mean energy in the LEP arcs of electrons and positrons (sawtooth effect) in a typical fill in 1995. The step between ALEPH and OPAL interactions points is due to emittance wigglers which were in operation at the beginning of fills in order to limit beam-beam effects by increasing the bunch emittance.

This effect cannot be measured directly and a RF model is used to calculate the energy offsets in order to account for variation of the RF voltages with time and changes of the energy loss per turn. Though the RF configuration in 1995 was more complicated than the one in 1993, the basic principles were quite similar in both years.

The copper (CU) cavities in LEP are operated with a sum of two frequencies which produces beating such that the microwave energy oscillates between the acceleration cavities and the storage cavities and overall heat losses are reduced. The

alignment has been done for the lower of these two frequencies, leading to a misalignment of the cavities for the mean frequency as seen by the beam. Consequently, the beam energies at the L3 (IP2) and OPAL (IP6) interaction points are shifted, higher by about 10 MeV. Hence, corrections to the average beam energy must be applied to obtain the proper value of the centre-of-mass energy, E_{CM}. Other geometrical effects, such as a non-zero path difference between IP2-IP4-IP6 and IP2-IP8-IP6, can also give rise to corrections at IP4 and IP8 as well.

The difference between the two frequencies f_1 and f_2 causes an average phase error ϕ_e :

$$\phi_e = \frac{(f_1 - f_2) \times d}{c} \tag{6.14}$$

where d is the distance of the effective centre of the RF units from the interaction points and c is the speed of light.

Very approximately, the energy offsets per beam at the interaction point can be calculated from the difference in energy gain on the incoming side and on the outgoing side, which are given by the accelerating voltage, U_{RF}, and the phase angles,

$$\Delta E^{IP}_{beam} = \frac{1}{2}(U^{in}_{RF} \sin(\phi_1 + \phi_e) - U^{out}_{RF} \sin(\phi_1 - \phi_e)) \tag{6.15}$$

where ϕ_1 is the stable phase angle of the beam bunches with respect to f_1

In practice, a more detailed and complicated model was used to calculate the energy offsets at each IP. The modelling of the corrections is carried out by the iterative calculation of the stable RF phase angle ϕ_s which proceeds by setting the total energy gain of the beams as they travel around the machine equal to all of the known energy losses.

The model accounts for variations of the RF voltages with time, changes of the energy loss per turn caused by the use the emittance wigglers during physics running, effective reduction of the accelerating voltage in the RF cavities due to the energy taken out of the cavities by the bunches. The RF model calculations utilize a database of patched and corrected input values, which include the RF voltages for all (used and unused) RF cavities, bunch currents, emittance wiggler currents, (approximate) beam energies, interwagon spacing as well as a complete set of

alignment and voltage calibration constants. Any necessary information that was not available from the variety of logging sources has been interpolated.

There are some quantities which can be measured as well as calculated from the RF model (with all the above inputs). These quantities provide powerful constraints on the RF model and help us to tune the model so as to achieve better agreement between the calculated and measured quantities. This finally also indicates how well the model represents the reality, which also help us in evaluating the systematic errors due to the RF corrections. These quantities include the following :

Q_s : The synchrotron tune, Q_s, provides a powerful constraint on the RF model. It is calculated from the expression

$$Q_s^i = \sqrt{-\frac{h_f \alpha_c}{2\pi \mathrm{E_{beam}}} \Sigma \frac{dE^i}{d\phi_s^i}}, \tag{6.16}$$

where h_f is the LEP harmonic number, α_c is the momentum compaction factor for the 90°/60° lattice, $\frac{dE^i}{d\phi_s^i}$ is the gradient of the bunchlet energy with respect to the stable phase angle for that bunchlet, which is the part actually calculated in the model.

Longitudinal vertex shift : The longitudinal shifts of the collision point in the IP's are sensitive to changes in the RF configuration. A comparison of these predicted and measured shifts provides another way of cross-checking the validity of the model.

R_{BOM} : The behaviour of the energy sawtooth (which refers to the shape of the evolution of e^+e- energies when they revolve around the ring, as shown in Fig. 6.8) in LEP has been analysed from the BOM data [5]. The quantity, R_{BOM}, which is sensitive to the phasing of both individual RF units at each IP and the relative phase of the RF between IP2 and IP6 is formed as

$$R_{BOM} = \frac{|\Delta^{+-}_{IP2Left}| + |\Delta^{+-}_{IP2Right}|}{|\Delta^{+-}_{IP6Left}| + |\Delta^{+-}_{IP6Right}|}, \tag{6.17}$$

where Δ^{+-} is the difference between the mean horizontal positions of the electron and positron beams at both sides of each IP ("Left" and "Right").

[5] The BOM data were extracted by J. Wenninger's program.

Based on the modelled energy loss and the known lattice dispersion, this quantity can also be calculated in the RF model. Comparison with the measured values places powerful constraints on whether or not the RF phases of the cavities input to the model are correct. This new cross-check was only introduced in the 1995 scan.

Fig. 6.9 shows the extent of the predictive power of RF model (after fine tuning). In general, the agreement between the measured quantities and their respective values calculated from the RF model is reasonably good.

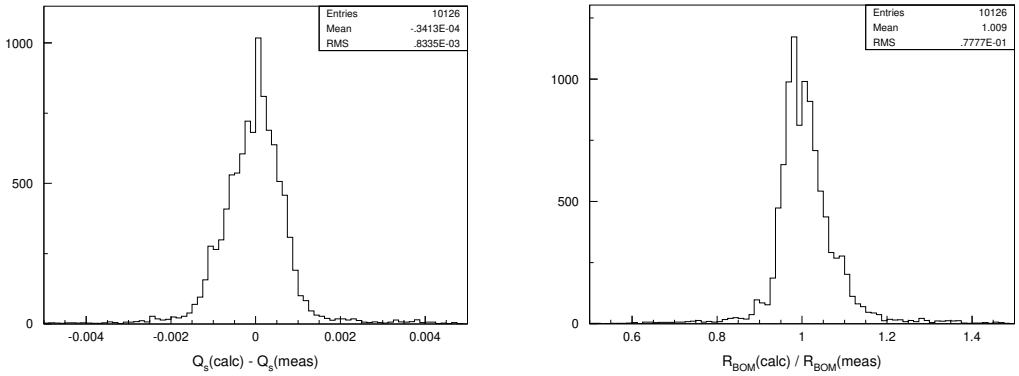


Figure 6.9: Comparison between the measured values Q_s and R_{BOM} and those calculated from the RF model. The discrepancies between the calculated and the measured values shown here give rise to an error about 0.2 MeV in the centre-of-mass energy.

The energy errors due to the uncertainties in the above-mentioned effects will be discussed in detail in sections 9.7 and 9.8. The effects which have been mentioned so far were known before the 1995 scan. New effects on the LEP collision energy discovered in the 1995 scan will be discussed in Chapter 8. Various energy models incorporating the new effects will be described in Chapter 9.

Chapter 7

1995 LEP Energy Scan

7.1 Operating Conditions During 1995 LEP Scan

To achieve improved measurements of M_Z and Γ_Z, the 1995 LEP energy scan was launched with the intention of accumulating high integrated luminosities at the off-peak energy points so that the experimental statistical errors in the measurements of M_Z and Γ_Z would be reduced. Another priority was to calibrate as many off-peak fills as possible in order to improve the precision of the LEP energy measurement. Calibrations both at the beginning and the end of fills were also thought to be necessary to have a better understanding on the energy variation during the course of fills.

7.1.1 Scan performance and strategy

The 1995 LEP run was devoted to a three point beam energy scan, i.e., with one point at the peak of the Z^0 resonance and two points roughly 880 MeV below and above the peak, i.e., 'P$-$2' and 'P$+$2'. The off-peak integrated luminosity was about 18pb^{-1}, delivered over 52 fills [1] and evenly distributed between the two energy points.

The efficiencies of the detectors in the four LEP experiments and the performance of the accelerator can vary with time. In order to cancel out possible time-dependent biases as far as possible, LEP adopted a scan strategy of alternate fills at on-peak and off-peak energies. Attempts were made to keep the machine conditions stable, and as similar as possible between the periods of physics collisions and calibrations at the two off-peak points.

[1] This definition of scan period encompasses all fills between the fill numbers 2852 and 3042.

7.1.2 Bunch train operation

In an attempt to raise the luminosity (especially for LEP2), LEP in the 1995 scan was operated with 4 equidistant trains [2] of 3 wagons (separated by 247 ns) of e^- and e^+ beams, instead of the 'Pretzel' mode — 8 equidistant single bunches — in 1993 (and 1994). In this new 'bunch train' operation, vertical electrostatic deflections ('bumps') are applied on either side of the IP to avoid parasitic collisions between wagons.

Unfortunately, these bumps induce opposite sign vertical energy dispersion for the two beams (e^- and e^+), which can lead to offsets in the centre-of-mass energy. Vernier scans have been used to minimize the collision offset and therefore the dispersion effect, which will be addressed in section 8.2. This new scheme also complicates the RF model as the interaction between each wagon in a train and the RF cavities must also be considered.

7.1.3 Calibration strategy and statistics

In 1995, attempts were made to calibrate essentially all off-peak fills after physics collisions, i.e., at the end of fill ('EOF'), using the technique of resonant depolarization (see section 6.2). This was realised for 14 fills at P+2 and 12 fills at P−2. These calibrated fills represent roughly 70% of the off-peak luminosity, to be compared with about only 40% achieved in 1993. One on-peak fill was also calibrated by the same technique.

7.1.4 Monitoring of the beam energy in a fill

In 1993, the dipole field of LEP during the course of a fill was monitored with only one NMR probe mounted in the reference magnet, NMRREF, as mentioned before. In the 1995 scan, another NMR probe, denoted by 'NMRVAC', was put inside a section of vacuum chamber. Moreover, two additional NMR's were installed within the tunnel itself, mounted in actual LEP dipoles. There were called 'NMROCT4' and 'NMROCT8', on account of their positions (octant 4 and octant 8 respectively around the LEP ring [3], see Fig. 2.1). The new instrumentation was expected to

[2] The length of each train (of three wagons) is about 220 m long.
[3] The exact codes for NMROCT4 and NMROCT8 are 418 and 818 respectively.

provide more direct measurements and give more understanding about the dipole field inside the LEP tunnel, albeit at specific locations.

The EOF calibration in each fill mentioned earlier is only able to calibrate the NMR readings with respect to the variation of the average beam energy from fill to fill, but not during the course of a fill. In order to examine the NMR measurements to see whether they reflect the change of beam energy during a fill, energy calibrations by resonant depolarization at the beginning of fill were also attempted in 1995.

Of those fills with EOF calibrations, 4 fills (fill numbers : 3022, 3029, 3030 and 3036) were also calibrated before physics collisions [4], at the beginning of fill ('BOF'). Such BOF/EOF calibrations were not performed in 1993. In addition to these physics fills, 2 fills of "machine developments" had an extended series of polarisation measurements continually over the entire fill (fills numbers : 2929 and 3064), giving a total of 6 BOF/EOF calibration experiments.

Although occasional field jumps (typically of a few MeV) were seen, the variation of the dipole field throughout the fill was considered to be very small (mainly due to measurements by the NMRREF in the reference magnet) in the energy analyses before the 1995 scan. Even though the comparison of the energy model with the calibration measurements could provide a direct measure of the understanding of the fill to fill energy variation, it is rather insensitive to any change during a fill itself. Knowledge of this short term variation was gained only after the BOF/EOF calibration experiments were carried out and the NMR measurements were 'upgraded' in 1995. Nevertheless, the improved magnetic dipole field measurements yielded somewhat unexpected results, which will be described later in Chapter 8.

7.1.5 Superconducting RF cavities

In preparation for upgrading the LEP energies, superconducting (SC) RF cavities were commissioned throughout the 1995 running period. The RF during the scan was a varying mixture of conventional copper and new superconducting cavities. This hybrid system has made the calculation of the IP-dependent RF corrections a challenging task. This will be further discussed in section 8.5.

Note that the SC cavities do not have the misalignment problem as in the case CU cavities (explained in section 6.4.1) because SC cavities are operated at only

[4] In fact, the fill 3039 had a successful BOF calibration, but EOF calibration was unsuccessful.

one single frequency. The misalignment in CU cavities is the main cause for the energy shifts at IP2 and IP6. Therefore, with (more) SC cavities running in 1995, the energy shifts are significantly smaller than in 1993. This is particularly true for IP6 as there have been some considerable periods of time during the 1995 scan when only SC cavities were used at IP6. Nevertheless, that was not the case for IP2 in 1995. Therefore, one expects that the RF corrections for IP6 in 1995 were much smaller than those for IP2. (See Table 9.5.)

7.1.6 Other aspects

In contrast to 1993, the magnet cooling was regulated to keep the variation of the core temperatures to a minimum. Fig. 7.1 shows the behaviour of the average temperature of the dipole magnets in the LEP ring during the scan period. The mean temperature excursion is less than 0.2° C in a 15 hour fill. The current in the QFQD compensation loop was held constant throughout the entire scan. Therefore, there is no QFQD correction and no associated systematic error in 1995.

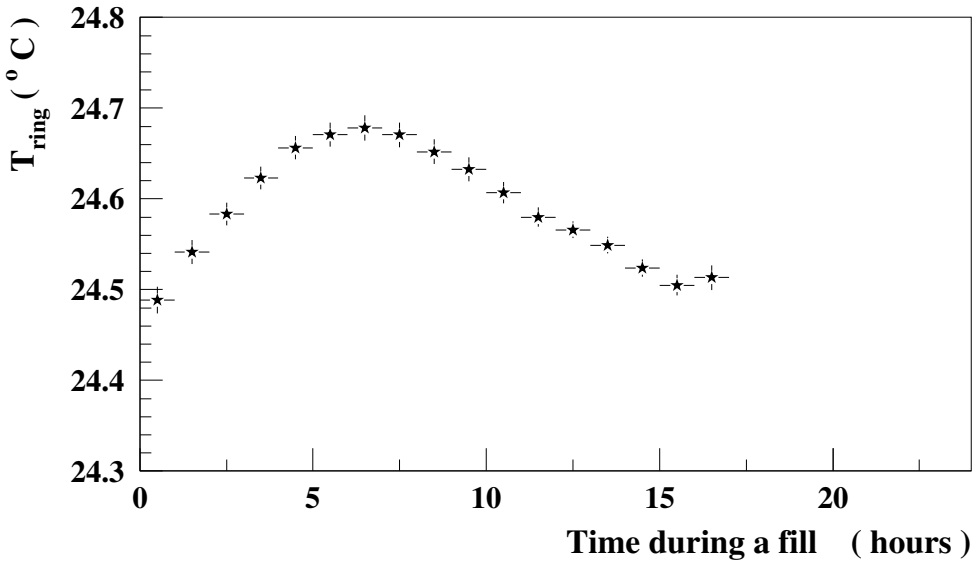


Figure 7.1: Average temperature of the dipole magnets in the LEP ring during fills of physics in the scan in 1995.

Special attention was also given to monitor logging of the parameters which would affect the beam energy.

7.2 Monitoring system

The energy model depends on a large number of measurements around the LEP ring. A monitoring system has been set up to supervise the data logging of various machine parameters at regular intervals so that any failures can be detected and fixed before they may significantly affect off-peak running. The parameters monitored include NMR magnetic fields, RF voltages, magnet temperatures, magnet currents, Q_s, BOM information, bunch currents, wiggler currents, Vernier scan information etc.

The machine parameters needed to be stored come from places all around the circumference of the LEP ring. Most useful information for the energy measurement was set to be put into the 'PCR Logging Database' [5] for permanent storage with backup. A less permanent 'Measurement Database' also existed to complement the PCR Logging Database. At CERN, the standard database management system adopted is 'ORACLE' [43] which allows one to store, retrieve and manipulate information with the help of the Industry Standard Language, SQL [6].

There was a 'watchdog' program [7] at the database level constantly checking whether the parameters were put into the database at regular time intervals. If there was a long period of absence of data, the software alarm would be set off to warn the LEP operators of the undesired situation and the operators would then execute the necessary remedies to restart the logging.

In addition to the above program, there was a team of people in shifts and a software chain (of which the author was in charge [8]) set up to check stringently the presence and quality of the parameters which were supposed to be stored in the database at a regular basis. The software first extracted various groups of data from databases by SQL commands. The output was then processed by Fortran routines

[5] PCR stands for Prevessin Control Room at CERN, where the author spent an enjoyable summer working.

[6] which stands for Structured Query Language.

[7] This program was written by Ronnie Billen.

[8] The author wrote a large part of this software and held the responsibility of adjusting it to different needs throughout the 1995 scan.

which includes statistical analysis of the data for each group, checks on logging failures, internal consistency checks and also graphical representations.

The groups involved are as follows :

MAGGROUP : The individual core temperatures of 32 magnets around the ring, their overall mean, the air and core temperatures of the reference magnet were monitored. Error codes would be given as alarms if the RMS of core temperature of any magnet was more than 0.2° C, or less than 0.01° C or a change of the temperature more than 2° C. A graph showing the progress of the temperature throughout the fill would be produced automatically if any of the above happened.

MNGROUP : The presence of the currents of the dipole magnets was checked. This check included both the requested setting and the readings from the meters.

RFGROUP : The 12 voltages of both copper and superconducting RF cavities were monitored and the percentages of missed RF items were closely supervised to see whether there was a substantial amount of lost RF data. A large loss of RF data would normally mean that the next fill would not be off-peak, if the problem was not cured immediately. This was one of the most crucial and also problematic groups for monitoring.

SAWGROUP : The concern here was the horizontal displacement (in μm) between the positron and electron orbits on either side of each IP and it actually came from the averages over selected BOM's. Also, the ratio of the absolute sum of the left and right displacements at both points (i.e., R_{BOM}, see equation 6.17) was checked to see whether it agreed approximately well with the ratio of total RF voltages at IP2 and IP6, R_{RF} [9] (see section 6.4.1).

---

[9] R_{RF} is defined as :

$$R_{RF} = \frac{|RF_{IP2Left}| + |RF_{IP2Right}|}{|RF_{IP6Left}| + |RF_{IP6Right}|} .$$

where $RF_{IP2Left}$ etc. represent the total voltages of the RF cavities at the indicated side of the indicated IP.

BCTGROUP : This group concerned the currents in the wagons of trains of electrons and positrons. A comparison was also made among the currents of the equivalent wagons in the 4 trains. Their ratios were calculated and significant deviations from unity would also trigger error codes on the monitoring output.

ENGROUP : This was another most important and also problematic group and included checking the four NMR's and the flipcoil readings. As this was the place where the dipole field measurements in the ring were stored, it was monitored very carefully. A serious deficiency of data in this group would lead a veto of going off-peak in the next fill.

WIGGROUP : Availability of wiggler currents of various kinds were checked here in this group.

QSGROUP : This concerned the Q_s values for each wagon of the 4 trains measured from one fixed train (family a). The Q_s is essential for cross-checking the calculation in the RF model and therefore was treated as a vital aspect of the logging. The information here came from the Measurement Database.

Vernier : An automatic procedure, called "Vernier scan", was used to control the vertical dispersion effect in the bunch train operation. This will be discussed in section 8.2. Here, a Vernier fitting program [10] was repeated to guarantee that Vernier scans were performed twice in each fill for each experiment and the essential information was logged. A plot was made for each IP to show the movement of the Vernier settings throughout the fill, with the fitted result of any Vernier scans on top of it.

Others : A RF model was used to make online calculation of the values of Q_s and ratios R_{BOM} throughout the fill to compare with the measured Q_s and R_{BOM}. An absolute difference between the measured and calculated Q_s values of more than 0.002 [11] was considered to be serious. Deviations in the ratio of the calculated and measured BOM values might directly indicate problems with the RF phasing; and it was intended to keep the ratio in the range of

[10] Aopted from P. Puzo .
[11] Typical values of Q_s are about 0.06 to 0.07.

$0.75 < R^{calc}_{BOM}/R^{meas}_{BOM} < 1.3$. These limits correspond to shifts in the centre-of-mass energy of about 1 MeV.

Figure 7.2 shows an example of a graphical output used during daily monitoring in 1995 scan. The comparison between the measured (and logged) values of the synchrotron tune Q_s and the calculated values of Q_s reflected the stability of the machine at that particular time. This is because the calculation of the Q_s values relied on RF voltages, Q_s, wigglers and bunch currents all being logged reliably. Unexpected low values of $Q_s^{\rm meas}$ were, among other problems, taken as an indication of the presence of phase errors and the RF system should be rephased.

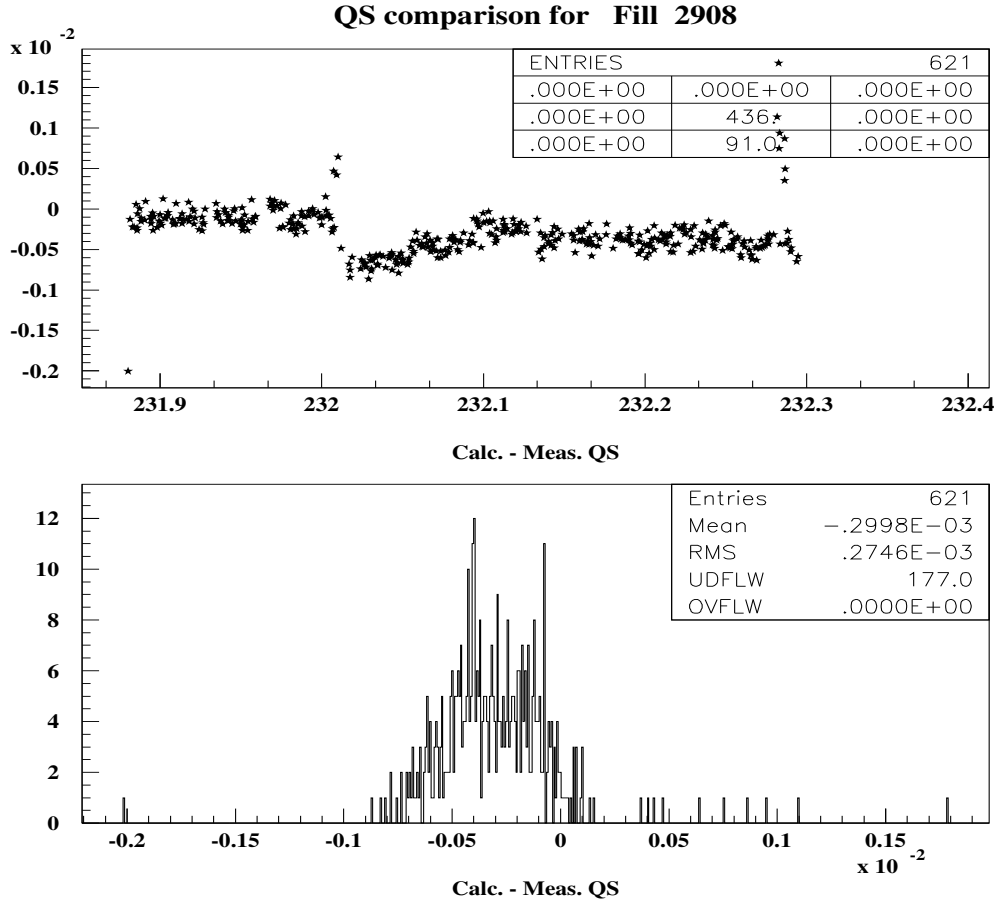


Figure 7.2: A logging online plot of (Calculated Q_s - Measured Q_s) for the fill 2908 during the summer, 1995. In the upper plot, the horizontal axis is the number of days (at the time of concern) with respect to 1st Jan., 1995 while the vertical axis is the difference between the values of calculated and measured Q_s. In the lower plot (the projection of the upper plot on its vertical axis), the horizontal axis is the difference between the values of calculated and measured Q_s while the vertical axis is the number of entries.

Before going off-peak in the following fill, the above software was executed and the result was assessed by a 'logging shifter' to see if the LEP machine appeared sufficiently stable and the logging itself reliable enough to provide usable data in the Γ_Z measurement, i.e. running in off-peak. The following criteria have been agreed upon as the minimum requirements for going off-peak in a successive fill:

- At least one of the NMR's in the reference magnet and at least one of the NMR's in the arcs to be logged at least 70% of the time ;
- The RF voltages to be logged at least 70% of the time ;
- The Q_s to be logged at least 70% of the time ;
- Q_s measured and Q_s calculated to agree with a certain tolerance (depends on the current confidence in the model) at least 70% of the time ;
- More than 75% of the experiments able to take data .

Failing the above conditions, an off-peak fill for energy scan would be vetoed until a healthy data logging condition was restored.

These logged quantities form the basis for us to calculate the LEP CM energies using an energy model at 15 minute intervals throughout the energy scan. This is why a great effort has been needed to make sure that the quality of data is good enough for the later analysis of LEP centre-of-mass energies.

7.3 Preparation of data for analysis

In contrast to the daily monitoring of the logging status, the offline analysis of the LEP collision energy during the scan requires all the information of the physics fills throughout the whole scan. Time has been spent on gathering all the necessary information and manipulating them into a data structure which is convenient for doing analysis. Though significant effort was devoted to monitoring the logging system during the scan, there were still some periods when there exists no information in that database due to breakdown in the logging system. Fortunately, some parameters were privately logged by accelerator experts who were in charge of certain components of the accelerator. These provide possible alternate sources of

information. Though none of these sources was 100% reliable during the 1995 scan period, for many of these breakdowns, we could find the information from alternative sources, which we term here as the "private logging". The information from the private logging was used to fill in those 'holes' in the standard database and as a result, a more or less complete dataset (or called the 'DST') has been established.

The procedures of making this dataset can be summarized as follows :

1. SQL programs were used to retrieve all the 'raw' information from various groups (as mentioned earlier) in the databases in a fill-by-fill format.

2. The 'raw' information of all groups in all scan fills was packed together in a sequential order and in a standard format — 'DST'.

3. Different databases have different time and frequency of logging and there are 'holes' in various databases. Interpolations and/or extrapolations between surrounding logged records from various databases or within the same databases have been made to synchronize all the information to one single clock system for each group.

4. Under certain circumstances, even though there are recorded values in the database, they are believed to be invalid. For example, a parameter may appear unchanged for many hours in a fill, which is obviously wrong in the case of bunch currents (say) of the e^-e^+ beams as the values of bunch currents should decrease during the course of a fill. This could happen when certain systems failed to update the information in the database during a period of time in the scan. Various checks have been made in the database to patch and fix such invalid information.

5. Flags have been also set in the 'DST' to signify what quality the particular information has at the particular time of concern, especially if the information has been fixed in the previous process (most often for the RF-related information). Some flags have also been made to facilitate the users of the 'DST' to carry out various analyses.

6. A package of routines was also provided for reading the 'DST' and synchronizing any given set of quantities.

Chapter 8

New effects and corrections in 1995

8.1 Investigation of the magnetic dipole field at LEP

The measurement and analysis of the magnetic dipole (bending) field at LEP is an important step in understanding the overall LEP energy during the 1995 energy scan. A concise 'history' of the investigation of the dipole field in 1995 is given here before the analysis of the LEP collision energy is described in next chapter. A more detailed description of the investigation of the LEP dipole energy may be found in [36].

8.1.1 Stability of the dipole field in a fill

Examination of the dipole field variation in a fill started from comparison between the NMR's in the reference magnets and in the LEP tunnel. Fig. 8.1 shows the NMR readings during a typical fill in 1995 and there were a few surprising results :

1. The NMR probes in the LEP tunnel measured significant field fluctuation (noise) during daytime (from 05:00 to 24:00) and the noise disappeared during 00:00 to about 05:00. This distinct time pattern of the NMR noise will be referred to as "Day-Night" effect hereafter. This time pattern repeated itself every day with an uncertainty of $\pm$ 30 minutes.

   However, the NMR probes in the reference magnet did not share the same pattern.

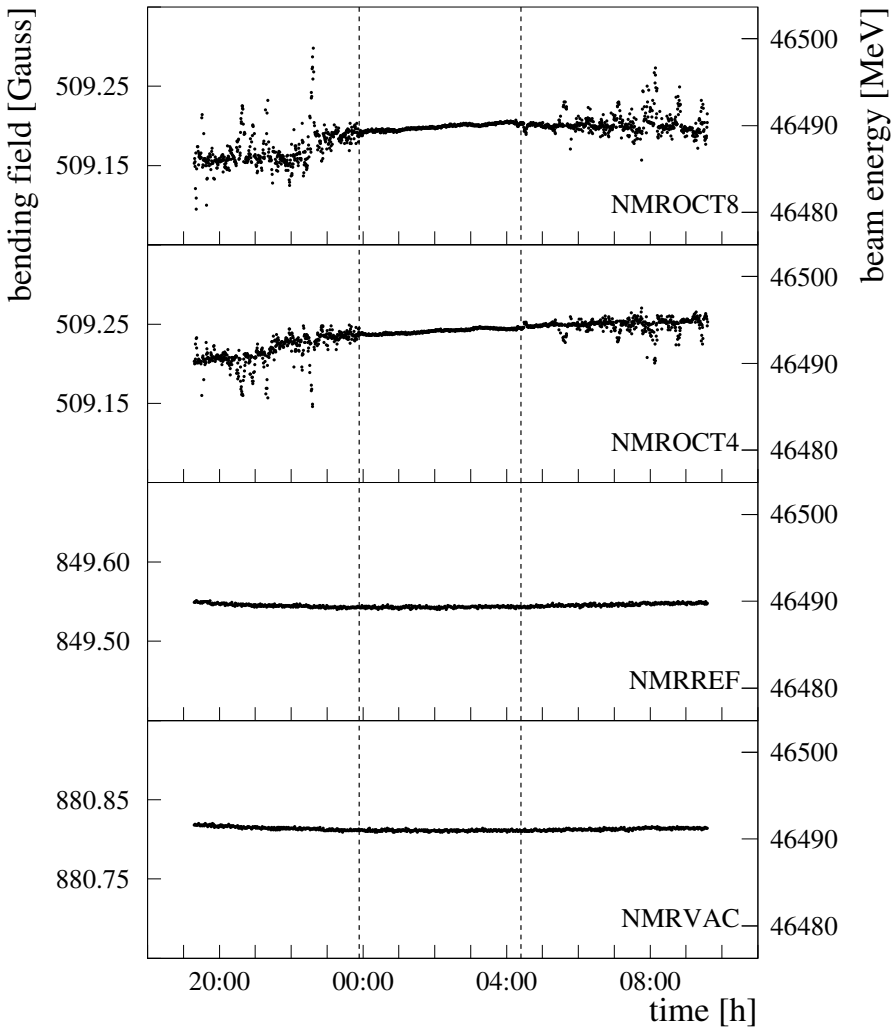


Figure 8.1: NMR reading during a typical fill. The magnetic field readings of NMRREF, NMRVAC, NMROCT4 and NMROCT8 are shown as a function of time during the fill 2969. The standard "conversion factors" used to translate the field unit into energy unit are 54.7, 52.8, 91.3 and 91.3 MeV/Gauss for NMRREF, NMRVAC, NMROCT4 and NMROCT8 respectively. These conversion factors are used throughout this thesis. Large fluctuation of magnetic field measurement from the NMR probes in the LEP tunnel was observed between about 05:00 and 24:00 (midnight).

2. It was also found that the short term variations ($\Delta t \leq 5$ min.) of NMROCT4 and NMROCT8 were anti-correlated; this is shown in Fig. 8.2. The 'anti-correlation coefficient' is about -1.7. That is to say, instantaneously, NMROCT8 field fluctuation changed 1.7 as much as NMROCT4 did, though in the opposite direction.

3. On a longer time scale ($\Delta t \geq 1$ h), both NMROCT4 and NMROCT8 have showed a gradual rise of the magnetic field regardless of the superimposed anti-correlated noise.

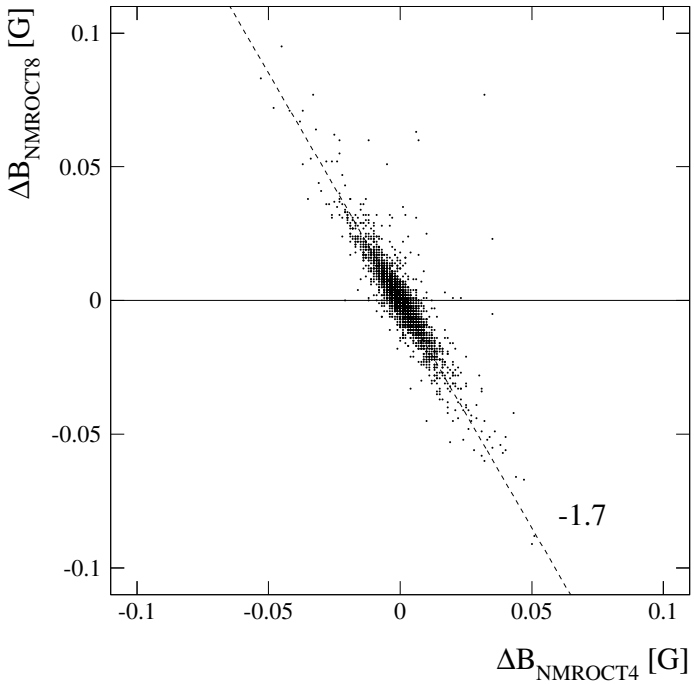


Figure 8.2: Anti-correlation between NMROCT4 and NMROCT8. The changes of magnetic field measurements ΔB (in Gauss) of NMROCT4 vs NMROCT8 are displayed on the plot.

The NMROCT8 field measurement in a specific fill, shown Fig. 8.3, further helps the above-mentioned effects be visualized. The distinction between the 'quiet period' (00:00 to about 05:00) and the 'noisy period' can be evidently seen in this plot. The large scatters on a small time scale represent the anti-correlated short term fluctuations with an equivalent amplitude of up to 10 MeV. In this particular fill, the long term field increase of 0.12 G corresponds to a change of almost about 12 MeV in equivalent beam energy, if the integral dipole field would increase by the same amount as measured by NMROCT8. There were both sudden level changes and smooth drift of magnetic field increment. The steps usually seem to be accompanied by high intensity short term fluctuation while the slow drift appear in both quiet and noisy period.

With all the previous information, the field measurement analysis in 1995 shows that the dipole field at LEP is more unstable than what one would expect from the NMRREF measurement seen in 1993. Since the NMR measurement is very important in the extrapolation of energy model throughout a fill, it is necessary to know whether the field rise measured by the NMR probes in the tunnel, namely NMROCT4 and NMROCT8, reflects a genuine rise of the average LEP beam energy.

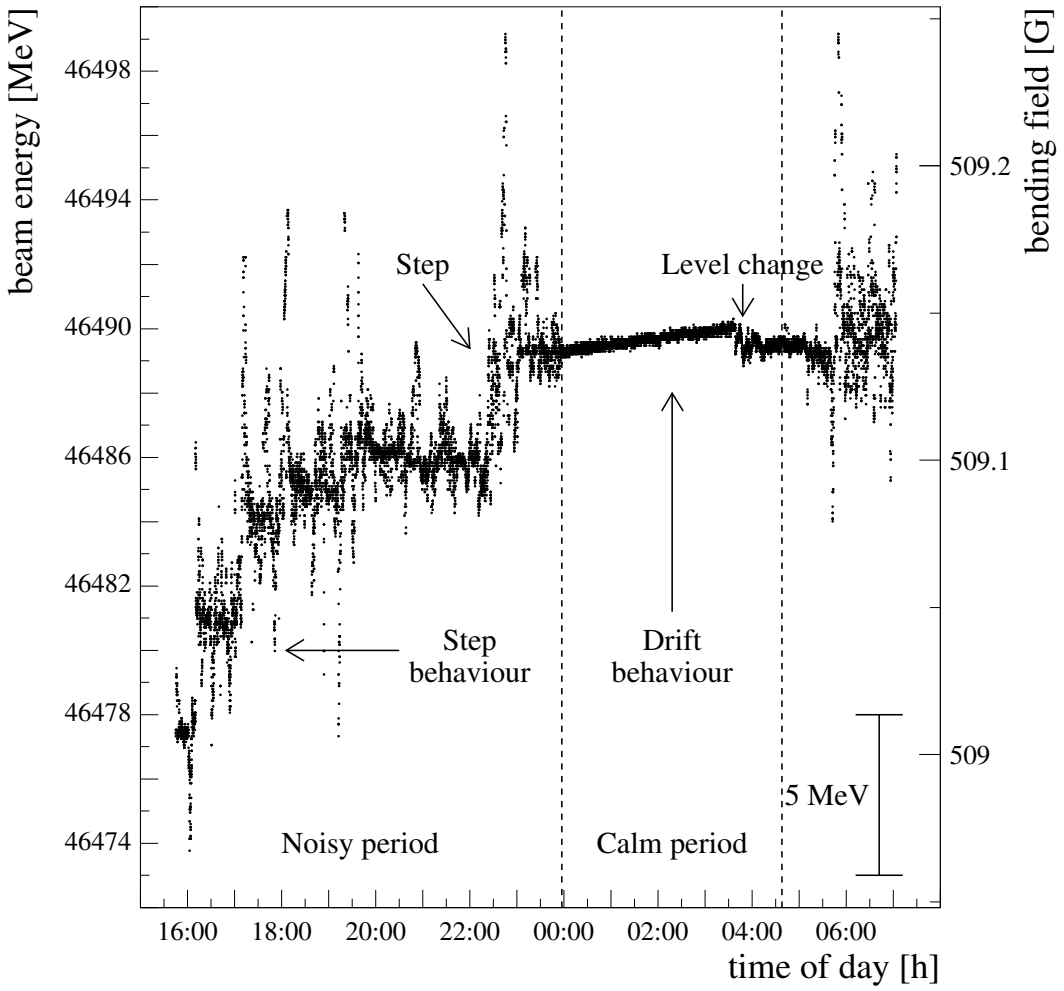


Figure 8.3: Field Measurement of NMROCT8 during a typical fill. The beam energy measurement shown came from the NMROCT8 field measurement (converted to MeV with the factors previously mentioned) during the fill 2899. Here, one can see 'Day-Night' effect, large short term field fluctuations as well as gradual long term field increase during the course of a fill.

1995 has been a year of chasing the origin of the noise measured by the NMR probes in the LEP tunnel.

8.1.2 Train Effect

It was a painstaking job to discover the origin of the magnetic field noise in the LEP tunnel. The details can be found in [44]. The essential details are as follows :

1. The reliability of the NMR probes was checked by giving artificial mechanical and electromagnetic disturbances. It was found that the NMR probes deliver an accurate magnetic field measurement regardless of possible mechanical or electromagnetic disturbances.

2. Electric disturbances close to the location of the tunnel NMR probes were excluded by switching on/off various instruments such as the beep system, carefully checking probe grounding and installing additional shielding and isolation devices.

3. The only way to reproduce the disturbance seen in the magnetic field recording was by placing a wire carrying a DC current inside the poles of the iron magnet. There were then only two possible conductors inside the LEP dipole magnets, namely, the fluxloop and the vacuum chamber, which gave this effect.

Fluxloop The measurement of fluxloops passing through the magnets 418 and 818 (where NMROCT4 and NMROCT8 were put) showed very similar 'Day-Night' pattern and anti-correlation as for the NMROCT4 and NMROCT8 (shown in Figures 8.1 and 8.2). Furthermore, since fluxloops measure the time derivative of the magnetic field, changes of field level should be accompanied by peaks of fluxloop signals. That has been observed to be true (see Fig. 8.4).

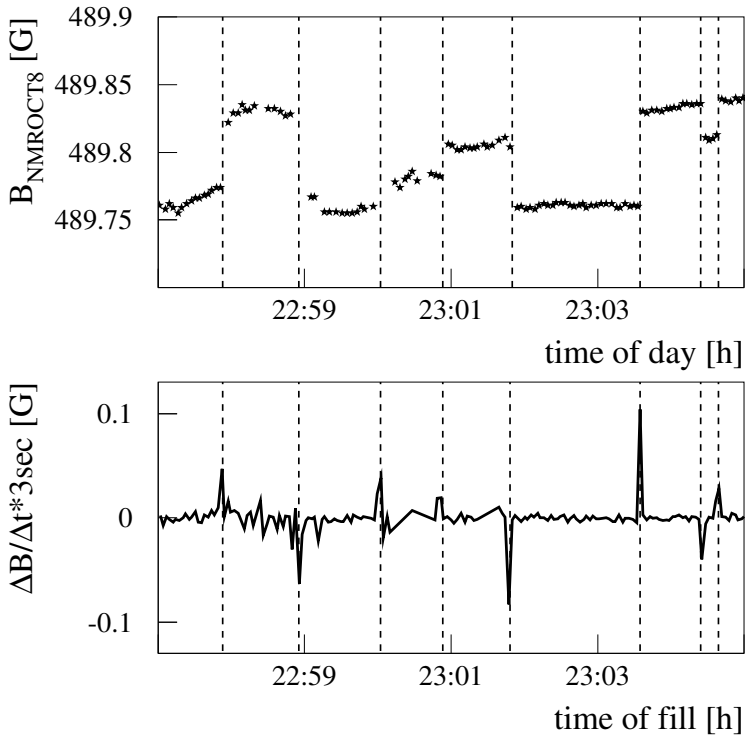


Figure 8.4: Correlation between fluxloop and NMR measurements in octant 8. Magnetic field jumps (in NMROCT8) occurred in coincidence with spikes in the time derivative of magnetic flux (the fluxloop in octant 8).

Disconnecting the induction wire and short-circuiting the instrument does not remove the magnetic field disturbances. Experiments also showed that the fluxloop itself was not capable of generating the observed magnetic field noises.

If the large field fluctuations seen in NMROCT4 and NMROCT8 were only due to the localized field disturbances, fluxloops would record no signal since the fluxloop records the average field changes over the whole octant. This seemed to show that the short term field fluctuations measured by the NMR probes represented the field fluctuations of the complete octant in question and also confirmed that the NMR probes measured the actual dipole field.

Vacuum Chamber Finally, DC currents in vacuum chamber were found by measuring the potential differences between the LEP vacuum chamber and ground, by measuring the DC currents on the LEP earth cable, and by measuring the varying magnetic flux around the vacuum chamber.

A DC power supply was used to simulate the earth current fluctuations by connecting it to the earth cable and the vacuum chamber. It was found that a considerable current was not detectable anymore on the earth cable behind a distance of 10 m. Therefore, local LEP equipment cannot be the source of the magnetic field fluctuations because it is not able to create a large earth current around the whole LEP storage ring. The real source was then thought to be external.

Amplitudes of the earth cable current at different positions of LEP were measured using portable current clamps. Fig. 8.5 shows the correlation between two simultaneous earth current measurements at two positions in which one is at magnet 818 (the position of NMROCT8) — the reference point — and the other moved around as marked on the horizontal axis of the plot.

The correlation ρ is defined as :

$$\rho = \frac{\sum(x_i - < x >)(y_i - < y >)}{\sum(x_i - < x >)^2 \sum(y_i - < y >)^2} \tag{8.1}$$

where x_i and y_i denote the set of measurements taken, and $< x >$ and $< y >$ their average values. The sign of correlation gives the direction of the earth current with respect to that near IP8. A zero correlation means that the direction of current flow was changing frequently.

One can see from Fig. 8.5 that the signs of correlations change around IP1 and IP6. At IP1, the inversion of correlation occurs within 90 m around e^+e^- injection

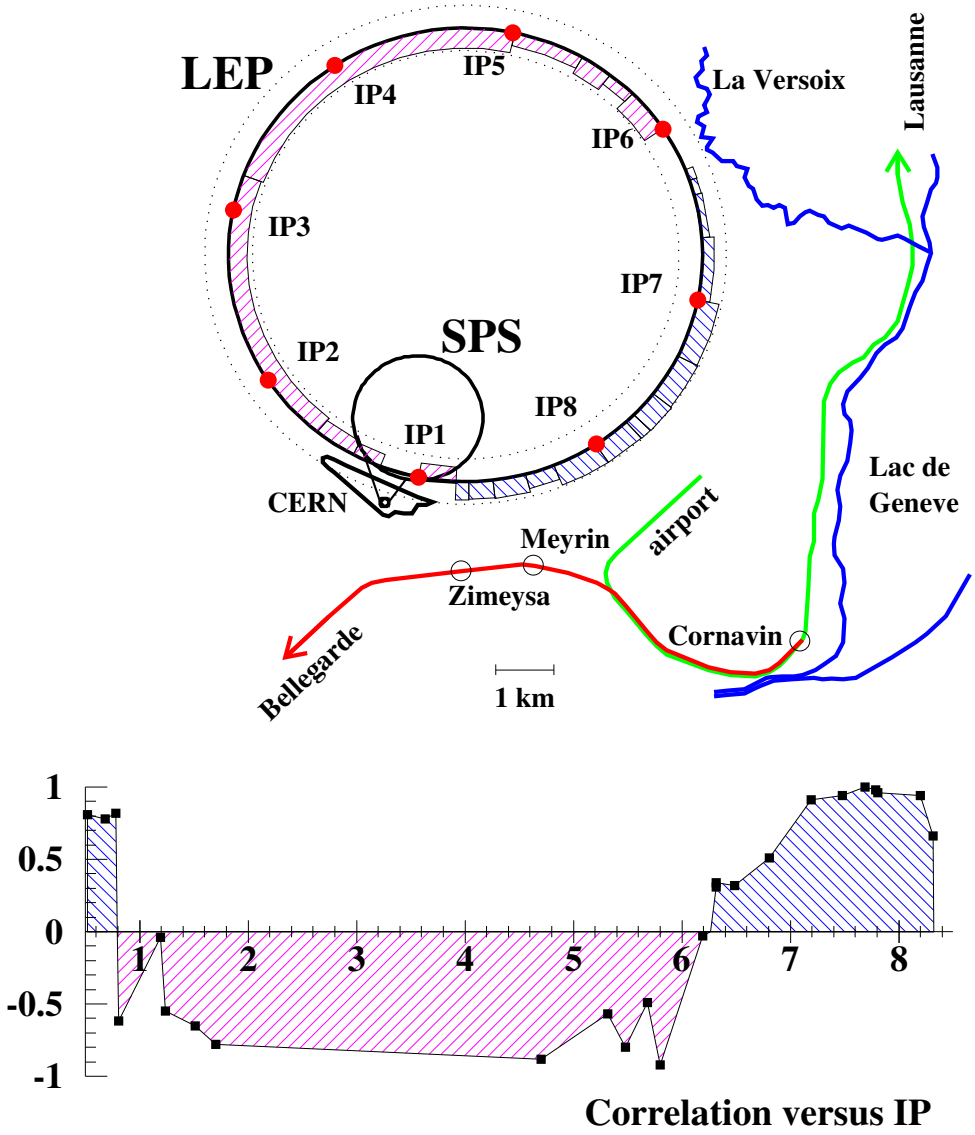


Figure 8.5: Correlation of earth cable currents within LEP. Bottom : The correlation between two simultaneous earth current measurements near the position of NMROCT8 and the position marked on the horizontal axis is shown. A positive correlation is located between LEP ring and the outer circle, while a negative correlation is between the inner circle and LEP ring. Top : Map of the Geneva area with LEP, the river Versoix, the Lake of Geneva and the railways to Lausanne, Bellegarde (to Lyon, Paris) and the airport. Cornavin is Geneva's main train station.

line. Between IP6 and IP7, a more gradual decrease of correlation is seen. It seems that the current enters close to IP1, flows in both directions around LEP, leaves near the river Versoix at IP6. It is like a current flowing between two electrical poles in the Geneva area.

The measured peak to peak amplitudes of the leakage currents travelling on the LEP earth cable range from 200 mA up to 1 A. The ratio of current amplitudes carried by the earth cable at the position of NMROCT4 and NMROCT8 is approxi-

mately -1.7, which is consistent with the anti-correlated magnetic field noise seen in these devices. The measurements of the earth currents match very well with those earlier results from fluxloop and NMR probes. This shows that the earth current is responsible for the field noise.

The question is then, where does the earth current comes from ? Possibilities such as the Geneva airport (Cointrin) and the electric power companies in Switzerland and France have been considered. However, their activities showed no apparent correlation with the field disturbances observed and could not explain the pattern of the fluctuations, especially the Day-Night effect.

After presenting the observed phenomenon to many departments at CERN, the solution was finally proposed by an EOS[1] engineer[2] at CERN. When given the pattern of the field noises, he immediately spotted the correlation between the magnetic field noise pattern and the train traffic.

An experiment was soon performed and confirmed what it is called the "train effect" that gives rise to the magnetic field fluctuation seen in the LEP tunnel. In a controlled experiment during a "busy" afternoon at the time a "TGV" train was passing, the potential differences against time were measured , between the rail and ground, between the LEP vacuum chamber and a reference ground as well as the NMR field response. The results are shown in Fig. 8.6. The potential difference between the rail and ground was measured at the Zimeysa train station (see Fig. 8.5), which is several kilometres away from the potential difference and magnetic field measurements near IP8. The measured potential difference between the rail and ground is proportional to the current leaking into ground and penetrating LEP. The correlation between the three distributions is evident and thus gives a convincing proof of the "train effect" being the origin of the noise of dipole field in LEP.

"Train Effect Explanation" : The driving mechanism of the earth leakage current is the potential difference between the rail and the ground. An ideal electric railway supplies power over the wire above the train and the circuit is closed by the rails. In principle, the current supplied by the power station to the train (over the cable wire above) should return to the power station over the railway tracks.

[1] EOS stands for 'Experiments Operational Support' group under ECP Division at CERN.
[2] M. Fleury

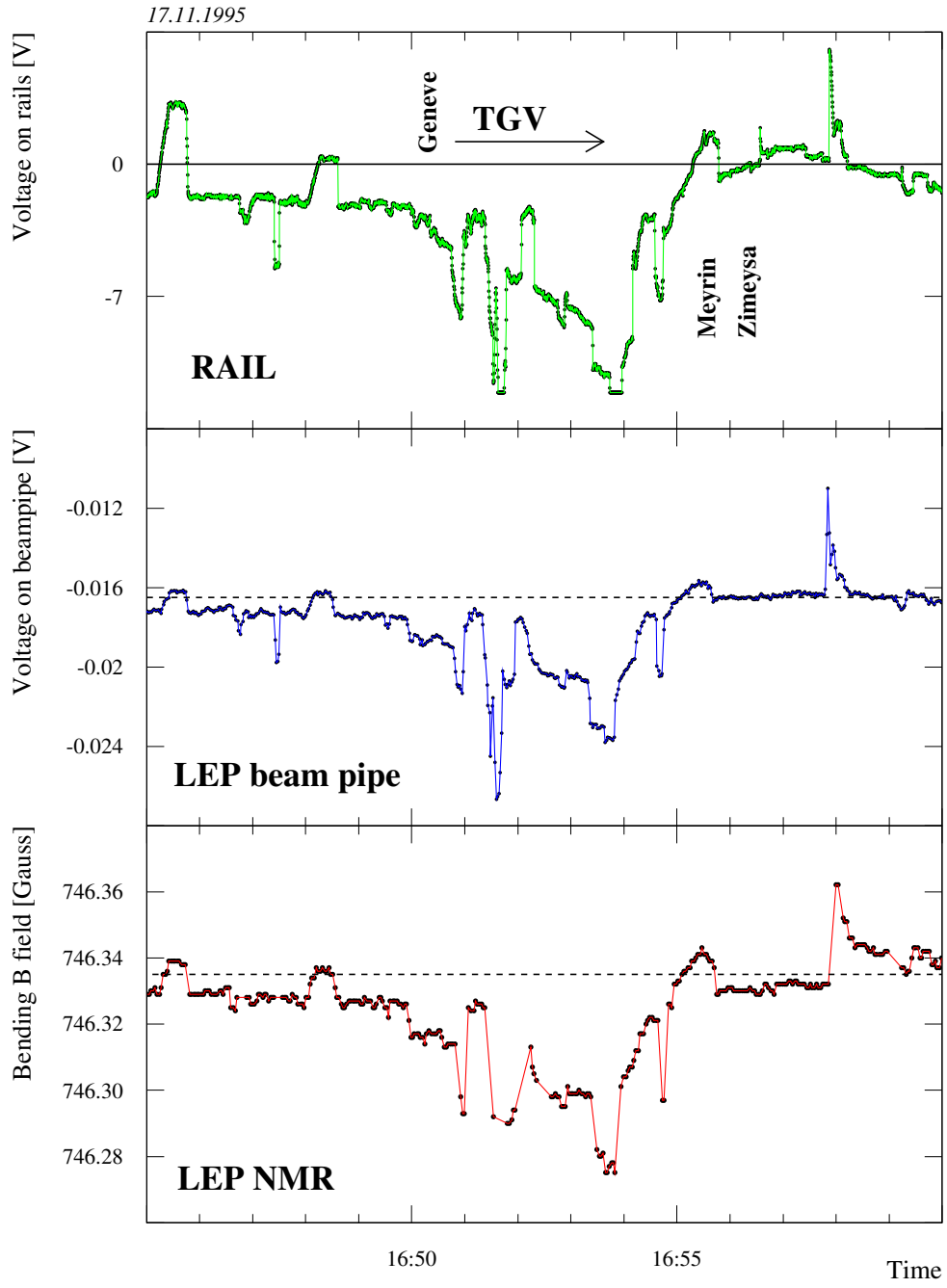


Figure 8.6: Time Dependence of three signals recorded at different locations in a controlled experiment for 15 minutes during a "busy" afternoon. Top : The potential difference between the rail and a reference ground at the Zimeysa train station (Fig. 8.5). Middle : The potential difference between the LEP vacuum chamber and a reference ground near IP8. Bottom : The magnetic field changes measured by NMROCT8 in the LEP tunnel.

However, the rail is not completely isolated from the ground and the current may leak into the earth from the rail and flow back to the generator along other "roads". In fact, measurements have shown that up to about 25% of the total current supplied

to the train leaks into the ground [45].

There are three major railway lines running routinely close to LEP, namely, the French SNCF [3] line "Geneva – Bellegarde" and the Swiss CFF [4] lines "Geneva – Lausanne" and "Geneva – Airport" (see Fig. 8.5). The leakage current from the French Geneva – Bellegarde line powered by DC is the direct cause of the LEP magnetic field disturbances. The leakage current from the AC powered Swiss railway lines is confined to several hundred metres whereas the DC leakage current can penetrate transversely over large distances [5].

Earth leakage current follows the least resistive path while travelling through the earth. LEP tunnel turns out to be a good choice. The current flowing between two poles, LEP tunnel and the rail, is conducted by ions dissolved in the earth and the conductivity varies according to many factors including soil composition and topological environment such as the presence of lakes and rivers.

As shown in the correlation measurement of the "vagabond" current (Fig. 8.5), the train leakage current enters or leaves the LEP tunnel through the transfer lines from the SPS around IP1 and over relatively large zone around IP6. Flowing on the LEP tunnel wall, the current travels from IP1 to IP6 on both directions along the storage ring. The reason why IP6 is another electrical pole is due to the presence of the river Versoix which passes close to IP6 before flowing into the Lake of Geneva. The river provides a better conductivity due to the abundance of water. The circuit is closed by the CFF railway of "Geneva – Lausanne" which crosses the river Versoix (see Fig. 8.5). The leakage current travels from LEP to the rail and finally goes back to the generator station. [6]

A rather melodramatic but yet convincing proof of the "train effect" came about through a French rail strike. Leakage current on the earth cable was measured at the position of NMROCT8 during a 4 day SNCF strike in late November which reduced the train traffic on the "Geneva – Bellegarde" line. It was found that the current was much reduced (by a factor of 2).

[3] Societé Nationale des Chemins de Fer

[4] Chemins de Fer Fédéraux

[5] The penetration depth is inversely proportional to square root of the frequency of the current [36].

[6] Though being the closest to the LEP tunnel, the rail line "Geneva-Airport" is not involved in this "train effect" because the rails along this rail line have been well insulated to protect the airport from electric disturbances.

The characteristics of the magnetic field fluctuation is well explained by the "train effect" :

- No trains run on the SNCF "Geneva – Bellegarde" line between midnight to about 05:00 in the morning.
- The anti-correlation between field fluctuations at NMROCT4 and NMROCT8 is due to the fact that the leakage currents travelling across octants 4 and 8 in opposite directions. The correlation factor of -1.7 ($\simeq 5/3$) can be explained by the fact that IP1 and IP6 split LEP into two parts by the length ratio of 5 to 3.

The Geneva power station had measurements of the train leakage current as early as in 1975 [7]. It is assumed that the "train effect" has been around for all years of LEP running.

The effect of the leakage current on the dipole field

The current on the vacuum chamber produces transverse magnetic field lines surrounding the beam pipe. The field lines traverse the iron yoke of the dipole magnet because of its high permeability. The transverse field strength depends on the current density on the vacuum chamber. The story has two parts :

- The short term fluctuation of the magnetic field is explained by a superposition of the transverse field produced by the leakage currents and the actual LEP dipole field.

  The anti-correlated short term fluctuations are not expected to affect the average beam energy since the current integrated over the propagation length between IP1 and IP6 along both semi-circles balances.

- The long term behaviour is believed to be due to the nonlinear effect of the magnet hysteresis. The superimposed transverse field shakes the magnetic domains of the dipole magnets. After the excitation, the domains realign themselves to attain a lower potential energy but this gives a higher magnetic

[7] That is also why M. Fleury, the EOS engineer, could spot the "train effect" when given the pattern of the magnetic field fluctuation.

field. After a large number of identical hysteresis excitation cycles, the magnetic field change per cycle becomes small. This corresponds to a saturation of the field rise in a fill and will be discussed later.

The long term field rise is the most important consequence of the "train effect" on the beam energy.

8.1.3 Confirmation from long calibration experiments

Whether or not the dipole field rise in the LEP tunnel measured by NMR's is a true effect on the beam energy can only be confirmed by the depolarization measurements. There were 6 fills in 1995 which had more than one set of depolarization measurements taken over a considerable period during the fill in question. The results from all these 6 experiments indicated that the beam energy of LEP on average did rise throughout a fill. This rise occurred independently of any variation induced by other causes of energy change such as temperature.

These long calibration fills exhibited a mean rise in the beam energy of 3.9 MeV, between the first and last depolarization measurements. This mean has a significant RMS scatter of 2.6 MeV. (Refer to Fig. 9.8 in Chapter 9.) Some of this scatter can be attributed to the variation in the length of the experiments (between 6 and 20 hours), but certainly the rate of energy change was different in each fill.

8.1.4 Conclusion on the LEP dipole field

Without doubt, trains running in the Geneva area perturb the LEP magnetic dipole field. A continuous modulation of the magnetic field causes an increase of the dipole field inside the LEP tunnel during the course of a fill.

The determination of Z^0 parameters is affected by the energy rise effect due to the beampipe current. Taking into account the effect of the dipole field rise during a fill, the mass of Z^0 would shift to lower energies (as the energy model is normalized to the EOF calibrations); whereas the width of Z^0 should remain more or less unaffected because of similar trend of the field rise at both off-peak points.

Though most of the LEP magnetic field has been well explained by the "train effect", a few open questions still remain. The individual long term response of the two NMR's in the tunnel and their behaviour during the quiet period after midnight is not completely explained by the "train effect". The field jumps in the

NMRREF have not been solved either. More controlled experiments and studies are needed to learn about the magnetic characteristics and their response to the current modulations due to the "train effect" or others.

8.2 Vertical Dispersion Correction

The usage of vertical electrostatic bumps in the 'bunch train' operation to avoid parasitic collision in 1995 scan introduces a significant vertical dispersion. This vertical dispersion of the two beams is roughly equal but of opposite sign, i.e., OSVD (opposite sign vertical dispersion).

It has to be stressed here that this effect is only significant in the bunch train operation of LEP started from 1995, but not in the 1993 scan. A detailed discussion can be found in [46]. Only a brief discussion is given below.

If the beams collide with a collision offset δy, which is the distance between the centre of the positron bunch and the electron bunch in collision at the IP, then the centre-of-mass energy is shifted from the nominal value by an amount ΔE_{CM} such that :

$$E_{CM} = E(e^+) + E(e^-) + \Delta E_{CM} \tag{8.2}$$

$$\Delta E_{CM} = -\frac{1}{2} \cdot \frac{\delta y}{\sigma_y^2} \cdot \frac{\sigma_E^2}{E} \cdot \Delta D_y^* \tag{8.3}$$

where σ_y is the individual beam size, D_y^* is the difference in the vertical dispersion ($D_{e^+}^* - D_{e^-}^*$), E is the beam energy and σ_E is the beam energy spread.

As ΔD_y^* is a characteristic of the bunch train bumps and σ_E cannot be reduced to zero, the only practical control of this effect is to reduce δy [8] as much as possible. In the 1995 energy scan, LEP was operated with 4 trains of 3 wagons per beam. Since the residual beam-beam kicks generate transverse distortions in the train, it is not possible to reduce δy simultaneously for all wagons[47].

In the case of one bunch, it is obvious that the optimization of the luminosity coincides with zero energy offset. This result can be generalized to a situation with many bunches with different collision offsets (δy's). Although the centre-of-mass

[8] E_{CM} typically changes about 1.5 MeV per μm of δy.

energy for each of the colliding bunch combinations can be different by tens of MeV, it can be demonstrated [48] that the overall energy shift (ΔE_{CM}) averages to zero if one considers the luminosity-weighted average over the bunches. The demonstration has made no other assumption than a gaussian particle distribution within the bunches and equal difference of OSVD (ΔD_y^*) for each family of the bunches. The three collisions in a train will be referred to as families a, b and c hereafter.

The strategy in the 1995 scan for controlling the collision offsets was to perform the so-called **Vernier scans** [9] during each off-peak fill (once near the beginning of the fill and once near the end). During a Vernier scan, the luminosities of different families of bunch trains were measured when the e^-e^+ beams were collided with different collision offset (δy). After the scan was completed, a display of the scan would appear, as shown in Fig. 8.7. The luminosity as a function of the collision offset indicated (by a Gaussian fit) the Vernier setting for the maximum luminosity for each family. The average of the three families gave the optimal Vernier setting, to which the operator then adjusted.

Measurements were also done to check the size of the effects due to each parameter in equation 8.3 :

Dispersion measurements The opposite sign vertical dispersion (OSVD) was measured with Vernier scans. The shift in the optimal Vernier setting when the beam energy is changed is directly proportional to the difference in the vertical dispersion. The beam energy can be changed by varying the RF frequency. The difference in the dispersion of the two beams is :

$$\Delta D_y^* = -\frac{\alpha_c \cdot f_{RF}}{\Delta f_{RF}} \cdot \Delta y_{opt} \tag{8.4}$$

where Δy_{opt} is the observed shift in the optimal Vernier setting when the RF frequency, f_{RF} is shifted by Δf_{RF} and α_c denotes the momentum compaction factor.

Dispersion measurements were made for each IP at each energy. The results were averaged over the energies and yielded ΔD_y^* measurements of about 2 mm at each IP, as expected.

[9] It is so called because the adjustment of vertical collision offset is of the order of μm.

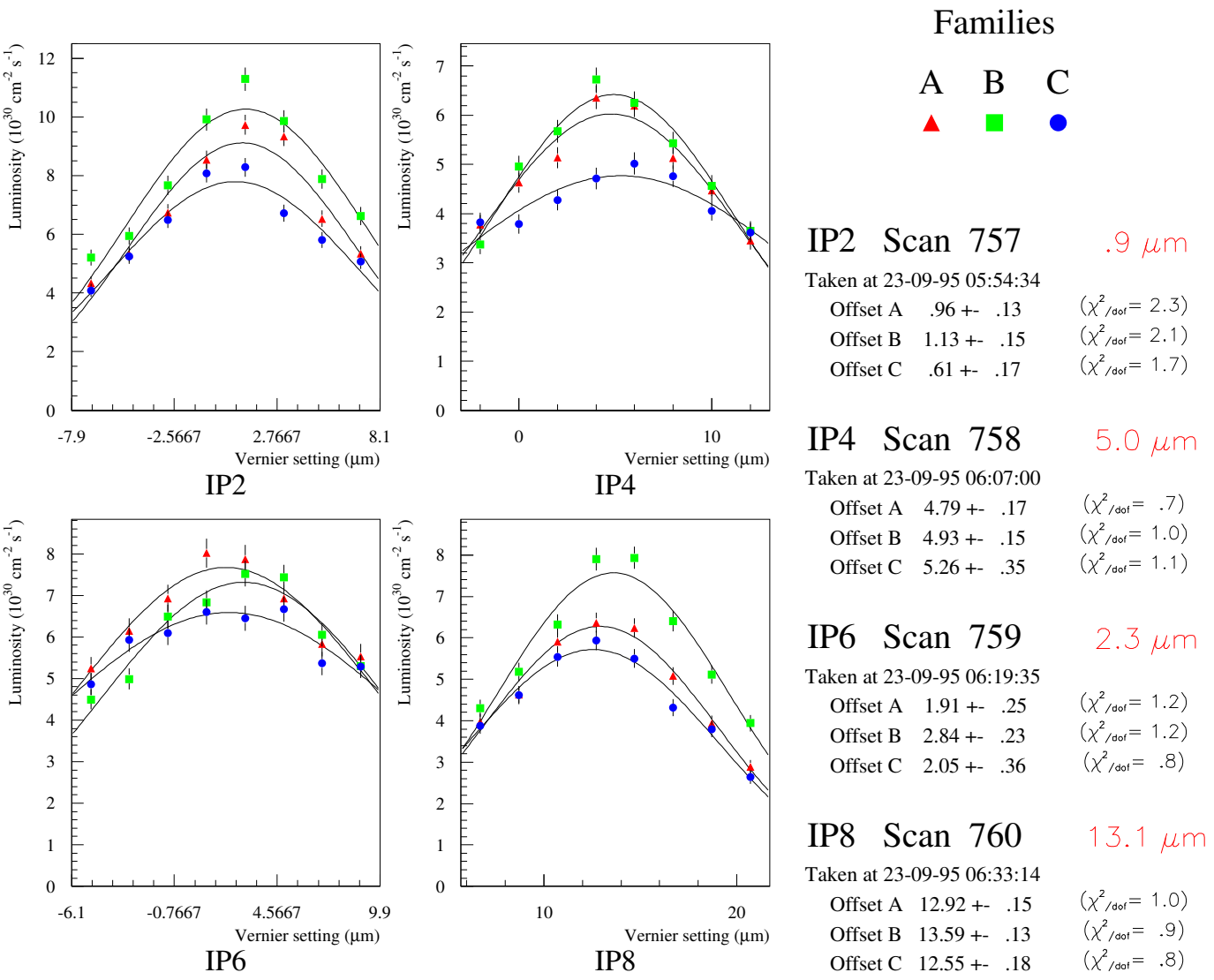


Figure 8.7: Typical online display of Vernier scans taken at each IP.

Stability The RMS variation of the optimal position is about 1.0 to 1.5 μm. With about 35 Vernier scans at each off-peak point at each IP, the mean position is therefore known to an accuracy of 0.2 μm.

Vertical Beam Size Vertical beam size (σ_y) comes out of Vernier scan fits since the shift of centre-of-mass energy (according to equation 8.3) is inversely proportional to the square of the beam size. Vertical beam sizes were measured at each IP and off-peak point. They fell in the range of 4 to 5 μm

Collision Offset In order to calculate the collision offset it is necessary to compare the optimal Vernier setting, y_{opt}, with the actual Vernier setting, y_{set}. The collision offset, δy, is defined as

$$\delta y = y_{set} - y_{opt} \tag{8.5}$$

The error on the luminosity-weighted collision offset, $\delta < \delta y >_{lum}$, comes from the error on $< y_{opt} >_{lum}$ since it is not known at all times and has a large RMS variation. In general, the average collision offset at each IP at each energy point is much below 1 μm.

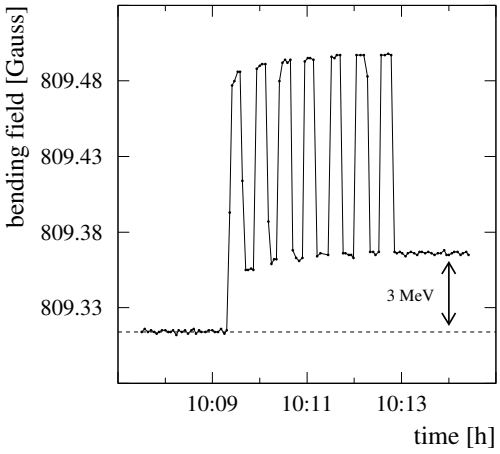
Using the results from these measurements for the mean collision offset, the beam size and the difference of dispersion, the sensitivity to collision offsets for each IP was determined to be -2.3, 1.3, -1.4 and 1.6 MeV/μm for IP 2, 4, 6 and 8 respectively. This sensitivity can be combined with the collision offsets to obtain an estimate of the centre-of-mass energy shifts at each IP and energy. In general, the shifts are well below 1 MeV, thanks to the many Vernier scans which have been carried out.

8.3 Bending Modulation

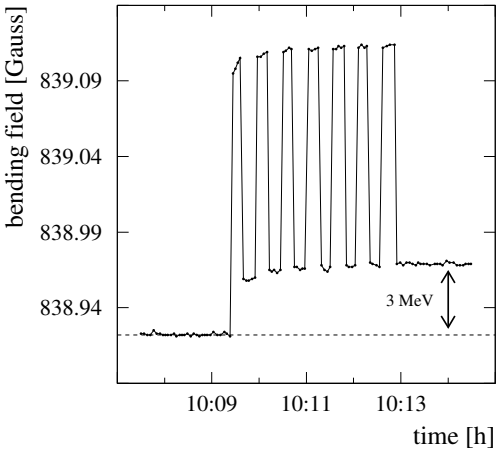
In order to stabilize the LEP magnets, "bending modulation" was used in 1995 as a method of conditioning the magnets. This procedure was first developed in 1993 [49] to understand and control the field jumps of the reference magnet.

The main dipole current was modulated by a train of seven square pulses with an amplitude of 1 A. [10] Typical responses measured from the four NMR's are shown in Fig. 8.8.

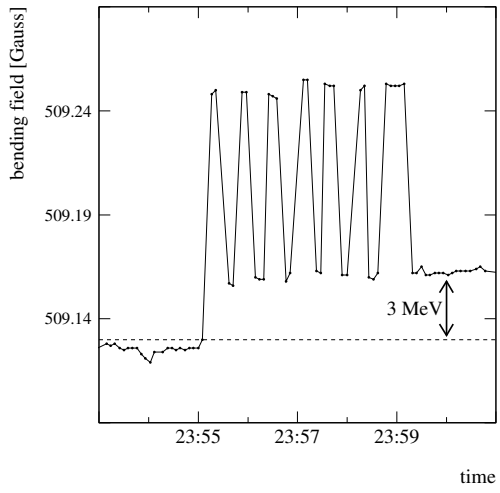
[10] The normal dipole current for LEP operated at 45 GeV is 2007 A.



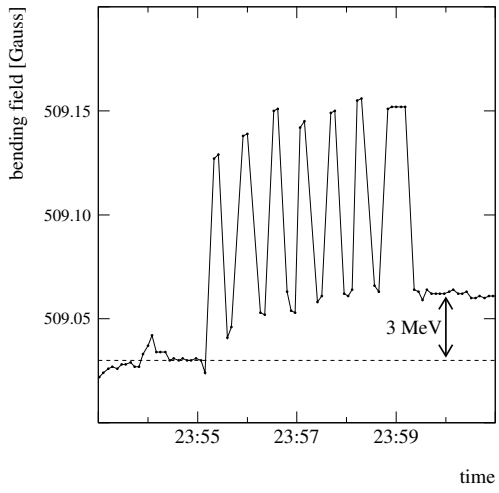
(a) NMRREF



(b) NMRVAC



(c) NMROCT4



(d) NMROCT8

Figure 8.8: Responses of 4 NMR's during bending modulations in 1995

Responses of 4 NMR's during bending modulations in 1995. The bottom two were taken during a "quiet period".

The field was in phase with the current modulation. The first modulation cycle caused the largest field increase and each additional cycle has less and less effect. At the end of the seven modulation cycles, the magnet had appeared to saturate and the field had risen by an energy equivalence of a few MeV. The plots for NMROCT4 and NMROCT8 in Fig. 8.8 were taken during a "quiet period" such that the "train effect" did not exist.

The practice of conditioning was instigated part way through the scan [11] and was executed at the beginning of fill. For a certain number of fills, it was also done at the end of fill. As expected, EOF modulations were found to cause less field increase than BOF modulations, indicating that indeed the modulations had improved the magnet stability.

Since the rate of dipole field increases before and after bending modulation are different, this will be considered as an additional ingredient as needed in the energy model in section 9.6. Fig. 8.9 shows the instantaneous jumps of NMR48 after bending modulations. The bending modulation was parameterized in the energy model by a step of 2.5 MeV in the beam energy just after it happened. Furthermore, in the model, the appropriate set was chosen for the rise term (which will be further discussed later) depending on whether a bending modulation has happened or not.

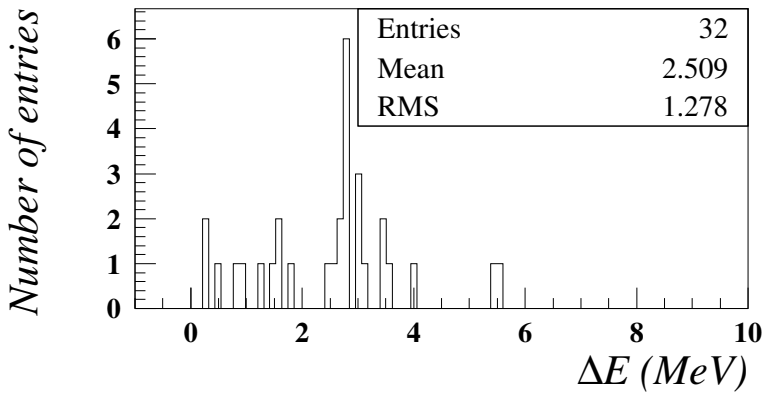


Figure 8.9: NMR48 field increases after bending modulation at the beginning of fills.

[11] It started from the fill 2948.

8.4 Corrector

A new consideration has been given to the effect of correctors in the later stage of the energy analysis. Correctors are small dipole magnets installed in LEP to compensate for the misalignment of the quadrupoles around the ideal orbit and to correct the beam orbit in both planes. Simulations have shown the horizontal corrector magnets could affect the beam energy significantly through a change in path length if the fields add up coherently. The main effect of the corrector is to change the path length of the beam proportionally to the product of its deflection angle and the horizontal dispersion. Since the orbit length is fixed by the RF frequency, the change in path induced by a corrector forces the beam to change its radial position in the quadrupole magnets. The additional fields seen by the beam in the quadrupoles then lead to a change in energy. This effect is implicitly included in the model by the horizontal beam position measurements in the arcs made with the BOM system. However, differences in corrector settings between calibration and physics modes must be properly taken into account and can potentially lead to a bias on the beam energy.

A correction was computed from the measured differences of corrector settings in physics and calibration. However, the effect of the horizontal correctors has not been observed directly up to now. Controlled experiments will be needed to investigate this effect. At present, in calculating the central values of the energies, only half of the predicted effect was applied, and half taken as error.

8.5 RF complication in 1995

Bunch train running in 1995 essentially leads to a new RF model 3 times more complicated than before. The new ingredients needed in the 1995 RF model can be summarized in the following points :

1. Independent simulation of RF phase ϕ_s for each wagon in the bunch trains;
2. The full set of voltages for each of the SC RF units;
3. The best known cavity alignment values and voltage calibrations [50];
4. The known phase errors and phase changes that existed/took place over the course of the scan;

5. A "weak" beam loading model for the unused cavities in which the wagons deposit energy equivalent to the measured induced voltage on the cavity but there is no interaction with the stored energy in the cavity.

The above are possible only because a virtually complete RF dataset has been set up by recovering data from the private logging or extrapolating/interpolating from the surrounding logged values (as described in section 7.3). Further elaboration can be found in [50].

Chapter 9

Analysis and systematic studies of the LEP Energy in 1995

This chapter is devoted to the analysis of the determination and modelling of the LEP collision energy. A brief discussion of the revision of the 1993 LEP collision energy is also given. Systematic errors and the corresponding covariance matrices for the 1993 and 1995 energy scans are provided at the end.

Although the author has contributed considerable work and time in producing and patching the necessary data for the RF and energy spread analyses, the author has not been directly involved in the analyses of the RF correction, OSVD correction and energy spread. These three subjects will therefore not be described in detail and the following sections mainly focus on what the author has directly contributed in the LEP Energy working group.

9.1 Pseudo device for measuring the dipole energy, NMR48

To analyze the energy rise in a fill, we have to rely on the NMR's in the tunnel, i.e., NMROCT4 and NMROCT8. Owing to the observation of the anti-correlation between NMROCT4 and NMROCT8, a pseudo device is 'constructed' :

$$\text{NMR48} \equiv \frac{5}{8}\text{NMROCT4} + \frac{3}{8}\text{NMROCT8} , \tag{9.1}$$

so that this 'average NMR' samples the magnetic field at both positions around the ring, eliminating almost completely the anti-correlated noise. This pseudo device is therefore more stable and is used to represent the dipole field in the LEP tunnel.

9.2 Temperature Coefficient

It is important to note that NMR readings may fluctuate due to various reasons which may or may not reflect the change of the LEP beam energy. In particular, the NMR fluctuations due to the local temperature variations at the places where the NMR's are situated do not directly indicate genuine changes of the beam energy. This is a consequence of the fact that the measurements from NMR probes are very localized. It is only when the average temperature in the entire length of the LEP tunnel changes that the beam energy would change accordingly.

Before NMR48 can be applied to model the dipole field behaviour in the model, it is necessary to disentangle the genuine change of the beam energy from the change due to the instability of the local temperature change in NMROCT4 and NMROCT8

The temperature coefficient of the pseudo-dipole corresponding to NMR48 has been determined from the data of the scan. We first mimic the definition of NMR48 as in equation 9.1 and construct the temperature of this device as :

$$\mathrm{T}_{48} \equiv \frac{5}{8}\mathrm{T}_4 + \frac{3}{8}\mathrm{T}_8 \ , \tag{9.2}$$

where T4 and T8 are the core temperatures of magnet 418 and magnet 818. The temperature changes in this pseudo device, ΔT_{48}, were fitted to the changes of energy, ΔE_{48} (or in fact ΔNMR48), and thus the temperature coefficient C_T^{48} was extracted from the fit. [1]

9.3 Determination of NMR48 Temperature coefficients

9.3.1 Facts and Difficulties

Various factors complicated this analysis :

- The core temperature of the LEP dipole magnets were kept as stable as possible throughout the scan due to the 'merit' of the cooling system in the tunnel. Most fills showed variations of less than 0.5° C. This is not large compared to the intrinsic precision of the temperature probes, which (up to 1995) was 0.1° C.

[1] The small correlation between the temperatures of NMROCT4 and NMROCT8 and the average temperatures (from 34 magnets) is ignored here.

- The noise and jumps seen in the NMR were a significant background to any field variation arising from temperature.

- Any measurements of C_T^{48} over long time intervals (~ 1 hour), were distorted by non-linear effects such as the "train effect".

The frequency of the standard NMR logging [2] is about once per 7.5 minutes whereas that of the magnet temperature logging is about once per 15.0 minutes. The accuracy of temperature readings is 0.1° whereas the accuracy of NMR readings is normally 0.001 Gauss. For NMR's in the tunnel at IP 4 and 8, this means that the accuracy of NMR readings is about 0.091 (or 0.1) MeV ; whereas for the reference NMR, it is about 0.055 MeV. In most cases, the temperature changes between successive readings, have only 3 categories, namely, -0.1°, 0.0° and 0.1°.

For a change of temperature of $\pm 0.1^\circ$, the NMR's in the tunnel would not be able to determine the absolute value of the temperature coefficient if its value is smaller than 2.0×10^{-5}; while the limit is 1.2×10^{-5} in the case of the reference NMR. This is a limitation of our measurement from the data during the scan in which the temperature changes (due to the merit of cooling system) are very small.

Another problem is that even if the temperature changes, the NMR readings remained unchanged, in a great proportion of the time, as shown in Figure 9.1.

9.3.2 Calculations

Intuitively, the temperature coefficients are better determined if there is more significant variation of temperature. In a bid to obtain larger temperature variations, the changes of temperature and accordingly the NMR readings at large time intervals, such as 1 hour, are used to calculate the temperature coefficients. The division of changes of temperature is in the unit of 0.1° as this is the case in the database. Any smaller divisions would be artificial and inappropriate.

To ensure the best quality of calculation, the following precautions have been made :

- ΔNMR < 2 MeV to eliminate those NMR jumps not due to temperature changes ;

[2] i.e., the PCR logging database.

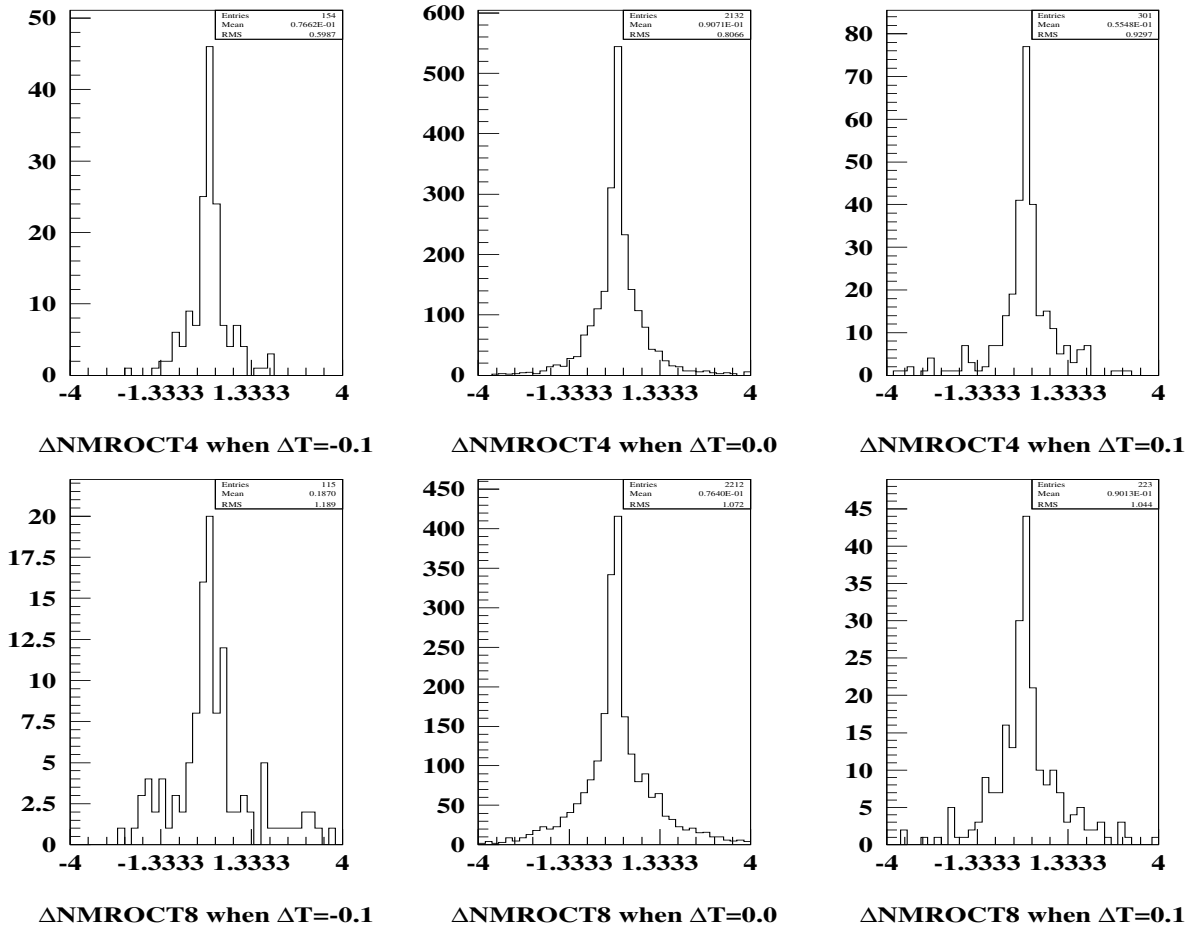


Figure 9.1: The changes of successive NMR readings (in the LEP logging database) at IP 4 and 8 when the temperature changes by $-0.1°$, $0.0°$ and $0.1°$ (where the unit of NMR readings is in MeV).

- Time of extrapolation for both the temperature and NMR readings are required to be < 1 hour.

Both the NMR data from the standard logging database and that compiled by M. Geitz and A. Drees [3] [44] (marked as "New") have been used for comparison. NMR48 data were extracted in exactly the same manner from these two databases.

Plots of variation NMR48 against the temperature changes are given in Figure 9.2.

[3]Derived from the BI (Beam Instrumentation group of SL Division at CERN) database, a mean and an error are given every 15 minutes in this smoothed and averaged database.

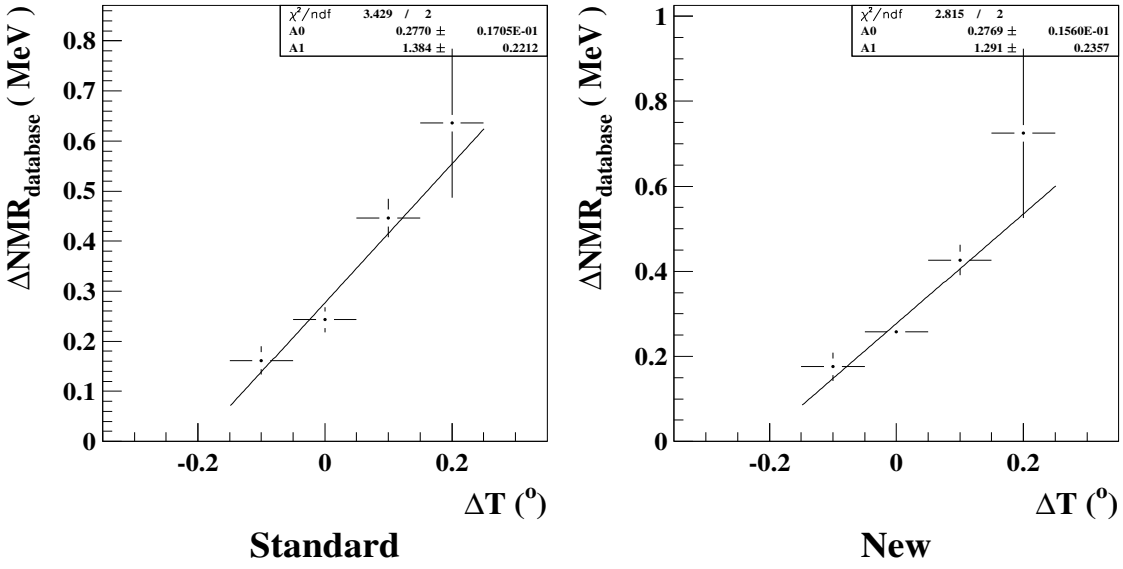


Figure 9.2: The temperature coefficients of NMR48 are evaluated on the data from two different databases at every hour after the physics/calibration started.. 'A1' in the plots shows the temperature coefficient in MeV per degree.

Owing to the beampipe current driven effect, the NMR's have an increasing trend through the time of fill (physics). Even if the temperature decreases, the NMR readings may still increase. The rise of NMR's is typically about 0.4 MeV per hour which is at least in the same order of magnitude as if the rise is due to temperature variation. However, though the rate of NMR rise changes with the time of fill, the average rate of NMR rise at a certain hour after the start of physics or calibration during a LEP run may be treated as a constant term. That is, we could use the following equation to model the temperature coefficient and the NMR rise :

$$\Delta \mathrm{E} = \mathrm{constant} + \mathrm{C_T^{48}} \times \Delta \mathrm{T} \times \mathrm{E}$$

A linear fit can be performed on the data of the changes of temperatures and NMR readings as in Figure 9.2. In this case, the constant value in the linear fit indicates the average NMR rise (in MeV) to some extent.

A model for the NMR rise can also be used to eliminate the effect of the NMR rise due to the beampipe current. The correction is done in the following manner :

$$\mathrm{NMR_{corr}} = \mathrm{NMR_{database}} - \Delta\mathrm{NMR_{model}}$$

where $\Delta\mathrm{NMR_{model}}$ is the NMR rise as a function of time of fill and time of day extracted from all the data during the scan, as described in section 9.5.2.

A similar fit to determine the temperature coefficients for the data from both databases has also been done in this case, Figure 9.3.

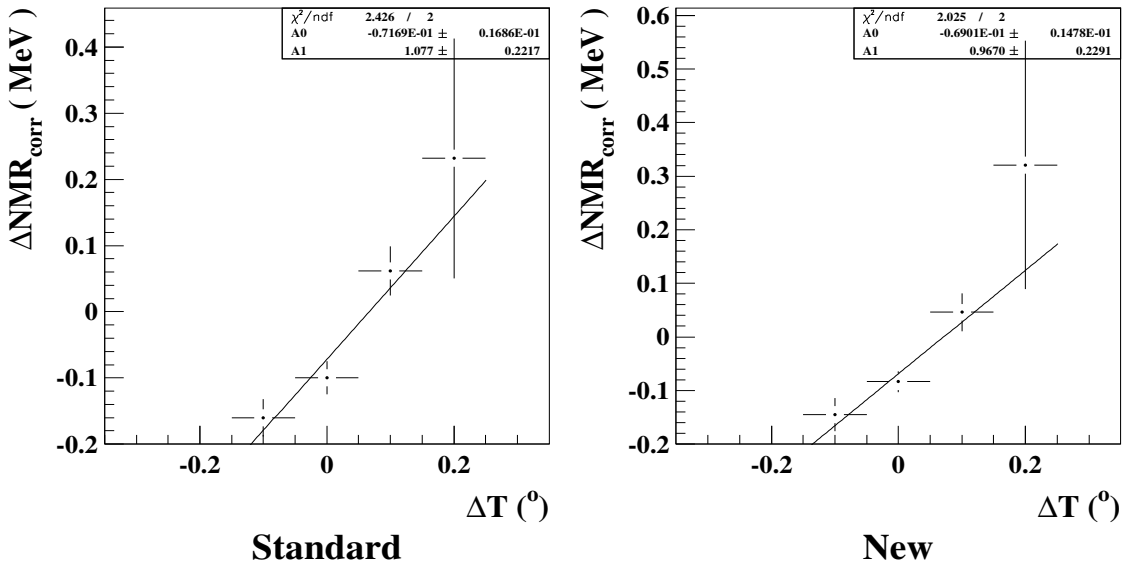


Figure 9.3: The temperature coefficients of NMR48 are evaluated, after correction for the NMR rise due to the beampipe current driven effect is made, on the data from two different databases. 'A1' in the plots shows the temperature coefficient in MeV per degree.

The results in the latter case are a bit lower than the previous though not entirely contradictory.

Moreover, the constraint of the allowable maximum ΔNMR used in the above calculation has also been varied in order to see its influence on the temperature coefficients derived in this method. The results are tabulated in Table 9.1 along with previous results. Indeed, the temperature coefficients derived in this method are sensitive the allowable maximum ΔNMR used. The largest change is up to $\sim$ 70% !

A similar procedure has been followed for the NMRREF in the reference magnet and the results are given in Figure 9.4 and Table 9.2.

As can be seen, the temperature coefficient of the reference NMR is comparatively less sensitive to the allowable maximum ΔNMR used.

9.3.3 Subtleties

The linear behaviour (though among 3 or 4 points) shown above is not so clear if one would use the changes of temperatures and NMR readings at shorter intervals,

Database	ΔNMR (MeV)	Correction for NMR rise	C_T^{48}
Standard	< 2	$\times$	$3.0 \pm 0.5 \times 10^{-5}$
Standard	< 4	$\times$	$3.8 \pm 0.8 \times 10^{-5}$
Standard	$< \infty$	$\times$	$4.4 \pm 0.9 \times 10^{-5}$
New	< 2	$\times$	$2.8 \pm 0.5 \times 10^{-5}$
New	< 4	$\times$	$3.5 \pm 0.6 \times 10^{-5}$
New	$< \infty$	$\times$	$4.5 \pm 1.6 \times 10^{-5}$
Standard	< 2	$\surd$	$2.4 \pm 0.5 \times 10^{-5}$
New	< 2	$\surd$	$2.1 \pm 0.5 \times 10^{-5}$

Table 9.1: Temperature Coefficients of the NMR48 evaluated from different ways in which readings are taken at every hour after the physics/calibration started.

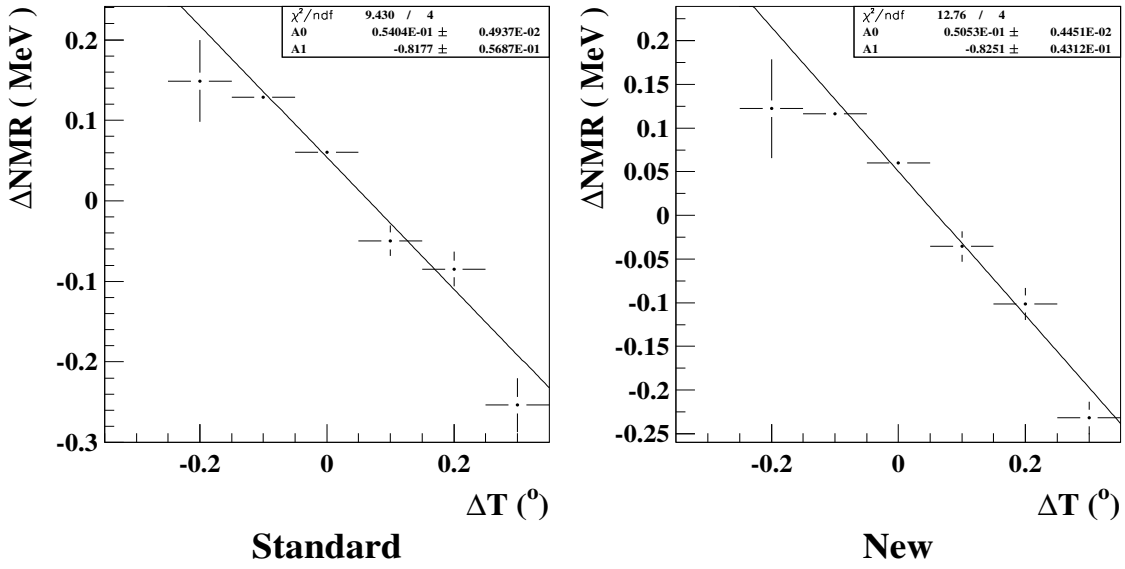


Figure 9.4: The temperature coefficients of the NMRREF are evaluated on the data from two different databases. 'A1' in the plots shows the temperature coefficient in MeV per degree.

Database	ΔNMR (MeV)	C_{Tref}
Standard	< 2	$-1.8 \pm 0.1 \times 10^{-5}$
Standard	< 4	$-2.1 \pm 0.2 \times 10^{-5}$
Standard	$< \infty$	$-2.1 \pm 0.2 \times 10^{-5}$
New	< 2	$-1.8 \pm 0.1 \times 10^{-5}$
New	< 4	$-2.1 \pm 0.1 \times 10^{-5}$
New	$< \infty$	$-2.1 \pm 0.2 \times 10^{-5}$

Table 9.2: Temperature Coefficients of the NMRREF evaluated from different ways in which readings are taken at every hour after the physics/calibration started.

such as half an hour or 15 minutes, to determine the temperature coefficient. A rather confused picture would be obtained if one follows the same procedure as presented here.

Furthermore, the individual temperature coefficients of NMR's at IP 4 and 8 are even more erratic. For instance, they may have completely different values if the allowable maximum ΔNMR used in the above calculation is changed. The temperature coefficient of the NMR at IP 8 obtained from the fit changes by more than a factor of 4 if one increases the allowable maximum ΔNMR from 4 MeV to 2 MeV , as shown in Figure 9.5 and Figure 9.6.

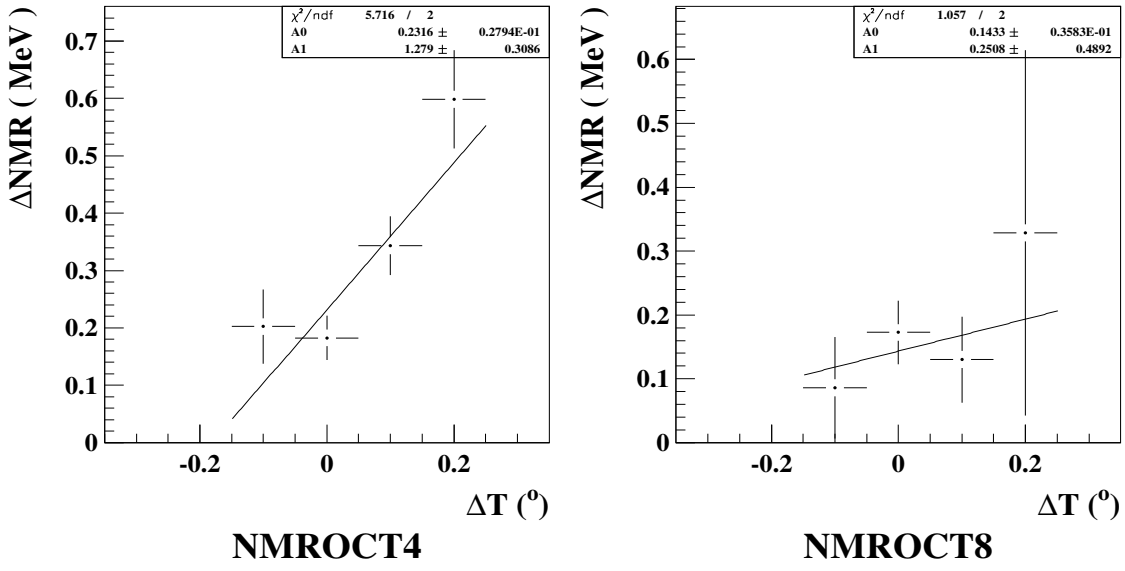


Figure 9.5: The temperature coefficients of the NMR's at IP 4 and 8 with the constraint that $|\Delta NMR| < 2$ MeV, in which the data from the standard logging database is used. (The temperature coefficient for NMROCT8 in the above fit is $0.6 \pm 1.1 \times 10^{-5}$ per degree.)

Fortunately, due to the anti-correlation of the two NMR's at IP 4 and 8, NMR48 has a smaller fluctuation which makes the determination of the temperature coefficient easier. It is also true that, the large or rather fuzzy fluctuation of NMR readings are washed out when one samples the changes over a larger period of time compared to period of the logging of temperature and NMR's.

9.3.4 Further Comments

- The temperature coefficient determined here for the reference NMR is quite close to the value which has been assumed, i.e, -1.5×10^{-5} per degree (see

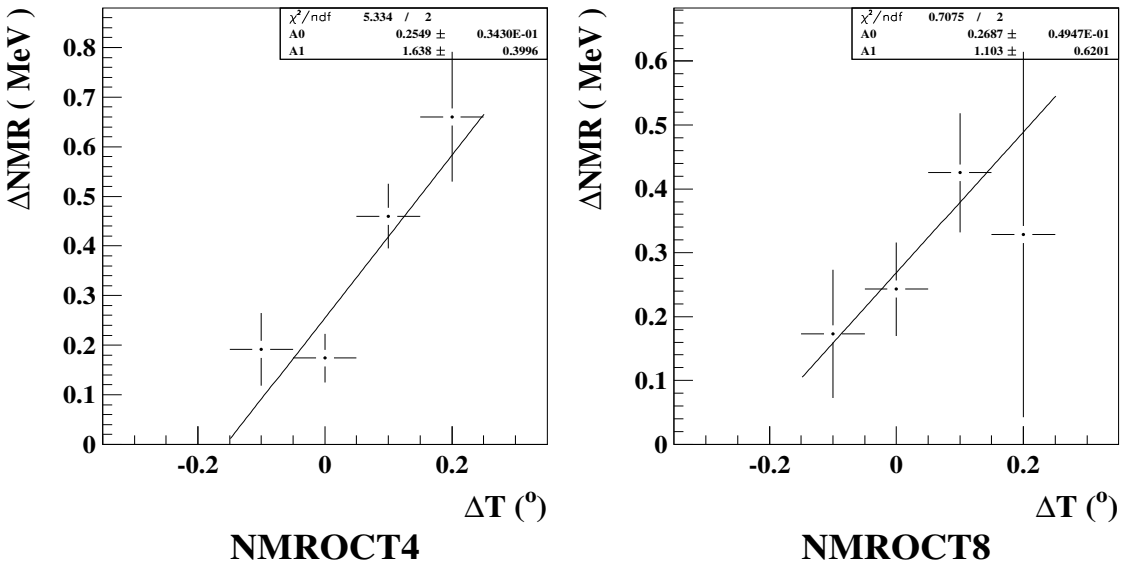


Figure 9.6: The temperature coefficients of the NMR's at IP 4 and 8 with the constraint that $|\Delta\text{NMR}| < 4\,\text{MeV}$, in which the data from the standard logging database is used. (The temperature coefficient for NMROCT8 in the above fit is $2.4 \pm 1.4 \times 10^{-5}$ per degree.)

[51]). The value determined here (about -1.8×10^{-5}) per degree is just over the threshold of the NMR sensitivity.

- The situation for the NMR48 is slightly better but it is also quite close to the threshold.

- The majority of the changes of ΔNMR, irrespective of the changes of temperature, are zeroes. Since the average ΔNMR is taken at each point of ΔT, this means that ΔNMR tends to be very small in any case.

- The possible non-linearity of the behaviour of NMR against temperature at small intervals is not well understood.

9.3.5 Evaluating C_T^{48} at different energies

Temperature coefficients at different energies have also been determined separately. Table 9.3 shows the result requiring $|\Delta\text{NMR}| < 4$ MeV.

The temperature coefficients at the two off-peak energies determined from both databases agree well within the errors. The temperature coefficients determined at peak energy are somewhat smaller. However, this difference is not significant in

Energy	Standard NMR	New NMR
P + 2	$3.6 \pm 0.7 \times 10^{-5}$	$3.4 \pm 0.7 \times 10^{-5}$
P - 2	$3.6 \pm 0.7 \times 10^{-5}$	$3.6 \pm 0.8 \times 10^{-5}$
Peak	$0.4 \pm 1.3 \times 10^{-5}$	$0.2 \pm 1.3 \times 10^{-5}$

Table 9.3: Temperature Coefficients of NMR48 evaluated at different energies.

view of the low statistics for the scan peak fills and the fact that peak fills are all relatively short, so that there was often no considerable temperature change.

Therefore, it is legitimate to claim the temperature coefficients at P−2, P and P+2 are the same.

9.3.6 C_T^{48} compared with C_T^{ring}

As shown, various systematic problems have prevented a precise determination of C_T^{48}. Nevertheless, different analyses have been shown to be consistent with one another. The final value adopted is :

$$C_T^{48} = (0.25 \pm 0.25) \times 10^{-4} \ / \ ^\circ\mathrm{C} \tag{9.3}$$

The average temperature of dipole magnets in the LEP ring has even less variation within fills. The limited precision obtained with C_T^{48} makes it difficult to measure the temperature coefficient of the dipole magnets in the ring directly from NMR48. The fact that there is a trend of dipole field rise regardless of temperature fluctuation also complicates the situation.

Limited progress has been made in 1995 to better understand the temperature coefficient for the dipole field in the LEP ring as a whole, C_T^{ring}.

Based on previous studies (see section 6.3.3), it has been decided to use essentially the same temperature coefficient as in 1993, i.e.,

$$C_T^{ring} = (1.00 \pm 0.50) \times 10^{-4} \ / \ ^\circ\mathrm{C} \tag{9.4}$$

though the error for this coefficient has been increased due to the complication of the newly discovered dipole field rise during a fill. This value is also supported by a fit to the depolarization data using the the depolarization model which will be described in section 9.5.3.

Note that the value of this coefficient (for all dipole magnets) is significantly larger than that for NMR48 (of 2 magnets). This difference is not yet understood.

A dedicated testbench has been established to study in detail the thermal behaviour of a LEP dipole magnet, which may give us some clues.

9.4 NMR48 behaviour during a fill and day

It is important to check how this pseudo device, NMR48, represents the new effect discovered during the 1995 scan. The plots of NMR48 shown in Figure 9.7, which has the temperature fluctuations due to T_{48} corrected (by the coefficient C_T^{48}), can summarize the two essential features explained in the previous chapters :

Energy rise in a fill The saturation of the rise of beam energy over a fill can be seen in Figures 9.7(a) and 9.7(b). These two plots are the integrated and differential rise of NMR48 averaged over all fills during the scan period in 1995. One can see that the integrated rise saturates after some 12 hours of physics running (magnet being ramped up at $\sim$ 45 GeV).

Day-Night effect Fig. 9.7(c) gives the rise of beam energy (also average over all scan fills in 1995) as a function of time of day where the Day-Night effect is obvious.

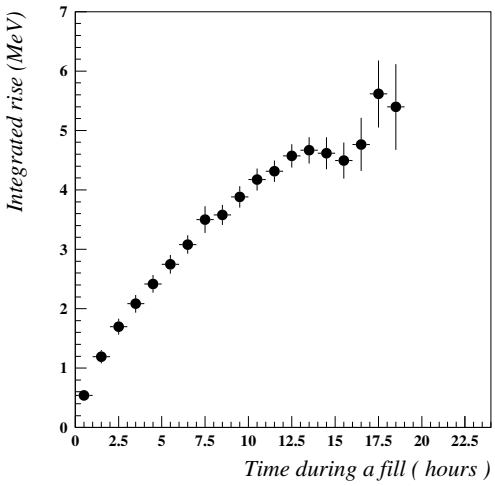
These distinctive behaviours form the basis for modelling the beam energy rise during a fill and a day. The goal of all the NMR-related models (which are to be described) is to simulate as close to the 'average behaviour' shown in the Fig.9.7 as is possible.

9.5 Modelling beam energy rise during a fill

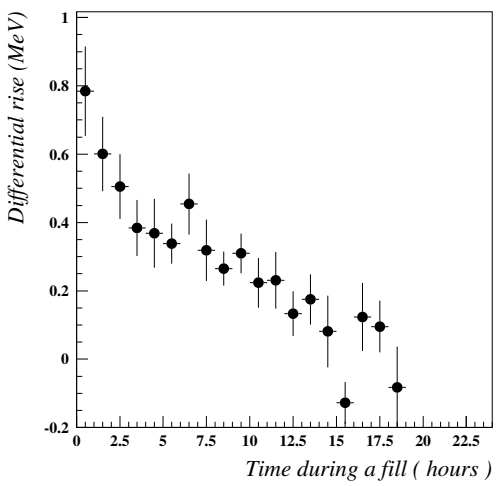
The beam energy rise during a fill must be included in the model of the LEP dipole field. This can be done through the use of NMR data, or from the use of the BOF/EOF depolarization data [52, 53]. Four categories of dipole models have been devised for describing the energy rise in fill, which will be described below.

9.5.1 Direct NMR48 model

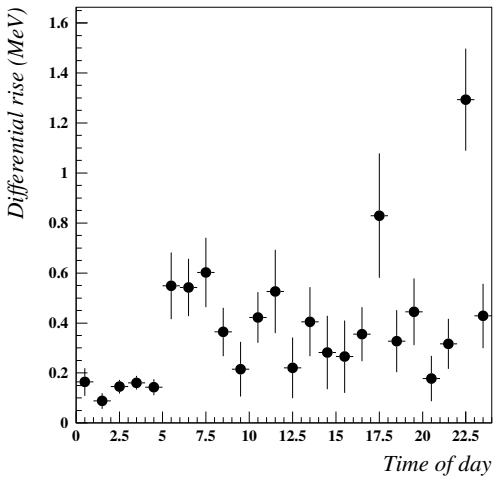
This model uses directly the instantaneous change of the quantities of NMR48 (as defined in equation 9.1) with respect to that at the beginning of the fill as the rise



(a) Integrated rise in fill.



(b) Differential rise in fill.



(c) Differential rise in day.

Figure 9.7: The variations of NMR48 (as defined in equation 9.1) during a fill and a day after the temperature fluctuations due to T_{48} have been subtracted (with C_T^{48}). The results plotted here are the averages of all fills during the 1995 scan. All effective energies are in (MeV) per beam.

of the dipole field. The temperature coefficient in equation 9.3 was used to correct for the temperature fluctuation of NMR48 as compared to the temperature at the beginning of the fill. This is the most straight-forward way of modelling the energy rise in a fill and it gives the possible instantaneous change of field at any time. However, the fact that NMROCT4 and NMROCT8 were not installed before 1995 means we cannot apply this model for 1993 and 1994.

9.5.2 Average NMR48 model

In the light of the dependence of the dipole field rise on the time of fill and time of day, a way of using the average behaviour of the NMR48 in terms of these two time dependences has been developed. There is no parameterization in this model but rather the numerical averages at any given time of fill and time of day are used.

The NMR48 data over the entire scan were histogrammed respectively as a function of time in fill, t_{fill} and time of day, t_{day}. That is, we have formed two functions of beam energy rise, namely, ΔE_{fill} and ΔE_{day}. The rise of beam energy in a fill, E_{rise}, is then equal to :

$$\Delta E_{rise} = \Delta E_{fill} \times \frac{\Delta E_{day}}{< \Delta E_{day} >} \tag{9.5}$$

where $< \Delta E_{day} >$ is the average of ΔE_{day} over a day (24 hours).

The model is set up in this way such that the beam rise in the energy model at a particular time depends on its t_{fill} and t_{day}, using the NMR48 data shown in in Figures 9.7 (a), (b) and (c). The distributions were broadly similar at P$-$2 and P+2 and thus all the data were taken together irrespective of P$-$2 or P+2.

This use of the average behaviour of NMR48 is preferred to making a direct correction from the synchronous data themselves, in order to permit a consistent treatment of the 1993, 1994 and 1995 data. In 1993 and 1994, there were no NMR's in the tunnel. Reference to the average behaviour in 1995 establishes a procedure which could be applied without technical difficulty to the previous years.

One intrinsic assumption we have to make in using the NMR data is that the beam energy exhibits the same dependence with time in fill, t_{fill} and time of day, t_{day} in magnitude and form as is observed in the NMR's.

This assumption can be checked by comparing the modelling of the beam energy rise during a fill from the NMR data with the 6 BOF/EOF experiments in 1995.

The comparison is shown in Fig. 9.8. In this figure the change between the first and last depolarization measurements has been corrected for the quadrupole field effects of tide and variations in the horizontal orbit (by BOM) in addition to the dipole magnet temperature correction, to leave the residual rise in the dipole field component. The observed rise from the depolarization measurements has a large scatter, but the comparison with the model gives a narrower distribution and one centred on zero. This tells us that the NMR data do represent the genuine picture of the beam energy to within a precision of about 1 MeV.

9.5.3 Fitted depolarization and NMR48 models

Another way of modelling the NMR48 data is by fitting a functional form to the NMR48 field rise during the course of a fill and to use this function to determine the energy rise with time — the "fitted NMR48 model". Alternatively, one can also fit the *same* functional form to the changes of calibrated energies during fills with more than one depolarization measurement – the "fitted depolarization model".

This function, for modelling the rise of beam energy depending on t_{fill} and t_{day}, is :

$$\Delta E_{rise} = \Delta E_{day} + \Delta E_{fill} + \sum c_1 E_{beam}(\Delta T_{48} - \Delta T_{ring}) \tag{9.6}$$

where

- $\Delta E_{day} = a_1\,\theta(t_{day} < 05:00) + a_2\,\theta(t_{day} \geq 05:00)$ [4] where a_1 and a_2 are constant coefficients.
- $\Delta E_{fill} = d_1 \left(1 - e^{-\sum_{j=2}^{4} d_j t_{fill}^{j-1}}\right)$
- T_{ring} is the average temperature in the LEP tunnel measured by temperature probes in 34 magnet cores distributed uniformly along the LEP ring.
- The coefficient c_1 is a temperature coefficient for the difference in the behaviour of T_{48} and T_{ring}.

A fit was made to the BOF/EOF depolarization measurements of 1995 and several long term calibration machine developments which involved depolarization measurements in 1993, using the above form as the function in the minimization.

[4] θ is the step function.

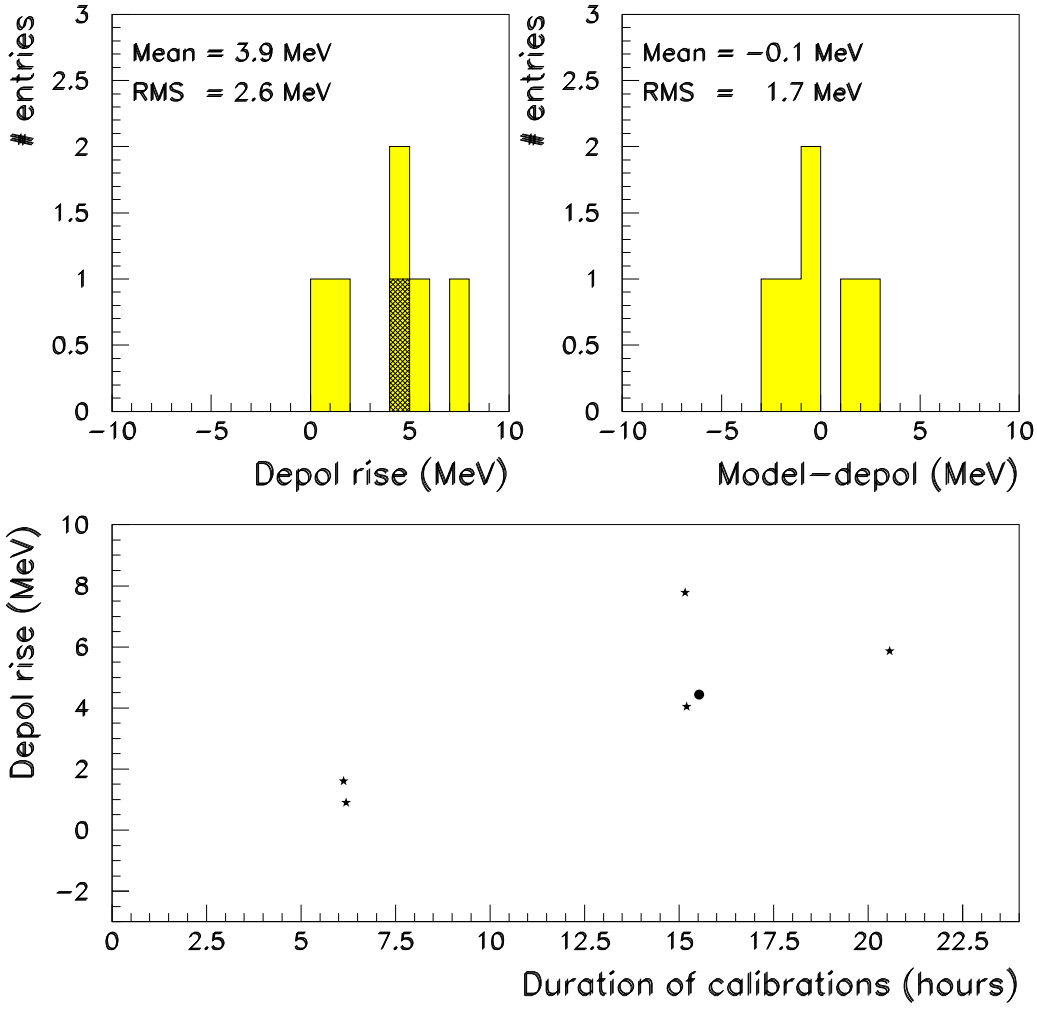


Figure 9.8: BOF - EOF calibrations in 1995 and comparison with the energy model. The long calibration experiments in 1995 considered here are 2929, 3022, 3029, 3030, 3036 and 3064. Figures shown above are the distribution of the dipole change seen between the first and last depolarization measurement (top left); the distribution of the depolarization dipole change minus the change predicted by the model (top right); the depolarization change against interval between first and last measurement (bottom). The fill indicated by dark hatching in the top left plot and by a circle in the bottom plot experienced a bending modulation between calibrations, which induced an energy jump of ~ 1 MeV. In every fill the first calibration occurred within 5 hours of the magnets being ramped to nominal field. All changes are given in MeV per beam.

The coefficients a_i's, c_1, and d_i's were free parameters determined from the fit. The results as found from the fit for P$-$2 and P$+$2 fills were consistent, and thus the full set was used to determine a common rise function independent of energy point.

The advantage of this approach is that it is independent of the questions of whether the NMR's are representative of the beam energy and what the NMR48

temperature coefficient is. However, we do not know exactly whether the above function is of the correct format and the available data sample from depolarization is much more limited than the NMR data.

The depolarization data did not suggest as strongly as the NMR data that the energy rise saturated after some 12 hours of fill, and the fitted depolarization model reflected this. However, when applied to the 1995 data, the two models agreed to within 0.5 MeV in the mean centre-of-mass energies at P−2 and P+2.

9.5.4 Comparison among different models

There is an intrinsic modelling difference between the fitted models and the average NMR48 model. The overall rise term from the average NMR48 model would saturate after some 12 hours of fill (see Fig. 9.7(a)). Nevertheless, though ΔE_{fill} in equation 9.6 of the fitted models would saturate in a similar fashion, another term ΔE_{day} in the same equation would keep on rising. This would affect those fills which have long durations, which include most of the calibrated fills.

The effects of the dipole field rise terms in different dipole models on the centre-of-mass energies have been evaluated. For this comparison, only the rise term in each model was varied and all the other terms in the model were the same. Table 9.4 shows the differences in the centre-of-mass energies for the 1995 scan between three models and the average NMR48 model and the differences are only due to the differences in the rise terms. These differences calculated at all energy points are quite small, especially for off-peak points. A larger difference is expected for on-peak fills because only one on-peak fill has been calibrated in 1995.

Model	Difference from the Average NMR48 model		
	Peak-2	Peak	Peak+2
Direct NMR48	−0.23	0.35	0.01
Fitted NMR48	0.03	0.01	0.47
Depolarization	−0.17	1.20	-0.07

Table 9.4: Effects of the dipole field rise terms on the centre-of-mass energies for the 1995 scan. The numbers (in MeV) show the differences between the three dipole models and the average NMR48 model, in which the only differences in evaluating the centre-of-mass energies are the rise terms applied in the models.

For the preliminary energy values released for the 1996 summer conferences, the "average NMR48 model" was adopted to calculate the centre-of-mass energies for the

years 1993 to 1995. Alternative methods provide cross checks and the differences in the mean centre-of-mass energies will be considered in the assignment of the systematic error in section 9.8.

9.6 Energy Model and the LEP Energies

The energy model can be summarized by the following equation :

$$\begin{aligned} E_{model} &= C_{norm}(fill) \times E_{Dipole} \times (1+F_T) \times (1+F_{tide}) \times (1+F_{\mathrm{BOM}}) \\ &\quad + \mathrm{RF}_{corr} + \mathrm{OSVD}_{corr} \end{aligned} \tag{9.7}$$

where

- C_{norm} is different depending on whether the fill in question was calibrated using the resonant depolarization method or not. If it was, then this normalization factor ensures that the energy of the model at the moment of the calibration equals the value of the calibration of this fill. If it was not, this term is equal to the mean normalization factor of all the calibrated fills at that energy point.

- E_{Dipole} represents the dipole field :

$$E_{Dipole} = E_{nominal} + \Delta E_{rise} + J_{bend-mod} + C_{corrector} \tag{9.8}$$

  where $E_{nominal}$ is 44.720 GeV at P$-$2, or 45.650 GeV at Peak, or 46.486 GeV at P+2; ΔE_{rise} is the rise term as mentioned in section 9.5, $J_{bend-mod}$ is the jump (of 2.5 MeV) just after a bending modulation (see section 8.3) and $C_{corrector}$ is the correction due to the differences of corrector settings between physics running and calibration (see section 8.4).

- F_T is the temperature correction for the main dipole magnets :

$$F_T = C_T^{ring} \times \Delta T_{ring} \ ,$$

  where C_T^{ring} is given in equation 9.4 and ΔT_{ring} is the average temperature variation of dipole magnets in the LEP ring.

- F_{tide} is the correction due to the effect of the tide :

$$F_{tide} = \kappa_{tide} \Delta g \quad ,$$

  see section 6.3.4.

- $F_{\rm BOM}$ is the correction for the horizontal position of the orbit :

$$F_{\rm BOM} = \frac{\rm X_{ARC}}{13\mu m}$$

  where $\rm X_{ARC}$ in μm is the horizontal beam orbit position. This effect is calculated using an average orbit position for each fill after the expected variations for tide have been removed. See section 6.3.4.

- $\rm RF_{\mathit{corr}}$ is the correction, different for each interaction point, due to the RF system. See section 6.4.1.

- $\rm OSVD_{\mathit{corr}}$ is the correction, also different for each interaction point, due to the OSVD effect. See section 8.2.

Note that there is no correction due to the difference between the beam energies of electron and positron. A dedicated experiment was performed in 1995 to measure this difference [5] and it was established that the electron and positron beam energies were identical with an uncertainty of 0.25 MeV [54].

The comparison between the energy model and the calibration measurements reflects the combined precision of the measurements and of the parameters of the model. Fig. 9.9 shows the difference between the energy model and the calibration measurement with a constant normalization factor at each energy point. All corrections, except C_{norm}, were applied according to the conditions at that particular time, whereas C_{norm} was applied on a fill-by-fill basis. In the first part of Fig. 9.9, there seems to exist a residual trend in the difference of calibration and model energies. This implies some degree of imperfection of our model at the moment and there may exist some unknown factors which we have not considered. However, this uncertainty has been taken into account by the scatter errors in the comparison between the model and calibration energies.

Fig. 9.10 show how the energy model works in interpolating the beam energy during two fills in the 1995 scan.

Based on the above model, the preliminary result of the average LEP beam energies at 3 different energy points and their IP-dependent corrections as for the summer conferences in 1996 is shown in Table 9.5.

[5] There were a few similar experiments in 1993 and 1994 as mentioned in section 6.3.5.

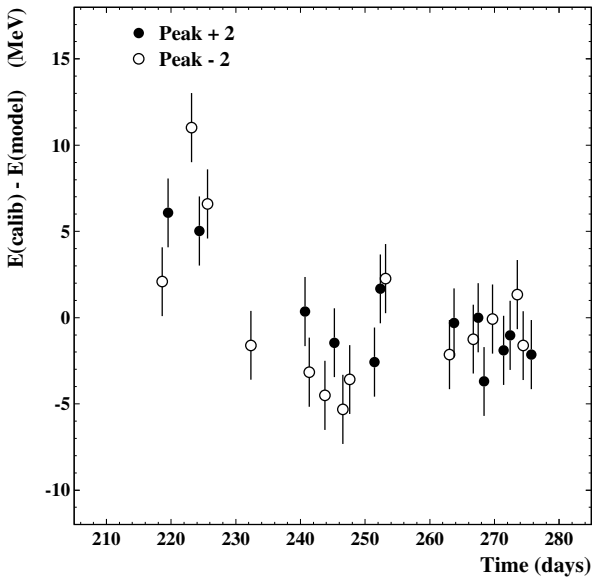


Figure 9.9: Difference between the centre-of-mass energies measured during the scan by the resonant depolarization method and those predicted by the model with a constant normalization factor. An error bar of 2 MeV is shown on each entry.

	Peak-2	Peak	Peak+2
Average LEP beam energy	44718.8	45638.5	46483.8
RF correction at L3	7.6	8.0	7.6
RF correction at ALEPH	0.4	0.8	0.7
RF correction at OPAL	2.1	1.8	2.3
RF correction at DELPHI	-0.4	-0.8	-0.8
VD correction at L3	-1.0	-0.5	0.0
VD correction at ALEPH	0.5	0.1	-0.4
VD correction at OPAL	-0.6	-0.2	-0.3
VD correction at DELPHI	0.4	1.0	-0.2

Table 9.5: Average LEP beam energies and the RF and OSVD corrections (also in terms of beam energies) in MeV at four experiments in 1995. This is the preliminary result for summer conferences in 1996.

9.7 Revision of 1993 Energies

The structure of the LEP energy model described in [23], which was used to evaluate the centre-of-mass energies in 1993, is fairly similar to the above. The differences are :

- The NMRREF in the reference magnet was used to give the value of the dipole field at the start of the fill. This was based on the observation that there were significant variations with time in the dipole field, which was attributed to the

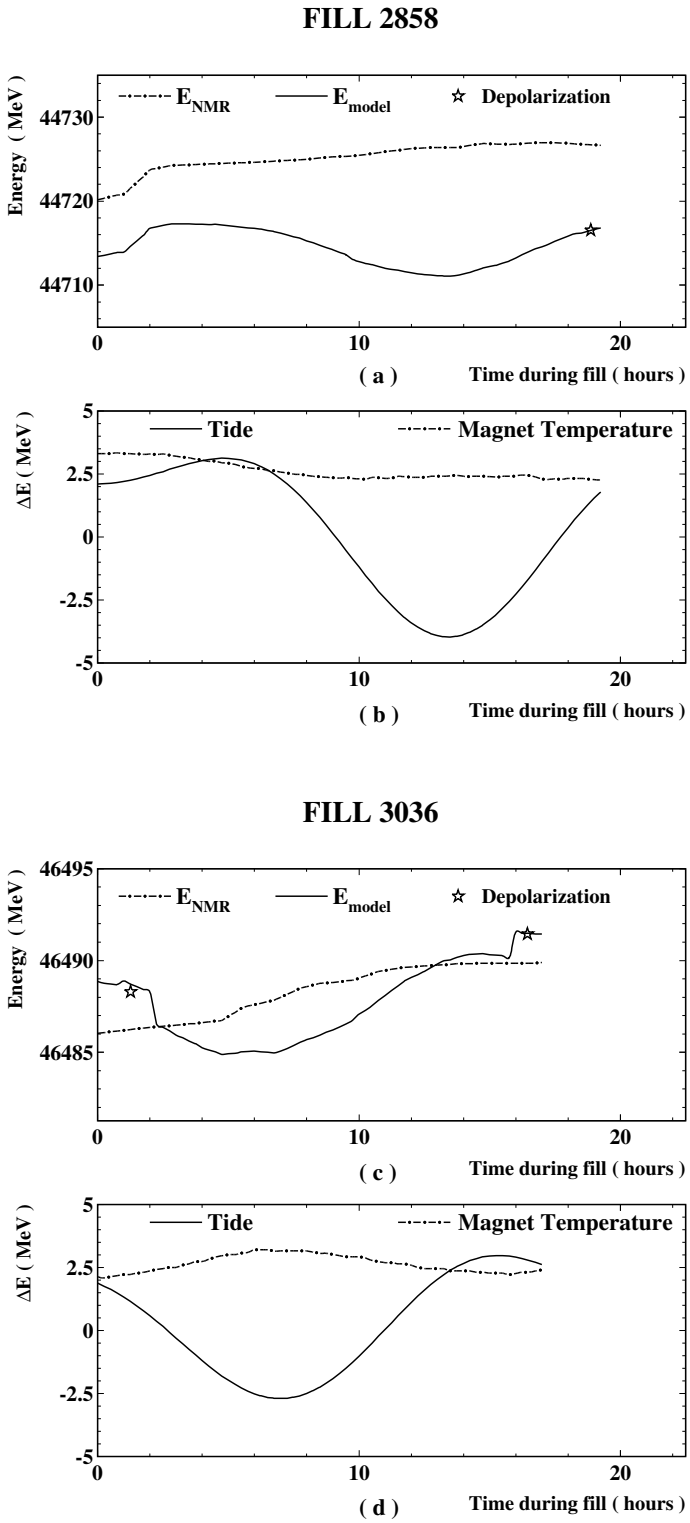


Figure 9.10: Exhibition of the modelled beam energy variations during two fills. Figures (a) and (c) show the beam energy variations of the NMR48 and the energy model as compared with the depolarization measurements in fills 2858 and 3036 respectively. In our energy model, the EOF (not BOF) depolarization result is used to do the calibration. Note that the 'steps' in these two plots are mostly due to the changes of corrector settings (see section 8.4). Figures (b) and (d) show the two largest corrections due to variations of terrestrial tide and ring temperature in fills 2858 and 3036 respectively.

effect of the fluxloop measurements performed regularly in 1993. [6]

- In the original 1993 energy model, instead of the rise term described above, half of the dipole field change measured by NMRREF with respect to that measured at the beginning of a fill was used. However, the field variation of NMRREF is very small as compared to those of NMROCT4 and NMROCT8 (in the LEP tunnel). Thus, the dipole field rise in the original 1993 model was much smaller than in the 1995 model.
- The temperature correction of NMRREF was used in the original 1993 model.
- There was no correction due to correctors in the original 1993 model.
- There was no bending modulation in the 1993 scan and hence no need of correction for this effect.

For the purpose of reference, the previous published results of the errors on the determination of the 1993 LEP energies, before any new knowledge was gained on the dipole behaviour from the 1995 scan, are listed in Table 9.6 (quoted from [23]).

Source	Peak-2	Peak+2	Correlation
Mean fill energy	1.60	0.72	0.00
Ring Temperature	0.16	0.35	1.00
NMR Uncertainty	0.93	0.93	0.81
Tide	0.04	0.41	1.00
QFQD	**0.40**	**0.36**	**1.00**
Energy Cal.	**0.50**	**0.50**	**0.04**
e^+ measurement	**0.30**	**0.30**	**0.50**
RF	**0.22**	**0.22**	**0.90**

Table 9.6: Systematic errors in the **previous analysis** of the LEP centre-of-mass energy in 1993 (in MeV). Note that only those in **boldface** are still valid now. The other items have been revised in this new analysis taking into account all new knowledges we have gained in the 1995 scan.

A brief explanation of the terms in Table 9.6 is as follows :

Mean fill energy : This error comes from the scatters of the old 1993 energy model with respect to the depolarization measurements (compared at the time of the depolarization measurement).

[6] The hysteresis loop induced by the fluxloop measurement affects the magnetic history of the magnets. No fluxloop measurement was carried out during the 1995 scan to avoid this complication.

Ring Temperature : The uncertainty on the temperature coefficient of dipole magnets, C_T^{ring}, in the LEP ring is this source of this error. Note that, however, the estimated error on the temperature coefficient C_T^{ring} has been increased in the new analysis, because the complication of energy rise during a fill makes it difficult to extract the temperature coefficient of dipole magnets in the ring.

NMR Uncertainties : The old 1993 energy model included half of the rise observed in the NMRREF reading between the start of fill and the current time. The effect on the mean centre-of-mass energy of half of the observed mean rise of the NMRREF at each energy point was taken as the systematic error from this correction.

Tide : The uncertainty on κ_{tide} gave rise to this source of error. In the new analysis, the uncertainty on κ_{tide} is the same but an additional consideration on the possible phase error in the calculation has been included.

QFQD : The systematic errors of QFQD in 1993 were found from the differences in the mean centre-of-mass energies before and after the QFQD was included in the energy model.

Energy Cal. : The error on energy calibration measurement in 1993 is exactly what actually is used for 1995.

e^+ measurement : The positron energy uncertainty has been explained in section 6.3.5.

RF : RF correction was analyzed with a simpler RF model in 1993 which does not have the complication of bunch train families and so the errors are slightly smaller than those in 1995.

The above results formed the basis of the LEP energy measurement contributing to the precision determination of Z^0 resonance parameters before the 1995 scan took place, as shown in Table 6.1. The errors claimed as above are now believed to be underestimated, mainly because of the ignorance of the beampipe current driven energy rise during a fill at that time.

Note that only those items in **boldface** in Table 9.6 are still valid now and they are used again in the evaluation of the total systematic errors for the 1993 centre-of-mass energies at different energy points in the new analysis. The other items are revised taking into account all new knowledges we have gained in 1995 scan. In addition, systematic errors due to the new effects discovered in 1995 scan are also added.

Adaptation the new model to 1993 scan

The modelling of the energy rise during a fill must be included in the 1993 and 1994 analyses as the effect was almost certainly present in these years. Lack of any NMR in the LEP tunnel during those years was the major reason that we did not see such an effect before the 1995 scan. This also means that we have to rely on the energy rise model derived from the 1995 energy scan for those years.

However, there did exist calibration experiments in these years, which, when interpreted in the light of the 1995 experience, gives confidence that the rise term was indeed present and of the same magnitude as observed in the 1995 scan.

The most significant experiment was during a machine development of almost 24 hours in the fill 1772 in 1993, in which a long series of depolarization measurements were made with the aim of determining the temperature coefficient C_T^{ring}. This experiment was not well understood before the 1995 scan. Reinterpreted with hindsight from the 1995 scan, the data are now consistent with a beampipe current driven rise of the same rate as in 1995 and with essentially the same C_T^{ring} as determined independently in the other temperature experiments [32].

The other tide and temperature experiments before 1995 were either too short to show a substantial rise, or performed many hours after the magnets had been ramped to 45 GeV which is equivalent to the period of physics collisions for so many hours in term of magnet condition. In the latter case, the energy rise would have reached its plateau and therefore no rise was present to be observed.

With the benefit of these hindsights, and the fact that the electric trains (which contributes mostly to the origin of beampipe current resulting in beam energy rise in a fill) were also running before 1995, it is reasonable to assume that the same energy model used for 1995 scan can be applied for the 1993 and 1994 scans. The treatment on the systematic errors from various sources is also the same in principle,

however larger systematic errors have been assigned as it cannot be assumed that the conditions were identical prior to 1995. Moreover, since the author has mainly concentrated on the evaluation of systematic errors for 1995, but not for 1993, only a couple of points on systematic errors in the 1993 scan will be made here.

Energy rise The uncertainties on the absolute rise of beam energy during a fill were checked against the new energy model. Seven 1993 fills, with more than one energy calibration performed at large time intervals, have been used to examine the energy rise. As a result, an error of 2 MeV was assigned for this source in 1993. Since there were no NMR48 data in 1993 and 1994, the other uncertainties on the energy rise due to the variations among different models estimated for 1995, which will be described in the next section, were taken to be the same for 1993.

Corrector As for 1995, it is unknown whether the difference in corrector settings between physics and calibration operation implies a change in dipole field which should be accounted for in the normalization of the model to the calibration points. No correction due to corrector (see section 8.4) is yet made in the new energy model for 1993 LEP energies [7]. So, the full effect from the corrector on the mean centre-of-mass energies at different energy points is taken as the error for this new analysis in 1993 scan. This source of error is estimated to be about 1.54 MeV in the whole 1993 scan.

9.8 Systematic studies in 1995

The systematic error on the peak energy is not as important as the off-peak ones because M_Z and Γ_Z are insensitive to the values and errors of peak energies. The same information and method are used to determine the systematic error on the peak energy. Less effort has been put to reduce the uncertainty on the peak energy during the scan. Indeed, the peak energy in only one fill was calibrated in the 1993 or 1995 scan. This results in a larger error on the peak energies in general. The following will concentrate on explaining the calculation of the off-peak errors.

[7] This was due to the practical problem that the corrector data for 1993 had to be recovered and was available only a few days before the Warsaw conference in 1996.

The luminosity-weighted energies at the IP's are affected by systematic errors inherent to the calibration measurement by depolarization and various corrections in the energy model. The energies of the calibrated fills were precisely measured at the ends of fills, using resonant depolarization. Here, systematic errors arise only to the extent that these energy measurements are not representative of the conditions earlier in the fills, during physics running. Any systematic difference between calibration and physics conditions must be corrected for and can lead to a systematic error. The correction for a quantity, X, whose variation can change the energy, is :

$$\Delta E = \alpha_X \cdot (< X_{phys} > - < X_{cal} >) \tag{9.9}$$

where $< X_{phys} >$ is the luminosity-weighted average of the quantity X, $< X_{cal} >$ is the average of the same quantity at the time of calibrations and α_X is the correction coefficient. Systematic error arises from the uncertainty of the coefficient α_X.

The mean energies of the uncalibrated fills are estimated from the calibrated ones on a statistical basis and additional systematic errors arise from the precision in evaluating this mean energy using the calibration measurements.

To a good approximation, the systematic errors on $\mathrm{M_Z}$ and Γ_Z arising from the LEP energy calibration are related to the energy errors by the following equations :

$$\Delta \mathrm{M_Z} \approx 0.5\Delta(E_{P+2} + E_{P-2}) \tag{9.10}$$

$$\Delta\Gamma_\mathrm{Z} \approx \frac{\Gamma_\mathrm{Z}}{E_{P+2} - E_{P-2}}\Delta(E_{P+2} - E_{P-2}) = 0.71\Delta(E_{P+2} - E_{P-2}) \tag{9.11}$$

The various contributions to the systematic error on the off-peak energies are discussed in the following and are summarized in Table 9.7. In general, the 'centre-of-mass energy' is assumed whenever 'energy' is mentioned in this section. The following preliminary result on the LEP energy scan in 1995 is what has been used by the LEP experiments for the summer conferences in 1996. The values are luminosity weighted, using results from the ALEPH experiment.

Mean fill energy Comparison between the energy model and calibration measurements was shown in Fig. 9.9. The RMS scatters, σ_{cal}, are respectively 4.4 MeV

Source	Peak-2	Peak+2	Correlation	ΔM_Z	$\Delta\Gamma_Z$
Mean fill energy	0.55	0.43	0.00	0.35	0.49
Ring Temperature	0.06	0.17	1.00	0.12	0.08
Energy Cal.	0.50	0.50	0.04	0.36	0.49
e^+ measurement	0.25	0.25	0.50	0.22	0.18
Tide (amplitude)	0.11	0.04	1.00	0.08	0.05
Tide (phase)	0.45	0.10	1.00	0.28	0.25
Rise term (scatter)	1.00	1.00	0.65	0.91	0.59
Rise term (model)	0.21	0.53	1.00	0.37	0.22
NMR48 (model)	0.22	0.83	0.50	0.48	0.52
Corrector	0.41	1.55	0.00	0.80	1.13
RF	0.58	0.58	0.63	0.52	0.35
OSVD	0.37	0.37	0.46	0.32	0.27
Total				1.61	1.65

Table 9.7: Systematic errors on the centre-of-mass energies (in MeV) in 1995 due to various corrections and their contributions towards the M_Z and Γ_Z.

and 3.0 MeV for the centre-of-mass energies of the P+2 and P−2 fills. Assuming all fills have equal luminosity, the error on the mean energy of all fills is [23] :

$$\Delta E_{CM}^{scat} = \frac{\sigma_{cal}\sqrt{N_{uncal}}}{\sqrt{N_{total}}\sqrt{N_{cal}}} \tag{9.12}$$

where N_{total} is the total number of fills, N_{cal} / N_{uncal} represent the number of calibrated / uncalibrated fills respectively. In reality, a more precise method has been used to calculate this error [55], which takes into account the fact that luminosities were different from fill to fill. The result gives errors of 0.55 and 0.43 MeV in E_{CM} for the P−2 and P+2 datasets, respectively. The peak point has a larger error of 3.7 MeV (which was computed using the combined RMS scatter from all calibrations in the same year) because there was only one resonant depolarization calibration at peak point.

The errors from this source in 1995 are significantly smaller than those in 1993 because a larger fraction of off-peak luminosity in 1995 have been calibrated.

Ring Temperature An uncertainty of 50% on the ring temperature coefficient C_T^{ring} translates into 0.06 and 0.17 MeV in the centre-of-mass energy at P−2 and P+2. The errors are fully correlated between energy points.

Energy Calibration The same systematic error in 1993, due to the uncertainty on the systematic differences between the conditions of LEP at the time of

calibration measurements and those during physics running, is assigned to 1995, i.e. 0.5 MeV [23]. A correlation of 4% is assigned due to the error on the electron mass.

e^+ measurement Since the calibrations were made using only the e^- beam, any unknown systematic energy difference between electron and e^+ beams would create a systematic error. The energies of the two beams are considered to be fully correlated and a systematic error of 0.25 MeV is assigned to their difference in 1995 [54]. As it is not known whether P+2 and P−2 points have identical differences, a correlation of 50% is assigned such that the systematic errors are distributed to M_Z and Γ_Z equally.

Tide correction An uncertainty of 10% on the coefficient κ_{tide} in the tide correlation (section 6.3.4) introduces errors of 0.11 and 0.04 MeV at P−2 and P+2. It also turns out that the fills were distributed in 1995 such that the errors between energy points are fully correlated, i.e., error in κ_{tide} gives energy shift of the same sign.

Besides the uncertainty on the amplitude of the tide correction, there is also an uncertainty on the phase of the tide calculation due to possible lapse in the synchronization among various databases. A conservative uncertainty of 15 minutes on the time of synchronization was introduced in the program for calculating the energies which gave rise to errors of 0.45 and 0.10 MeV at P−2 and P+2, again with full correlation.

Rise Term The uncertainty on the absolute energy rise during a fill gives an error on M_Z while the uncertainty on whether this rise is the same at P−2 and P+2 also translates into an error on Γ_Z. Our knowledge of the absolute rise comes from the BOF/EOF experiments and the result of the comparison was summarized in Fig. 9.8. Since each fill is of different duration, a weight corresponding to the length of each fill is used to calculate the statistical error on the absolute energy rise of the model. This procedure gives an error of 1 MeV on the knowledge of the energy rise.

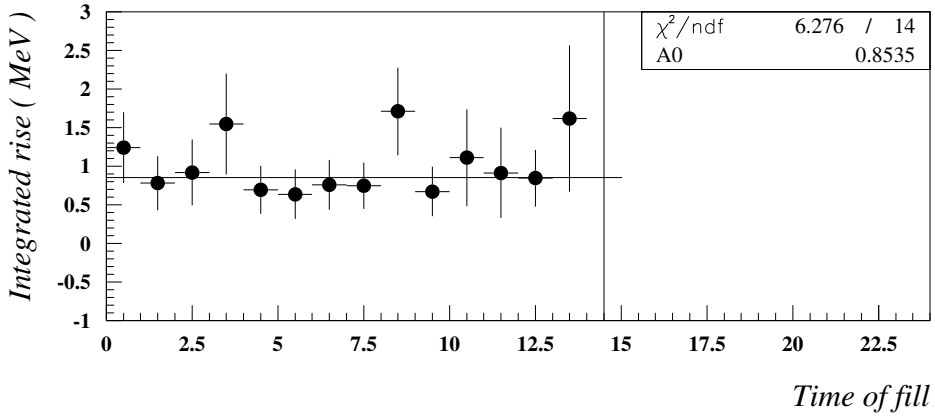
To what degree the rise term has the same magnitude and shape at P−2 and P+2 can be quantified from the NMR data. Fig. 9.11 shows the ratios of beam

energy rise (in terms of NMR48) at P−2 and P+2 against the time of fill and time of day. It shows evidence of some differences in the beam rises at P−2 and P+2. A conservative estimate of the correlation coefficient between the errors at P−2 and P+2 of 0.65 is assigned. Another independent analysis [56] has indicated that this error induced on Γ_Z should be 0.6 MeV, which is approximately equivalent to the assignment of the correlation coefficient above.

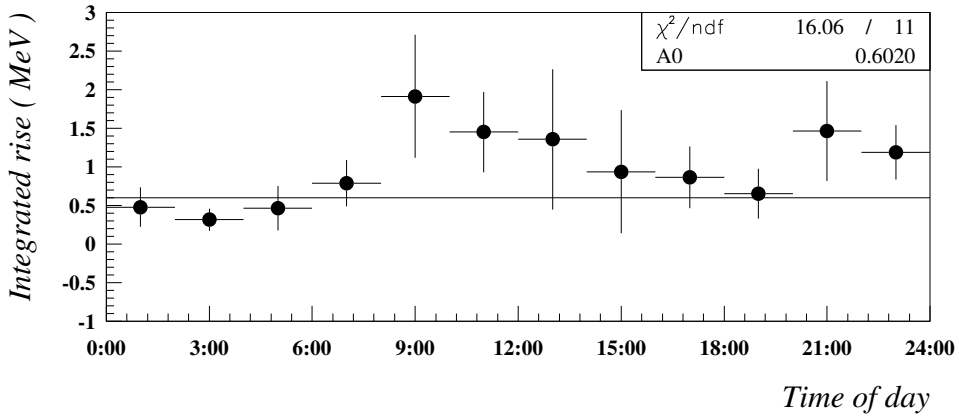
As discussed in section 9.5, there are considerable differences in various models in the treatment of the energy rise in a fill, especially in the behaviour of the energy rise for the fill of a longer length of time. Fortunately, for 1995 scan, the mean time length of fills at P-2 is almost the same as that at P+2 — about 10 hours during the scan. This modelling difference is 'absorbed' by the normalization factor C_{norm} which calibrates the model (NMR48) with respect to the depolarization measurements. Consequently, either using NMR48 data or the depolarization data gives a similar result on the mean centre-of-mass energy in 1995.

The difference between the mean energies obtained with fitted NMR48 model and fitted depolarization model (which is the largest) was taken as a modelling error. These differences, 0.21 and 0.53 MeV at P−2 and P+2 respectively, are not the same at different energy points and therefore the uncertainty affects both M_Z and Γ_Z.

NMR48 model Small additional modelling errors were assigned to account for the variations observed when different assumptions were used in constructing the NMR based model (which uses the data from both NMROCT4 and NMROCT8) . This includes the uncertainty of the temperature coefficient C_T^{48} (see section 9.2) which are 0.22 and 0.79 MeV at P-2 and P+2 respectively, and that from modelling the bending modulation jumps (see section 8.3) which are 0.04 and 0.24 MeV respectively at P-2 and P+2. These uncertainties result in total systematic errors of 0.22 MeV at P-2 and 0.83 MeV at P+2. A correlation coefficient of 0.5 is conservatively taken between errors of different energies, which results in equal share of the errors on M_Z and Γ_Z.



(a) Ratio of average beam rises in fills at two off-peak energies.



(b) Ratio of average beam rises vs time of day at two off-peak energies.

Figure 9.11: Comparison of NMR48 rises at P−2 and P+2. (a) The ratio of NMR48 rises at P−2 and P+2 vs time of fill. (b) The ratio of NMR48 rises at P−2 and P+2 vs time of day. In both cases, a cut requiring that the difference between successive readings < 5 MeV is applied, and the rise here is per beam.

Correction due to correctors Until the effect of correctors on the beam energy is empirically studied in a dedicated experiment, a systematic error must be assigned to account for this uncertainty. This was done, taking as the scale of the effect that indicated by simulation. Half of the effect was included in the central values and half assigned as an error. The error due to this correction is much larger in P+2 (1.55 MeV) than in P−2 (0.41 MeV) and the correlation

between different energies is negligible.

RF correction A detailed RF systematic study of errors on the LEP centre-of-mass energies at the four IP's can be found in [50]. The errors are mainly due to uncertainties of the parameters needed in the RF model calculation, such as alignments of RF cavities and path differences between IP's. Approximately one-third of the records used in 1995 contain at least one interpolated value. A systematic error based on the quality of this data is included in the final set of errors. The numbers quoted in Table 9.7 are the averages over experiments at LEP [8].

OSVD correction A detailed study of systematic errors due to the OSVD effect on LEP energies can be found in [46]. The numbers shown in Table 9.7 are again the averages over experiments at LEP. These systematic errors turn out to be quite small and this indicates the success of the Vernier scan programme in coping with this potentially troublesome source of uncertainty.

Summing up all these items of systematic errors, the uncertainties of the centre-of-mass energies result in total errors about 1.61 MeV on M_Z and 1.65 MeV on Γ_Z in the 1995 scan, Table 9.7.

Checks have been done to see how large the effects would be if certain corrections were left out. Table 9.8 shows the energy shifts with respect to the standard strategy if we re-run the complete chain of the program producing LEP energies with certain correction terms switched off. These figures give us an idea how sensitive the energy

strategy	Peak - 2	Peak + 2
no ring temperature correction	-0.26	-0.50
no tide correction	1.34	0.33
no BOM correction	-0.83	1.47
no rise term	4.73	4.92
no Corrector correction	0.41	1.55

Table 9.8: Energy shifts in E_{CM} (MeV) with respect to the standard strategy after switching off certain corrections in our energy model.

[8] The contribution from the OPAL experiment (IP6) was excluded in the calculation of the preliminary result for the summer conferences, as OPAL presented no preliminary results from the 1995 scan.

model is to the presence of various corrections.

Taking away the temperature correction for the dipole magnets in the LEP ring and the tide correction, the shifts in energy are about 4 and 10 times as much as the corresponding errors shown in Table 9.7. This is well explained by the 25% and 10% errors assigned for the ring and tide corrections.

The BOM measurements of the relative transverse orbit position have no identified additional systematic error. This is because their scale factor is well understood both from theory and from measurement. Any fluctuation due to the finite reproducibility of the BOM system is automatically included in the scatter calculation.

It is also not surprising to see that the presence of the beam energy rise term during a fill does give a very large change to the overall centre-of-mass energies. This reflects the fact that the average rise in E_{CM} during a fill is about 5 MeV.

9.9 Energy Files and Error Covariance Matrix

Before the 1996 summer conferences, two sets of preliminary energy files with all corrections at all four IP's were made, including the set [9] from the author for 1995. These energy files contained the centre-of-mass energies at every 15 minutes during the time when physics collisions happened during the scan. The files also contained the IP-dependent corrections (also at every 15 minutes) from which different experiments can extract the appropriate centre-of-mass energies at their IP's.

Studies were made to check whether the two set of files in 1995 were the same and to find out the reasons for any discrepancies. Eventually, after discovering some bugs and subtle modelling differences, the centre-of-mass energies produced in the two sets were essentially identical. There were some differences in the IP-dependent corrections. This is because there existed more than one model to calculate the IP-dependent corrections and also some technical differences in interpolation between different times. However, these differences were negligible.

The energy files for the 1993, 1994 and 1995 scans were then given to the four experiments for calculating the centre-of-mass energies in the measurements of cross-sections and asymmetries, just in time for the Warsaw conference in 1996.

[9] Another set of energy files was made by M. Koratzinos.

The exact calculation of the errors on M_Z and Γ_Z must be made from the covariance matrix of energy errors, as the RF and OSVD corrections involve differences between the experiments. All other terms are identical from experiment to experiment. The preliminary covariance matrix, which held the correlations between the P-2, P and P+2 in 1993 and 1995, to use (for the summer conferences in 1996) when averaging the results of the four experiments is given in Table 9.9

	93 P–2	**93 P**	**93 P+2**	**95 P–2**	**95 P**	**95 P+2**
93 P–2	8.4	4.4	4.3	0.4	0.0	0.0
93 P	4.4	40.0	6.9	0.1	1.7	0.7
93 P+2	4.3	6.9	9.4	0.1	1.4	1.3
95 P–2	0.4	0.1	0.1	2.6	1.4	1.2
95 P	0.0	1.7	1.4	1.4	22.2	2.1
95 P+2	0.0	0.7	1.3	1.2	2.1	5.4

Table 9.9: Energy common error matrix for the scan points of 1993 and 1995. The values are for collision energy in units of $(\mathrm{MeV})^2$.

This matrix was given to the Electroweak working group to use for averaging the results of the measurements of Z^0 resonance parameters from the four experiments, taking account the correlations between different experiments.

Using a simple approximation method based on equations 9.10 and 9.11, the total errors in the 1993 and 1995 energy scans due to the uncertainty in the absolute LEP energy scale are about 1.6 MeV on M_Z and 1.5 MeV on Γ_Z.

A more complete method used by the LEP Electroweak working group, which used 93–95 hadronic cross-sections of all four LEP experiments and took into account the correlations of the experimental errors between years in different experiments (such as those due to the luminosity measurements), showed that the LEP energy uncertainty gives rise to about 1.5 MeV on M_Z and and 1.7 MeV on Γ_Z [57].

9.10 Energy spread

A brief description of the energy spread is given here and the details can be found in [58].

Because of the emission of synchrotron radiation, there is finite spread on the LEP beam energy. The beam energy spread gives rise to a shift of the effective cross-section at each energy point with respect to the cross-section if the beam energy is

monochromatic, and this has to be corrected for in the cross-section measurements. The effect of the OSVD in the bunch train scheme gives a little more complication in the energy spread analysis, as explained below.

The beam energy spread $\sigma_{E_{beam}}$ is related to the observed longitudinal size of the interaction region σ_z through the following formula [10] :

$$\sigma_{E_{beam}} = \frac{\sqrt{2}E_{beam}}{\alpha_c R_{LEP}} \times Q_s \times \sigma_z \tag{9.13}$$

where E_{beam} is the beam energy, α_c is momentum compaction factor, R_{LEP} is the LEP bending radius, Q_s is the synchrotron tune and σ_z is the RMS of the longitudinal event vertex distribution observed in an experiment [11]

Note that the bunch length can be observed most precisely from the RMS scatter of positions of reconstructed Z decays in the experimental detectors. Studies done [60] have shown the expected effects on bunch length from changes in Q_s and from the use of wigglers early in the fill. For several fills (before 1995), these studies have been confirmed by a direct measurement of the bunch length using a streak camera [61].

The centre-of-mass energy spread $\sigma_{E_{CM}}$ is related to the beam energy spread $\sigma_{E_{beam}}$ by :

$$\sigma_{E_{CM}} = \sqrt{2} \cdot C \cdot \sigma_{E_{beam}} \ , \ (0 \leq C \leq 1) \ . \tag{9.14}$$

This is mainly because the colliding electrons and positrons have arbitrary energy distributions. Before 1995, colliding beams have no or identical energy dispersions,

---

[10] A simple derivation is as follows :
The spread of time displacement σ_τ due to energy oscillations is [59] :

$$\sigma_\tau = \frac{\alpha_c \sigma_E}{\omega E}$$

which is has the same format as equation 6.9; α_c is the momentum compaction factor and ω is the angular frequency of energy oscillation.
By definition,

$$\begin{aligned} \sigma_l &= v_b \times \sigma_\tau \\ Q_s &= \frac{\omega R}{v_b} \end{aligned}$$

where σ_l in our case is the bunch length and v_b is the speed of the beam. With little manipulation, we therefore have

$$\sigma_{E_{beam}} = \frac{E_{beam}}{\alpha_c R} \times Q_s \times \sigma_l \ .$$

Finally, converting the uncertainty in bunch length σ_l to the uncertainty in longitudinal position, we need an extra factor of $\sqrt{2}$ which explains the above equation.

[11] ALEPH's data were used in the analysis of energy spread by E. Lancon.

the monochromatization factor C is approximately equal to 1 [48]. However, due to the introduction of bunch train scheme in 1995, this is no longer the case.

The main uncertainty on $\sigma_{E_{beam}}$ comes from the definition of Q_s. Equation 9.14 is written in terms of the incoherent Q_s^{inc}, for example, that of individual particles. Collective effects modify the Q_s value. Only the coherent value Q_s^{coh} is measured regularly.

A determination of Q_s^{inc} was obtained by accurate determination of the Q_s side band of the depolarizing resonance during an energy calibration [12]. Parameterizing the relation between Q_s^{coh} and Q_s^{inc} as $\frac{Q_s^{coh}}{Q_s^{inc}} = 1 - \kappa \frac{I}{I_0}$ (where I is the bunch current), the measurement yielded $\kappa = 0.044 \pm 0.022$, for $I_0 = 300$ μA. This value of κ was used to compare the 1995 beam energy spread as determined through equation 9.14 to a model based on the energy loss around the ring [13]. Data and model agreed using the above measured value of κ.

In the presence of opposite sign energy dispersion between electrons and positrons, $\sigma_{E_{CM}}$ can be less than $\sqrt{2} \cdot \sigma_{E_{beam}}$ [48]. The energy dispersion for the 1993 and 1994 pretzel running has been evaluated [62] and the reduction on the centre-of-mass energy spread is estimated to be less than 0.2%. The dispersion in 1995 due to bunch train bumps leads to a rather significant monochromatization and gives a correction of about 2% on $\sigma_{E_{CM}}$, with an IP dependence [46].

The LEP centre-of-mass energy spread is given in Table 9.10 for different energy points in 1993 and 1995. The error on the energy spread (dominated by the uncertainty on κ) for 1993 and 1994 is 1.1 MeV while this error is increased to 1.3 MeV for 1995 due to beam dispersion. These numbers are fully correlated between experiments.

	1993	1995			
		IP2	IP4	IP6	IP8
P−2	54.6	55.0	55.7	55.7	55.7
P	55.4	55.6	56.2	56.2	56.3
P+2	55.6	56.0	56.6	56.7	56.7

Table 9.10: Centre-of-mass energy spread (in MeV) in 1995.

[12] The experiment was carried out on 2nd September, 1995.
[13] The model was due to J. M. Jowett, in SL division, CERN.

The beam spread information is used as a correction on the absolute Z^0 cross-section measurement. The above error on beam energy spread attained from this new analysis represent a fourfold increase in precision over previous evaluations (which was of 5 MeV). This now contributes negligible error to Γ_Z.

The beam spreads at different IP's were given to the four experiments and were used to correct for the measured cross-sections due to the beam spread effect at different energy points. Table 5.5 in section 5.1 is the result of this application.

9.11 Conclusion

The decision that LEP could in fact scan in 1995 was not taken until the summer that year. At the end, although the 1995 scan did not yield as much luminosity as was hoped for, similar statistics to 1993 were accumulated and valuable knowledge concerning the LEP dipole behaviour was gained. The preliminary analysis of the 1995 LEP energy scan already allows the collision energy to be determined with good precision, as compared with the statistical error from the experiments in the measurements of M_Z and Γ_Z.

Of particular importance in the analysis is the modelling of the energy rise in the course of a fill. We now understand that, because the energy rise in a fill was not accounted for, the mass of the Z^0, M_Z, in 1993 was overestimated. Without an energy scan in 1995, this mistake on a fundamental parameter of the Standard Model would probably have remained uncorrected.

It is possible that the understanding of the energy rise will improve as a result of future experimental data. These data will come from the ongoing testbench studies of a LEP dipole and from additional calibration experiments and NMR data in the present run (1996). The latter will be particularly interesting as, in addition to the 2 NMR's of 1995, 16 new devices have been installed. This will help examine whether NMROCT4 and NMROCT8 have shown typical behaviour in the LEP tunnel. Moreover, dedicated experiments scheduled for the present run will also show whether the effect of the corrector magnets on the beam energy is as predicted by simulation. At the time of writing this thesis, the author cannot benefit from these studies as they have not been completed.

The preliminary analysis of the IP specific corrections in 1995 gives small errors. At one point, the potentially dominant systematic error due to the effect of OSVD

had called into question the feasibility of the 1995 energy scan. The Vernier scan has been a very successful tool in minimizing the potentially large energy shifts arising from the bunch train induced vertical beam dispersion, and the associated error is one of the smallest in the whole list of systematic errors (Table 9.7). RF corrections have been complicated by the introduction of superconducting cavities and the bunch train scheme. Again, the uncertainty seems to be controlled finally.

The discovery of the tide effect to that of the water level of Lake Leman and finally the "train effect" in 1995 are not just entertaining stories but a beautiful chapter of machine physics written by LEP (especially every time there is an energy scan), which is not yet fully closed.

Chapter 10

Discussion of Results

10.1 Comparison between the results from the inclusive and identified leptonic analyses

A comparison between the results of the cross-sections and forward-backward asymmetries of this inclusive analysis, which has been described in earlier chapters, and the lepton-identified analyses done by 3 leptonic teams (namely, electron, muon and tau) in DELPHI was made for the year 1993. [1] The results used for the lepton-identified analyses are the ones presented by the DELPHI collaboration at the International Conference on High Energy Physics (ICHEP) in Warsaw (1996).

The data set (from which the lepton candidates were selected) used in this inclusive (flavour-independent) analysis is the same as that used by the individual lepton-identified analysis teams. Event lists of electrons, muons and taus selected for the lepton-identified analyses were compared with the event list for this inclusive analysis. It was found that the overlap of events is about 80% (in the barrel region), which shows a good coherence in the selection process though different methods have been applied. The residual difference in the selected sample of events is due to the different angular acceptances and different experimental cuts. Especially, different detectors may be used in one analysis but not in another. For example, electrons/positrons might be selected based on the shape of their energy clusters in the HPC, even if there was no track reconstructed in the TPC, which would be rejected in our inclusive leptonic analysis.

[1] At the time of writing this thesis, the individual identified leptonic analyses (noticeably, the tau analysis) of cross-sections and asymmetries in 1994 are not all ready for comparison.

Cross-section comparison

The comparison is expressed in the form of the ratio of the average cross-section of lepton-identified analyses to the cross-section of the inclusive leptonic analysis at each energy point.

A few points are worth noting here :

- Since the cross-sections given by individual teams are not corrected for the different angular acceptances and the experimental cuts such as momentum and acollinearity, the values of cross-sections from individual analyses were corrected to full solid angle and the condition of no experimental cuts by ZFITTER, before making the comparison.

- The two types of analyses have a substantially overlapped portion of data (about 80%) and the statistical errors are obviously correlated. To give a more meaningful comparison, this part of correlated statistical error is taken out from the final error on the ratio of the two sets of cross-sections.

- The weighted average of the cross-sections of 3 different leptonic channels in the lepton-identified analyses is used to be compared with the cross-section of the inclusive leptonic analysis.

The ratio between the cross-sections from the two types of analyses at each energy point in 1993 is shown in Table 10.1. The agreement is fairly good in general. It is a bit worse at P-2. This is due to the fact that the cross-section from the tau analysis at P-2 is about 2 to 3 standard deviations lower than those of the other identified analyses and also the inclusive analysis.

Forward-backward asymmetry comparison

A similar approach has been used to test the agreement in forward-backward asymmetries between the two types of analyses. Instead of the ratios used in the cross-section comparison, the difference between the two types of analyses at each energy point was evaluated. The fraction of common events in both samples of events of the two analyses is essentially the same as above. The results are also shown in Table 10.1.

Collision energy	Cross-section ratios identified/inclusive	Asymmetry differences identified - inclusive
PS	1.0017 ± 0.0063	0.0074 ± 0.0118
P-2	0.9833 ± 0.0075	0.0133 ± 0.0140
P	0.9918 ± 0.0056	-0.0008 ± 0.0082
P+2	0.9941 ± 0.0066	0.0077 ± 0.0132

Table 10.1: Comparison of the inclusive lepton cross-sections and forward-backward asymmetries with the weighted averages of the lepton-identified results in 1993. The errors shown include the systematic plus uncorrelated statistical errors.

10.2 Standard Model Fit

The measurements of cross-sections and asymmetries are sensitive to various Z^0 resonance parameters or observables in the Standard Model. One can therefore extract the parameters by fitting the experimental cross-section lineshape and asymmetries against the theoretical predictions.

Apart from the leptonic results from the inclusive analysis, the DELPHI results of hadronic cross-sections are also used in the following fits. The hadronic cross-sections of the Z^0 is almost 7 times that of the inclusive leptonic cross-sections. Only by inclusion of the much greater hadronic data would the fitting procedure give a competitive accuracy.

ZFITTER (Version 5.0) was used to calculate a theoretical curve, which was then fitted to the data using the CERN standard minimization package, MINUIT[63], using a χ^2 minimization procedure. The parameters to be fitted were treated as free parameters by the program. The cross-sections were re-calculated by varying the free parameters until a best fit was found.

10.2.1 5-parameter fit

Assuming lepton universality, a standard set of 5 parameters is chosen to describe the information contained in hadronic and leptonic cross-sections and leptonic forward-backward asymmetries. These parameters are chosen because they are convenient for fitting and averaging due to their small correlations. The parameters are :

- M_Z, the mass of the Z^0 boson;

- Γ_Z, the total width for the decay of Z^0;
- σ_h^0, the hadronic peak cross-section of Z^0 decays :

$$\sigma_h^0 \equiv \frac{12\pi\,\Gamma_e\Gamma_{had}}{M_Z{}^2\,\Gamma_Z{}^2} \quad ; \tag{10.1}$$

- R_l, which is defined as

$$R_l \equiv \Gamma_{had}/\Gamma_l \tag{10.2}$$

  where Γ_{had} and Γ_l represent respectively the partial Z^0 widths for the decays into (massless) leptons and hadrons;

- $A_{FB}^{0,l}$, the forward-backward asymmetry for the leptonic Z^0 decays at peak, which is just as defined in equation 1.23.

The result of the 5-parameter fit is shown in Table 10.2 and the correlations between the 5 parameters are shown in Table 10.3. The data used for 1993 and 1994 included the results from this inclusive leptonic analysis and the DELPHI hadronic cross-sections. For 1995, only the hadronic cross-sections have been used. The DELPHI results were those presented for the ICHEP in Warsaw, 1996.

Parameter	Including 1995	excluding 1995
M_Z (GeV)	91.1854 ± 0.0030	91.1816 ± 0.0042
Γ_Z (GeV)	2.4895 ± 0.0045	2.4868 ± 0.0062
σ_h^0(nb)	41.592 ± 0.080	41.559 ± 0.084
R_l	20.616 ± 0.085	20.608 ± 0.086
$A_{FB}^{0,l}$	0.0139 ± 0.0034	0.0136 ± 0.0034
χ^2 / d.o.f.	17/14	14/10

Table 10.2: The results of the 5-parameter fit for the inclusive lepton data and the hadronic data. The second column shows the fit results when 95 hadronic cross-section was included for the fitting; while the third column shows the fit results when only 93 and 94 data were used.

The errors shown above included all the statistical and systematic errors in the experimental measurements. Apart from those in the analyses of the cross-sections and asymmetries, the errors from the LEP energy and the DELPHI luminosity measurements have also been included in the form of correlation matrices. The LEP energy errors and the corresponding correlation matrix are provided by the LEP Energy working group which has been described in detail in the previous chapters. The

Parameter	M_Z	Γ_Z	σ_h^0	R_l	$A_{FB}^{0,l}$
M_Z	1.000	0.099	-0.043	-0.062	0.061
Γ_Z	0.099	1.000	-0.267	-0.044	-0.010
σ_h^0	-0.043	-0.267	1.000	0.172	0.004
R_l	-0.062	-0.044	0.172	1.000	0.015
$A_{FB}^{0,l}$	0.061	-0.010	0.004	0.015	1.000

Table 10.3: The covariance matrix for the set of 5 parameters given in Table 10.2 in which the 1995 hadronic cross-section data have also been used.

luminosity errors and the correlation matrix were given by the DELPHI luminosity team [19].

From Table 10.2, one can see that by including the 1995 energy scan cross-section information, there is significant improvement in the precision of the measurements of M_Z and Γ_Z. This exemplifies the significance of the 1995 scan in the contribution to the precision determination of Z^0 resonance parameters and thus the stringent test of the Standard Model.

10.2.2 Derived parameters

By applying certain transformations to the above fitted results, one may also obtain the other Z^0 resonance parameters which can be derived from the previous 5 parameters based on equations 1.23, 10.1 10.2 and other parameters in the scheme of the Improved Born Approximation defined in section 1.8. The important ones are shown in Table 10.4.

Parameter	including 1995	excluding 1995
Γ_l (MeV)	84.16 ± 0.23	84.05 ± 0.26
Γ_{had} (MeV)	1735.0 ± 4.9	1732.0 ± 5.8
Γ_{inv} (MeV)	502.3 ± 4.1	502.9 ± 4.3
Γ_{inv}/Γ_l	5.968 ± 0.040	5.984 ± 0.042
$\bar{a}_f$	0.2521 ± 0.0007	0.2518 ± 0.0008
$\bar{v}_f$	$(1.18 \pm 0.29) \times 10^{-3}$	$(1.15 \pm 0.29) \times 10^{-3}$

Table 10.4: The derived Z^0 resonance parameters derived from the 5-parameter fit shown in Table 10.2.

Number of neutrino species

Γ_{inv} stands for the partial width for Z^0 decaying into invisible final states (neutrinos). Its relationship with other partial widths and the total Z^0 decay width

is :

$$\Gamma_{\rm inv} = \Gamma_{\rm Z} - \Gamma_{\rm had} - 3\,\Gamma_{\rm l} \tag{10.3}$$

An important aspect of our measurement concerns the information related to Z^0 decays into invisible channels. The fitted results of $\Gamma_{\rm l}$ and $\Gamma_{\rm inv}$ can be converted into the number of light neutrino species N_ν since

$$\begin{aligned} N_\nu &= \frac{\Gamma_{\rm inv}}{\Gamma_\nu} \\ &= \frac{\Gamma_{\rm inv}}{\Gamma_{\rm l}} \times \left(\frac{\Gamma_{\rm l}}{\Gamma_\nu}\right)^{\rm SM} \end{aligned} \tag{10.4}$$

$(\Gamma_{\rm l}/\Gamma_\nu)^{\rm SM}$ in the above equation is the Standard Model value for the ratio of the partial widths $\Gamma_{\rm l}/\Gamma_\nu$, which is [57]

$$\left(\frac{\Gamma_{\rm l}}{\Gamma_\nu}\right)^{\rm SM} = 1.991 \pm 0.001 \ . \tag{10.5}$$

Substituting the above value and the value of $\Gamma_{\rm inv}/\Gamma_{\rm l}$ in Table 10.4 (the one obtained including 1995 hadronic data) into the equation 10.4, the number of neutrino species is thus determined to be

$$N_\nu = 2.997 \pm 0.020 \ . \tag{10.6}$$

Sensitivity to $\Gamma_{\rm l}$

The inclusive leptonic analysis has the most contribution in extracting the value of $\Gamma_{\rm l}$ (or R_l), because the other parameters are predominantly dictated by the data of hadronic cross-sections which contain far more statistics than the corresponding leptonic data. However, $\Gamma_{\rm l}$ or R_l can only be determined in the presence of leptonic data. $\Gamma_{\rm l}$ is very sensitive to the value of the masses of top quark ($\rm m_t$) and Higgs Boson ($\rm M_H$) but is comparatively insensitive to QCD corrections. Figure 10.1 shows the behaviour of $\Gamma_{\rm l}$ as a function of the mass of top quark, $\rm m_t$ and also its dependence on the mass of the Higgs Boson, $\rm M_H$. This also gives us an idea of the sensitivity of $\Gamma_{\rm l}$ to $\rm m_t$ and $\rm M_H$. The measurement of $\Gamma_{\rm l}$ from this analysis is compatible with both the Standard Model and the direct measurement of $\rm m_t$ [64].

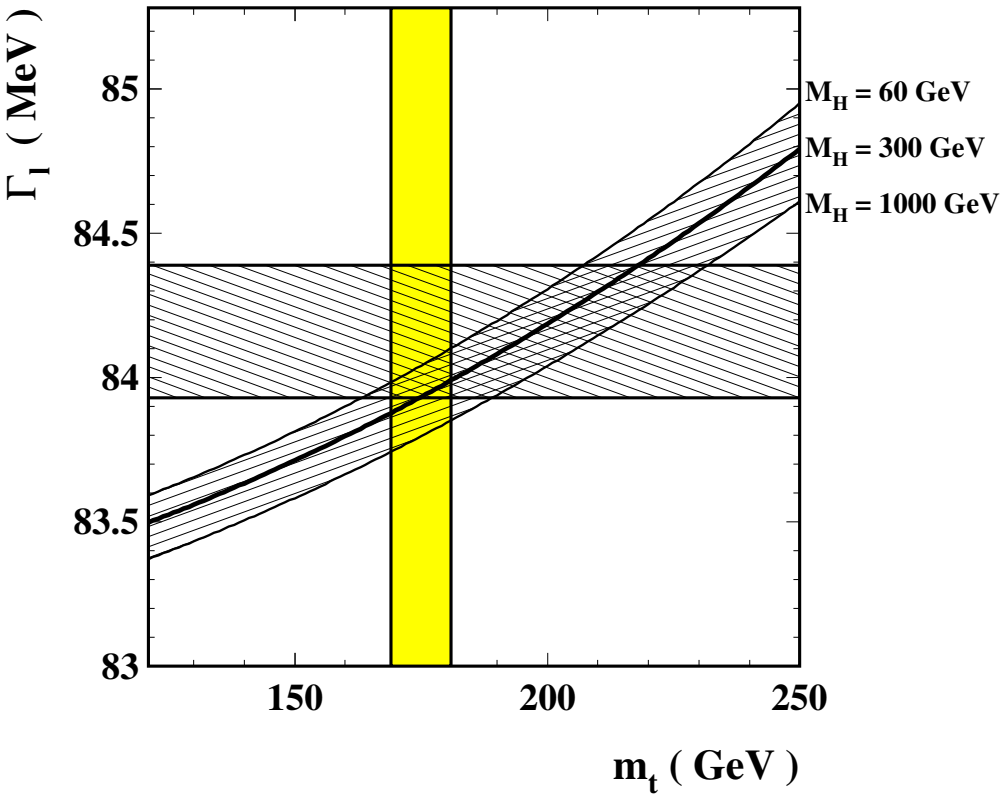


Figure 10.1: Comparison of Γ_l measurement with the Standard Model prediction as a function of m_t. The hatch pattern parallel to the axis of m_t corresponds to a variation of $\Gamma_l = 84.16 \pm 0.23$MeV, while the diagonal hatch pattern indicates the variation of the Standard Model prediction with M_H spanning the interval 60 GeV $\leq$ M_H $\leq$ 1000 GeV. The vertical bands indicates the experimental errors on the direct measurement of m_t from CDF/DØ, i.e., 175 ± 6 GeV.

Top quark mass and strong coupling constant

The cross-section and asymmetry measurements are also sensitive to the top quark mass m_t and α_s to a certain extent. In chapter 1, we have shown (in equation 1.36) that ρ_{eff} has a rather strong (quadratic) dependence on the top quark mass but much weaker with M_H [2]. Moreover, the strong coupling constant can be determined from the parameter R_l because

$$R_l = R_l(\alpha_s = 0)\,(1 \; + \; \delta_{\rm QCD}) \; , \tag{10.7}$$

which can be deduced from equation 1.34. The details of the QCD correction, $\delta_{\rm QCD}$, can be found in [8].

[2] It was found that with the set of data mentioned here it was very difficult to obtain any sensible constraint on M_H.

Using the previous 5 parameters in Table 10.2 (with all 93–94 leptonic and 93–95 hadronic data), a fit for extracting the mass of top quark and the α_s at $Q^2 = {M_Z}^2$ simultaneously was performed in the framework of the theoretical Standard Model calculation. The following results were obtained :

$$\alpha_s({M_Z}^2) = 0.102 \pm 0.008 \pm 0.002 \tag{10.8}$$

$$m_t = 181 \pm 21 \pm 15 \quad \text{GeV} \tag{10.9}$$

where the central values and the first errors quoted refer to $M_H = 300$ GeV while the second errors account for the variations of the results when varying M_H in the range 60 GeV $\leq M_H \leq$ 1000 GeV. Here, the correlation coefficient between m_t and $\alpha_s({M_Z}^2)$ is -0.597.

If we further impose $m_t = 175 \pm 6$ GeV (which is the updated result from the direct measurement of m_t from CDF/DØ at Fermilab) as a constraint in the Standard Model fit, the following value of strong coupling constant α_s at $Q^2 = {M_Z}^2$ was obtained :

$$\alpha_s({M_Z}^2) = 0.106 \pm 0.007 \pm 0.005 \tag{10.10}$$

where the errors have the same meaning as mentioned above.

10.3 Conclusion

The measurements of cross-sections and forward-backward asymmetries obtained by the inclusive and lepton-identified analyses have been compared in reasonable detail. The two results have been found to be consistent with each other. This supports the assumption of lepton universality.

Z^0 resonance parameters have also been extracted from this inclusive leptonic and the overall DELPHI hadronic data. The parameter, which the inclusive leptonic analysis is most sensitive to, has been determined to be $\Gamma_l = 84.16 \pm 0.23$ MeV, which is compatible both with the Standard Model prediction and with the direct measurement of the top quark mass m_t.

The 1995 energy scan around the Z^0 resonance peak has considerably improved the precision of Z^0 parameters, most importantly, M_Z and Γ_Z. The 1995 energy and lineshape analyses have not been finalized at the time of writing this thesis. The precision of these parameters may be further improved in the final version of their analyses at LEP which will remain unbettered for the forseeable future.

Appendix A

t-channel correction in A_{FB}

What is to be proved is that :

$$A^s_{FB} = A^{s+t}_{FB} \ - e_f(asym) \times A^{t-chan}_{FB} \tag{A.1}$$

where A^s_{FB} denotes the forward-backward asymmetry for leptons in s-channel, A^{s+t}_{FB} for leptons of all channels [1], A^{t-chan}_{FB} is the difference between the electron forward-backward asymmetry for all channels and that for s-channel, i.e., $A^e_{FB}(s+t) - A^e_{FB}(s)$, and $e_f(asym)$ is as in 5.20.

Here we assume an ideal detector with full coverage and no inefficiency. Let $N^{\mu/\tau}_F$ denote the number of muons and taus (of s-channel) in the forward region and $N^{\mu/\tau}_B$ in the backward region. Moreover, let N^e_F and N^e_B be the of number of electrons of all channels in the forward and backward regions respectively.

We then have the following equations :

$$A^{s+t}_{FB} = \frac{N^{\mu/\tau}_F - N^{\mu/\tau}_B + N^e_F - N^e_B}{N^{\mu/\tau}_F + N^{\mu/\tau}_B + N^e_F + N^e_B} \ , \tag{A.2}$$

$$e_f(asym) = \frac{N^e_F + N^e_B}{N^{\mu/\tau}_F + N^{\mu/\tau}_B + N^e_F + N^e_B} \ , \tag{A.3}$$

and

$$A^{t-chan}_{FB} = \frac{N^e_F - N^e_B}{N^e_F + N^e_B} - \frac{N^{\mu/\tau}_F - N^{\mu/\tau}_B}{N^{\mu/\tau}_F + N^{\mu/\tau}_B} \tag{A.4}$$

in which we have assumed universality that the s-channel forward-backward asymmetries of electrons, muon and taus are all the same and equal to

$$\frac{N^{\mu/\tau}_F - N^{\mu/\tau}_B}{N^{\mu/\tau}_F + N^{\mu/\tau}_B} \ .$$

[1] All channels actually include s-channel, t-channel and s–t interference.

Consider

$$
\begin{aligned}
& A_{FB}^{s+t} - e_f(asym) \times A_{FB}^{t-chan} \\
= & \frac{N_F^{\mu/\tau} - N_B^{\mu/\tau} + N_F^e - N_B^e}{N_F^{\mu/\tau} + N_B^{\mu/\tau} + N_F^e + N_B^e} - \\
& \frac{N_F^e + N_B^e}{N_F^{\mu/\tau} + N_B^{\mu/\tau} + N_F^e + N_B^e} \times \left(\frac{N_F^e - N_B^e}{N_F^e + N_B^e} - \frac{N_F^{\mu/\tau} - N_B^{\mu/\tau}}{N_F^{\mu/\tau} + N_B^{\mu/\tau}} \right) \\
= & \frac{(N_F^{\mu/\tau} + N_B^{\mu/\tau})(N_F^{\mu/\tau} - N_B^{\mu/\tau}) + (N_F^e + N_B^e)(N_F^{\mu/\tau} - N_B^{\mu/\tau})}{(N_F^{\mu/\tau} + N_B^{\mu/\tau})(N_F^{\mu/\tau} + N_B^{\mu/\tau} + N_F^e + N_B^e)} \\
= & \frac{(N_F^{\mu/\tau} - N_B^{\mu/\tau})}{(N_F^{\mu/\tau} + N_B^{\mu/\tau})} \\
= & A_{FB}^s
\end{aligned}
$$

The last step has assumed universality as before and also proves A.1.

Appendix B

Momentum compaction factor

The derivation here follows [65].

Consider that the nominal orbit is distorted and the orbit length changes from L to $L + \Delta L$, i.e.

$$L = \oint ds \quad \text{and} \quad (L + \Delta L) = L = \oint d\sigma \tag{B.1}$$

where ds is the infinitesimal path length on the equilibrium orbit while $d\sigma$ is on the adjacent distorted equilibrium orbit.

Let Δx be the radial displacement from the equilibrium orbit corresponding to $d\sigma$. By simple proportionality relation, to first order, we have

$$\frac{ds}{\rho} = \frac{d\sigma}{\Delta x + \rho} \qquad \text{or} \qquad d\sigma = \left(1 + \frac{\Delta x}{\rho}\right) ds. \tag{B.2}$$

where ρ is the radius of curvature of the equilibrium orbit.

But, Δx can also be expressed as :

$$\Delta x = D_x(s)\frac{dp}{p}. \tag{B.3}$$

$D_x(s)$ is the horizontal dispersion.

Combining equations B.2 and B.3, we have

$$d\sigma = \left(1 + \frac{1}{\rho} D_x(s)\frac{\Delta p}{p}\right) ds. \tag{B.4}$$

Taking the difference of the two equations in B.1 and using B.4, it becomes

$$\Delta L = \frac{\Delta p}{p} \oint \frac{D_x(s)}{\rho}\, ds. \tag{B.5}$$

By the definition of equation 6.8, the momentum compaction factor α_c can therefore be expressed as a function of $D_x(s)$ and ρ :

$$\alpha_c = \frac{\Delta\rho}{\rho} \Big/ \frac{\Delta p}{p} = \frac{1}{L} \oint \frac{D_x(s)}{\rho}\, ds. \tag{B.6}$$

A more detailed study (referred to [65]) further indicates that α_c scales with the horizontal betatron tune Q_x like :

$$\alpha_c \approx \frac{1}{Q_x^2}. \tag{B.7}$$

References

[1] C. N. Yang and R. L. Mills, "Conservation of Isotopic Spin and Isotopic Gauge Invariance", Phys Rev. **96** (1954) 191.

[2] G. 't Hooft, Nucl. Phys. **B33** (1971) 173; ibidem, **B35** (1971) 167.

[3] S. L. Glashow, Nucl. Phys **B22** (1961) 579;
S. Weinberg, Phys. Rev. Lett. 19 (1967) 1264;
A. Salam, "Elementary Particle Theory", in Proc. of the 8th Nobel Symp., p. 367, ed. N. Svartholm, Almqvist and Wiksell, Stockholm, (1968).

[4] G. Arnison et al., Phys. Lett. **122B**, 103 (1983). G. Arnison et al., Phys. Lett. **126B**, 398 (1983).

[5] M. Consoli and W. Hollik, "Electroweak radiative corrections for Z physics", in "Z Physics at LEP 1", Volume 1, p. 7, CERN 89-08 (1989).

[6] F. Berends, "Z Line Shape", "Z Physics at LEP 1", Volume 1, p. 89, CERN 89-08 (1989).

[7] Z. Kunszt and P. Nason, "QCD", "Z Physics at LEP 1", Volume 1, p. 373, CERN 89-08 (1989).

[8] D. Bardin et al., "ZFITTER : An Analytical Program for Fermion Pair Production in e^+e- Annihilation", CERN-TH 6443/92 (1992) ; and Phys. Lett. **B229** (1989) 405.

[9] DELPHI Collaboration, P. Aarino et al., Nucl. Instr. and Meth. **A303** (1991) 233.

[10] DELPHI Collaboration, P. Abreu et al., Nucl. Instr. and Meth. **A378** (1996) 57.

[11] S. Jadach et al., "Higher-Order Radiative Corrections to Low-Angle Bhabha Scattering : The YFS Monte Carlo Approach", preprint CERN-TH/95-38 (1995).

[12] R. Brun et al., "GEANT3", CERN report DD/EE/84-1, CERN Program Library Long Writeup W5013 (1987).

[13] Y. Belokopytov, B. Bouquet, T. Camporesi et al., "DELPHI Online Data Processing", DELPHI 92-145 DAS 131 (1992).

[14] L. Benetau, P.S.L. Booth, B. Bouquet et al., "Architecture and Performance of the DELPHI Trigger System", DELPHI 92-161 DAS 135 (1992).

[15] D. Bertrand and L. Pape, "TANAGRA User Guide, Vers 3.12", DELPHI 87-95 PROG 98 (1989).

[16] Y. Sacquin, "Description of the DELPHI DST Content Version 3.15", DELPHI 94-161 PROG 210 (1994).

[17] DELPHI Collaboration, "DELSIM, Delphi Event Generation and Detector Simulation User's guide", DELPHI 89-67 PROG 142 (1989).

[18] P. D. Dauncey, PHYANA - Offline Analysis Package (1990).

[19] Alexander Olchevski, private communication.

[20] J. Fuster, C. Lacasta, G. Valenti and J. Vallas, 'The 1st and 2nd level Trigger User Manual; Summary of the 1992 trigger performance', DELPHI 93-42 PROG 197 DAS 144 (1993).

[21] G. Montagna et al., Nucl. Phys. **B401** (1993) 3; and Comput. Phys. Commun. **76** (1993) 328.

[22] W. J. P. Beenakker et al., Nucl. Phys. **B349** (1991) 323.

[23] The working group on LEP energy, R. Assmann et al., "The energy calibration of LEP in the 1993 scan", Zeit. Phys. **C66** (1995) 567.

[24] The working group on LEP energy, "LEP Energy Calibration in 1993, 1994 and 1995", LEP Energy Group/96-05 (1996).

[25] P. Checcia, private communication.

[26] O. Nicrosini (co-author of TOPAZ0), private communication.
W. J. P. Beenakker (co-author of ALIBABA), private communication.

[27] The Working Group on LEP Energy and the LEP Collaborations, Phys. Lett. **B307** (1993) 187.

[28] The LEP Collaborations ALEPH, DELPHI, L3, OPAL and The LEP Electroweak Working Group, "Comibined Preliminary Data on Z Parameters from the LEP measurements and Constraints on the Standard Model", CERN-PPE/94-187 (1994).

[29] A.A. Sokolov and I.M. Ternov, "On Polarization and Spin Effects in the Theory of Synchrotron Radiation", Sov. Phys. Dokl. 8 (1964) 1203.

[30] D. P. Barber et al., Phys. Lett. **135B** (1984) 498.

[31] W. W. McKay et al., Phys. Rev. **D29** (1984) 2483.

[32] L. Arnaudon et al., "Accurate Determination of the LEP Beam Energy by Resonant Depolarization", Zeit. Phys. **C66** (1995) 45.

[33] A. Hofmann, "Transporting the Energy Calibration across optics", Proc. of the Third Workshop on LEP Performance, Chamonix, CERN-SL/93-19 (DI) (1993).

[34] The working group on LEP energy, L. Arnaudon et al., "The Energy Calibration of LEP in 1991", CERN-PPE/92-125 (1992).

[35] J. P. Gourber, "Properties of the LEP magnets", Proc. of the Second Workshop on LEP Performance, Chamonix (1992).

[36] M. A. Geitz, "Investigation of Environmental Effects on the LEP Beam Energy : Magnetic Field Perturbation", Diploma Thesis, RWTH Aachen, Germany, PITHA Nr. 96/14 (1996).

[37] The working group on LEP energy, R. Assmann et al., "The Energy Calibration of LEP in 1991", CERN-PPE/92-37 (1992).

[38] J. Billan, J. P. Gourber, K. N. Henrichsen, H. Laeger and L. Resegotti, "Influence of mortar-induced stresses on the magnetic characteristics of the LEP dipole cores", IEEE Trans. on Magnetics **24** (1988) 843.

[39] L. Arnaudon et al., "Effect of Terrestrial Tides on the LEP Beam Energy", CERN-SL/94-07 (BI) (1994).

[40] P. Melchior, "The Tides of the Planet Earth", 2nd edition, Pergamon Press (1993).
Program and input data from P. Melchior, International Centre for Earth Tides, Bruxelles, Belgium.

[41] J. Wenninger, "Radial Deformations of the LEP ring", CERN-SL/95-21 (OP) (1995).

[42] J. Wenninger, "Study of the LEP Beam Energy with Beam Orbits and Tunes", CERN-SL/94-14 (BI) (1994).

[43] Oracle Corporation, 500 Oracle Parkway, Redwood City, CA 94065, USA.

[44] B. Dehning, M. Geitz and A. Drees, "A Study of the Magnetic Dipole Field of LEP during the 1995 Energy Scan", CERN-SL/96-54 (BI) or LEP Energy Group/96-06 (1996).

[45] F. J. Lowes, "Remote measurement of earth-leakage currents", IMechE **C396/047** (1995) 107.

[46] P. Puzo and J. Yamartino, "Preliminary Centre-of-mass Energy Corrections from Dispersion and Collision Offset for the 1995 Scan", LEP Energy Group/96-01 (1996).

[47] E. Keil, "Truly Self-Consistent Treatment of the Side Effects with Bunch Trains", CERN-SL/95-75 (1995).

[48] J.M. Jowett, J. Wenninger and J. Yamartino, "Influence of Dispersion and Collision offsets on the Centre-of-Mass Energy at LEP", CERN-SL/95-46(OP) (1995).

[49] P. Galbraith, R. Genand, Y. Jacquemard and A. Beuret, "Jumps in the Magnetic Field induced by Current Spikes", Minutes of the 39th Energy Calibration Working Group (ECWG) Meeting, 1st Oct., 1993.

[50] M. D. Hildreth, G. Duckeck, G. Quast, G. Wilkinson and K. Yip, "Preliminary RF Corrections to the LEP Energy for the '95 Scan", LEP Energy Group/96-02 (1996).

[51] K. Henrichsen, "Field Display and Flux-Loop Performance in 1992", Proc. of the Third Workshop on LEP Performance, Chamonix, CERN-SL/93-19 (DI) (1993).

[52] M. Koratzinos, 'The Energy of LEP in the 1995 Scan – Dipole Model', LEP Energy Group/96-03 (1996).

[53] P. Renton, G. Wilkinson and K. Yip, "Studies of the LEP Energies in the 1993 and 1995 Scans", LEP Energy Group/96-04 (1996).

[54] A. Drees, contribution to the 95th LEP Energy working group meeting (14th June, 1996).

[55] T. R. Wyatt, "Further Studies of the Influence of Energy Calibration and Scanning Strategy on the Γ_Z Measurement at LEP", MAN/HEP/95/2 (1995).
P. Renton, private communication.

[56] Alain Blondel, contribution to the 92th LEP Energy working group meeting (17th May, 1996).

[57] LEP Electroweak Working Group, "A Combination of Preliminary LEP and SLD Electroweak Measurements and Constraints on the Standard Model", Internal Note, LEPEWWG/96-02 or DELPHI 96-121 PHYS 631 (1996).

[58] Detailed note in preparation by E. Lançon and A. Blondel.

[59] M. Sands, "The Physics of Electron Storage rings. An Introduction", SLAC-121 and UC-28 (1970).

[60] R. Jacobsen, "1993 LEP Energy Spread and Variation From Spot Size Measurements", ALEPH 94-060 (1994).
D. Strom, "Determination of the LEP energy spread from the longitudinal beam size in OPAL", OPAL Technical Note TN264, November 1994.

[61] E. Rossa, "Real Time Single Shot Three-Dimensional Measurement of Picosend Photon Bunches", CERN SL/94-79 (BI) (1994).
K. Hanke, "Measurement of the bunch length at LEP with a streak camera and comparison with results from LEP experiments", Diploma work, RWTH Aachen, Germany, PITHA Nr. 94/1 (1994).

[62] J. Wenninger, "Centre-of-Mass Energy shifts from Difference Dispersion and Collisions Offsets in Pretzel Operation at LEP, CERN-SL/95-64 (OP) (1995).

[63] F. James and M. Roos, "MINUIT - Function Minimization and Error Analysis", CERN Program Library D506 (1992).

[64] CDF Collaboration, "Measurement of the Top Quark Mass at CDF", contributed paper to ICHEP96, PA-08-018;
DØ Collaboration, "Measurement of the top mass from events with two isolated leptons produced in $p\bar{p}$ collisions at DØ", contributed paper to ICHEP96, PA-05-027;
DØ Collaboration, "Measurement of the top mass from events with single isolated leptons produced in $p\bar{p}$ collisions at DØ", contributed paper to ICHEP96, PA-05-028.

[65] P. J. Bryant and K. Johnsen, "The Principles of Circular Accelerators and Storage Rings", Cambridge University Press (1993).